DYNAMICS OF HARMONICALLY FORCED NONPREMIXED FLAMES

A Dissertation
Presented to
The Academic Faculty

by

Nicholas A. Magina

In Partial Fulfillment
of the Requirements for the Degree
Doctor of Philosophy in the
School of Aerospace Engineering

Georgia Institute of Technology
August 2016

DYNAMICS OF HARMONICALLY FORCED NONPREMIXED FLAMES

Approved by:

Dr. Tim Lieuwen, Advisor
School of Aerospace Engineering
Georgia Institute of Technology

Dr. Lakshmi Sankar
School of Aerospace Engineering
Georgia Institute of Technology

Dr. Jerry Seitzman
School of Aerospace Engineering
Georgia Institute of Technology

Dr. Wenting Sun
School of Aerospace Engineering
Georgia Institute of Technology

Dr. Devesh Ranjan
School of Mechanical Engineering
Georgia Institute of Technology

Date Approved: April 6, 2016

[To the students of the Georgia Institute of Technology]

ACKNOWLEDGEMENTS

It would take an additional thesis length document to fully express my thanks and appreciation for all the support I have received over the years. All my family which has provided persistent and unfaltering encouragement and love. All my friends which helped keep me sane and (relatively) well-balanced (most likely implicitly extending my academic career 😑). All the wonderful people at the Ben T. Zinn Combustion Laboratory, foreign scholars, undergraduate students, graduate students, and Bobby Nobles alike, which helped keep my research/work focused, of the highest quality, and on track. All the "Students of Lieuwens Past", such as Donghyuk (i.e. Tom) Shin, Vishal Acharya, and, Ben Emerson who were infinite sources of wisdom and mathematical prowess. All my Georgia Tech resources, including academic advisor Dr. Lakshmi Sankar, undergraduate research advisor Dr. Mitchell Walker, and countless other staff members. My thesis committee, who recklessly agreed to read and assist with this dissertation. Professor/Dr/ Advisor/Friend/Mentor/ Tim Lieuwen who took a chance on me, throwing me into the warzone that calls itself the theory group, and introducing me to the fascinating topic of flame dynamics. He (who has also sent me emojis on ***two*** different platforms, as well as taught me some new words/spellings throughout my in-paper review comments) is truly the best graduate research advisor I could have asked for. My mom, who is the bravest, strongest, and most determined person I know, reminding me the value of hard work and how she is always right, and my dad, who possesses infinite patience, resolve, composure, and work ethic, reminding me to wake up on time and to eat lunch. But for brevity sake, this will have to do. Thank you. It is hard to believe that this wonderful academic adventure has reached this milestone. √ Life goal/dream achieved.

This work has been partially supported by the National Science Foundation under contract CBET-1235779, contract monitor Professor Ruey-Hung Chen, and by the US Department of Energy's University Turbine Systems Research Program under contracts DEFG26-07NT43069 and DE-NT0005054, contract monitor Mark Freeman. Although it may not be a direct and instantaneous return on investment, like many experimental efforts, and the assumptions and simplifications imposed on a "real system" in order to make the problem tractable seem unpractical, the use of analytical techniques to decipher and truly **understand** flame dynamics is extremely powerful and elucidating, enabling better designs and faster problem resolution. It is by their continual and persistent thirst for knowledge and deep understanding that this work was possible.

TABLE OF CONTENTS

LIST OF TABLES

LIST OF FIGURES

LIST OF SYMBOLS AND ABBREVIATIONS

$\mathscr{D}$: diffusion coefficient
Fr : Froude number
L_f : flame length measured in flow direction
M : molecular weight
P : pressure
Pe : Peclet number
$\dot{Q}$: spatially integrated heat release rate
R_f : radial distance to fuel lip
R_w : radial distance to confining wall
Sk : Stokes number
St_{L_f} : Strouhal number based on flame length, $f\,L_f / u_{x,0}$
St_R : Strouhal number based on fuel port half-width, $f\,R_f / u_{x,0}$
St_p : Strouhal number definition for premixed flames, $St_{L_f} / \cos^2\theta$
St_ω : Strouhal number utilizing angular frequency, $\omega\,R_f / u_{x,0}$
T : period of oscillation
$\mathscr{T}$: temperature
$\mathscr{T}_a$: ambient temperature
$\mathscr{T}_f$: adiabatic flame temperature
U_c : experimentally observed wrinkle convection velocity
U_n : normal component of mean velocity
U_r : experimentally observed radial flow velocity
U_x : experimentally observed axial flow velocity
$U_{0,\mathrm{des}}$: experimentally targeted fuel and oxidizer axial flow velocity
V : atomic diffusion volume
Y : species mass fractions
$\mathcal{Z}$: rescaled mixture fraction
$\tilde{\mathcal{Z}}$: true mixture fraction
$\mathcal{Z}_{st}$: stoichiometric mixture fraction value
$\mathcal{Z}^*$: experimentally utilized mixture fraction value
f : forcing frequency
f_b : buoyant natural instability frequency
f_f : experimental forcing frequency
g : gravitational force
n : coordinate normal to unforced flame front
r : coordinate in the radial direction
s : ratio of fuel port radius to wall radius, R_f / R_w
s_c : flame consumption speed
s_d : flame displacement speed
u : scalar velocity components
u_c : wrinkle convection velocity
u_n : velocity in the n-direction

u_r : velocity in the *r*-direction (radially)
u_x : velocity in the *x*-direction (axially)
x : coordinate in the flow direction; axial
y : coordinate normal to the flow direction; transverse
z : coordinate perpendicular to *x*-*y* plane
θ : local angle of flame surface with respect to axial coordinate
θ_{pq} : phase between the pressure and heat-release oscillations
∇ : gradient operator
δ : model piecewise linear inlet mixture fraction profile thickness
δ_f : experimentally extracted flame thickness
ε : small perturbation amplitude parameter
λ : wavelength corresponding to u, u / f
λ_c : wavelength corresponding to u_c, u_c / f
σ_c : Markstein length
σ_C : scaled Markstein length
$\hat{\sigma}_c$: rescaled Markstein length
ω : angular frequency, $2\pi f$
ξ : flame position measured in *y*- , *r*-, or *n*-direction
φ_{ox} : stoichiometric mass ratio of oxidizer to fuel
$(\,)_{st}$: stoichiometric value
$(\,)_0$: mean/steady state component
$(\,)_1$: fluctuating component
$\hat{(\,)}$: frequency domain variable
$\tilde{(\,)}$: non-dimensional form of a variable
$\bar{(\,)}$: time average

SUMMARY

This thesis describes the dynamics, both spatio-temporal and heat release, of harmonically excited non-premixed flames. Analytical, numerical, and, experimental analyses were performed, along with combined analyses methods, to study excitation and evolution of wrinkles on the flame front. Comparisons to established premixed flame dynamics are made throughout. Modern gas turbines, along with other various advanced combustion systems, face major challenges from the onset of combustion instabilities. In order to avoid this problem, or to utilize it advantageously, an in-depth understanding of the flame front dynamics is required. This thesis is devoted to elucidating the governing features of these complex combustion dynamic problems, and figuring out how to utilize this knowledge to improve existing or design better combustion systems.

The space-time dynamics of the non-premixed flame sheet in the fast chemistry limit is described by the stoichiometric mixture fraction surface, extracted from the solution of the $\mathcal{Z}$ -equation. This procedure has some analogies to premixed flames, where the premixed flame sheet location is extracted from the G=0 surface of the solution of the G-equation. A key difference between the premixed and non-premixed flame dynamics, however, is the fact that the non-premixed flame sheet dynamics are a function of the disturbance field everywhere, and not just at the reaction sheet, as in the premixed flame problem. Although appearing subtle, this point is what makes the non-premixed flame dynamics problem unique and significantly more complicated, requiring a completely new solution approach. Although mixture fraction field solutions are

obtainable, extensive mathematical techniques are used in order to obtain explicit space-time and heat release solutions for the flame dynamics.

The heat release dynamics are also complicated due to the significant mixture fraction field gradients encountered in non-premixed flame problems, which are often strong functions of spatial location. The local heat release distribution has been shown to have a strong axial dependence, and the flame surface area no longer remains the sole dominant heat release parameter, as the reactant mass burning rate takes an important form. The spatially integrated heat release, $\dot{Q}(t)$, is of particular interest for combustion instability or noise related issues for acoustically compact flames, and thus this surface integral over the reaction sheet will be examined extensively, often times through the use of a flame transfer function. This useful measure provides an input-output relationship between the forcing characteristics and the resulting heat release dynamics.

Starting simply, a two-dimensional model problem was investigated in the $Pe \rightarrow \infty$ limit, exposed to spatially uniform forcing. An explicit expression for the space-time dynamics of the flame sheet was obtained, which shows the importance of velocity fluctuations normal to the mean flame surface and the role of axial convection in propagating flame wrinkles downstream, leading to nodes and anti-nodes in the flame response, similar to premixed flames. In addition, an explicit heat release transfer function was obtained along with equations for the contributions due to area and mass burning rate fluctuations. Differing completely from premixed flames, non-premixed flames heat release dynamics are dominated by mass burning rate fluctuations. Their gain sensitivities both tend towards unity at low *St* values, but the non-premixed flame response is larger than premixed flames for $St \sim O(1)$.

Inclusion of axial diffusion in the non-premixed governing equation, i.e. finite *Pe* values, was shown to correlate to enabling burning velocity stretch sensitivity in the premixed case, introducing additional flame front physics, such as wrinkle dissipation and dispersion. These effects act to smooth the wrinkle magnitude and phase, abolishing previously spatio-temporal nodes. The heat release response of non-premixed flames was analytically shown to roll off much slower with frequency, $O(St^{-1/2})$ compared to $O(St^{-1})$ for premixed flames, implying increased sensitivity to flow perturbations than premixed flames at high Strouhal numbers. The asymptotic tendencies of the non-premixed flame, however, are largely controlled by the near burner exit region with high transverse gradients and, thus, are expected to be quite sensitive to burner exit details and finite chemistry effects.

Desiring consistency, other qualitatively new features resulting from the inclusion of axial diffusion to the problem were investigated. In particular, back diffusion alters the steady state and fluctuating mixture fraction profiles entering the domain, i.e. the inlet profiles. Although for analytical tractability we previously prescribed the inflow boundary condition, the proper treatment of this feature renders the problem analytically intractable and so it must be solved computationally. It also causes the leading edge position of the flame front to oscillate, even for infinitely fast chemistry. In addition, it introduces a three-zone structure into the asymptotic character of the unsteady heat release, so that the flame transfer function is $O(1)$ for $St<<1$, $O(1/St^{1/2})$ for intermediate Strouhal numbers, and $O(1/St)$ for very high Strouhal numbers. Differentiating between inflow boundary and dynamical effects on the flame dynamics is essential to understanding non-premixed flame dynamics.

Realizing the limitations of two-dimensional analyses, a three-dimensional geometry was investigated exposed to various three-dimensional forcing configurations, including axial, transverse, and convecting helical disturbances. The results show the significance of phase interference processes, due to wrinkle convection in the axial and azimuthal direction, in controlling the space-time wrinkle characteristics. Significantly, these results show that these different induced fluctuations exhibit very different sensitivities to helical mode number, swirl strength, and dimensionless forcing frequency. The helical mode with the dominant contribution to local flame wrinkling is generally different from the mode with dominant contribution to spatially integrated heat release fluctuations. In fact, only the axisymmetric, m=0, mode leads to heat release fluctuations in both premixed and non-premixed axisymmetric flames.

Efforts have been made to obtain an equation for the wrinkle dynamics directly, as is done for the premixed problem, rather than having to solve for the mixture fraction field first. As this desired partial differential equation for the fluctuating flame front is an equation for a specific iso-surface with variables evaluated at this surface, the result is not straightforward. However, an equation was obtained for the limiting case of Pe>>1, which produces consistent results with previous results obtained using established methods.

Lastly, experimental efforts were performed in order to assess the validity of previously utilized assumptions, accuracy of purely analytical models, and to investigate real life diffusion flame behavior. High speed PIV data was taken on a coflowing methane-air diffusion flame, equipped with speakers for harmonic forcing, over a variety of flow velocities, forcing frequencies, and forcing amplitudes. These measured velocity

fields were used as inputs to a $\mathcal{Z}$ -equation solver, and the resulting space-time dynamics of iso- $\mathcal{Z}$ surfaces were extracted from the $\mathcal{Z}$ field solutions. Both experimental and numerical results show that flame wrinkles propagate axially at the mean flow velocity, a result consistent with previous analytical findings. These wrinkles start with near zero magnitude at the fuel tube lip and grow with downstream distance, until peaking at some axial location. Further downstream, the wrinkle magnitude modulates, indicative of interference effects which have been previously predicted in analytical studies. The largest discrepancies between calculations and results are observed near the burner lip, and it is shown that these are due to errors in predicted spreading angle of the unforced non-premixed flame at the attachment point. These errors in spreading angle, in turn, are likely due to errors in computed inflow mixture fraction profiles at the burner exit, illustrating the importance of predicting the time averaged mixture ratio for predicting the flame wrinkle dynamics.

Body force effects, i.e. gravity and buoyancy, neglected in the models, were observed to significantly influence the steady state flame shape, a key input to our dynamical results, since velocity fluctuations normal to the mean flame are important. Modified analytical models were also developed to account for this accompanying flow acceleration effect.

Some of the key results of this thesis involve comparing the space-time and heat release dynamics predicted by these various analysis methods. These comparisons will demonstrate the accuracy of the various models and the validity of the assumptions utilized. They will also shed light onto prioritizing what to improve in future works.

CHAPTER 1

Introduction

1.1 Motivation

Flames, fire, and combustion have been observed and contemplated from earliest times. Rigorous evidence of controlled fire generation and use was found at Neanderthal camp sites, dating to between 71 and 91 thousand years ago [1]. Less concrete evidence can push this date back to ~300,000 years ago when hominins started using fire to alter tools. Possible hearths have also been found corresponding to this date, although little information exists on whether they were controlling natural fire or producing it of their own accord. Preliminarily, there is speculation (and circumstantial evidence) of fire use as early as 800,000 years ago. “Burnt material” found in clusters could perhaps indicate fires, although none of the actual fires have been found. Further, the frequency of these clusters is low and so exploitation of natural fire could be a cause.

The various explanations for fire and combustion has also greatly changed over time. The Greeks interpreted combustion in terms of philosophical doctrines, one of which was that a certain “inflammable principle” was contained in all combustible bodies and this principle escaped when the body was burned to react with air [2]. The existence of fire was also thought to be the result of Prometheus’ brave act of stealing fire from Zeus, for all of mankind. The inadequacy of these various theories became apparent only in the late 18th century, when it proved unable to explain a host of new facts about

combustion that were being observed for the first time as the result of increasing accuracy in laboratory experiments.

One fact that is well established is the importance of combustion as part of our cultural evolution. Taking advantage of two of its defining features, it allowed us to extend daylight hours artificially, keep warm, and efficiently process a wider range of foods. It also enabled the modification of various objects and materials into more useful forms. Today, combustion's highly exothermic nature is harnessed for many different purposes, in devices with a wide range of complexities. Gas ovens, heating devices, steam engines, internal combustion engines, transportation devices, explosives, and fossil fuel power plants are just a few different ways that combustion reactions are used in our modern world.

As we grow as a civilization, so does our desire and need for harnessable power and energy. Burning of fossil fuels has long existed as one such method, and although the world is currently undergoing a Green Movement towards renewable energy sources for various specific applications, combustion remains and will continue to remain the dominant method for providing useful energy.

However, "with great power comes great responsibility"… and regulations, costs, emission taxes, and restrictions, because albeit all the benefits and uses of combustion, some of the negative side effects of burning fossil fuels has become a concern, primarily the production of harmful pollutants such as unburned hydrocarbons (UHC), nitrogen oxides (N_yO_x), sulfur oxides (SO_x), carbon monoxide (CO), etc. Causing major climate change concerns, potential risks to both air and water quality, as well as health concerns to living creatures, the quantity of these byproducts emitted need to be minimized. In

addition to these socio-environmental reasons, federal regulations have been imposed by the US Environmental Protection Agency, as shown by Figure 1.1, which are constantly tightening. Although making system design and engineering more complicated, these methods have succeeded in evolving towards cleaner technologies, as shown by Figure 1.2.

Pollutant [final rule cite]		Primary/ Secondary	Averaging Time	Level	Form
Carbon Monoxide [76 FR 54294, Aug 31, 2011]		primary	8-hour	9 ppm	Not to be exceeded more than once per year
			1-hour	35 ppm	
Lead [73 FR 66964, Nov 12, 2008]		primary and secondary	Rolling 3 month average	0.15 µg/m^3 (1)	Not to be exceeded
Nitrogen Dioxide [75 FR 6474, Feb 9, 2010] [61 FR 52852, Oct 8, 1996]		primary	1-hour	100 ppb	98th percentile of 1-hour daily maximum concentrations, averaged over 3 years
		primary and secondary	Annual	53 ppb (2)	Annual Mean
Ozone [73 FR 16436, Mar 27, 2008]		primary and secondary	8-hour	0.075 ppm (3)	Annual fourth-highest daily maximum 8-hr concentration, averaged over 3 years
Particle Pollution Dec 14, 2012	$PM_{2.5}$	primary	Annual	12 µg/m^3	annual mean, averaged over 3 years
		secondary	Annual	15 µg/m^3	annual mean, averaged over 3 years
		primary and secondary	24-hour	35 µg/m^3	98th percentile, averaged over 3 years
	PM_{10}	primary and secondary	24-hour	150 µg/m^3	Not to be exceeded more than once per year on average over 3 years
Sulfur Dioxide [75 FR 35520, Jun 22, 2010] [38 FR 25678, Sept 14, 1973]		primary	1-hour	75 ppb (4)	99th percentile of 1-hour daily maximum concentrations, averaged over 3 years
		secondary	3-hour	0.5 ppm	Not to be exceeded more than once per year

as of October 2011

Figure 1.1. US Environmental Protection Agency's National Ambient Air Quality Standards as established by the Clean Air Act [3].

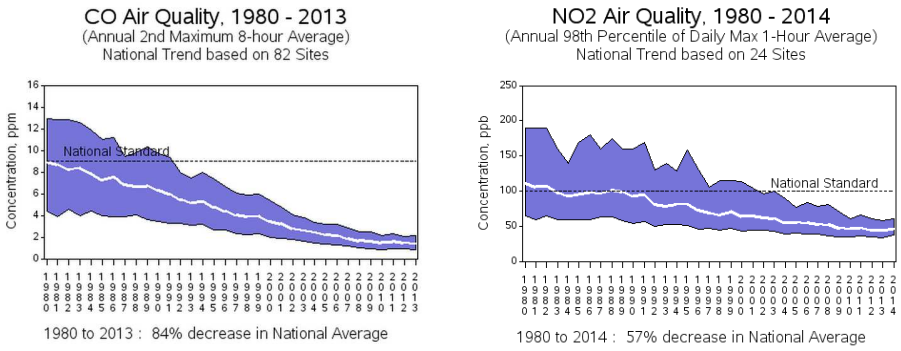

Figure 1.2. National CO and NO_2 Air Quality Trends from 1980-2013 [3].

While post device treatment is one option, it is generally preferred to avoid the formation of these pollutants in the combustion system rather than implementing post combustion system cleanup, in order to avoid the additional capital and maintenance costs of cleanup equipment [4]. The emission of sulfur oxides can be effectively

minimized by removing sulfur from the fuel in the preprocessing stage, a commonly established technique. However, carbon monoxide and nitrogen oxides, both of whose elemental components originate from the primary reactants, i.e. hydrocarbon fuel and air, cannot be completely removed in the burning process, but rather their production and ultimate emission levels must be minimized by controlling the combustion process.

As this process involves a plethora of chemical kinetic interactions, with a multitude of species, it could encompass a thesis dissertation on its own. However, the CO and NO_x reaction mechanisms are of focus for combustor designers, and it is understood that over most of the operating range for combustors these evolve with opposing trends. For example, over the premixed burning process, CO decreases by conversion into CO_2, while NO_2 increases being mainly produced from NO, processes which both occur more rapidly at higher temperatures. One decreases with residence time and temperature while the other increases; thus a balance must be found that satisfies ALL of the emission regulations. In addition, performance metrics must be factored in, such as power and thermal efficiency, which increase with inlet pressure and temperature, durability, stability, and operability limits [5].

Accordingly, new combustion systems and thermodynamic cycles have been proposed to meet this cocktail of emission regulations and performance desires. Catalytic combustion, for example, reduces pollutant formation, with the tradeoff of high costs, low durability, and safety concerns. Rich-burn quick-mix lean-burn (RQL) combustion reduces NO_x and expands fuel diversity, yet suffers from soot formation and durability problems. Dry low NO_x (DLN) lean-premixed combustion has the advantages of massive NO_x reduction and control, but suffers with flashback, lean blow out, and combustion

instabilities. Significant efforts have been put into resolving these operability issues in premixed systems, since their NO_x reduction potentials are so large, however, the issue of combustion instabilities, being part of the broader topic of combustion dynamics, remains at large and is the key motivator for this thesis work.

Thus in summary, combustor design must allow an optimal residence time for CO oxidation while minimizing the formation of NO_x during the CO burnout process, all the while obtaining high levels of power and thermal efficiency, with reasonable durability and operability limits, whilst avoiding combustion instabilities… seems easy enough.

1.2 Combustion Instabilities

As someone who has gone camping probably knows, or perhaps a s'mores connoisseur, when gathered around the hearth there is a distinctive sound made by the fire. This fact is also elaborated upon by writers who often times describe fires as "roaring". Flames can be thought of as volumetric sources, and the fundamental mechanism for this sound generation is the unsteady gas expansion as the mixture reacts. In fact a whole discipline called thermoacoustic instabilities encompasses the study of acoustic oscillations excited by thermal sources. Focusing specifically on combustion-driven oscillations, denoted "singing flames" by early scientists, studies found that spontaneous acoustic oscillations of considerable amplitude could be generated when a flame was confined inside a larger-diameter tube [4]. For unconfined flames, this is manifested as broadband noise emitted by turbulent flames, while for confined flames, these oscillations generally manifest themselves as discrete tones at the natural acoustic modes of the system.

Combustion instabilities, characterized by large-amplitude oscillations of one or more natural acoustic modes of a combustor, are spontaneously excited by a feedback loop between an oscillatory combustion, i.e. heat release, process and one more of these natural acoustic modes, as depicted in Figure 1.3. They have been encountered during the development and operation of various propulsion devices, power generation equipment, heating systems, and industrial furnaces and are problematic because of the large amplitude pressure and velocity oscillations they produce. Having the potential to be on the order of thousands of psi swings in fractions of seconds, these oscillations can result in thrust oscillations, severe vibrations that interfere with control-system operation, enhanced heat transfer and thermal stresses to combustor walls, oscillatory mechanical loads that result in component fatigue, and flame blowoff or flashback [6]. All of these issues may result in premature component or system wear leading to costly shutdown or even catastrophic failure. Thus, in order to develop efficient, safe, and eco-friendly combustion systems, the understanding of combustion instabilities is a key step.

Figure 1.3. Schematic depicting the combustion instability feedback loop (left) and an image of gas turbine blade damage due to combustion instabilities (right).

1.2.1 Issue Realization

Early detection of combustion instabilities dates all the way back to 1777, and relied on sensory observation [7]. It was found that confining gas flames in a larger-diameter tube could yield spontaneous acoustic oscillations of considerable amplitude, denoted “singing flames”. Unknowingly only studying half of the feedback loop (the same half that is focused upon in this thesis), in 1858 the sensitivity of flames to music was noted, denoted “dancing flames”, as musical party guests observed the flame exhibiting “pulsations exactly synchronous with the audible beats”, so significant at times that “a deaf man might have seen the harmony” [8].

With the development of high-intensity combustion systems, combustion oscillations moved beyond academic curiosity and party tricks. Detrimental, combustion-driven oscillations have been observed in boilers, blast furnaces, and a variety of other oil, coal, and gas-fired heating units causing serious safety and performance concerns [9]. Landfill gas flares have been historically susceptible to these, while burning off excess gas. Instabilities have also been a major challenge for aircraft and rocket propulsion system development, causing numerous delays, destroyed hardware, and wasted money.

The iconic F-1 engine, responsible for powering the Saturn rockets and placing men on the moon, experienced tremendous instability problems during its development. Instabilities with amplitudes up to 100% of the mean combustor pressure (2000+ psi) with frequencies in the 200-500 Hz range were experienced, and due to the lack of proper understanding of the instability dynamics at the time, engineers had to rely on expensive repeated trial and error experiments (3000+ full scale tests) to mitigate the issue and make the rocket functional [6]. The solution involved welding a series of baffles to the

injector face in order to prevent the excitation of transverse acoustic oscillations. Pogo oscillations are another potentially dangerous type of self-excited combustion oscillation occurring in liquid fuel rockets, responsible for delaying several rocket launching missions over the past few decades [10]. In addition, many solid rockets have experienced instability issues during their development and life, such as the Space Shuttle solid-propellant rocket boosters, Standard Missile (SAM), Sidewinder (AIM), Harm (ASM), Trident (SLBM), Hellfire (ASM) and Minuteman (ICBM) just to name a few [11].

For example, in rocket engines, it is known that longitudinal oscillations cause severe damage to the combustion chamber. Figure 1.4 shows the time trace of unsteady pressure inside a solid rocket motor, where two pulses are utilized to excite instabilities. The first small pulse excites the tangential oscillation, which is small compared to the mean pressure. However, the second larger pulse excites longitudinal oscillations, leading to significant fluctuations in the pressure, along with an increase mean pressure. This depicts an example of a subcritical instability, where the system is stable with respect to small-amplitude disturbances but is unstable when subjected to larger disturbances. This illustrates the high sensitivity of rocket systems to small external disturbances, such as fuel composition, something passing through the nozzle, or sudden changes in burning conditions.

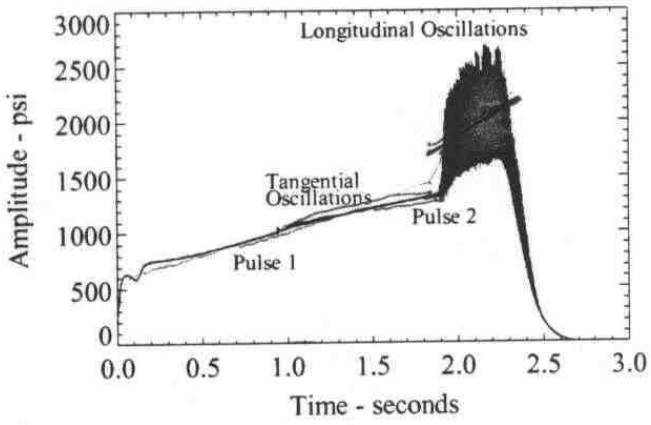

Figure 1.4. Example of solid rocket motor experience from Blomshield [12].

Gas turbines and advanced high-speed propulsion devices are not exempt from having to deal with the issue of combustion instabilities, and rather the modern design and operation of these technologies places themselves directly in harm's way. In the context of gas turbines, burning at lean operating conditions is attractive from the standpoint of reduced NO_x formation, whereas in propulsion devices, such as ramjet engines, burning under near-stoichiometric conditions is desirable as this leads to enhanced heat release and therefore high performance. However, both of these desired results push towards operating conditions where the onset of combustion instabilities is prevalent.

Combustion instabilities will continue to be a challenge as long as heat release is a dominant energy source for our advancing world. Early attempts at mitigating and avoiding these instabilities involved costly "trial and error" methods or tests. A rudimentary diagnostic technique consisted of detonating small explosive charges outside the combustion chamber while the engine was firing, allowing engineers to observe chamber response to sudden condition fluctuations. However, in order to prevent detrimental safety or performance concerns, or to eliminate the chance for catastrophic or

mission failure, more robust diagnostic, issue identification, and, prediction techniques are required. These will aid in the understanding of combustion dynamics, allowing better energy extraction from chemical reactions in clean, safe, and efficient way.

1.2.2 Understanding the Combustion Instability

As a starting point for understanding combustion instabilities, we can look no further than a park playground. A playground swing is a perfect example of a resonant system, with its own (rider independent) resonant, or natural, frequency given by:

$$f = \frac{1}{2\pi}\sqrt{\frac{g}{L}} \tag{1.1}$$

assuming small displacement amplitudes. Certain forcing patterns, pulsing in sync with the swings back and forth cycle, can be applied to the swing to make it resonate, increasing its amplitude with each cycle. It only takes a very small force, but it has to be well-timed to get an enjoyable ride. Luckily, this particular system is naturally limited, Eq.(1.1) losing validity at large swing amplitudes, saving the rider from spinning over the top or flying off the swing.

This same principle applies to combustion systems. Each combustion chamber contains various natural acoustic modes, which are geometry dependent, and the forcing pattern comes from the flame's fluctuating heat release, i.e. acting as an unsteady source of volume or sound. Lord Rayleigh was the first one to take note of this effect, stating the conditions under which a periodic heat addition process adds energy to acoustic oscillations, yielding self-excited oscillations, in his book, *The Theory of Sound* [13]:

"If heat be periodically communicated to, and abstracted from, a mass of air vibrating (for example) in a cylinder bounded by a piston, the effect produced will depend upon the phase of the vibration at which the transfer of heat takes place. If heat be given to the air at the moment of greatest condensation, or be taken from it at the moment of greatest rarefaction, the vibration is encouraged. On the other hand, if heat be given at the moment of greatest rarefaction, or abstracted at the moment of greatest condensation, the vibration is discouraged."

This criterion, named the Rayleigh criterion, states that a periodic heat-transfer process, such as combustion, locally adds (removes) energy to (from) the acoustic disturbances if unsteady heat release and unsteady pressure are in (out of) phase, represented as $0 < |\theta_{pq}| < 90$ ($0 < |\theta_{pq}| < 90$). However, simply transferring energy from the combustion process to the acoustic field, does not necessarily imply that the combustor is unstable. Acoustic oscillations are **spontaneously** excited in a combustor **only** when the rate of energy supplied by the periodic combustion process to the acoustic field is larger than the rate at which acoustic energy is dissipated within the combustor and/or transmitted through its boundaries [6]. This idea can be formulated mathematically as [9]:

$$\int_V \int_T p'(x,t)q'(x,t)\,\mathrm{d}t\,\mathrm{d}V > \int_V \int_T \sum_i L_i(x,t)\,\mathrm{d}t\,\mathrm{d}V \qquad (1.2)$$

where $p'(x,t)$ and $q'(x,t)$ are the combustor pressure and heat-addition oscillations respectively, and $L_i(x,t)$ are the various acoustic energy loss processes. The left hand side of this expression shows Rayleigh's integral, which is positive (negative) if the combustion process adds (removes) energy from the acoustic oscillations locally. The

sign of this integral depends on the phase difference between the heat-release and pressure oscillations and is positive (negative) when this phase difference is smaller (larger) than 90 deg.

Figure 1.5 depicts the generic feedback loop responsible for combustion instabilities schematically. It consists of a series of sequential events, wherein fluctuations in the velocity and/or thermodynamic-state variables induce a fluctuation in the heat-release rate; the heat release fluctuation then excites acoustic oscillations; and the acoustic oscillations generate the velocity and thermodynamic state variable fluctuations, thus closing the feedback loop. As will be discussed later, this thesis focuses on the flames response to velocity fluctuations, identified with a red arrow in Figure 1.5.

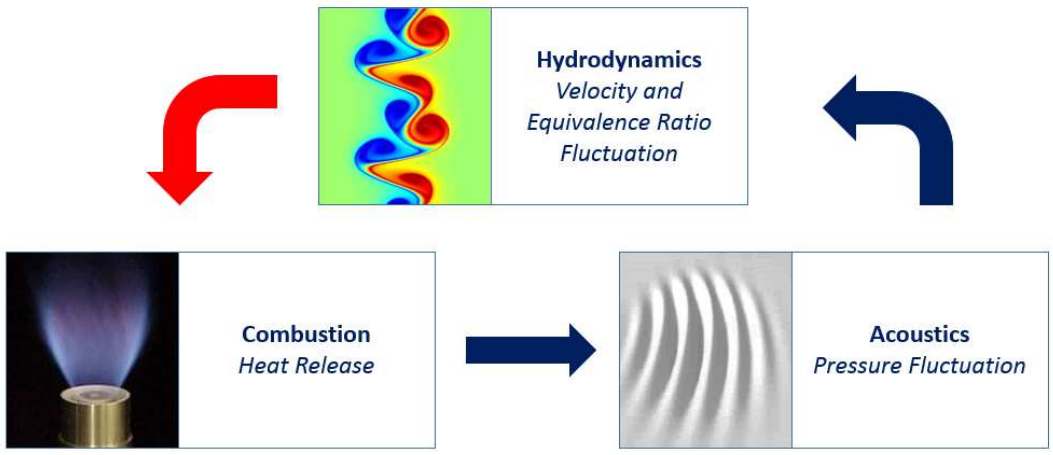

Figure 1.5. Schematic depicting the generic feedback loop responsible for combustion instabilities.

Depending on the relative magnitudes of the energy added and removed from the acoustic oscillations, the amplitude of oscillations may decrease, remain constant, or grow during each cycle of this loop, the latter of which are denoted as combustion instabilities [6]. Some mechanisms, participating in the tug of war for stability, capable of adding and removing energy from an unstable mode are shown in Table 1.1. The

particular driving mechanism of interest in this study is, once again, denoted in red. If only a small amount of available energy (sometimes less than one percent) is diverted to an acoustic mode, combustion instability can be generated.

Table 1.1. Mechanisms capable of driving/damping combustion instabilities

Driving mechanisms	Damping Processes
Fuel feed line-acoustic coupling	Viscous and heat-transfer damping
Equivalence-ratio oscillations	Convection and/or radiation
Uneven atomization, vaporization, mixing	Transfer of energy between acoustic modes
Oscillatory flame-area variation	
Vortex shedding	

Thus, on the surface, it seems that combustion instabilities are easy to identify and understand, requiring only knowledge of the pressure and unsteady heat release, along with a plug-and-chug evaluation technique for Eq.(1.2). This however, is not the case, and would make for a rather boring thesis. Although the above discussions pinpoint the basic components that induce the dynamic instability, the problem of understanding and modeling, is a precise quantification of both the dynamics of these individual components and of all of the coupling mechanisms between them to produce the stability behavior.

Complex intra-modal coupling processes occur at boundaries, in regions of flow inhomogeneity, and through nonlinearities, altering the individual oscillatory parameters. In addition, several unsteady flame-flow interactions, acting over a large range of scales, contribute to the overall combustor dynamics, such as acoustics, fluid dynamics, transport processes, chemical kinetics, flame kinematics, heat transfer, feedline dynamics of the reactants, and atomization or vaporization dynamics. Adding to the complexity, these components then couple with each other in variety of different ways. Two such coupling schematics are illustrated in Figure 1.6.

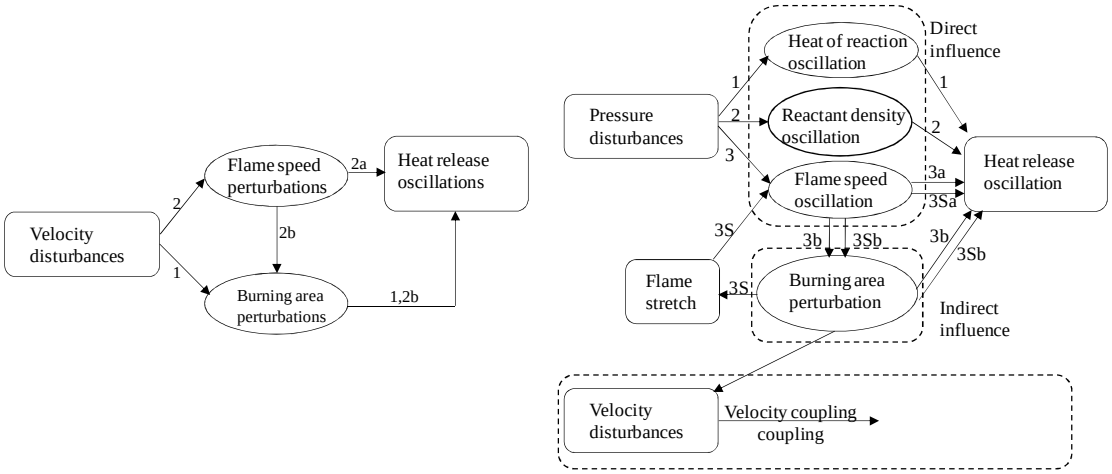

Figure 1.6. Schematic depicting the physical mechanisms through which velocity (left) and acoustic pressure fluctuations (right) lead to heat release oscillations. Note the velocity mechanism is referred to within the acoustic schematic [4].

1.2.3 A Daunting Task

An accurate and detailed modeling of such a complex system with all of its couplings is an extremely challenging task. Dynamic models that quantify all of the interactions and predict all system properties have to include an extremely large range of time and length scales. Therefore, these various coupling mechanisms and pathways, depicted in Figure 1.6, are dissected and scrutinized one by one. For example, as it is the focus of this thesis, the key physical process behind the mechanism by which flow perturbations lead to heat release oscillations is the distortion of the flame surface by the oscillatory flow, leading to oscillations in burning area [14, 15]. These distortions in flame surface then lead to additional secondary effects through unsteady burning rate and stretch. This is the reason this study encompasses both space-time and (then) heat release dynamics.

Thus, to make this work empirically relevant, various basic instability characteristics must be predicted and understood, such as the frequency of the oscillations,

the conditions under which the oscillations occur, and their final limit-cycle amplitude. This implicitly requires a sound understanding of the processes responsible for driving and damping along with oscillation signal properties, such as spatio-temporally varying magnitude and phase. The introduction of instability active control, which is a current topic of interest for many, adds the additional requirement for the study of actuator dynamics, and its interactions with all of the above.

The saving feature in such a daunting task is the strong spatial coherence that accompanies several of the thermoacoustic instabilities, so that approximations such as acoustically compact or infinite chemistry flames can be utilized to bring order to the chaos. Additionally, definitions and analysis tools have been discovered to aid understanding of these interactions, such as flame transfer functions. Dowling developed a theory for nonlinear oscillations [16], exploiting the fact that the main nonlinearity is in the heat release rate, which essentially saturates, and the amplitudes of the pressure fluctuations are sufficiently small that the acoustic waves remain linear. Thus, gas dynamic processes essentially remain in the linear regime, even under limit cycle operation [17]. For a linear process, a transfer function is a useful tool to understand instabilities as it provides the input-output relationship between a forcing parameter and heat release oscillations, as a function of forcing frequency. Since this function answers the majority of the practically relevant requirements mentioned before, identifying the heat release transfer function due to flow oscillations becomes the major objectives for understanding combustion instabilities.

1.3 Non-premixed Combustion

Used throughout our world are two fundamental types of flames, as shown by Figure 1.7: non-premixed (diffusion) and premixed. Although these two flames may appear similar at times in appearance and effect, they are fundamentally different processes, with different physics, governing equations, and flame dynamics. In non-premixed flames, being the focus of this thesis, it is the rate of molecular diffusion, rather than chemical kinetics, which greatly controls the flame position and burning rate. The pure fuel migrates towards the combustion zone, as it does for premixed flames, however due to the lack of oxygen the fuel is pyrolized and broken down into smaller molecules and radicals. This process is the cause of soot formation which gives the distinctive bright yellow color to the majority of these flames. As the products of pyrolysis approach the combustion zone they encounter increasing levels of oxygen until the optimal, i.e. stoichiometric, ratio of fuel-to-air is obtained to perform the stoichiometric oxidation reactions.

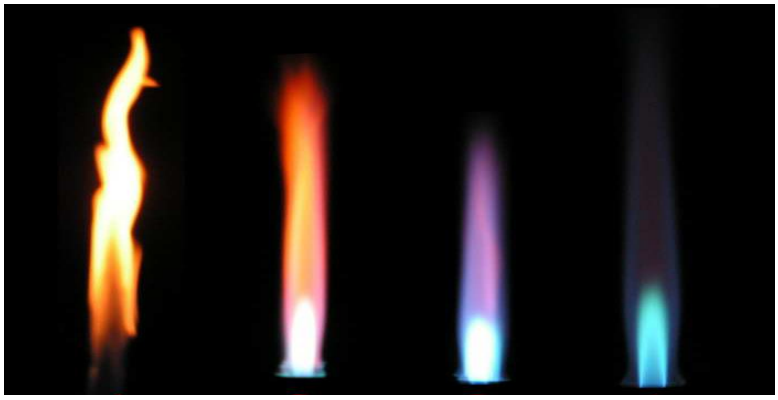

Figure 1.7. Spectrum of flames of the combustion of methane (CH_4), from pure non-premixed/diffusion flames on the left to pure premixed flames on the right [18].

1.3.1 Burning with Relevance

With the recent restrictions on emissions, there has been a migration in combustion technologies towards premixed combustion. Having the ability to operate in the lean or rich regimes, the flame temperatures can be reduced, and thus the NO_x emissions minimized. However, this does not mean that non-premixed combustion systems are completely obsolete. Having the advantages of substantial stability and fuel flexibility, there is a place for these systems in current and future technologies. The allowance for fuel diversification is extremely appealing, and is in fact the cornerstone of some industries and various technology development teams. For example, many test fuels, such as ethanol-gasoline, jet-algae, and biofuel blends, are studied first in non-premixed combustion systems. In addition, they are largely more unexplored than premixed combustion systems, and throw in the additional complications of unburned hydrocarbons and particulate matter to the chemical kinetics, and thus make for an exceptional thesis topic.

Some examples of diffusion flame based combustion systems, ranging from simple to complex, are candle flames, wood fires/stoves, coal burners, residential gas applications, radiant burners for heating, pulverized coal combustion, industrial furnaces, and solid/liquid propellant rocket engines. In addition, diffusion flames are a key component of liquid-fueled, partially premixed, and diesel combustion systems, as well as being effectively utilized as pilot systems to stabilize premixed systems where industrial operators routinely note the profound influence of non-premixed pilot fuel on combustor oscillation limits.

Although, the majority of gas turbines currently manufactured are lean-premix staged combustion turbines, “conventional” gas turbine systems have historically operated with diffusion flame combustion, where the fuel/air interaction and combustion take place simultaneously in the primary combustion zone. This, however, generates regions of near-stoichiometric fuel/air mixtures where the temperatures, and thus NOx emissions, are higher. Figure 1.8 shows simplified versions of these two gas turbine systems.

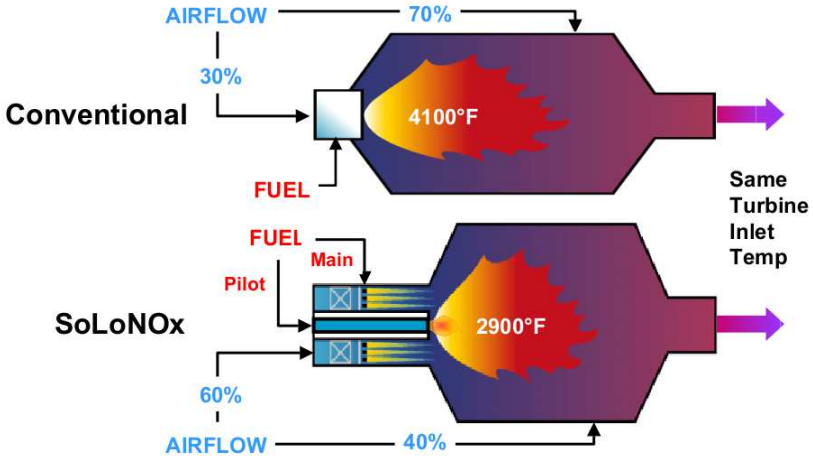

Figure 1.8. Simplified depictions of conventional (non-premixed) combustion and dry low NO_x (lean-premixed) combustion gas turbine systems [19].

Combustion systems that put system stability, design simplicity, or fuel flexibility as main priorities will continue to utilize non-premixed combustion technologies. Also since lean-premixed gas-turbines only became available within the past two decades, any still operational turbines manufactured prior to this will still operate in this non-premixed regime. In addition, designs and ideas for next-generation gas turbines are continuing to utilize various degrees of non-premixed combustion. A number of new combustion systems have been recently introduced, some available in the market and others under

development, such as staged air combustion, have the advantages of operating in full diffusion mode or in partially premixed mode, hydrogen diffusion flame array injectors, and reduced NO_x diffusion flame combustors [20].

1.3.2 Past and Existing Studies

This thesis describes and analyzes the dynamics, both space-time and heat release, of non-premixed flames responding to uniform bulk fluctuations in flow velocity. A great deal of literature on the linear and nonlinear response of premixed flames to flow disturbances and the combustion instability characteristics of lean, premixed combustors has been generated over the last decade [4, 21-27]. Additionally, substantial work has been done to obtain the flame transfer function characteristics of premixed flames. This includes experimental investigations of various nozzle and combustor configurations [25, 28-31], numerical simulations with detailed binary diffusion and turbulence [32-34], and modeling efforts using the G-equation for fuel-air ratio, velocity, and pressure fluctuations [25, 27, 29, 31, 35-39]. As a result of this work, the controlling physics in laminar flames appears to be understood and capabilities have been developed to predict the space-time dynamics of the flame position and heat release [21, 40]. Furthermore, while some fundamental questions remain in highly turbulent flames, exciting progress has been made in obtaining similar predictive capabilities in turbulent flows as well [41].

In contrast, the behavior of non-premixed flames responding to flow disturbances, both in terms of the space-time reaction sheet dynamics, as well as the temporally varying heat release, both local and spatially integrated, is much less well understood.

A number of studies have delved into the natural dynamics of non-premixed flames. In the buoyancy dominated regime where the Froude number, $Fr = U_0^2 / (gR_f)$, is

not too high, these flames are globally unstable and exhibit narrowband oscillations due to the periodic generation and traveling of vortical structures vertically along the flame. These are manifested as flame flicker at a low frequency (~12Hz) that is remarkably insensitive to flow rate, burner size, and gas composition [42, 43]. The amplitude of spatial flickering is, however, a function of these parameters. Recent studies have shown that this global instability disappears at small Froude numbers, or when the flame becomes momentum dominated at large Froude numbers [44]. Additional studies have investigated instability (oscillatory) onset and mitigation characteristics, with dependence upon Damköhler and Lewis numbers [45-47].

External excitation of non-premixed flames, such as by acoustic forcing, has also been studied extensively, often with the motivation of enhancing mixing and/or decreasing pollutant emissions. When subjected to external excitation, lower Froude number, nominally unstable flames exhibit a variety of response features that depend upon the frequency and magnitude of the excitation. For example, Chen et al. studied the response of a non-premixed flame exposed to acoustic excitation [48], showing oscillations in both the fuel jet flow and flame sheet position, both of which were dependent upon the forcing frequency and amplitude. They and others [49-51] also showed nonlinear behavior, such as the presence of sum and difference frequencies of the buoyant instability and external forcing frequencies, subharmonics and harmonics of the excitation frequency, and frequency locking – i.e., the disappearance of oscillations associated with the natural buoyant instability at sufficient excitation amplitudes. For example, Williams et al. [52] explored this lock-in behavior, showing that forcing the fuel stream at a frequency close to the natural buoyant instability frequency was accompanied

by the presence of large vortices on the air side of the flame, coupling the overall flame response to the forcing frequency. They also observed that a related lock-in phenomenon could happen at the first subharmonic of the forcing frequency, when the forcing frequency was close to twice the natural instability frequency.

As a result of the strong effect of forcing on the ambient/co-flowing air and its entrainment with the fuel jet, a number of studies have also noted significant influences on soot and NOx production from the flame [53-57] – sensitivities which are much stronger in non-premixed flames than in premixed flames. For example, Saito et al. [53] showed that soot can be suppressed in acoustically excited non-premixed flames, with reductions of up to 50% in a laminar flame, and 90% for a turbulent flame.

Additional studies have looked into the dynamics of laminar, momentum dominated flames, focusing more on the flame's space-time dynamics due to velocity and equivalence ratio perturbations. The interaction between the acoustic field and the flame produces a spatially varying, oscillatory velocity component that is normal to the flame, causing wrinkling, as well as oscillatory reaction and heat release rates [56, 58]. Dworkin et al. [58] showed how large amplitude modulation can lead to pinch-off of the top portion of the flame into a pocket. Such pinching off only occurs below a certain frequency of excitation and above a critical amplitude for that frequency. In addition, they showed that the magnitude of the flame wrinkling diminished and was smoothed with downstream distance. Tyagi et al. [59] also investigated velocity forcing numerically, presenting results for the flame's heat release transfer function, a quantity which indicates the input-output relation between forcing and unsteady heat release. Significantly, they observed the effects of Peclet number, Pe, forcing amplitude, ε, and fuel-port half width,

R_f, on the heat release transfer function response amplitude and phase. For significant forcing amplitudes, the magnitude of the response function decreased and its phase (magnitude) increases with *Pe*. In addition, the magnitude of the response function decreased monotonically as the excitation frequency was increased, and the onset of the frequency rolloff was observed to scale as 1/*Pe*.

A number of analytical studies have also considered the response of non-premixed flames. A significant theoretical literature on the unforced problem exists and, indeed, the Burke-Schumann flame is a classic problem [55, 60, 61]. Several treatments of the forced, unsteady problem have been reported, in particular those of Sujith [62-64], Chakravarthy [59, 64], Juniper et al. [65], and Magina et al. [66, 67]. These studies have analyzed this problem within the infinite reaction rate, $\mathcal{Z}$ -equation formulation for the mixture fraction. Solutions were developed for the flame position and heat release for several problems, including the flame response to axial velocity and mixture fraction oscillations, some examples of which are shown in Figure 1.9.

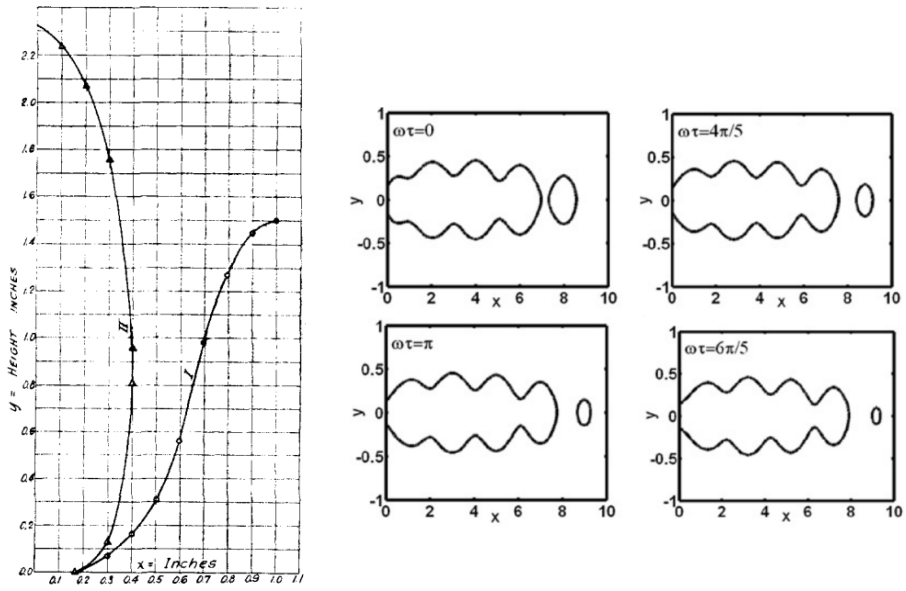

Figure 1.9. Early hand-plotted computed steady flame locations [61] (left) and modern computed forced flame locations over a forcing cycle [59] (right).

Although various mixture fraction field solutions exist, all the results regarding steady and instantaneous flame position are implicit. This is due to the complex form of the field solutions, generally involving infinite summations or error functions. Thus, work is still needed to develop analytical **explicit** solutions for the for the fluctuating flame dynamics.

1.4 Overview of Present Work

The objective of this research is to understand the spatio-temporal and heat release characteristics of harmonically forced non-premixed flames. This includes the mechanisms by which flame surface wrinkles are excited, transported, and smoothed, as well as their influence upon local and global heat release. Throughout the entirety of this work, comparisons will be made to premixed flame systems with similar configurations. The remainder of this thesis is arranged as follows.

Chapter 2 starts with discussing the governing features and properties of field and surface equations. The mixture fraction governing equation, i.e. $\mathcal{Z}$ -equation, is introduced and its features are compared with those of the premixed G-equation. The additional complexity of the non-premixed problem is discussed along with the complications of iso-surface dynamics. The various analytical and numerical solution methods are also mentioned. Additionally, an approach similar in methodology to the way premixed flame dynamics are studied, is investigated, wherein a governing partial differential equation for the flame wrinkles is obtained, and the explicit dynamical equations obtained directly.

Chapter 3 through Chapter 5 present the majority of the new analytical and numerical findings of this work, presented in order of increasing complexity. Chapter 3 elucidates isothermal diffusion flame dynamics, discussing the spatio-temporal and heat release dynamics of harmonically forced non-premixed flames. Various geometries are investigated, such as slot and cylindrical systems, exposed to various forcing configurations. The limiting case of $Pe \rightarrow \infty$ is then isolated to build intuition and ease of understanding. Chapter 4 builds upon this by investigating the effects of axial diffusion, anisotropic diffusion, and, multi-dimensional forcing effects. Accompanying numerical investigations are performed on an alternate extended inlet geometry to identify and capture specific dynamical features. Additionally, the $Pe >> 1$ limit is then explored so that various wrinkle dynamic behaviors are easily identified. Chapter 5 introduces various asymptotic analyses on the heat release to investigate the rich low and high *St* asymptotic trends.

Chapter 6 then rounds out the study, transforming this thesis from a spear to a trident, by investigating non-isothermal diffusion flame dynamics via experimental and accompanying computational efforts. Details regarding the developed forced non-premixed flame experimental setup are provided, along with the results of various diagnostics methods. Improved analytical models were developed to incorporate more of the "real" effects observed from the experimental results, in addition to enhanced computational models, utilizing experimental results as model inputs to predict flame dynamics. Comparisons between experimental results and the various models developed was done throughout.

1.5 The BIG Picture

So with the threatening emission restrictions and shifting public opinions, it could seem that the end of combustion driven power systems is near, and these thesis results irrelevant. However, this is not the case, as internal combustion engines are not going away anytime soon. In fact, a recent report from former U.S. Secretary of Transportation, Norman Mineta, stated that “the quickest and most cost-effective way to achieve our energy usage goals is through faster adoption of fuel-efficient downsized gasoline and diesel engines” [68]. Volkswagen’s CEO, Martin Winterkorn, Fords vice president of powertrain engineering, Joe Bakaj, and various other powertrain companies seem to agree [69].

So what justifies these claims, regarding combustion power systems continued and unabated dominance as the powertrain of choice for the future, over existing alternative systems, such as battery/electric powertrains? The answer lies within the thermodynamic properties of the various fuel sources. Carbon-based liquid fuels have superior energy densities, both gravimetric and volumetric, as well as storage and transportation advantages over most alternative fuels, including batteries. Additionally, they are easily accessible and cost effective.

Figure 1.10 shows the energy densities of various fuels used throughout our modern world. Those located closer to the top-right corner have higher energy densities. Notice how, diesel and gasoline fuels have roughly 100 times the gravimetric and volumetric energy density as a lithium-ion battery. The batteries of the Tesla Roadster, for example, weigh 450 kg and have the same amount of energy capacity as less than 1.5 gallons (4.5 kg) of diesel fuel [68]. This additional weight and size to vehicle powertrains

makes them less efficient and convenient. Moreover, batteries are very expensive, costing around $5,500, $9,000, and $40,000 per unit for the Nissan Leaf, Chevy Volt, and Tesla batteries respectively, and have strict regulations on disposal.

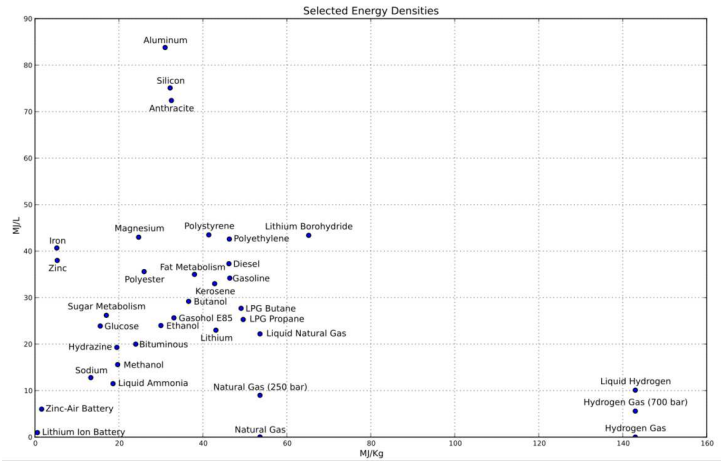

Figure 1.10. Plot of the energy densities, both gravimetric and volumetric, for various common fuels [70].

Additional advantages of combustion power systems is that liquid hydrocarbon fuels, such as diesel and gasoline, are easily transported, widely available (as the infrastructure is already existing) and can be re-fueled quickly (minutes versus charging which takes hours), advantages which do not apply to their battery-electric counterparts. These points, plus the combination of performance, low cost and fuel flexibility of internal combustion engines make it likely that they will continue to dominate the vehicle fleet for “at least the next several decades”. Gas turbines will also continue to be an important combustion-based energy conversion device for many decades to come, for aircraft propulsion, ground-based power generation, and mechanical-drive applications.

Thus, combustion based power systems are here to stay for the foreseeable future, and non-premixed combustion is a key component of this functional process. Although

the task is well-defined, it is very complicated. To make clean, diverse, sustainable energy systems, avoiding combustion instabilities. These instabilities are dependent upon many factors, such as fuel type, combustor geometry, equivalence ratio, operating conditions, etc., which are constantly changing from design to design. Coupled with the fact that tightening emissions regulations are pushing towards operating under conditions where instabilities are prominent, make the need for understanding the dynamics and characteristics of combustion instabilities as important as ever.

CHAPTER 2

Evolution of Fields and Iso-surfaces

This chapter provides the building blocks and background of our modeling approaches by discussing the evolution of field equations and iso-surfaces. Decoupling the complex internal chemical kinetics from the flame dynamics, the flame front is often times assumed to be an infinitely thin surface within the flow field. Conserved scalars are extremely useful when investigating non-premixed combustion and flame dynamics problems analytically, as they can help eliminate chemical source terms from the governing equations, making them mathematically tractable. Naturally obtained as temporally varying field equations, implicit solutions are straightforward, however, converting these into meaningful explicit equations for the evolution of a specific iso-contour, corresponding to the flame sheet, is a more complex challenge. This chapter discusses the dynamics and evolution of fields and iso-surfaces, from both a general mathematical standpoint, and specifically for combustion related systems. It concludes by introducing some key tools, techniques, and, variables, which will be used to study spatio/temporal flame response throughout the remainder of this thesis, along with some points to aid interpretation of the results to follow.

2.1 Mixture Fraction Field Formulation

To layman and experts alike, combustion is an intimidating topic to research and understand. It is a multicomponent reacting mixture problem, consisting of a blend of complex flow features, detailed chemical kinetics, expansive length scales, and

instabilities, making it challenging to understand physically, and even more so mathematically. Thus, in order to make this task analytically tractable, simplified governing equations expressing the conservation of mass, species, momentum, and energy must be obtained.

For non-premixed combustion problems it is convenient to begin with the species conservation equation, given by:

$$\frac{\partial \rho_i}{\partial t} + \nabla \cdot (\rho_i \vec{v}_i) = \dot{\omega}_i \tag{2.1}$$

where i indicates the various species involved, $\dot{\omega}_i$ is the chemical production rate, ρ_i is the partial density, and $\vec{v}_i$ is the species velocity. This species velocity can be decomposed into contributions due to convection, $\vec{v}$, and diffusion, $\vec{V}_i$. Utilizing this along with the species mass fraction, $Y_i = \rho_i / \rho$, results in a revised form of the species conservation equation:

$$\rho \frac{DY_i}{Dt} + \nabla \cdot (\rho Y_i \vec{V}_i) = \dot{\omega}_i \tag{2.2}$$

where the material derivative has been used for simplicity. Derivations for the diffusion velocity exist, however they are implicit in nature and extremely complex, revealing the dependence of mass diffusion upon concentration gradients, pressure gradients, body forces, and temperature gradients [71, 72].

Among these four processes, concentration diffusion dominates in most situations of physical interest. Thus neglecting the other contributions and assuming equal binary diffusion coefficients, Fick's law of mass diffusion, $\vec{V}_i = -\mathscr{D} \nabla \ln Y_i$, can be obtained and utilized to cast the species conservation equation into its final simplified form:

$$\rho \frac{DY_i}{Dt} - \nabla \cdot (\rho \mathscr{D} \nabla Y_i) = \dot{\omega}_i \tag{2.3}$$

The primary remaining difficulty in the solution of chemically reacting flows is the presence of the reaction term, which not only is nonlinear but also couples the energy and species equations [73]. In addition, this term is spatially variant, existing only at the flame sheet, whose spatio-temporal location is also an unknown. However, under certain conditions these quantities can be stoichiometrically combined such that the resulting term is no longer affected by chemical reactions in the flow, eliminating the compication of spatial sources and sinks. Such a combined quantity is called a conserved scalar or coupling function, and as the name reveals, this scalar property is conserved throughout the flowfield, existing on both sides the flame and having a constant integral.

Some examples of these variables are elemental mass fraction, total enthalpy (assuming negligible radiation, viscous dissipation, and body forces) and mixture fraction, which will be utilized here. For the work presented in this thesis, the utility of the conserved scalar is that it can be used to generate a sourceless species conservation equation, containing no reaction rate terms, enabling analytical tractability. Although this work focuses on the species equation, if a unity Lewis number is assumed, then the energy equation can be cast into a similar form, making the analytical solution techniques developed equally applicable.

To utilize this concept, consider an elementary system consisting of a pure fuel source and a pure oxidizer source, which react to form a single product. Recall that Eqn.(2.3) can be written for each of these simplified species. Adding this form of the fuel conservation equation, to the normalized product conservation equation results in:

$$\rho \frac{D\left(Y_F + Y_{\mathrm{Pr}}/(\varphi_{ox}+1)\right)}{Dt} - \nabla \cdot \left[\rho \mathscr{D} \nabla \left(Y_F + Y_{\mathrm{Pr}}/(\varphi_{ox}+1)\right)\right] = \dot{\omega}_F + \dot{\omega}_{\mathrm{Pr}} / (\varphi_{ox}+1) \qquad (2.4)$$

where φ_{ox} is the stoichiometric mass ratio of oxidizer to fuel. This choice of normalization can be understood by considering mass conservation for this combustion system, where fuel and oxidizer react at stoichiometric proportions to produce products, i.e. $-\dot{\omega}_F = \dot{\omega}_{\mathrm{Pr}} / \left(1+\varphi_{ox}\right)$. The negative sign indicates that fuel and oxidizer are being consumed and products are being produced, but more importantly, the chemical production terms in Eqn.(2.4) cancel out and this equation becomes sourceless!

The new grouping of species mass fractions that falls out is thus a conserved scalar, and can be denoted as the mixture fraction, defined explicitly as:

$$\mathcal{Z} = Y_F + \frac{Y_{\mathrm{Pr}}}{(\varphi_{ox}+1)} \qquad (2.5)$$

Physically representing the amount of material having its origin in the fuel stream, this variable takes values of zero and unity in the pure oxidizer and fuel streams, respectively. Shown below is the general form of the species conservation equation, which utilizes the mixture fraction variable:

$$\rho \frac{D\mathcal{Z}}{Dt} - \nabla \cdot \left(\rho \mathscr{D} \nabla \mathcal{Z}\right) = 0 \qquad (2.6)$$

Lastly, to be able to solve this problem, requires that the density be related to the mixture fraction. Rather than assuming constant properties, the less restrictive assumption of constant $\rho\mathscr{D}$ can be utilized, although it actually varies as $T^{1/2}$ [70]. Using this, along with mass conservation results in the density canceling, and thus the final modified form of the mixture fraction equation is obtained, and will be referred to throughout this work as the $\mathcal{Z}$-equation:

$$\frac{\partial \mathcal{Z}}{\partial t} + \vec{u} \cdot \nabla \mathcal{Z} = \nabla \cdot \left(\mathscr{D} \nabla \mathcal{Z} \right) \tag{2.7}$$

2.2 Comparison with Premixed Level-set G-equation

The space-time dynamics of a non-premixed flame system, with equal species diffusivities, have been shown to be described by the mixture fraction field using the $\mathcal{Z}$-equation. The *G*-equation is an analogous expression for premixed flames in the reaction sheet limit [21, 71, 74], given by:

$$\frac{\partial G}{\partial t} + \vec{u} \cdot \nabla G = S_L |\nabla G| \tag{2.8}$$

where S_L is the burning velocity and the normal direction to the flame front is $\vec{n} = \nabla G / |\nabla G|$. Products and reactants are assigned positive and negative *G* values, respectively. First formulated by Williams, the *G*-equation is used extensively for various premixed combustion problems such as theoretical flame transfer functions [27], theoretical turbulent consumption rate [75], and many computational fluid dynamics [23, 76, 77].

Both of these flame front kinematic equations relate the motion of the flame front with various flow/flame parameters implicitly, meaning the flamelet is treated as a gas dynamic discontinuity in three dimensional space described by a specific iso-surface within the field. This locus of points defining the flame sheet is given by the parametric equations $\mathcal{Z}(\vec{x},t) = \mathcal{Z}_{st}$ and $G(\vec{x},t) = 0$ for non-premixed and premixed flames, respectively, and are general enough that they can handle flames with complex, multi-connected surfaces. Simple schematics of the two fields are shown in Figure 2.1.

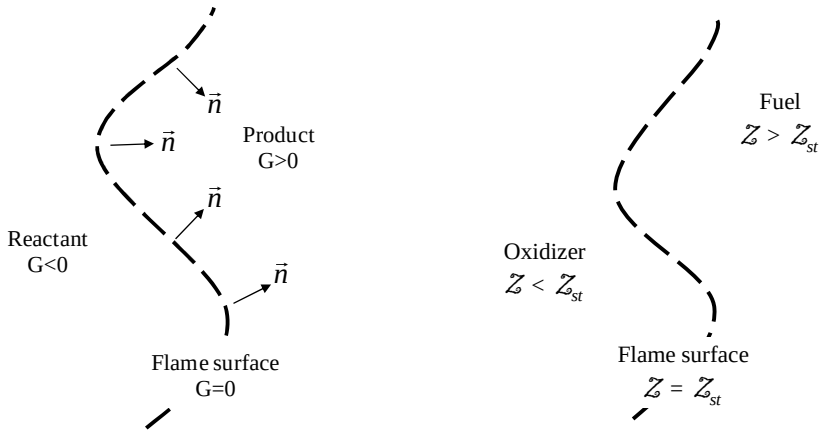

Figure 2.1. Schematic of the premixed *G*-field (left) and non-premixed $\mathcal{Z}$ -field (right) with denoted iso-contours representing the flame sheet.

It is helpful to compare the dynamics and governing features of the $\mathcal{Z}$ -equation, given by Eq.(2.7) for non-premixed flames, with the *G*-equation, given by Eq.(2.8) for premixed flames. The two expressions have the same convection operator on the left-hand side which illustrates the importance of flow perturbations in the direction normal to the flame sheet in pushing the flame sheet around. However, the right-hand sides of these two expressions are different. The premixed flame expression has the normal flame propagation operator, $S_L|\nabla G|$, while the non-premixed flame expression has a diffusion operator, $\nabla\cdot(\mathscr{D}\nabla\mathcal{Z})$. This difference is significant and reflects, among other things, the fact that non-premixed flames do not propagate. Moreover, the premixed flame dynamics equation is nonlinear, while the non-premixed flame dynamics equation is linear (assuming that U_n and $\mathscr{D}$ are not functions of $\mathcal{Z}$).

Another significant, yet subtle difference is that the *G*-equation is physically meaningful and valid <u>*only*</u> at the flame itself where $G(\vec{x},t)=0$ (i.e., although it can be solved away from the flame, the resulting *G* values have no physical significance [77]).

In contrast, the $\mathcal{Z}$-equation describes the physical values of the mixture fraction field *everywhere*. Thus the entire mixture fraction field must be solved in the non-premixed problem and the $\tilde{\mathcal{Z}}\left(\vec{x},t\right)=\tilde{\mathcal{Z}}_{st}$ surface extracted from the resulting solution field (which generally cannot be expressed explicitly). Consequently, developing explicit solutions for the non-premixed flame problem is substantially more difficult than for the premixed problem. This observation has important consequences for both solution approaches of these problems, as well as the $\mathcal{Z}\left(\vec{x},t\right)=\mathcal{Z}_{st}$ flame sheet dynamics that are discussed in the next section.

2.3 The Evolution of Surfaces

Gaining both theoretical and experimental knowledge about the behavior of iso-value surfaces in multicomposition fluid problems is an important issue [78]. This is especially the case when an attempt is made to understand and characterize turbulent combustion, where, for both non-premixed and premixed turbulent flames the factors controlling reactive species or temperature iso-concentration surfaces need to be clearly understood. Importantly, the behavior of these surfaces is strongly connected to the properties of transport phenomena at **all** scales of the fluid motion, information which is essential to understanding the dynamics of combustion instabilities.

Several phenomena can be described, both physically and mathematically, in terms of surfaces within a laminar or turbulent fluid. Mixing layers, premixed flames, and, non-premixed flames fit into this class under material surfaces, propagating surfaces, and constant property surfaces, respectively [79]. Flamelet models constitute one of the most common approaches for computationally/theoretically analyzing and experimentally

investigating laminar, and especially turbulent, flames and combustion systems [80]. Based on the flame sheet assumption, which requires chemical reactions to occur with short length scales relative to the flow (turbulence), the flame is confined to relatively thin layers within the flow field and the reaction zone is considered a burning surface. For the turbulent case, this burning surface is simply corrugated and translated by the turbulence, with no change to the internal flame structure.

This thin flamelet assumption is utilized for both premixed and non-premixed flames, with the distinction being the segregated quantity or parameter. For premixed systems this surface separates unburnt reactants from burnt products, while for non-premixed systems this surface separates fuel species from oxidizer species. In this case, the reaction sheet can be referred to as a stoichiometric surface, where the reactants meet in chemically/atomically ideal proportions for combustion. Being the topic of this thesis, this section discusses some basic features of the dynamics of surfaces in the fast chemistry, thin reaction sheet limit.

Some existing studies devoted to iso-surface dynamics and the derivation of parametric transport (evolution) equations, characterizing their physical properties, have been based on simple geometrical considerations [81], while others have utilized coherent flame models [82], and probability density function (pdf) or surface density function (sdf) formulations [78]. The pdf concept provides a one point statistical description of a variable, such as the temperature or concentration level of a chemical species, and has been shown to be an efficient tool for studying highly non-linear problems involving reactive flows. This approach has great potential due to its enabling the inclusion of detailed chemistry in a closed form. As will be discussed in depth, the pdf and sdf are

transported in scalar space by the same mechanism, depending upon the mean (conditional and surface, respectively) of the quantity representing the imbalance between diffusion and the reaction that characterized the internal structure of the reactive layers [78]. This surface-specific imbalance term, however, is dependent upon the physics, i.e. mathematical type, of that surface.

The preceding sections discussed the formulation of fields through which the iso-surfaces were to be tracked for both premixed and non-premixed flames. They utilized different conservation equations to derive their respective governing field equations, yet the end task was the same; tracking the evolution of an iso-surface in space and time within a domain. Thus, here we discuss some generalizations of these surface dynamics. The local geometry of surfaces is described by the spatiotemporal surface element properties, consisting of position, surface normal direction, principal curvatures, and fractional area increase [79]. Exact evolution equations for these properties can reveal the effects of various physical processes, such as straining and surface propagation. This is convenient, since the two key elements of surfaces, with regards to flame dynamics, are a representative speed, with respect to the flow, and a position that characterizes the flame wrinkling. These surface elements retain their identity during the flame development, being strained in their own plane by the fluid motion, a process that not only extends their surface area, but also establishes the rate at which a flame element consumes the reactants. Thus, the flame density and mass fractions of reactants are described by non-linear diffusion equations, where for the reactant equations each contain a consumption or production term proportional to the local flame density [82]. Additional parameters of interest, such as heat release, can be obtained through these surface dynamics as both

local and global parameters. As will be discussed in the following sections, spatially integrated heat release is an important quantity for acoustically compact flames, and as such the nonlinear scalar field equation governing the propagation of an unsteadily convected interface can be used to derive a convenient expression for the average volume flux through such an interface in a homogeneous flow field [83].

As mentioned, mixing layers, premixed flames, and, non-premixed flames can be investigated as material surfaces (involving the mixing of two bodies of fluid that initially contain uniform but different concentrations of a contaminant), propagating surfaces (involving a surface-normal passive Huygens propagation mechanism) and constant property surfaces, respectively. Physically interestingly and mathematically conveniently, all three types of surfaces can be uniformly regarded as propagating surfaces, where the front propagation speed, w, or as constant-property surfaces, where the dynamical surface, Ψ, is defined for each in Table 2.1 [79]. The left column shows the original surface type, while the other columns show the necessary w or $D\Psi / Dt$ required to be cast as a propagating or constant property surface, respectively.

Table 2.1. Uniform casting of material, propagating, and constant property surfaces.

	Treated as a Propagating Surface with…	**Treated as a Constant Property Surface with…**
Material Surface	$w = 0$	$\frac{D\Psi}{Dt} = 0$
Propagating Surface		$\frac{D\Psi}{Dt} = -w\lvert\nabla\Psi\rvert$
Constant-Property Surface	$w = -\frac{D\Psi}{Dt} / \lvert\nabla\Psi\rvert$	

The specified rate of propagation can be constant, as for a material surface where the surface point is also a material point, i.e. fluid particle, or can vary over the surface, as for a propagating surface. Many parameters, such as principal curvatures, principal directions, and, stretch factor are intrinsic properties of the surface, depending on the initial surface element position, yet independent of the parameterization [79]. Significantly, for a material surface, or propagating surface with constant w, the surface element equations are closed with respect to surface properties, and thus each surface element evolves independently; while a constant property surface evolves in time, being completely determined by the current property field at any instant, independent of the surfaces past history! This phenomena has been observed and derived in the study of combustion instabilities of premixed flames (and non-premixed flames), described as the flame response exhibiting limited "memory" [4]. Additionally, this has important implications for the solution methods, since rather than considering evolution equations for a constant-property surface, an alternative approach is to deduce the surface properties from the property field and its evolution [79].

Considered here are surfaces that are initially "regular", defined as having finite curvature everywhere with no-self intersections, critical points, or cusps [84], yet whether they remain regular is an important question regarding the behavior of the unique surface. A material surface remains regular, while a propagating surface can develop singularities, i.e. values of infinite local curvature, and self-intersections [79]. Once again for corrugated premixed flames, it is well known and understood how flame front propagation can lead to destruction of flame area, via kinematic restoration, producing trailing edge cusps [4]. As will be seen later, forcing complicates (yet still follows) this

behavior, producing multi-connected, i.e. segregated, material surfaces and constant-property surfaces; a feature known as flame clipping for non-premixed flames, which occurs under certain critical conditions.

Defining our normalized general scalar field as Ψ, a surface can be defined implicitly, through an equation of the form $\Psi(X,t)= \Psi_{des}$, or explicitly, as $X(\vec{x},t)$, where the evolution of each respective entire surface is given by $\partial\Psi/\partial t$ or $\partial X/\partial t$. Additionally, the evolution equation for the position of a surface is given by:

$$\frac{dX(\vec{x},t)}{dt} = \vec{v}\left(X(\vec{x},t),t\right) + w(\vec{x},t)N(\vec{x},t) \tag{2.9}$$

where $\vec{v}$ is the medium velocity and N is the surface normal given by:

$$N(\vec{x},t) = \frac{\nabla\Psi}{|\nabla\Psi|} \tag{2.10}$$

From this, other various properties of the surface elements can be obtained, including the principal curvatures, principal directions, and the stretch factor [79].

Refining our discussion to combustion applications, an important quantity of interest is the local imbalance between reactive and diffusive effects, denoted $\Omega_\Psi(\vec{x},t)$. This parameter characterizes the inner structure of the reactive layers, and explains how diffusion at small scales, as well as mixing, are strongly related to the movement of the iso-surfaces. A transport equation for a diffusive and reactive scalar field (with convection) may be written as:

$$\frac{D\Psi(\vec{x},t)}{Dt} = \Omega_\Psi(\vec{x},t) \tag{2.11}$$

Within a laminar premixed flame, the local imbalance between reactive and diffusive effects is responsible for the appearance of a self-induced propagation phenomenon; thus

iso-surfaces feature a self-propagation mechanism [78]. In the general situation of a reactive diffusive scalar, a relative progression velocity, $S_\psi(\vec{x},t)$, can be defined along the surface, and related to the fluid velocity and absolute velocity, resulting in:

$$\Omega_\Psi(\vec{x},t) = S_\psi(\vec{x},t)\left|\nabla\Psi(\vec{x},t)\right| \tag{2.12}$$

Combined with Eq.(2.11), this equation takes the same appearance as the *G*-equation, given by Eq.(2.8). For non-premixed flames, $\Omega_\Psi(\vec{x},t)$ is fundamentally different, since casting this constant-property surface as a propagating surface, *w* takes a different form, as seen by Table 2.1. The curvature, $\nabla \cdot N$, can be expressed in terms of the scalar field, by using Eq.(2.10), and after manipulating the diffusive-reactive term, it may be organized as a function of curvature as:

$$\Omega_\Psi(\vec{x},t) = \frac{1}{\rho}\nabla\cdot\left[\rho\mathscr{D}\nabla\Psi(\vec{x},t)\right] + \dot{\omega}_\Psi \tag{2.13}$$

where $\dot{\omega}_\Psi$ is the surface reaction rate term. Combined with Eq.(2.11), this equation takes the same appearance as $\mathcal{Z}$-equation, given by Eq.(2.7). Thus, the modeling of internal flame diffusion has to be achieved in a slightly different way for each modeling procedure, i.e. surface, based on the concept of a propagating front and the unique definition for the propagation speed, *w*.

In addition to the local properties discussed, the evolution equations for global properties of level surfaces can also be expressed [85]. This is of particular interest for combustion systems, as total heat release and surface area are significant dynamical parameters of interest. The nature of the resulting equation to be established will be kinematic, expressing the time rate of change of global variables in terms of the

progression velocity and geometric parameters of the level surface. A global variable can be defined as:

$$\Upsilon_\Psi(\Psi,t) \equiv \oint_\Psi f(\vec{x},t)dA(\vec{x}) \tag{2.14}$$

where $f(\vec{x},t)$ denotes a scalar of Ψ, and is a smooth function of location and time. The contributions to the time rate of change of the global variable are; a convective transport term in scalar space and two source terms determined by the evolution of f and $|\nabla\Psi|$, as can be seen with differentiation with respect to time [85].

Limiting our discussion to kinematic relations and assuming the scalar $f(\vec{x},t)$ appearing in the global variable is governed by:

$$\rho\left(\frac{\partial f}{\partial t}+v_i\frac{\partial f}{\partial x_i}\right)=\frac{\partial}{\partial x_i}\left(\rho\mathscr{D}\frac{\partial f}{\partial x_i}\right)+\rho\dot{W}_f(f) \tag{2.15}$$

then the dynamic equation for the global variable can be expressed as [85]:

$$\frac{\partial\Upsilon_\Psi(\Psi,t)}{\partial t}=\oint_\Psi\left\{\begin{array}{l}\frac{1}{\rho}\frac{\partial}{\partial x_i}\left(\rho\mathscr{D}\frac{\partial f}{\partial x_i}\right)+\dot{W}_f(f)+f\left(\frac{\partial v_i}{\partial x_i}-n_in_j\frac{\partial v_j}{\partial x_i}\right)+\\ +\frac{1}{|\nabla\Psi|}\left[\frac{1}{\rho}\frac{\partial}{\partial x_i}\left(\rho\Gamma\frac{\partial\Psi}{\partial x_i}\right)+\dot{W}_\Psi\right]\frac{\partial}{\partial x_i}(n_if)\end{array}\right\}dA(x) \tag{2.16}$$

Various relevant parameters can be considered by this equation, such as global heat release and flame surface area, utilizing unique scalars, $f(\vec{x},t)$, for each.

2.3.1 Surface Area Special Case

Special cases of this equation can be derived for useful quantities, such as surface area, $\mathscr{A}_\Psi$, which changes as a result of the deformation caused by the motion of the fluid and the dynamic change of the scalar field defining the iso-surface [85]. The dynamic equation for this variable can be obtained by setting $f(\vec{x})=1$, and is given as:

$$\frac{\partial \mathscr{A}_\Psi}{\partial t} = \oint_\Psi \left\{ \begin{array}{l} \dfrac{\partial v_i}{\partial x_i} - n_i n_j \dfrac{\partial v_j}{\partial x_i} + \\ + \dfrac{1}{|\nabla \Psi|} \left[\dfrac{1}{\rho} \dfrac{\partial}{\partial x_i} \left(\rho \Gamma \dfrac{\partial \Psi}{\partial x_i} \right) + \dot{W}_\Psi \right] \dfrac{\partial n_i}{\partial x_i} \end{array} \right\} dA(x) \qquad (2.17)$$

where Γ is an effective iso-surface diffusion term. Specifically, the surface area changes because of the rate of strain acting in the tangential plane, and the change of the scalar variable defining the level surface, however, both phenomena may increase or decrease the surface area; expansion or compression in the tangential plane will increase or decrease the surface area, respectively [85]. The dynamics of the scalar variable defining the iso-surface appear in Eq.(2.17) as molecular diffusion and source terms. Both may be positive or negative and hence, increase or decrease the surface area as time evolves.

As it was shown to be an important controlling feature for the iso-surface evolution equations, the molecular diffusion term can be analyzed in more detail if the variation of density is disregarded and the diffusivity is assumed constant. It follows then that [85]:

$$\frac{1}{|\nabla \Psi|} \Delta \Psi \frac{\partial n_i}{\partial x_i} = \frac{\partial n_i}{\partial x_i} \frac{\partial n_j}{\partial x_j} + \frac{\partial n_k}{\partial x_k} \frac{n_i n_j}{|\nabla \Psi|} \frac{\partial^2 \Psi}{\partial x_i \partial x_j} \qquad (2.18)$$

The first term on the right is purely geometrical, depending only on the mean curvature, while the second term depends on the variation of the defining scalar normal to the iso-surface. Importantly, the effect of molecular diffusion on the surface area is not monotonic, as can be seen by utilizing mean curvature, κ, and recasting this equation as:

$$\frac{1}{|\nabla \Psi|} \Delta \Psi \frac{\partial n_i}{\partial x_i} = 4\kappa^2 - \frac{2\kappa}{|\nabla \Psi|} \frac{\partial^2 \Psi}{\partial n^2} \qquad (2.19)$$

The first term on the right in this equation always monotonically alters the surface area (mean curvature being nonzero), but the second term may decrease or increase it depending on the signs of the normal derivative and the mean curvature.

2.3.2 Flame Surface Dynamics

In the fast chemistry limit, the reaction sheet collapses to a surface, a general condition for both flame types. Specific to non-premixed flames, this surface is defined by the equation $\mathcal{Z}\left(\vec{x},t\right)=\mathcal{Z}_{st}=1/\left(1+\varphi_{Ox}\right)$, being dependent upon the specific combination of fuel and oxidizer of the system, several of which are listed in Table 2.2. We define the instantaneous position of this reaction sheet by $y=\xi\left(x,t\right)$, which is shown in Figure 2.2 for representative two-dimensional premixed and non-premixed systems.

Table 2.2. Stoichiometric mixture fraction values for various hydrocarbon fuels in air.

Stoichiometric mixture fractions
$\mathcal{Z}_{st,CH_4/Air}=0.055$
$\mathcal{Z}_{st,C_3H_8/Air}=0.060$
$\mathcal{Z}_{st,C_8H_{18}/Air}=0.063$

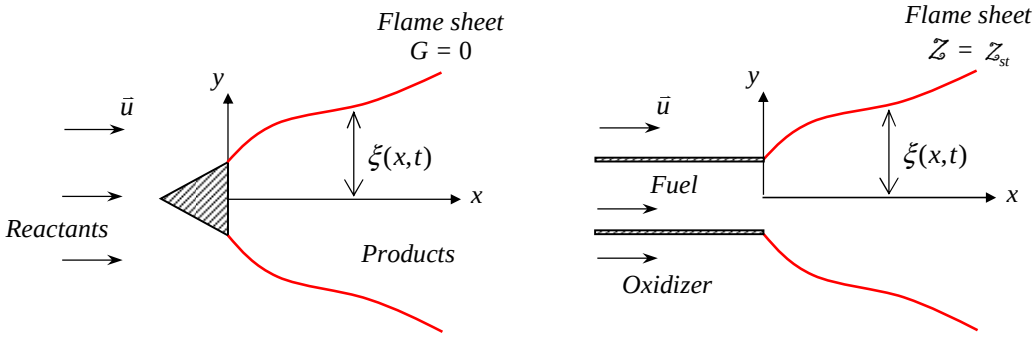

Figure 2.2. Schematic of bluff-body stabilized premixed flame (left) and jet non-premixed flame (right) with its corresponding coordinates and flame front dynamical parameter, *ξ(x,t)*.

Again, if the goal is to only consider the dynamics of the infinitely thin flame surface, then the space-time dynamics of the rest of the scalar field is of lesser interest. The premixed problem can resolve this issue by utilizing a useful transformation, $G(\vec{x},t) = y - \xi(x,t)$, which alters the *G*-equation into a differential equation in terms of the flame position, ξ. Although the equation for the flame position becomes less general than the *G*-equation, requiring "single-valued" flames, it enables us to track the flame location **explicitly** - note that in the *G*-equation, the flame position is an implicit function of *G* [24-27, 86]. Additionally, note that this substitution arbitrarily assigns values to the *G* field away from the flame itself, namely that *G* varies linearly with coordinate *x* away from the flame. Since the *G* field is completely arbitrary away from the flame, this is allowable. However, we cannot make an analogous substitution for the non-premixed system, such as $\mathcal{Z}(\vec{x},t) - \mathcal{Z}_{st} = y - \xi(x,t)$, as this assigns values to the $\mathcal{Z}$ field away from $\mathcal{Z}(\vec{x},t) = \mathcal{Z}_{st}$. As mentioned earlier, unlike the *G*-equation which is valid <u>only</u> at the flame front, the $\mathcal{Z}$ -equation describes the <u>*entire*</u> spatial distribution of the mixture fraction field. The implication of this fact is that the entire mixture fraction field must be solved and the $\mathcal{Z}(\vec{x},t) = \mathcal{Z}_{st}$ surface extracted from the resulting solution field (which generally cannot be written as an explicit expression).

This discussion reflects important underlying physics of the two flames. Consider a premixed and non-premixed flame embedded in a velocity field given by $\vec{u}(x,y,z,t)$, where the velocity field at the flame sheet is given by $\vec{u}(x,\xi(x,z,t),z,t) = \vec{u}^u$. The premixed flame dynamics are only a function of $\vec{u}^u$; this implies that for a given $\vec{u}^u$, its

space-time dynamics are the same for a variety of different velocity fields $\vec{u}(x,y,z,t)$. In contrast, the space-time dynamics of the non-premixed reaction sheet are a function of the entire velocity field, $\vec{u}(x,y,z,t)$, not just its value at the reaction sheet.

2.4 Dynamics Analysis Overview

Being dependent upon the specific system geometry, flow conditions, and boundary conditions, the dynamics of the flame sheet can be extremely complex; even more so with the addition of forcing mechanisms, key to combustion instabilities. Thus, prior to diving blindly into various analytical, computational, and experimental solutions, it is helpful to introduce some of the various analysis techniques, procedures, and key variables fundamental to the understanding of non-premixed flame dynamics. Additionally, unique methods to interpret these results are presented, which clarifies the information being provided, and enhances its utility.

2.4.1 Linearization and Key Variables

The position of the flame front, denoted as ξ, is assumed to be a single-valued function of one less spatial dimensions than the geometry of interest, and time, *t*. Necessary in order to enable analytical tractability of the problem, this assumption only loses credibility for highly wrinkled flames, resulting from strong forcing or turbulence, or for extremely complex geometries, flow, or boundary conditions. Thus to ensure this condition remains valid and analytical progress possible, we focus on simple laminar co-flowing non-premixed flames, exposed to small amplitude disturbances.

As such, linearized solutions to the z -equation are derived, valid in the limit of small perturbations. This can be done by expanding each variable as:

$$(\ )(\vec{x},t)=(\ )_0(\vec{x})+(\ )_1(\vec{x},t) \tag{2.20}$$

Since the governing equation, Eq.(2.7), is linear, this procedure is not necessary in order to obtain analytic solutions for the mixture fraction fields, and in fact, this assumption was not made in the work by Balasubramanian and Sujith [62]. However, this expansion is useful in analyzing controlling features of the flame dynamics at the forcing frequency and, very significantly, it enables an explicit analytic expression for the space-time dynamics of the flame position, $\xi_1(x,t)$, and spatially integrated heat release, $\dot{Q}(t)$, which is otherwise not possible.

As a note, often for the analytical solutions presented, a spatially and temporally invariant diffusion coefficient is utilized for simplicity, although the spatially dependent case is presented and discussed in a later chapter.

Linearizing and neglecting higher order terms, the mixture fraction field in the absence of forcing can be obtained from Eq.(2.7) as:

$$\vec{u}_0 \cdot \nabla \mathcal{Z}_0 = \mathscr{D}_0 \nabla^2 \mathcal{Z}_0 \tag{2.21}$$

Similarly, the dynamical equation for the fluctuating component of the mixture fraction field is given by:

$$\frac{\partial \mathcal{Z}_1}{\partial t} + \vec{u}_0 \cdot \nabla \mathcal{Z}_1 + \vec{u}_1 \cdot \nabla \mathcal{Z}_0 = \mathscr{D}_0 \nabla^2 \mathcal{Z}_1 + \mathscr{D}_1 \nabla^2 \mathcal{Z}_0 \tag{2.22}$$

It can be observed that these two dynamical equations show an interaction between convective and diffusive processes. This important balance reveals the natural way to non-dimensionalize these dynamical equations:

$$\tilde{x} = \frac{x}{PeR_f} \qquad\qquad \tilde{y} = \frac{y}{R_f} \tag{2.23}$$

where the Peclet number, *Pe*, is a key parameter given by:

$$Pe_{i,j} = \frac{u_{i,0} L}{\mathscr{D}_j} \tag{2.24}$$

and where "*i*" and "*j*" indicate the direction of steady convection and diffusion of interest, respectively, and *L* is a physical length scale of interest. As our primary system of interest is an axially coflowing non-premixed flame system with fuel port radius R_f and isotropic invariant diffusion ($\mathscr{D}_1 = 0$), unless specified otherwise $\mathscr{D} = \mathscr{D}_0$ and:

$$Pe = \frac{u_{x,0} R_f}{\mathscr{D}} \tag{2.25}$$

This Peclet number physically corresponds to the relative time scales for convective and diffusive processes to transport mass over a distance R_f:

$$\frac{\tau_{diffusion}}{\tau_{convection}} = \frac{R_f^2 / \mathscr{D}}{R_f / u_{x,0}} = \frac{u_{x,0} R_f}{\mathscr{D}} \tag{2.26}$$

As such, the *Pe* >>1 limit physically corresponds to the limit where convective processes are much faster than diffusive ones. This is an important limit that will be discussed in depth in the upcoming chapters, yet for now it is sufficient to note that the solutions to Eqns.(2.21) and (2.22) in the $Pe \to \infty$ limit are equivalent to the solutions excluding axial diffusion effects.

Another important parameter used for describing oscillating flow mechanisms is the Strouhal number, *St*, given by:

$$St_{f,L} = \frac{f L}{u_{x,0}} \tag{2.27}$$

where similar definitions can be made based on forcing frequency form, such as linear or angular, and alternate length scales of interest, such as R_f and L_f. This number physically

corresponds to the relative size of the disturbance wavelength compared to the physical length scale of interest:

$$\frac{L}{L_\lambda} = \frac{L}{u_{x,0} / f} = \frac{fL}{u_{x,0}} \tag{2.28}$$

and unless otherwise specified, $St = fR_f / u_{x,0}$.

2.4.2 Space-time Dynamics

As was stated previously, it is the dynamics of the reaction sheet, rather than the entire scalar field, which we are interested in. For non-premixed flames, this sheet is defined by the locus of points where $\mathcal{Z}\left(\vec{x},t\right) = \mathcal{Z}_{st}$. Alternatively, the instantaneous position of this reaction sheet can be explicitly defined by the variable ξ, which successfully reduces the number of spatial dependent variables required. While Figure 2.2 showed this value schematically, Figure 2.3 shows ξ for two representative premixed and non-premixed experimental systems.

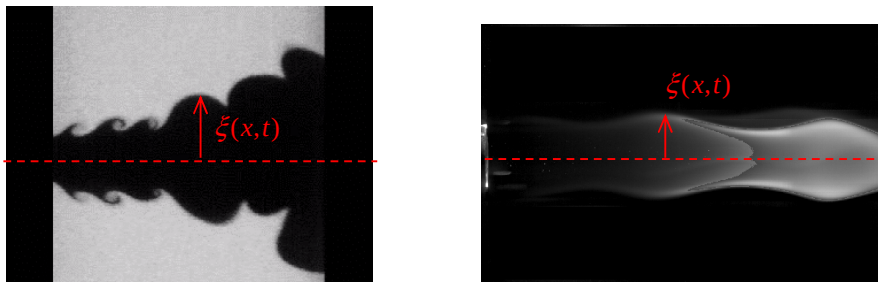

Figure 2.3. Experimental images of forced bluff-body stabilized premixed flame (left) and jet non-premixed flame (right) with its corresponding coordinates and flame front dynamical parameter, *ξ(x,t)*.

Additionally, due to the physical meaning of the $\mathcal{Z}$-equation, explicit expressions for the flame position are not generally possible. However, this is where the assumption

of small disturbances becomes essential for analytical progress. Expanding the implicit equation for the fluctuating flame, $\mathcal{Z}\left(\vec{x},t\right)=\mathcal{Z}_{st}$, in terms of $\mathcal{Z}$ and ξ, results in:

$$\mathcal{Z}_0\big|_{flame}+\mathcal{Z}_1\big|_{flame,t}+\mathcal{Z}_2\big|_{flame,t}=\mathcal{Z}_{st} \tag{2.29}$$

where these quantities are field variables evaluated at the specific flame location, general for a three dimensional system of arbitrary scalar orientation. As the utility of ξ is that it reduces the order of the problem, in order to demonstrate its functionality we must focus on a specific case, i.e. system and scalar orientation; chosen to be the two-dimensional problem of $\xi(x,t)$ as shown in Figure 2.3, although the case of $\xi(y,t)$ and similar three-dimensional orientations can be derived in a similar fashion.

As such, expanding the implicit equation for the fluctuating flame in terms of $\mathcal{Z}$ and $\xi(x,t)$, results in:

$$\begin{aligned}&\mathcal{Z}_0(x,y=\xi_0(x)+\xi_1(x,t)+\xi_2(x,t))+\mathcal{Z}_1(x,y=\xi_0(x)+\\&+\xi_1(x,t)+\xi_2(x,t),t)+\mathcal{Z}_2(x,y=\xi_0(x)+\xi_1(x,t)+\xi_2(x,t),t)=\mathcal{Z}_{st}\end{aligned} \tag{2.30}$$

where these quantities are field variables evaluated at the specific flame location, as a function of *x*. Furthermore, a Taylor-series expansion yields:

$$\begin{aligned}&\mathcal{Z}_0(x,y=\xi_0(x))+\xi_1(x)\left|\nabla\mathcal{Z}_0(x,y=\xi_0(x))\right|+\mathcal{Z}_1(x,y=\xi_0(x),t)+\\&+\xi_2(x)\left|\nabla\mathcal{Z}_0(x,y=\xi_0(x))\right|+\tfrac{1}{2}\xi_1(x)^2\left|\Delta\mathcal{Z}_0(x,y=\xi_0(x))\right|+\\&+\xi_1(x)\left|\nabla\mathcal{Z}_1(x,y=\xi_0(x),t)\right|+\mathcal{Z}_2(x,y=\xi_0(x),t)+O(\varepsilon^3)=\mathcal{Z}_{st}\end{aligned} \tag{2.31}$$

where ε is the small amplitude parameter and $\left|\nabla\mathcal{Z}\right|$ is mathematically equal to $\partial\mathcal{Z}/\partial n$.

Notice how grouping the leading order terms results in the following implicit equation for the steady flame position:

$$\mathcal{Z}_0(x,y=\xi_0(x))=\mathcal{Z}_{st} \tag{2.32}$$

while the first order terms lead to the following *explicit* expression for fluctuating flame position:

$$\xi_1(x,t) = -\frac{\mathcal{Z}_1(x, y=\xi_0(x), t)}{\left|\nabla \mathcal{Z}_0(x, y=\xi_0(x))\right|} \tag{2.33}$$

Similarly, although not considered further in this work, second order terms are:

$$\xi_2(x,t) = \frac{-\frac{1}{2}\xi_1(x,t)^2\left|\Delta \mathcal{Z}_0(x, y=\xi_0(x))\right| - \xi_1(x,t)\left|\nabla \mathcal{Z}_1(x, y=\xi_0(x), t)\right| - \mathcal{Z}_2(x, y=\xi_0(x), t)}{\left|\nabla \mathcal{Z}_0(x, y=\xi_0(x))\right|} \tag{2.34}$$

Thus, even though the steady state, ξ_0, and instantaneous, ξ, flame positions remain imprisoned in implicit equations, the dynamics of the flame fluctuations/wrinkles, ξ_1, are explicitly available! Importantly, ξ_1 can be measured radially or normally to the mean flame surface in the direction of the oxidizer, indicated by a subscript. Generally throughout this work, the normal displacement, i.e. $\xi_{1,n}$, is utilized for quantifying flame motion due to the substantial change in the angle of the reaction sheet with axial location (in contrast, if flame motion is measured as radial displacement, its value is infinite at the flame tip). Once again, however, an explicit governing equation for ξ_1 cannot be obtained by plugging this expression into Eq.(2.22), since expressions as such are not valid:

$$\left.\frac{\partial \mathcal{Z}_1}{\partial x}\right|_{x, y=\xi_0(x), t} \neq \frac{\partial \left.\mathcal{Z}_1\right|_{x, y=\xi_0(x), t}}{\partial x} \tag{2.35}$$

Figure 2.4 shows a representative two-dimensional forced mixture fraction field, with representative steady and instantaneous $\mathcal{Z}_{st}$ contours denoted by red and black lines, respectively. Additionally, the steady flame location is depicted, along with the normally and radially defined fluctuating wrinkle parameters.

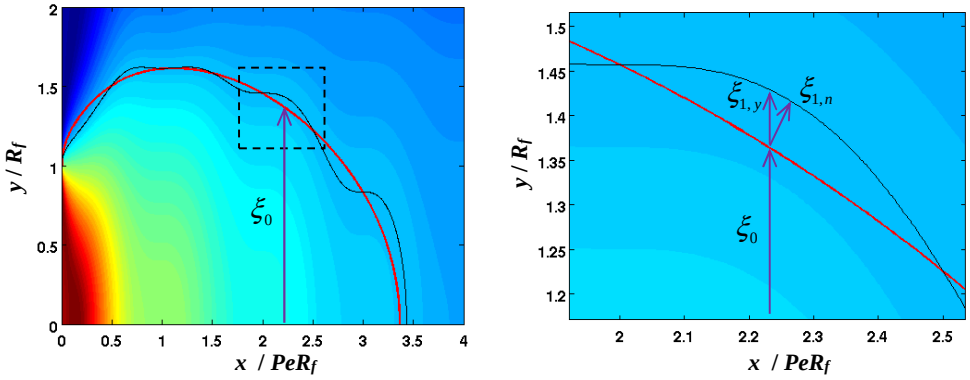

Figure 2.4. Representative two-dimensional non-premixed flame mixture fraction field (left) with steady state (red) and instantaneous (black) flame contours denoted. A close-up view of a "flame wrinkle" (right) shows the steady, $\xi_0(x)$, and fluctuating wrinkle location denoted radially, $\xi_{1,y}(x,t)$, and normally to the mean flame, $\xi_{1,n}(x,t)$.

The steady flame location is a function of spatial location, while the instantaneous location is a function of both spatial location and time. Figure 2.5 shows this instantaneous flame location for several discrete temporal values over a forcing cycle. Additionally, the entire flame brush swept out by the dynamic instantaneous flame over a temporally resolved forcing cycle is also shown.

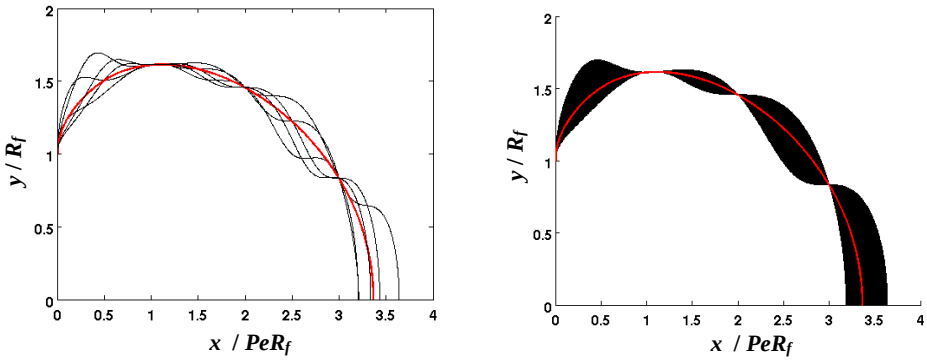

Figure 2.5. Steady (red) and instantaneous (black) flame locations over a forcing cycle for a few discrete times (left) and the entire flame brush (right.

An alternative way to visualize these results, focusing on the wrinkle dynamics, is through the magnitude and phase of ξ_1, which can be obtained mathematically via Eq.(2.33). As an alternate method of interpretation, the wrinkle magnitude can be

obtained by extracting the maximum wrinkle height of the flame brush at each axial location. These results, corresponding to the same conditions shown in Figure 2.4 and Figure 2.5, are shown in Figure 2.6. Information regarding the flame wrinkle amplitude and convection speeds as a function of downstream distance can be gathered from these plots, and thus they will be utilized throughout the remainder of this thesis.

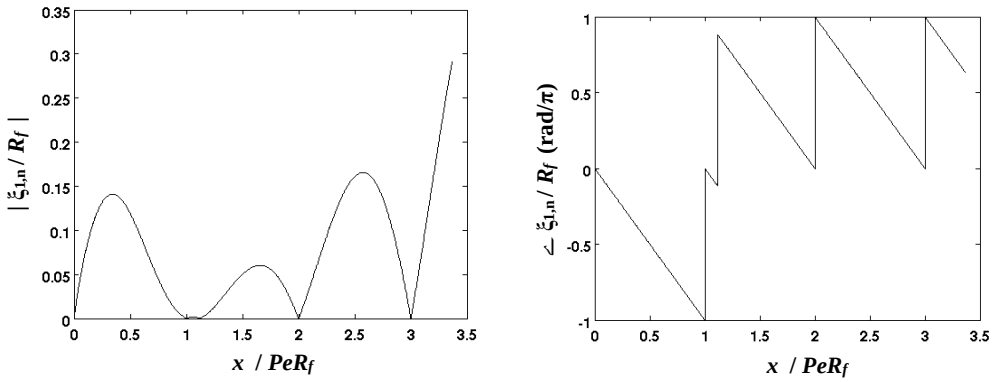

Figure 2.6. Flame wrinkle magnitude (left) and phase (right) plots for a representative two-dimensional non-premixed flame.

2.4.3 Heat Release Analysis

Having introduced the local space-time wrinkling characteristics of the flame, next the heat release dynamics are discussed, in particular the spatially integrated heat release, $\dot{Q}(t)$, due to its applicability for combustion instability or noise related issues for acoustically compact flames.

As was discussed in Chapter 1, oscillations in heat release generate acoustic waves via unsteady gas expansion, which are manifested as broadband noise and discrete tones, for unconfined and confined flames, respectively [4]. If the combustion region of interest is much smaller than an acoustic wavelength, then disturbances originating from different points in the flame arrive at the measurement location with negligible phase shift. This describes a “compact flame” in which the distribution of the heat release is

unimportant; rather the quantity of relevance is the total, spatially integrated value [4]. This spatially integrated quantity is given by the following surface integral over the reaction sheet:

$$\dot{Q}(t) = \int_{flame} \dot{m}_F'' \, \mathcal{h}_R \, dA \tag{2.36}$$

This expression can also be related back to Eq.(2.16) where a special (untractable) form of $f(\vec{x},t)$ is utilized, such that the term inside the "{ }" can be represented by $\dot{m}_F'' \, \mathcal{h}_R$, where $\dot{m}_F$" is the reactant mass burning rate per unit area, and $\mathcal{h}_R$ is the heat release per unit mass of reactant consumed.

For premixed flames, the mass burning rate can be written in terms of the burning velocity as $\dot{m}_F" = \rho^u s_c^u$, where ρ^u is the density and s_c^u is the laminar consumption speed of the unburned reactant, yielding:

Premixed flame:
$$\dot{Q}(t) = \int_{flame} \rho^u s_c^u \mathcal{h}_R dA \tag{2.37}$$

For non-premixed flames, the reactant mass burning rate can be written in terms of the fuel mass fraction as:

$$\dot{m}_F^" = \dot{m}_{Ox}^" + \dot{m}_{Fuel}^" = \rho \mathscr{D} \frac{\partial Y_{Ox}}{\partial n} - \rho \mathscr{D} \frac{\partial Y_{Fuel}}{\partial n} = -(1+\varphi_{Ox}) \rho \mathscr{D} \frac{\partial Y_{Fuel}}{\partial n} \tag{2.38}$$

where *n* represents the direction normal to the flame surface into the oxidizer. By also relating the fuel mass fraction and the mixture fraction gradients as:

$$\frac{\partial Y_{Fuel}}{\partial n} = \frac{(\varphi_{ox}+1)}{\varphi_{ox}} \frac{\partial \mathcal{Z}}{\partial n} \tag{2.39}$$

and assuming fixed composition fuel and oxidizer, so that the heat of reaction and mixture density remain constant, the corresponding spatially integrated heat release can be written as:

Non-premixed flame:
$$\dot{Q}(t) = \int_{flame} \frac{-(1+\varphi_{Ox})^2}{\varphi_{Ox}} \rho \mathscr{D} \mathscr{h}_R \frac{\partial \mathscr{Z}}{\partial n} dA \tag{2.40}$$

This quantity is defined for a non-premixed flame under specific conditions, both steady and fluctuating. As the study of combustion instabilities inherently deals with oscillatory disturbances, a more encompassing, and relevant, parameter is known as the transfer function, defined as follows for the case of velocity oscillations resulting in heat release oscillations:

$$\mathscr{T}(\omega) = \frac{\hat{\dot{Q}}_1(\omega) / \dot{Q}_0}{\hat{\bar{u}}_1 / \bar{u}_0} \tag{2.41}$$

Alternate definitions can be utilized for the other various heat release coupling mechanisms, such as pressure or equivalence ration oscillations, where this parameter physically represents an input-output relation between the disturbance fluctuations and the resulting heat release fluctuations. Mathematically, these transfer function are complex numbers, whose magnitude and phase indicate the relative magnitude ratios and phase differences between the heat release and disturbance quantity. Additionally, this parameter is a function of disturbance forcing frequency, rather than time, making it extremely useful when considering the response of flames to discrete tones, as is often experienced with combustion instabilities. Premixed or non-premixed transfer functions will be denoted as $\mathscr{T}_P$ and $\mathscr{T}_N$, respectively.

It is useful to decompose the results in Eq.(2.41) into contributions from mass burning rate and flame area fluctuations; i.e., $\mathscr{F} = \mathscr{F}_{mbr} + \mathscr{F}_{wa}$. This can be done by linearizing and expanding Eq.(2.36) as:

$$\dot{Q}(t) = \mathscr{k}_R \Bigg[\underbrace{\int_{flame} \dot{m}''_{F,0}\, dA_0}_{\dot{Q}_0} + \underbrace{\int_{flame} \dot{m}''_{F,1}\, dA_0}_{\dot{Q}_{mbr}(t)} + \underbrace{\int_{flame} \dot{m}''_{F,0}\, dA_1}_{\dot{Q}_{wa}(t)} \Bigg] \tag{2.42}$$

This first term represents the steady state spatially integrated heat release. The second term defines the mass burning rate term. For non-premixed flames, this contributes to heat release oscillations due to the fluctuations in spatial gradients of the mixture fraction. For premixed flames, the mass burning rate fluctuations are linked to the stretch sensitivity of the burning velocity, which fluctuates because of the oscillatory curvature of the wrinkled front [87]. The last term is a weighted area term, named such due to the weighting of the flame surface area fluctuations by the time averaged burning rate, which unlike premixed flames, is spatially non-uniform for general non-premixed flames (to be discussed in Chapter 3). The un-weighted area term (important for constant burning velocity premixed flames) is given for a spatially constant time averaged burning rate by:

$$\dot{Q}_a(t) = \mathscr{k}_R \dot{m}''_{F,0} \int_{flame} dA_1 \tag{2.43}$$

where these fluctuating, instantaneous, and steady area terms, i.e. integral terms of dA_1 and dA_0 along the flame, can in turn be related back to $\mathscr{I}_\Psi$ from Eq.(2.17).

There are significant variations in time-averaged heat release rate along the non-premixed flame (e.g., no heat release at the tip in the absence of axial diffusion). Thus,

the weighting of flame area is a very significant effect influencing how area fluctuations lead to heat release. Moreover, as will be discussed in the next Chapter, the characteristics of the weighted and un-weighted area transfer functions are quite different for non-premixed flames, while they are identical for premixed flames with spatially uniform burning velocities. For example, in the low Strouhal number limit, the non-premixed flame weighted and un-weighted area transfer functions differ in phase by 180 degrees and have appreciably different magnitudes.

2.5 Explicit Flame Front Governing Equations

As was discussed in Section 2.3, the physical differences with the governing field equations, for premixed and non-premixed flame systems, results in vastly different solution approaches to understanding the dynamics of these flames analytically.

A useful transformation of the *G*-equation is done by expressing Eq.(2.8) in terms of the flame position, ξ. Although the resulting equation for the flame position becomes less general, it enables an explicit representation of the flame locations, whereas this quantity must be implicitly obtained with the *G*-equation. With these explicit expressions, dynamical quantities, such as flame surface area fluctuations and flame curvature, can be obtained and investigated. As mentioned, a common method of variable transformation, in two-dimensions, from the *G*-equation to the flame position equation is done by substituting $G(x,y,t) = y - \xi(x,t)$ (see Figure 2.2). This results in a new differential equation for the premixed flame position:

$$\frac{\partial \xi}{\partial t} + u_x \frac{\partial \xi}{\partial x} - u_y = S_L \sqrt{1 + \left(\frac{\partial \xi}{\partial x}\right)^2} \tag{2.44}$$

Unfortunately, a similar change of variables cannot be done for the general non-premixed flame system, for reasons previously discussed. However, in order to build familiarity with the $\mathcal{Z}$ -equation and to have a reference equation for later, we can consider the simplified case of a flat flame in a uniform flow field, for the geometry considered in Figure 2.2.

This can be done by first taking the series expansion of $\mathcal{Z}$ at the flame, i.e. $y = \xi$, formulated as:

$$\mathcal{Z}(x, y, t, \mathcal{Z}_{st}) = \mathcal{Z}_{st} + \alpha\left(y - \xi(x, t, \mathcal{Z}_{st})\right) + HOTs \tag{2.45}$$

where α is a function of x, t, and $\mathcal{Z}_{st}$, defined **at** the flame as:

$$\alpha = \left.\frac{\partial \mathcal{Z}}{\partial y}\right|_{x,\, y=\xi_0,\, t,\, \mathcal{Z}_{st}} \tag{2.46}$$

By plugging Eq.(2.45) into Eq.(2.7), neglecting higher order terms, results in:

$$\begin{aligned} &\frac{\partial \alpha}{\partial t} y - \frac{\partial \xi}{\partial t}\alpha - \frac{\partial \alpha}{\partial t}\xi + u_x\left[\frac{\partial \alpha}{\partial x} y - \frac{\partial \alpha}{\partial x}\xi - \frac{\partial \xi}{\partial x}\alpha\right] + u_y[\alpha] = \\ &\qquad = \mathscr{D}\left[\frac{\partial^2 \alpha}{\partial x^2} y - \frac{\partial^2 \alpha}{\partial x^2}\xi - 2\frac{\partial \alpha}{\partial x}\frac{\partial \xi}{\partial x} - \frac{\partial^2 \xi}{\partial x^2}\alpha\right] \end{aligned} \tag{2.47}$$

or by regrouping terms:

$$\begin{aligned} &[y - \xi]\frac{\partial \alpha}{\partial t} + \left[-\frac{\partial \xi}{\partial t} - u_x\frac{\partial \xi}{\partial x} + \mathscr{D}\frac{\partial^2 \xi}{\partial x^2} + u_y\right]\alpha + \\ &+\left[u_x y - u_x\xi + 2\mathscr{D}\frac{\partial \xi}{\partial x}\right]\frac{\partial \alpha}{\partial x} - \mathscr{D}[y - \xi]\frac{\partial^2 \alpha}{\partial x^2} = 0 \end{aligned} \tag{2.48}$$

Noting that for a nominally flat flame $\alpha >> \alpha_x, \alpha_{xx}, \alpha_t$, a simplified flame position equation, similar to Eq.(2.44) can be obtained as:

$$\frac{\partial \xi}{\partial t} + u_x \frac{\partial \xi}{\partial x} - u_y = \mathscr{D} \frac{\partial^2 \xi}{\partial x^2} \tag{2.49}$$

Thus, Eq.(2.49) is a simplified flame position equation, similar to Eq.(2.44). Notice how the left-hand sides of these equations both show the standard convective operator. Therefore, in the absence of right-hand side terms, any disturbance on the flame front is simply convected in the flow direction. For the premixed equation, the nonlinear term on the right-hand side in Eq.(2.44) originates from the physical nature of normal flame front propagation. Geometrically, this property is similar to waves which propagate from every point source. This nonlinear operator can cause discontinuities in the slope of flame fronts, which is very hard to track by conventional asymptotic analysis [88]. For the non-premixed case this right-hand side term is a linear diffusion controlled term responsible for front smoothing.

To gain some insight into the properties of this equation, we investigate the evolution equation for the flame slope, $h = \partial \xi / \partial x$, which can be obtained by differentiation with respect to *x*:

$$\frac{\partial h}{\partial t} + \frac{\partial u_x}{\partial x}\frac{\partial \xi}{\partial x} + u_x \frac{\partial h}{\partial x} - \frac{\partial u_y}{\partial x} = \mathscr{D} \frac{\partial^2 h}{\partial x^2} \tag{2.50}$$

For simplicity, consider a case with only spatially uniform axial flow:

$$\frac{\partial h}{\partial t} + U_0 \frac{\partial h}{\partial x} = \mathscr{D} \frac{\partial^2 h}{\partial x^2} \tag{2.51}$$

At *t*=0, we impose a step increase in flow velocity. The long term *t*>>0 behavior is straightforward, however the transient is not. This problem can be analyzed by considering a traveling diffusion wave, and utilizing a transformation of variables $h(x,t) = \mu(x - ut, t)$ to simplify this problem to:

$$\frac{\partial \mu}{\partial t} = \mathscr{D} \frac{\partial^2 \mu}{\partial x^2} \tag{2.52}$$

whose resulting solution is:

$$\mu = \frac{1}{\sqrt{4\pi t}} \exp\left[\frac{-x^2}{4t\mathscr{D}}\right] \tag{2.53}$$

Eq.(2.53) gives the non-premixed flame slope as a function of space and time, for this discontinuous velocity change. Similar solutions can be obtained for the case of a premixed flame, utilizing Eq.(2.44), for similar attachment and flow conditions, resulting in [4]:

$$\frac{\partial h}{\partial t} - c(h)\frac{\partial h}{\partial x} = 0 \tag{2.54}$$

where $c(h)$ is the component of the disturbance propagation velocity in the x-direction. It was shown by Whitham [89-91], and more specifically for combustion systems by Lieuwen [4], that when this previously stationary flame was abruptly modified with a step change in flow velocity, that this equation could develop discontinuities in the flame slope, analogous to shock waves. The flame relaxation transient process consists of a wave that propagates along the flame in the flow direction. The abrupt change in slope from the initial t=0 value, h_i, to the final t>>0 value, h_f, is initiated at the attachment point (x=0), and this slope discontinuity travels along the flame front at the "shock" velocity. This shock propagation velocity lies between the wave propagation velocities of the initial condition and final steady state solutions [4]. However, this slope discontinuity remains sharp during the propagation.

Whereas this traveling slope discontinuity remains sharp/discontinuous for the premixed case, in the non-premixed solution the diffusion term helps smooth out the initially abrupt shock discontinuity as it convects downstream. The degree of and speed

of smoothing is dependent upon the *Pe* value; while in the $Pe \to \infty$ limit, as the diffusion term becomes vanishingly small, the smooth solutions converge non-uniformly to the appropriate discontinuous shock wave!

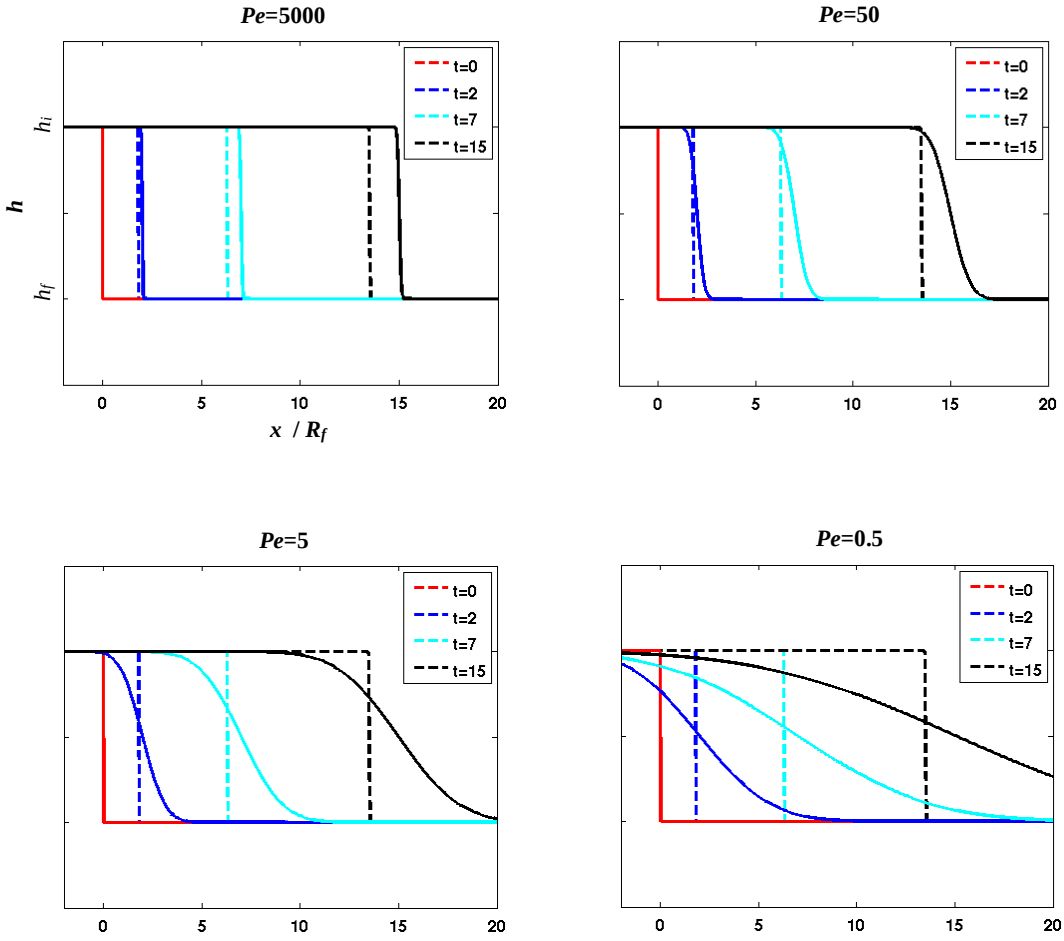

Figure 2.7. Flame slope, *h*, for a premixed (dashed) and non-premixed (solid) flame, exposed to a step change in flow velocity, U_0, at *t*=0, for various values of diffusion. The premixed solutions utilize a representative *c* value of 0.9.

Figure 2.7 shows the normalized slope of a premixed (Eq.(2.54)) and non-premixed (Eq.(2.51)) flame responding to a discontinuous step change (increase) in flow velocity for various *Pe* values (U_0 was held constant while $\mathscr{D}$ was modified). It can be seen that the non-premixed solution smooths with downstream motion, while the

premixed solution remains sharp. The smoothing effect of the diffusion term, no matter how small, prevents the appearance of a discontinuous shock. These solutions demonstrate how the wave equation is energy conserving, while the heat equation is energy dissipating. An additional subtle difference, visible from the high *Pe* case, is that the slope discontinuity propagation speed for the non-premixed solution is greater than that of the premixed case, due to the premixed front propagation controlling $c(h)$. Lastly, as can be seen from the sub-unity *Pe* case, the condition $Pe<1$ for non-premixed flames is similar to flashback in premixed flames!

CHAPTER 3

Isothermal Diffusion Flame Analysis – Fundamental Dynamics

This chapter examines the basic dynamical characteristics of a non-premixed flame responding to harmonic flow perturbations. The key assumptions of this analysis are (1) infinitely fast chemistry, wherein the flame sheet collapses to the $\mathcal{Z}_{st}$ surface, (2) all species have equal diffusivities, (3) negligible radiative heat loss effects, (4) constant-isotropic diffusion coefficients, (5) specified disturbance fields, and (6) small perturbation amplitudes. Following assumption (2), the space-time dynamics of a non-premixed flame with constant species diffusivities is described by the mixture fraction field using the $\mathcal{Z}$ -equation.

In this study the flame front is continuously perturbed by spatially uniform field, *i.e.* bulk flow, disturbances, although the flame front can also be excited through unsteady motion of the flame base, as was shown for a premixed flame by D.H. Shin [92]. Significantly, the steady and fluctuating velocity fields are imposed, thus decoupling the momentum equation from the energy and species equations – this assumption implicitly assumes an isothermal field. The analytical formulation is presented and explicit expressions are obtained for the fluctuating flame position and spatially integrated heat release for various flame/system configurations. The first section presents a detailed walkthrough for the case of a two-dimensional confined axially bulk forced system. The important $Pe \to \infty$ limit is discussed, along with term-by-term analysis of the various explicit analytical expressions for the space-time and heat release dynamics. Then, the effects of various features, such as system confinement and forcing direction/type, on the

steady flame location and fluctuating dynamics are discussed. Lastly, the complications of differential diffusion, i.e. $\mathscr{D}_F \neq \mathscr{D}_{Ox}$ are discussed, and a model problem is introduced to gain insight into the implications on the dynamics. Additional, more mathematically intensive dynamical features, resulting from the inclusion of additional system physics, will be covered in Chapter 4.

As mentioned, previous studies have also analyzed this problem within the infinite reaction rate, $\mathcal{Z}$ -equation formulation for the mixture fraction [62-64, 66, 93] and **implicit** solutions were developed for the flame position and heat release for several problems, including the flame response to axial velocity and mixture fraction oscillations. However, this work, and thesis, is unique in that **explicit** expressions are presented and the dynamical / physical features dissected from them.

3.1 Two-dimensional Bulk Axial Forcing

In a multidimensional duct, the presence of external forcing can excite motions associated with multiple natural duct modes [4]. The behavior of the system is fundamentally different depending on whether the forcing frequency is higher or lower than natural transverse duct frequency [94]. Below this “cutoff frequency”, only one-dimensional plane waves propagate while all multidimensional disturbances decay exponentially. Thus, “one-dimensional analyses of the acoustic frequencies and mode shapes in complex, multidimensional geometries are often quite accurate in describing the bulk acoustic features of the system for frequencies below cutoff” [4]. Additionally, the assumed spatially uniform disturbance field, is most valid for these low frequencies. Thus, this section formulates the two-dimensional problem of spatially uniform one-dimensional velocity fluctuations, which is illustrated in Figure 3.1. The analysis begins

with a confined system since **most** combustion instabilities occur within confined chambers, an assumption which is relaxed in the next section.

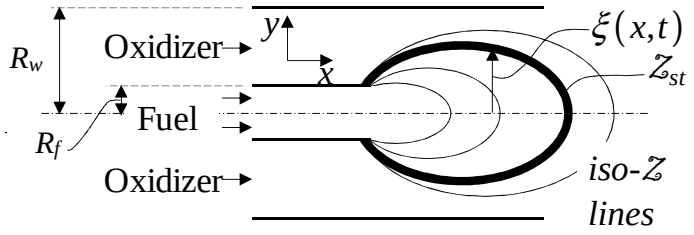

Figure 3.1. Schematic of the forced two-dimensional non-premixed flame model problem.

We consider a two-dimensional flame in a uniform axial flow field, $u_{x,0}$. At the inlet (x=0), fuel and oxidizer flow into the domain as indicated in the figure, leading to the following step inflow conditions:

$$\mathcal{Z}(x=0,y)=\begin{cases}1 \text{ for } 0\le |y| < R_f \\ 0 \text{ for } R_f \le |y| < R_w\end{cases} \tag{3.1}$$

The solution can also be easily generalized to include more general inflow fuel/oxidizer compositions (e.g., such as if the fuel were diluted) by shifting and rescaling the value of $\mathcal{Z}_{st}$. Enforcing this boundary condition enables an analytic solution of the problem. However, in reality there is axial diffusion of fuel into the oxidizer and vice versa, so that the solution must actually be solved over a larger domain that includes the fuel/oxidizer supply systems. As such, the boundary condition in Eq.(3.1) implicitly neglects axial diffusion at $x=0$, a point we will return to in Chapter 4. Assuming symmetry at $y=0$ and no diffusion through the walls at $y=R_w$, leads to the following two additional boundary conditions:

$$\frac{\partial \mathcal{Z}}{\partial y}(x,y=0)=0 \qquad \frac{\partial \mathcal{Z}}{\partial y}(x,y=R_w)=0 \tag{3.2}$$

For reasons discussed in Chapter 2, we will derive the solution in the limit of small perturbations, and so expand each variable as $(\ )(x,y,t)=(\ )_0(x,y)+(\ )_1(x,y,t)$. Neglecting higher order terms, the steady state, i.e. unforced, mixture fraction field, for a system with no transverse flow, i.e. $u_{y,0}=0$, can be acquired from Eq.(2.21) as:

$$U_0\frac{\partial Z_0}{\partial x}=\mathscr{D}\frac{\partial^2 Z_0}{\partial y^2}+b\mathscr{D}\frac{\partial^2 Z_0}{\partial x^2} \tag{3.3}$$

where $u_{x,0}=U_0$ for visual compactness and "*b*" is an axial diffusion indicator, taking values of unity and zero, depending upon whether axial diffusion effects are enabled or disabled within the domain, respectively. Similarly, the dynamical equation for the fluctuating, i.e. forced, component, of the mixture fraction field can be obtained from Eq.(2.22) and written in the frequency domain as:

$$-i\omega\hat{Z}_1+U_0\frac{\partial\hat{Z}_1}{\partial x}-\mathscr{D}\frac{\partial^2\hat{Z}_1}{\partial y^2}-b\mathscr{D}\frac{\partial^2\hat{Z}_1}{\partial x^2}=-\hat{u}_{x,1}\frac{\partial Z_0}{\partial x}-\hat{u}_{y,1}\frac{\partial Z_0}{\partial y} \tag{3.4}$$

The solution to these equations can be derived in an analogous way as the Burke-Schumann solution, using separation of variables. The full solution, including axial diffusion (*b*=1), for the steady state mixture fraction field, utilizing Eqs.(3.2) and (3.1) as boundary and inlet conditions, respectively, is given by:

$$Z_0=\frac{R_f}{R_w}+\sum_{n=1}^{\infty}\frac{2}{n\pi}\sin(\mathscr{A}_n)\cos\left(\mathscr{A}_n\frac{y}{R_f}\right)\exp\left(\frac{x}{PeR_f}\left[\frac{Pe^2-\sqrt{Pe^4+4Pe^2\mathscr{A}_n^2}}{2}\right]\right) \tag{3.5}$$

where $\mathscr{A}_n=n\pi(R_f/R_w)$ are the eigenvalues and the Peclet number, *Pe*, is given by Eq.(2.25).

For the subsequent analysis, we will focus on the following simplified version of the solution that neglects axial diffusion, since we have already done so implicitly in formulating the boundary condition in Eq.(3.1). The resulting steady state mixture fraction field solution is:

$$\mathcal{Z}_0 = \frac{R_f}{R_w} + \sum_{n=1}^{\infty} \frac{2}{n\pi} \sin\left(\mathcal{A}_n\right) \cos\left(\mathcal{A}_n \frac{y}{R_f}\right) \exp\left(-\mathcal{A}_n^{\,2} \frac{x}{PeR_f}\right) \tag{3.6}$$

This equation can be derived by solving Eq.(3.3) and neglecting the axial diffusion term, i.e. setting b=0, or equivalently, taking the $Pe \to \infty$ limit of Eq.(3.5). We next consider the solution for the fluctuating flame position responding to uniform bulk axial fluctuations in flow velocity:

$$u_{x,1} = \varepsilon U_0 \exp\left[-i\omega t\right] \tag{3.7}$$

The resulting full solution for the fluctuating mixture fraction field, $\mathcal{Z}_1$, is:

$$\mathcal{Z}_1 = \sum_{n=1}^{\infty} \left[\frac{2/(n\pi)\sin\left(\mathcal{A}_n\right)\varepsilon\beta_-}{2\pi i PeSt} \right] \cos\left(\mathcal{A}_n \frac{y}{R_f}\right) \left\{ \exp\left(\frac{x}{PeR_f}\beta_-\right) - \exp\left(\frac{x}{PeR_f}\beta_{\mathrm{h}-}\right) \right\} \exp\left[-i\omega t\right] \tag{3.8}$$

where the Strouhal number based on the half-width of the fuel nozzle is defined by Eq.(2.27) ($St = St_{f,R}$), and

$$\beta_- = \frac{Pe^2 - \sqrt{Pe^4 + 4Pe^2\mathcal{A}_n^{\,2}}}{2} \qquad \beta_{\mathrm{h}-} = \frac{Pe^2 - \sqrt{Pe^4 + 4Pe^2\mathcal{A}_n^{\,2} - 8\pi i Pe^3\, St}}{2} \tag{3.9}$$

Again we will focus the subsequent analysis in the absence of axial diffusion, i.e. in the $Pe \to \infty$ limit, whose solution is:

$$\mathcal{Z}_1 = \sum_{n=1}^{\infty} \left[\frac{i\varepsilon\mathcal{A}_n^{\,2}(2/n\pi)\sin\left(\mathcal{A}_n\right)}{2\pi\, St\, Pe} \right] \cos\left(\mathcal{A}_n \frac{y}{R_f}\right) \exp\left(-\mathcal{A}_n^{\,2} \frac{x}{Pe\, R_f}\right) \left\{ 1 - \exp\left(2\pi i\, St \frac{x}{R_f}\right) \right\} \exp\left[-i\omega t\right] \tag{3.10}$$

Alternatively, this expression can also be written in terms of $\mathcal{Z}_0$ as:

$$\mathcal{Z}_1 = \left[\frac{-i\varepsilon R_f}{2\pi St}\right]\frac{\partial \mathcal{Z}_0}{\partial x}\left\{1-\exp\left(2\pi i St\frac{x}{R_f}\right)\right\}\exp\left[-i\omega t\right] \tag{3.11}$$

This form is significant in that it no longer contains the mathematically complicating infinite summation, a key point that will be emphasized and utilized shortly.

3.1.1 Space-time Dynamics

An implicit expression for the flame sheet position, $\xi_0(x)$, can be determined from Eq.(2.32), yielding:

$$\mathcal{Z}_{st} = \frac{R_f}{R_w} + \sum_{n=1}^{\infty}\frac{2}{n\pi}\sin\left(\mathcal{A}_n\right)\cos\left(\mathcal{A}_n\frac{\xi_0(x)}{R_f}\right)\exp\left(-\mathcal{A}_n^{\,2}\frac{x}{PeR_f}\right) \tag{3.12}$$

Similarly, the position of the fluctuating flame can be determined from the implicit expression, Eq.(2.29). However, as was previously discussed, Eq.(2.33) is an explicit expression for the fluctuating flame position. Utilizing Eq.(3.11), this expression can be re-written as:

$$\frac{\xi_{1,n}\left(x,t\right)}{R_f} = \left(\frac{\partial \mathcal{Z}_0/\partial x}{\left|\nabla \mathcal{Z}_0\right|}\right)_{\left(x,y=\xi_0(x)\right)}\left[\frac{i\varepsilon}{2\pi St}\right]\left\{1-\exp\left(2\pi i St\frac{x}{R_f}\right)\right\}\exp\left[-i\omega t\right] \tag{3.13}$$

where $\xi_{1,n}$ is measured normal to the mean flame surface in the direction of the oxidizer. The $\left(\frac{\partial \mathcal{Z}_0/\partial x}{\left|\nabla \mathcal{Z}_0\right|}\right)$ term can be written in terms of the local angle of the flame, using the geometric relation:

$$\left|\nabla \mathcal{Z}_0\right| = \left[\left(\frac{\partial \mathcal{Z}_0}{\partial x}\right)^2 + \left(\frac{\partial \mathcal{Z}_0}{\partial y}\right)^2\right]^{1/2} = \frac{\partial \mathcal{Z}_0/\partial x}{\sin\theta_0(x)} \tag{3.14}$$

where θ_0 denotes the angle of the mean flame with respect to the axial coordinate. Using these results, and a modified definition for *St* for ease of comparison ($St_{L_f} = St_{f,L} = L_{f,0} / R_f \times St_{f,R}$), the solution for $\xi_{1,n}(x,t)$ can be written as:

$$\xi_{1,n}(x,t) = \frac{i\varepsilon U_0}{2\pi f}\sin\theta_0(x)\left\{1-\exp\left(i2\pi St_{L_f}\frac{x}{L_{f,0}}\right)\right\}\exp[-i2\pi ft] \qquad (3.15)$$

This expression is an important contribution of this thesis and very significant in that it is an **explicit** equation for the space-time dynamics of the flame position. For reference, the corresponding fluctuations of an attached premixed flame with constant burning velocity subjected to bulk flow oscillations are given by [86]:

$$\xi_{1,n}(x,t) = \frac{i\varepsilon U_0}{2\pi f}\sin\theta\left\{1-\exp\left(i2\pi St_p\frac{x}{L_{f,0}}\right)\right\}\exp[-i2\pi ft] \qquad (3.16)$$

where St_p is the flame Strouhal number for premixed flames, defined as $St_p = St_{L_f} / \cos^2\theta$, and the angle θ is a constant (the expression is more involved if θ is varying, which would occur if the flow or flame speed varies spatially).

Notice the similarities in the premixed and non-premixed solutions, with the exception of the spatial phase dependence, $1-e^{i2\pi f\, x/U_0}$ term. Both solutions contain a magnitude term, depicting the low-pass filter characteristic of the flame, i.e. as the forcing frequency is increased the response magnitude degreases, and a flame angle term, showing the importance of the fluctuations normal to the mean flame surface in generating wrinkles. Although the flame angle term contains a subtle difference, being the axial dependence of the flame location for the non-premixed case, the primary

difference in these solutions is contained within the waveform term, and reflects the influence of premixed flame propagation on wrinkle convection speeds; i.e., the wrinkle convection speed in the axial direction, $U_0 / \cos^2\theta$, is the vector superposition of the axial flow velocity and the axial projection of a vector pointing normal to the flame with a magnitude equal to the burning velocity, s_d. In contrast, the non-premixed flame does not propagate and wrinkles convect downstream at a speed of U_0, as is depicted in Figure 3.2.

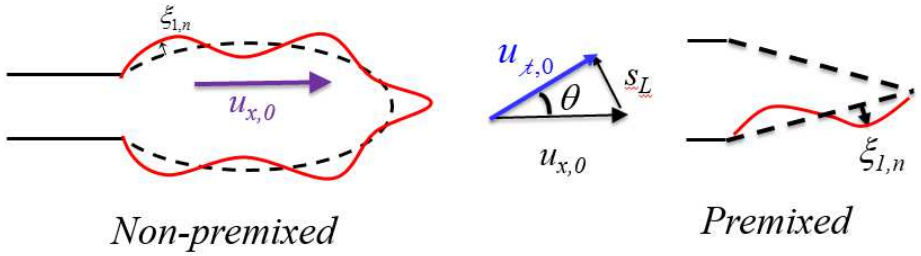

Figure 3.2. Schematics depicting the difference in wrinkle convection speed for non-premixed and premixed flame system.

In both cases, local maxima and minima arise through this $1-e^{i2\pi f\, x/U_0}$ waveform term, due to interference between wrinkles generated at the x=0 boundary and disturbances excited locally. This can be seen by re-writing it as:

$$1-e^{i2\pi f\, x/U_0} = 2\sin\left(\pi f\, x/U_0\right)e^{i(\pi f\, x/U_0-\pi/2)} \tag{3.17}$$

For both premixed and non-premixed flames, wrinkles are generated at the boundary because of flame attachment. For the premixed flame, this is invoked through the attachment boundary condition i.e., $\xi_{1,n}(x=0,t)=0$. In the non-premixed case, wrinkles are generated through the assumption of constant mixture fraction at the burner outlet, i.e., $\mathcal{Z}_1(x=0,t)=0$.

Finally, we note that incorporating stretch effects into the premixed flame analysis modifies Eq.(3.17) by multiplying the complex exponential inside the braces by the factor $\exp\left(-4\pi^2\sigma_c St_p^2\, x/L_{f,0}\right)$ [87], where σ_c is the Markstein length normalized by the burner half-width. For a thermo-diffusively stable flame, this stretch correction leads to an exponential decay in wrinkle magnitude because of the flame front curvature. These additional flame dynamics will be revisited in Chapter 4.

We next present several illustrative solutions of the space-time dynamics for the flame position. Note that the solution is a function of the four dimensionless parameters St_{L_f}, R_f / R_w, Pe, and Z_{st}. The temporal evolution of the flame position is plotted in Figure 3.3 at two Strouhal numbers. Note the bulk axial pulsing of the flame at lower Strouhal numbers, and the spatial wrinkling at higher values. The unforced flame is indicated by the dashed lines.

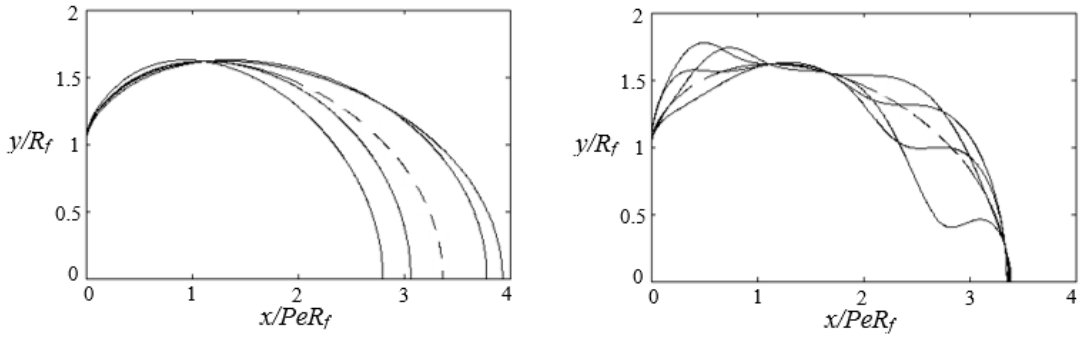

Figure 3.3. Shapshots showing four instantaneous positions of a forced non-premixed flame at two different forcing frequencies using nominal values of $Z_{st}=0.3$ and $Pe=50$ (left) $\varepsilon=0.2$, $St_R=0.0018$, $St_{L_f}=0.3$ (right) $\varepsilon=1.0$, $St_R=0.012$, $St_{L_f}=2.0$.

Mohammed et al. [56] have reported measurements and computations of a forced CH_4-air diffusion flame, which are reproduced in Figure 3.4 (left). In this experiment,

only the fuel flow rate was perturbed, as opposed to both fuel and air flow oscillations in these calculations. However it is still useful to compare results, using conditions that approximately simulate those from the experiment. Figure 3.4 (right) shows calculations of the unsteady flame position at several instants of time for similar conditions. Similar bulk axial pulsing of the flame is evident in the measurements.

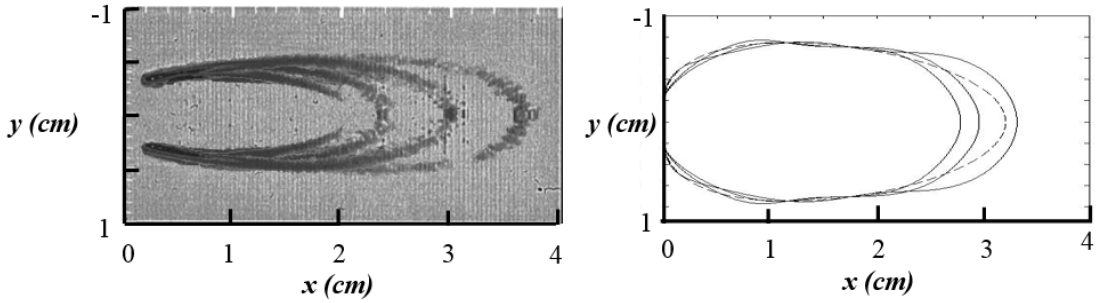

Figure 3.4. (left) CH mole fraction isopleths of the steady and time-varying laminar CH4-air diffusion flame [56]. Experimental isopleths at steady state, 0.00, 0.01, 0.02, 0.03, and 0.04 s. (right) Theoretical results using parameters chosen to match experiments of *Pe* = 0.86, $St_{L_f} = 1.82$, $Z_{st} = 0.13$, and $\varepsilon = 0.5$ for CH_4-air diffusion flame.

An alternative way to visualize these results is through the magnitude and phase of $\xi_{1,n}$, illustrated in Figure 3.5. The nodes and local maxima and minima referred to above are clearly evident in the figure. The phase rolls off linearly with axial distance, again reflecting the convection process described by the interference waveform term in Eq.(3.17), and jumps 180 degrees across the nodes.

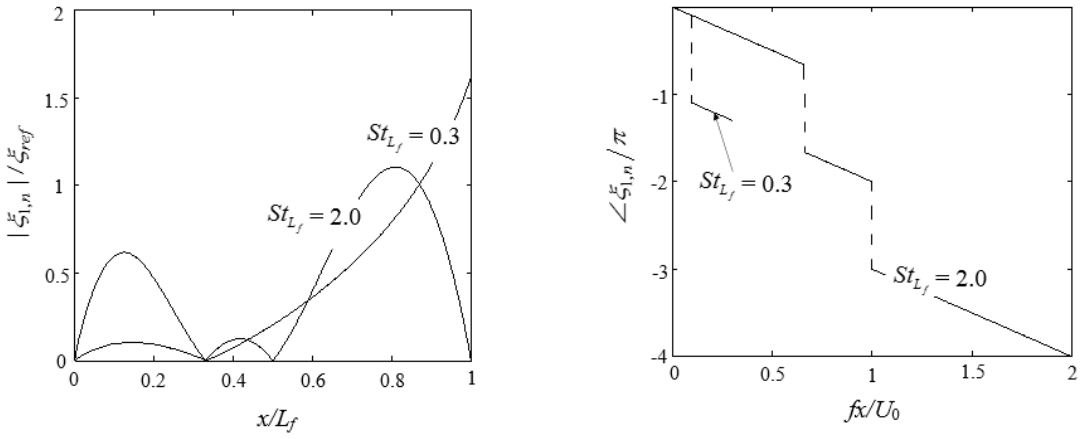

Figure 3.5. Axial dependence of (left) magnitude and (right) phase of flame response, where $\xi_{ref} = \frac{\varepsilon \cdot U_0}{Pe \cdot 2\pi f}$, and using nominal values of $\mathcal{Z}_{st} = 0.3$ and $Pe = 50$ for St_{L_f} values of 0.3 and 2.0. Note the abscissa, ($x/U_0/f$), can equivalently be written as $x/L_f * St_{L_f}$.

Lastly, the speed of the flamelet (differing from that of a passive scalar) with respect to the flow, can be determined for this non-premixed system. In analogy with premixed flames, we will refer to this velocity as $s_d(x,t)$ (recognizing that the non-premixed flamelet does not propagate, being a constant property surface) defined by:

$$\frac{\partial \mathcal{Z}}{\partial t} + \vec{u} \cdot \nabla \mathcal{Z} = \nabla \cdot \left(\mathscr{D} \nabla \mathcal{Z} \right) = s_d \left| \nabla \mathcal{Z} \right| \tag{3.18}$$

This spatio-temporally varying quantity can be non-dimensionalized and expressed as:

$$\frac{s_d(x,t)}{U_0} = \frac{1}{Pe} \frac{\nabla^2 \mathcal{Z}}{\left| \nabla \mathcal{Z} \right|} \Bigg|_{\xi_0(x)} = \sin\theta(x,t) \tag{3.19}$$

or similarly, decomposed into steady and fluctuating components as:

$$\frac{s_{d,0}(x)}{U_0} = \frac{1}{Pe} \frac{\nabla^2 \mathcal{Z}_0}{\left| \nabla \mathcal{Z}_0 \right|} \Bigg|_{\xi_0(x)} = \sin\theta_0(x) \tag{3.20}$$

$$\frac{s_{d,1}(x,t)}{U_0} = \frac{1}{Pe} \frac{\nabla^2 \mathcal{Z}_1 - \dfrac{s_{d,0}(x)}{U_0} Pe \left|\nabla \mathcal{Z}_1\right|}{\left|\nabla \mathcal{Z}_0\right|} \Bigg|_{\xi_0(x)} = \sin\theta_1(x,t) \qquad (3.21)$$

Representative results are shown in Figure 3.6. These results agree with those formulated for premixed flames, and similarly can be justified since from a quasi-steady viewpoint the flame front is stationary, and hence the relative flamelet speed must be equal to the flow velocity normal to the flame front. Interestingly, now s_d can be either positive or negative, and varies with both x and t, whereas for premixed flames it was strictly positive with the possibility to have non-spatiotemporally varying values. Also note how the fluctuating burning speed amplitude looks similar to the flame wrinkle amplitude plot, having the same noding pattern. The slight difference in magnitude results from the definition of the fluctuating flame angle (θ_1), having dependence upon the significantly axially varying steady angle (θ_0).

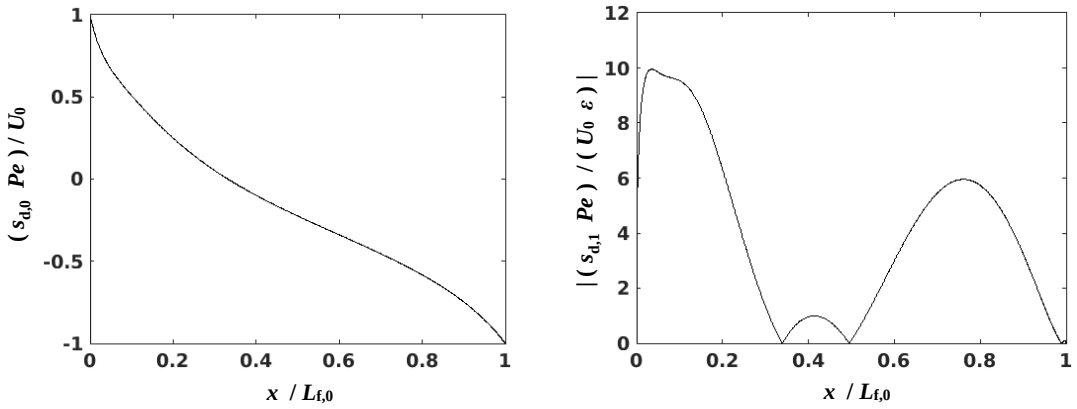

Figure 3.6. Non-dimensionalized relative burning speed along the non-premixed flame surface, using nominal values of $\mathcal{Z}_{st} = 0.3$, $Pe = 20$, St_{R_f} = 0.05, and, ε = 0.01.

3.1.2 Heat Release Analysis

Having considered the local space-time wrinkling of this two-dimensional flame, we next consider the spatially integrated heat release, $\dot{Q}(t)$, which was discussed in Section 2.4.3, including expressions for both premixed and non-premixed flames. For this particular two dimensional system, Eq.(2.40) can be written as:

$$\dot{Q}(t) = \int_{flame} \frac{(1+\varphi_{ox})^2}{\varphi_{ox}} \rho \mathcal{H}_R \mathcal{D} \left(\frac{\partial \mathcal{Z}}{\partial x} \sin\theta - \frac{\partial \mathcal{Z}}{\partial y} \cos\theta \right) dA \tag{3.22}$$

The first term in Eq.(3.22) includes the effect of axial diffusion and is, consequently, neglected in the following analysis, yielding:

$$\dot{Q}(t) = \int_0^{L_f(t)} \frac{-(1+\varphi_{ox})^2}{\varphi_{ox}} \rho \mathcal{H}_R \mathcal{D} \frac{\partial \mathcal{Z}(x,\xi(x,t))}{\partial y} dx \tag{3.23}$$

Decomposing $\mathcal{Z}$, L_f, and ξ into their mean and fluctuating components results in:

$$\dot{Q}(t) = \frac{-(1+\varphi_{ox})^2}{\varphi_{ox}} \rho \mathcal{H}_R \mathcal{D} \left\{ \int_0^{L_{f,0}+L_{f,1}(t)} \frac{\partial \mathcal{Z}_0}{\partial y}\left(x, \xi_0 + \xi_1(x,t)\right) dx + \int_0^{L_{f,0}+L_{f,1}(t)} \frac{\partial \mathcal{Z}_1}{\partial y}\left(x, \xi_0 + \xi_1(x,t)\right) dx \right\} \tag{3.24}$$

Then, linearizing this expression yields:

$$\dot{Q}(t) = \frac{-(1+\varphi_{ox})^2}{\varphi_{ox}} \rho \mathcal{H}_R \mathcal{D} \left\{ \int_0^{L_{f,0}} \frac{\partial \mathcal{Z}_0}{\partial y} dx + \int_0^{L_{f,0}} \frac{\partial \mathcal{Z}_1}{\partial y} dx + \int_0^{L_{f,0}} \xi_1 \frac{\partial^2 \mathcal{Z}_0}{\partial y^2} dx \right\} \tag{3.25}$$

where the steady and fluctuating components are given by:

$$\dot{Q}_0(t) = \frac{-(1+\varphi_{ox})^2}{\varphi_{ox}} \rho \mathcal{H}_R \mathcal{D} \int_0^{L_{f,0}} \frac{\partial \mathcal{Z}_0}{\partial y} dx \tag{3.26}$$

$$\dot{Q}_1(t) = \frac{-(1+\varphi_{ox})^2}{\varphi_{ox}} \rho \mathcal{H}_R \mathcal{D} \left\{ \int_0^{L_{f,0}} \frac{\partial \mathcal{Z}_1}{\partial y} dx + \int_0^{L_{f,0}} \xi_1 \frac{\partial^2 \mathcal{Z}_0}{\partial y^2} dx \right\} \tag{3.27}$$

Note that fluctuations in L_f do not contribute to this linearized expression since $\partial Z_0 / \partial y$ is zero along the centerline and, therefore, at the flame tip (axial diffusion would provide a non-zero contribution).

The transfer function, defined by Eq.(2.41), can be rewritten for this two-dimensional axially forced system as:

$$\mathcal{T} = \frac{\hat{\dot{Q}}_1 / \dot{Q}_0}{\hat{u}_{x,1} / U_0} \tag{3.28}$$

Additionally, the mass burning rate and flame (weighted) area fluctuation contributions, given by Eq.(2.42), will be retooled for further clarity. Benefitting from the substitution of dx by $\cos\theta dA$ in Eq.(3.25) and similarly expanding the solution, the resulting mass burning rate contribution to the transfer function is:

$$\mathcal{T}_{N,mbr} = \frac{\int_0^{L_{f,0}} \frac{\partial Z_1(x,\xi_0)}{\partial y} dx + \int_0^{L_{f,0}} \frac{\partial Z_0(x,\xi_0)}{\partial x} \sin(\theta_1) dx + \int_0^{L_{f,0}} \xi_1(x,t) \frac{\partial^2 Z_0(x,\xi_0)}{\partial y^2} dx}{\varepsilon \int_0^{L_{f,0}} \frac{\partial Z_0(x,\xi_0)}{\partial y} dx} \tag{3.29}$$

Similarly, the weighted area contribution is given by:

$$\mathcal{T}_{N,wa} = \frac{\int_0^{L_{f,0}} \frac{\partial Z_0(x,\xi_0)}{\partial y} \cos(\theta_0) dA_1}{\varepsilon \int_0^{L_{f,0}} \frac{\partial Z_0(x,\xi_0)}{\partial y} dx} = \frac{-\int_0^{L_{f,0}} \frac{\partial Z_0(x,\xi_0)}{\partial x} \sin(\theta_1) dx}{\varepsilon \int_0^{L_{f,0}} \frac{\partial Z_0(x,\xi_0)}{\partial y} dx} \tag{3.30}$$

The physical meaning of these terms was discussed in Chapter 2. It is important to recall that the weighting term, i.e. the time averaged burning rate, is a very strong function of the axial coordinate for non-premixed flames, but is constant for comparable premixed flames, as is shown by Figure 3.7.

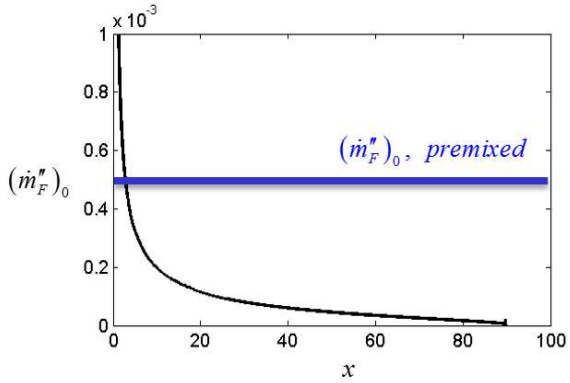

Figure 3.7. Depiction of the time averaged burning rate for comparable non-premixed and premixed systems.

The un-weighted area transfer function (important for constant burning velocity premixed flames) can be formulated using Eq.(2.43) and can be cast as:

$$\mathcal{T}_{N\&P,a} = \frac{1}{\varepsilon \int_0^{L_{f,0}} \left[1+\left(d\xi_0/dx\right)^2\right]^{1/2} dx} \int_0^{L_{f,0}} \frac{d\xi_0/dx}{\left[1+\left(d\xi_0/dx\right)^2\right]^{1/2}} \frac{\partial \xi_{1,y}(x,t)}{\partial x} dx \qquad (3.31)$$

or equivalently:

$$\mathcal{T}_{N\&P,a} = \frac{1}{\varepsilon \int_0^{L_{f,0}} \left[1/\cos\theta_0(x)\right] dx} \int_0^{L_{f,0}} \frac{\sin\theta_0}{\cos^2\theta_0} \sin\theta_1 dx \qquad (3.32)$$

There are significant variations in time averaged heat release rate along the non-premixed flame, as was shown by Figure 3.7 (e.g., no heat release at the tip in the absence of axial diffusion). Thus, the weighting of flame area is a very significant effect influencing how area fluctuations lead to heat release. Moreover, the characteristics of the weighted and un-weighted area transfer functions are quite different for non-premixed flames, while they are identical for premixed flames with spatially uniform burning velocities. For example, in the low Strouhal number limit, the non-premixed flame

weighted and un-weighted area transfer functions differ in phase by 180 degrees and have appreciably different magnitudes.

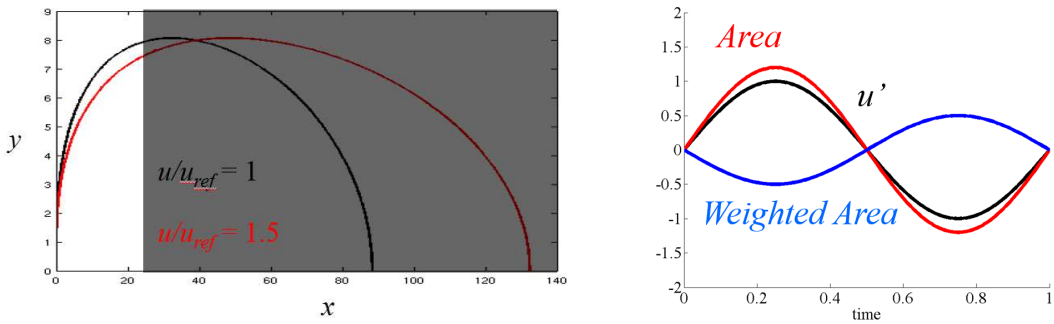

Figure 3.8. Plots shedding light onto the behavior of the weighted area and area transfer functions. (left) Shows mean flame positions for two different mean flow velocities and (right) shows the fluctuations over one forcing cycle for the various terms.

Figure 3.8 illustrates this behavior. The first plot (on the left) shows the mean flame position for two different mean flow velocities. As is expected, the higher velocity case, produces a flame with a larger total area. However, Figure 3.7 showed that for non-premixed flames, the near base-region is of greater importance, containing the dominant portion of the mean mass burning rate. Significantly, restricting our attention to the near-base region of the flame, i.e. the white region in Figure 3.8, it can be observed that the resulting (weighted) area actually decreases with increasing mean flow velocities. The second plot (on the right) shows how for low forcing frequencies, the area contribution is in-phase with the velocity forcing, while the weighted area contribution is 180 degrees out of phase.

The solutions for the premixed flame transfer functions are simpler, as the unforced flame is flat in a uniform velocity field. Following Wang *et al*. [87], and retaining only leading order terms in Markstein length, the transfer function is:

$$\mathcal{F}_P = \underbrace{\left\{\hat{\sigma}_c\left(1+2\pi i St_p\hat{\sigma}_c\right)\left(1-e^{2\pi i St_p-4\pi^2\hat{\sigma}_c St_p^2}\right)\right\}}_{=\mathcal{F}_{P,mbr}} + \underbrace{\left\{-1/(2\pi i St_p)\left(1-e^{2\pi i St_f-4\pi^2\hat{\sigma}_c St_p^2}\right)\right\}}_{=\mathcal{F}_{P,a}} \quad (3.33)$$

where $\hat{\sigma}_c$ is given by $\hat{\sigma}_c = \sigma_c \sin\theta \tan\theta$.

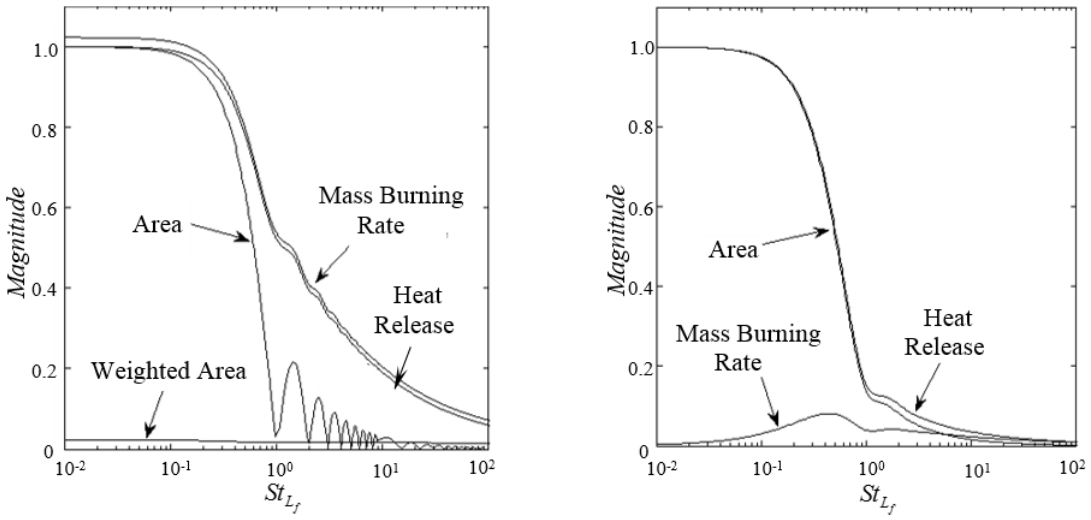

Figure 3.9. Strouhal number dependence of the magnitude of the heat release, area, and mass burning rate transfer functions for a (left) non-premixed flame with parameters $Z_{st}=0.06$, $Pe=10$, and (right) premixed flame with parameters $\hat{\sigma}_c=0.05$ and $L_f/R_f=932$.

Typical solutions for the overall unsteady heat release, as well as the contributions from flame area and mass burning rate are shown in Figure 3.9 for the non-premixed and premixed flame. Both premixed and non-premixed transfer functions have magnitudes of identically unity at zero *St*, indicating a direct 1:1 relation between the fluctuation in velocity and induced fluctuation in heat release, and then roll off with increasing *St*, indicating a progressively smaller induced heat release fluctuation [4]. Starting with the left plot, note how the non-premixed flame heat release fluctuations for $St_{L_f} \ll 1$ are dominated by mass burning rate fluctuations over the entire Strouhal number range. For $St \ll 1$, the mass burning rate contributions to $\mathcal{F}$ are of O(1) and O(St_p) for non-premixed and premixed flames, respectively. In contrast, premixed flames at low and

O(1) Strouhal numbers are dominated by area fluctuations, shown in the right plot. The mass burning rate fluctuations are a much smaller effect and only exert a comparable response as area fluctuations at high Strouhal numbers where $St_f \sim O(\hat{\sigma}_c^{-1})$ [87]. The mass burning rate fluctuations do also exert an indirect influence on the flame area perturbations when $St_f \sim O(\hat{\sigma}_c^{-1/2})$, by smoothing out flame wrinkles, causing the "smoothing" of the area gain curve in the premixed case, relative to the much more oscillatory curve for the non-premixed flame.

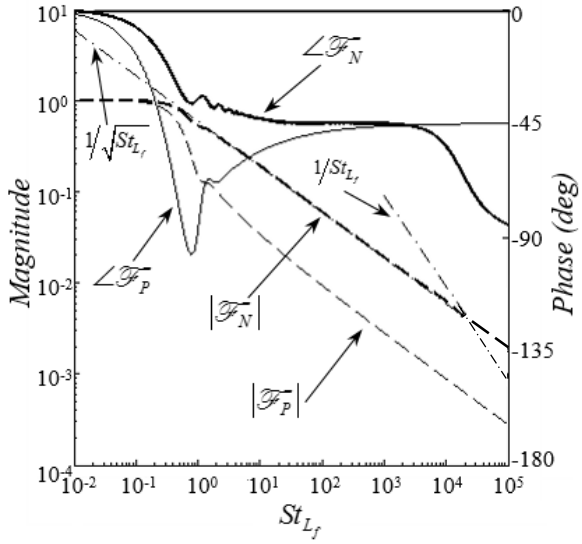

Figure 3.10. Strouhal number dependence of the magnitude and phase of the heat release transfer function for a non-premixed and premixed flame with the same properties as Figure 3.9.

Direct comparisons of the gain and phase response of the premixed and non-premixed flame results are shown in Figure 3.10. Significantly, these results show that non-premixed flames are significantly more sensitive to flow perturbations than premixed flames when St_{L_f} >O(1), an important and somewhat unexpected conclusion. It will be shown, and proven, in later chapters, that the *St*>>1 response of both flames scales as $\mathcal{F}$ ~O(1/*St*) under certain assumptions. Interestingly, this figure shows that the non-

premixed flame considered here has an intermediate/high region where its response rolls off more slowly; the analytical derivation of this regions *St* sensitivity is also deferred till Chapter 5, however, for now it suffices to note that computations suggest that $\mathscr{T}_N \sim O(1/St^{1/2})$ in this region. The $1/St$ scaling is less obvious for the corresponding premixed case as stretch effects do modify the results for the Strouhal number ranges shown in the plot.

The corresponding phases of the premixed and non-premixed flame transfer functions are also included in Figure 3.10. Both curves start at zero for low Strouhal numbers, indicating that low frequency flow modulation induces heat release fluctuations that are in phase. The curves roll off with different slopes toward negative values and asymptote to -90 degrees (for a stretch-insensitive flame; as shown in the graph, stretch modifies this result), indicating the delay in heat release relative to the forcing, due to convection of disturbances along the front. Note also the nearly constant phase in the non-premixed flame in the intermediate Strouhal number range discussed above. The undulations in phase for the premixed flame correspond to ripples in the gain, and reflect the influence of interference processes in controlling the flame area. The differences in phase between the two flames again reflects the different processes controlling unsteady heat release. The corresponding phases of the area contributions alone are much closer between the two flames for a broader St_{L_f} range for $\hat{\sigma}_c^{-1/2} << 1$.

3.1.3 One Term Approximations

Although various parameters, such as the steady flame length, remain confined in implicit equations, simple and approximate explicit solutions are obtainable by retaining

a single term of the infinite summation. For example, retaining a single term of Eq.(3.6), an explicit equation for the steady flame location can be obtained:

$$\frac{\xi_{0,y}}{R_f} = \frac{1}{\pi s}\cos^{-1}\left(\frac{\mathcal{Z}_{st} - s}{\frac{2}{\pi}\sin(\pi s)\exp\left(-\pi^2 s^2 \frac{x}{R_f Pe}\right)}\right) \tag{3.34}$$

where s is the ratio of fuel port to wall radius, i.e. $s = R_f / R_w$. This approximation is suitable for large arguments of the exponential function, except near x=0. Using the same approximations, we can derive an expression for the flame length, L_f, since at $x = L_f$, $\xi_0(x)$ is equal to 0:

$$\frac{L_{f,0}}{R_f} = -\ln\left[\frac{\pi(\mathcal{Z}_{st} - s)}{2\sin(\pi s)}\right]\frac{Pe}{\pi^2 s^2} \tag{3.35}$$

3.1.4 Explicit Governing Equation Validation

Section 3.1.1 presented the general procedure utilized throughout this thesis to obtain explicit equations for the fluctuating wrinkle dynamics for non-premixed flames, yielding Eq.(3.15) as a major contribution of this work. Section 2.5 showed how this method was different from that of premixed flames, which utilized an arbitrary substitution of variables to yield an explicit flame front governing equation. Although not general, a similar explicit governing equation, Eq.(2.49), was presented for the specific case of an infinitely long, flat non-premixed flame. Although physically unrealistic, it is interesting to observe under what conditions and parameters, a non-premixed flame could be considered flat enough to make this governing equation valid.

Figure 3.11 shows steady flame location contours for various parameters, such as *Pe* and $\mathcal{Z}_{st}$. It can be observed that as *Pe* is increased the flame becomes longer, and thus

flatter in the near base region. Consequently, in the $Pe \to \infty$ limit the flame becomes both infinitely long and flat. Additionally, a proactive choice of $\mathcal{Z}_{st}$ can make this flat-flame assumption more convincing, as seen by the plot on the right. As the results presented in this section, Section 3.1, have focused on the $Pe \to \infty$ limit, they should agree with the solution obtained via the explicit governing equation. Thus, in order to validate the solution given by Eq.(3.15), we will utilize the explicit governing equation and compare corresponding solutions.

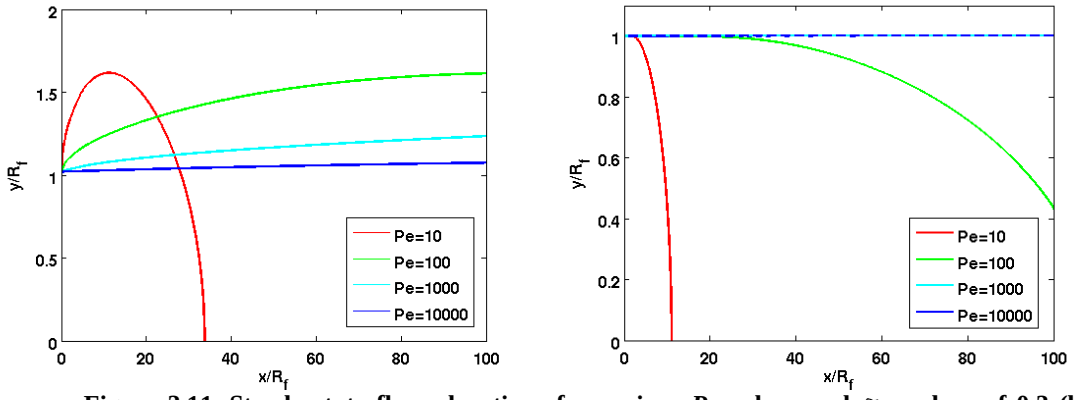

Figure 3.11. Steady state flame locations for various *Pe* values and $\mathcal{Z}_{st}$ values of 0.3 (left) and 0.5 (right).

This condition of "flat-enough" was further validated by ensuring the condition $\alpha >> \alpha_x, \alpha_{xx}$ was met computationally, where α was previously defined by Eq.(2.46). Figure 3.12 shows these terms for a non-premixed flame with *Pe*=100, clearly showing the dominance of α over the extent of the flame, except at the tip. However, in the $Pe \to \infty$ limit, the flame becomes infinitely long and this issue irrelevant.

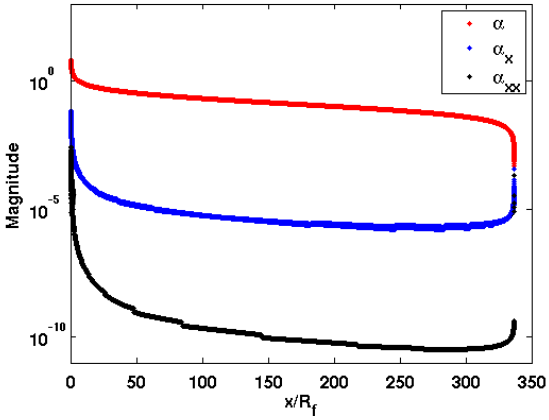

Figure 3.12. Validating the assumptions made in the derivation of the non-premixed explicit governing equation, for a non-premixed flame for *Pe*=100 and $\mathcal{Z}_{st}$ =0.3.

Assuming a harmonic velocity disturbance, and resulting flame position, of the form:

$$\bar{u} = \bar{u}_0 + \mathrm{Re}\left\{\hat{\bar{u}}_1 e^{-i\omega t}\right\} \tag{3.36}$$

$$\xi\left(x,t,\mathcal{Z}_{st}\right) = \xi_0\left(x,\mathcal{Z}_{st}\right) + \mathrm{Re}\left\{\hat{\xi}_1\left(x,\mathcal{Z}_{st}\right)e^{-i\omega t}\right\} \tag{3.37}$$

then Eq.(2.49) can be rewritten as steady and fluctuating equations:

$$u_{x,0}\frac{\partial \xi_0}{\partial x} - u_{y,0} = \mathscr{D}\frac{\partial^2 \xi_0}{\partial x^2} \tag{3.38}$$

$$i\omega\hat{\xi}_1 - u_{x,0}\frac{\partial \hat{\xi}_1}{\partial x} + \mathscr{D}\frac{\partial^2 \hat{\xi}_1}{\partial x^2} = \hat{u}_{x,1}\frac{\partial \xi_0}{\partial x} - \hat{u}_{y,1} \tag{3.39}$$

Once again we will accept that the steady flame location remains locked in an implicit equation, and focus our attention on the fluctuating flame dynamical equation, i.e. Eq.(3.39). The right hand side of this equation contains all the velocity perturbation inputs. Utilizing geometric relations, this right hand side can be rewritten as:

$$i\omega\hat{\xi}_1 - u_{x,0}\frac{\partial \hat{\xi}_1}{\partial x} + \mathscr{D}\frac{\partial^2 \hat{\xi}_1}{\partial x^2} = \left[\hat{u}_{y,1}\cos\theta_0(x) - \hat{u}_{x,1}\sin\theta_0(x)\right]\sqrt{1+\left(\frac{\partial \xi_0}{\partial x}\right)^2} \tag{3.40}$$

Furthermore, since the steady flame is essentially flat, $\partial\xi_0 / \partial x << 1$, and thus the equation simplifies to:

$$i\omega\hat{\xi}_1 - u_{x,0}\frac{\partial\hat{\xi}_1}{\partial x} + \mathscr{D}\frac{\partial^2\hat{\xi}_1}{\partial x^2} = \hat{u}_{y,1}\cos\theta_0(x) - \hat{u}_{x,1}\sin\theta_0(x) \tag{3.41}$$

This is a general form of the explicit governing equation for harmonic disturbances. Considering the previous case of bulk axial forcing, i.e. $\hat{u}_{x,1} = \varepsilon U_0$ and $\hat{u}_{y,1} = 0$, this equation can be solved and yields:

$$\hat{\xi}_1(x) = \frac{i\varepsilon U_0}{2\pi f}\sin\theta_0(x)\left(1 - \exp\left[\left(\frac{Pe - \sqrt{Pe^2 - 8\pi iPeSt}}{2}\right)\frac{x}{R_f}\right]\right) \tag{3.42}$$

and for consistency, in the $Pe\to\infty$ limit the exponential term simplifies to:

$$\hat{\xi}_{1,y}(x) = \frac{i\varepsilon U_0}{2\pi f}\sin\theta_0(x)\left(1 - \exp\left[i2\pi St\frac{x}{R_f}\right]\right) \tag{3.43}$$

Thus, Eq.(3.43) is the solution to the explicit governing equation for the non-premixed system considered in this section. Notice how this solution exactly matches and validates Eq.(3.15), which was derived via the other method, noting that in the $Pe\to\infty$ limit for an infinitely long flat flame, $\xi_{1,y} = \xi_{1,n}$.

3.2 Confinement Effects

Most combustion systems of industrial interest are confined, however, there exist some which are unconfined and vulnerable to combustion instabilities, such as gas ranges and rocket plumes. Thus, an interesting question is the extent to which confinement effects modify the flame dynamics, assuming a similar disturbance field, compared to the results presented in Section 3.1.

As was done previously, the full solution, including axial diffusion, for the steady and fluctuating mixture fraction fields can be obtained. Considering now an unbounded domain, a modified form of the step inlet boundary condition, given by Eq.(3.1), must be utilized:

$$\mathcal{Z}(x=0,y)=\begin{cases}1 \text{ for } 0\le |y| < R_f \\ 0 \text{ for } R_f \le |y|\end{cases} \tag{3.44}$$

along with the absence of the wall boundary condition listed in Eq.(3.2). The resultant steady state mixture fraction field is given by:

$$\mathcal{Z}_0=\frac{1}{2\pi}\int_{-\infty}^{\infty}\frac{2\sin(w)}{w}\exp\left[\frac{x}{PeR_f}\frac{\left(Pe^2-\sqrt{Pe^4+4Pe^2w^2}\right)}{2}\right]\exp\left[iw\frac{y}{R_f}\right]dw \tag{3.45}$$

while the corresponding general solution for the fluctuating mixture fraction field, exposed to spatially uniform axial velocity oscillations, given by Eq.(3.7), subject to the flame attachment boundary condition, i.e. $\mathcal{Z}_1(x=0,y,t)=0$, at the fuel port lip, is:

$$\mathcal{Z}_1=\frac{1}{2\pi}\int_{-\infty}^{\infty}\left[\begin{array}{l}\frac{\exp(gx)d}{2\pi Pe^3St}\left[h\left\{-2g+Pe^2\right\}\cos(hx)\right]+ \\ +\frac{\exp(gx)d}{2\pi Pe^3St}\left[\left\{-g^2+h^2+gPe^2+w^2Pe^2\right\}\sin(hx)\right]+ \\ +id\exp(gx)\sin(hx)+k\exp[cx]\end{array}\right]\exp(iwy)\,dw \tag{3.46}$$

where variables *c, d, g, h,* and *k* are defined in Appendix A, along with their corresponding high *Pe* series expansions.

As was done for the confined case, we will focus on the following simplified version of the solution that neglects axial diffusion, since we have already done so implicitly in formulating the boundary condition in Eq.(3.44). The resulting steady state and fluctuating mixture fraction field solutions are given:

$$\mathcal{Z}_0 = \frac{1}{2}\left[erf\left(\frac{1 - y/R_f}{\sqrt{4x/(PeR_f)}} \right) + erf\left(\frac{1 + y/R_f}{\sqrt{4x/(PeR_f)}} \right) \right] \tag{3.47}$$

$$\mathcal{Z}_1 = \frac{\varepsilon}{8\pi^{3/2} iPeSt} \left[\begin{array}{l} \dfrac{(y/R_f - 1)\exp\left(-\dfrac{(1 - y/R_f)^2}{4x/(PeR_f)} \right)}{\left(4x/(PeR_f)\right)^{3/2}} + \ldots \\ \ldots - \dfrac{(y/R_f + 1)\exp\left(-\dfrac{(1 + y/R_f)^2}{4x/(PeR_f)} \right)}{\left(4x/(PeR_f)\right)^{3/2}} \end{array} \right] \left(1 - \exp\left(2\pi i St\, x/R_f\right)\right)\exp\left[-i\omega t\right] \tag{3.48}$$

This equation can be derived by solving Eq.(3.3) neglecting the axial diffusion term, i.e. setting b=0. Analytical convergence of Eq.(3.45) and Eq.(3.46) into Eq.(3.47) and Eq.(3.48), respectively, in the $Pe \to \infty$ limit has not been attained due to the complex improper integrals. This convergence has, however, been verified computationally.

Dealing with these simplified solutions in the absence of axial diffusion, once again provides a major mathematical benefit of eliminating the improper integrals, making analytical progress for the space-time and heat release dynamics possible. Unfortunately, these expressions are still non-invertible, due to the dual error/exponential function form, making explicit solutions for the flame position non-obtainable.

As was done previously, the fluctuating field solution can be written in terms of the steady field, utilizing $\partial \mathcal{Z}_0 / \partial x$, and flame angle relations used, i.e. Eq.(3.14), to rewrite Eq.(2.33) as:

$$\xi_{1,n}\left(x,t\right) = \frac{i\varepsilon U_0}{2\pi f} \sin\theta_0(x) \left\{ 1 - \exp\left(i2\pi St \frac{x}{R_f} \right) \right\} \exp\left[-i2\pi ft\right] \tag{3.49}$$

Significantly, this expression is identical to Eq.(3.15), reflecting the same dynamical features of the flame sheet winkles: the low-pass filter magnitude behavior, flame angle

dependence, i.e. velocity fluctuations normal to the flame sheet, and wave form interference term. However, this does not mean that confinement has no effect on the wrinkle dynamics – rather, these influences occur through the mean field, $\theta_0(x)$. Figure 3.13 shows the steady state flame position extracted from unconfined, Eq.(3.47), and confined, Eq.(3.6), mixture fraction field solutions for various degrees of confinement. Note that these comparisons involve R_f/R_w values where $s < \mathcal{Z}_{st}$, so that the flame remains over-ventilated, closing at the flame tip. This was done since the under-ventilated configuration is not possible for the unconfined case.

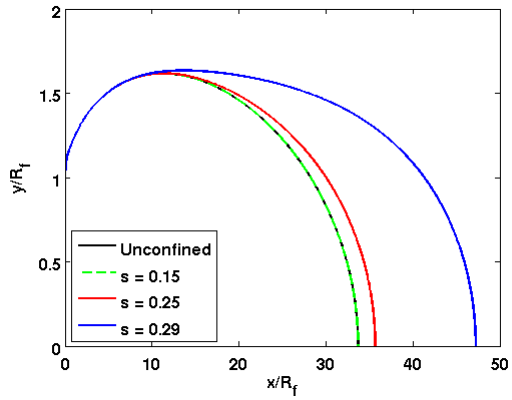

Figure 3.13. Steady state flame locations for an unconfined and confined non-premixed flames experiencing different degrees of bounding, i.e. *s* values, for *Pe* = 10 and $\mathcal{Z}_{st}$ = 0.3.

For small degrees of confinement (small *s* values), the bounded and unbounded solutions are coincident, as is expected. For larger degrees of confinement (increasing *s* towards $\mathcal{Z}_{st}$) the flame becomes slightly wider and significantly longer, resulting in more spatial wrinkles and an extended middle portion of the flame, where the flame is flatter. Additionally the location of maximum width moves downstream. This location is significant because for the axially forced case, this is the where the forcing is parallel to the flame position, and as was shown from our analytical solution, yields no unsteady

flame motion, i.e. is a spatial node. The importance of these effects can also be seen by observing the wrinkle magnitude and phase plots, shown in Figure 3.14.

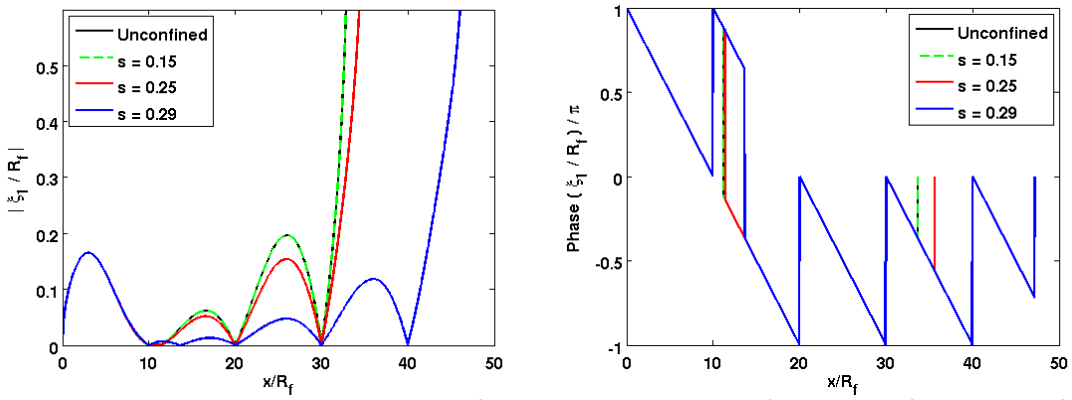

Figure 3.14. Wrinkle magnitude (left) and phase (right) plots for an unconfined and confined non-premixed flames experiencing different degrees of bounding, i.e. *s* values, for *Pe* = 10, $\mathcal{Z}_{st}$ = 0.3, and *St* = 0.1. The corresponding steady flame positions are shown in Figure 3.13.

As *s* is increased, there is more flame sheet, and thus more wrinkles exist overall. However, for equivalent axial locations, the wrinkle magnitude is lower for higher degrees of confinement. This is due to the shallower angle of the mean flame at this positon, an effect which can be seen from Figure 3.13. Additionally, as Figure 3.14 considers an *St* value of 0.1, every $10R_f$ (disturbance wavelength) a spatio-temporal node occurs due to the forcing. However, there is an additional node due to the location of maximum width, independent of *St*, occurring around ~$11R_f$ for the unconfined solution and moving downstream with increasing confinement.

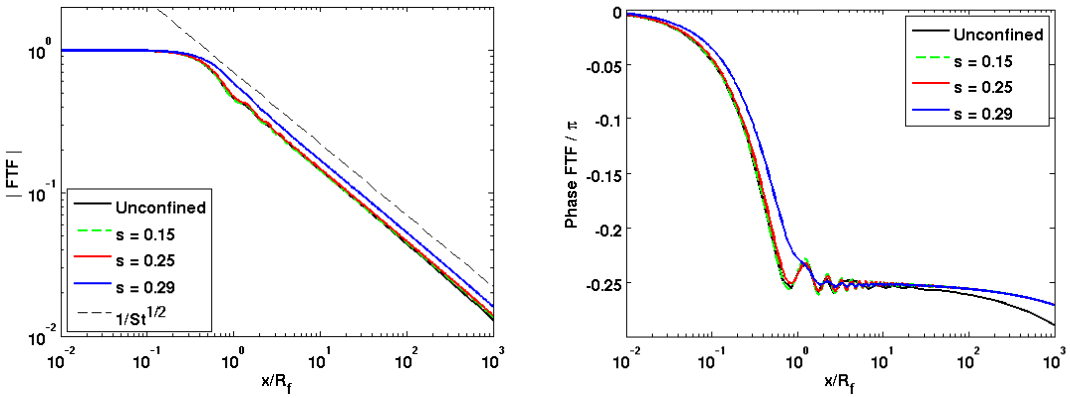

Figure 3.15. Heat release transfer function magnitude (left) and phase (right) plots for an unconfined and confined non-premixed flames experiencing different degrees of bounding, i.e. *s* values, for *Pe* = 10 and $\mathcal{Z}_{st}$ = 0.3.

Figure 3.15 shows comparisons of the heat release transfer functions. The magnitude plot reveals asymptotics which are independent of confinement. For low *St* values, the unity magnitude reflects a direct 1:1 relation between disturbance magnitude and resulting heat release fluctuations, while for large *St* values the curves all roll off as $1/St^{1/2}$. However, for these large *St* values, the curves become smoother and the total magnitude of the transfer function increases with increasing degree of confinement, due to both the increased number of flame wrinkles and increased mean flame length. This smoothness can also be seen in the phase plot.

3.3 Forcing Direction Effects

The previous sections focused on longitudinal disturbances which, although important, are not the sole contributors to the issue of combustion instabilities. Thermoacoustic oscillations associated with transverse disturbances and acoustic modes are routinely encountered in combustion chambers [95]. For example, transverse oscillations in annular aircraft or aeroderivative combustors have been described and

documented by many industrial companies, such as General Electric, Pratt & Whitney, Rolls Royce, Alstom, and Siemens [6, 96-100] and have been discussed frequently in relevance to afterburner [101-104], solid rockets [105, 106], and liquid rockets [107-112]. Often referred to as “screech” due to its high-pitched tone (in the range of 150-600Hz), the transverse mode in augmentors can be excited, in addition to lower frequency longitudinal acoustic oscillations, referred to as “rumble” or “buzz” (in the range of 50-120Hz) [103].

A good portion of the existing work has been done on longitudinally forced systems, however, there are two key application regimes where transverse acoustic oscillations are of significant practical interest: the first being large scale annular combustion systems where lower frequency transverse instabilities occur, typical of and in the spectral vicinity of longitudinal instabilities, and the second being higher frequency transverse oscillations encountered in can-combustion systems [113]. An additional importance of transverse forcing, which ties into the previous sections, is the pathway in which transverse acoustics trigger/generates longitudinal acoustics.

This section builds upon the previous ones, with a focus on the transverse forcing configuration. From a local point of view, the flame does not differentiate between transverse and longitudinal forcing, as both premixed and non-premixed flames are ultimately sensitive to the scalar component of the velocity fluctuations that are normal to the iso-$\mathcal{Z}$ surfaces or the premixed flame front. In contrast, from a global heat release point of view, transverse and longitudinal excitation is fundamentally different. In the latter case, the fuel flow rate and/or reactant flow rate into the domain is modulated, which leads to heat release oscillations, at least in the quasi-steady case. In the former,

transversely forced case, they are not, implying that fluctuations in heat release may not be excited, even though significant local wrinkling of the flame may be induced. These points were emphasized by Acharya *et al*. [14] in the context of premixed flames, where they showed that bulk transverse forcing excited zero heat release fluctuations for all frequencies. Only if the there was a transverse phase lag in the transverse flow field were heat release fluctuations excited. Thus here we go through a similar analysis for non-premixed flames in order to determine and isolate the influence of forcing direction on flame dynamics.

Retaining the step inlet boundary condition, Eq.(3.1), the steady state mixture fraction field solutions presented in Section 3.1 are still valid, being independent of forcing. The familiar dynamical equation for the fluctuating mixture fraction field, Eq.(3.4), will also be reutilized, now exposed to spatially uniform transverse fluctuations in flow velocity of the form:

$$u_{y,1} = \varepsilon U_0 \exp[-i\omega t] \tag{3.50}$$

Additionally, no penetration boundary conditions must be enforced at both walls, due to the lack of axial symmetry, modifying the boundary conditions to:

$$\frac{\partial \mathcal{Z}}{\partial y}(x, y = -R_w) = 0 \qquad \frac{\partial \mathcal{Z}}{\partial y}(x, y = R_w) = 0 \tag{3.51}$$

The resulting full solution for the fluctuating mixture fraction field, $\mathcal{Z}_1$, is:

$$\mathcal{Z}_1 = \sum_{n=1}^{\infty}\left[\frac{-2\varepsilon sPe\sin(\mathcal{A}_n)}{2\pi iPeSt}\right]\sin\left(\mathcal{A}_n\frac{y}{R_f}\right)\left\{\exp\left(\frac{x}{PeR_f}\beta_-\right)-\exp\left(\frac{x}{PeR_f}\beta_{h-}\right)\right\}\exp[-i\omega t] \tag{3.52}$$

where the Strouhal number based on the half-width of the fuel nozzle is defined by Eq.(2.27) ($St = St_{f,R}$), parameters $\mathcal{A}_n$, β_-, and β_{h-} are the same as from the axially

forced case (Section 3.1 and Eq.(3.9)), and *s* is the dimensionless ratio, R_f / R_w. Again we will focus the subsequent analysis in the absence of axial diffusion, i.e. in the $Pe \to \infty$ limit, whose solution is:

$$Z_1 = \sum_{n=1}^{\infty} \left[\frac{i\varepsilon s \sin(\mathcal{A}_n)}{\pi St} \right] \sin\left(\mathcal{A}_n \frac{y}{R_f} \right) \exp\left(-\mathcal{A}_n^2 \frac{x}{Pe R_f} \right) \left\{ 1 - \exp\left(2\pi i St \frac{x}{R_f} \right) \right\} \exp[-i\omega t] \quad (3.53)$$

Alternatively, this expression can also be written in terms of Z_0 as:

$$Z_1 = \left[\frac{-i\varepsilon R_f}{2\pi St} \right] \frac{dZ_0}{dy} \left\{ 1 - \exp\left(2\pi i St \frac{x}{R_f} \right) \right\} \exp[-i\omega t] \quad (3.54)$$

An explicit expression for fluctuating flame position can be obtained in a similar manner as was done for the axial forced case in Section 3.1. Recall that $\xi_{1,n}$ is measured normal to the mean flame surface in the direction of the oxidizer. Using mixture fraction and flame geometric relations similar to Eq.(3.14), i.e. $|\nabla Z_0| = \mp[\partial Z_0 / \partial y] / \cos\theta_0(x)$, the solution for $\xi_{1,n}(x,t)$ can be written as:

$$\xi_{1,n}(x,t) = \frac{\mp i\varepsilon U_0}{2\pi f} \cos\theta_0(x) \left\{ 1 - \exp\left(i2\pi St_{L_f} \frac{x}{L_{f,0}} \right) \right\} \exp[-i2\pi ft] \quad (3.55)$$

where θ_0 denotes the angle of the mean flame with respect to the axial coordinate and the – and + signs are for the top and bottom half-flame branches, respectively. These signs indicate the out of phase nature of the two flame branches. For reference, the corresponding fluctuations of an attached premixed flame with constant burning velocity subjected to transverse bulk flow oscillations with a similar coordinate system are given by:

$$\xi_{1,n}(x,t) = \frac{\mp i\varepsilon U_0}{2\pi f}\cos\theta\left\{1-\exp\left(i2\pi St_p\frac{x}{L_{f,0}}\right)\right\}\exp[-i2\pi ft] \qquad (3.56)$$

Notice the similarities in the premixed and non-premixed solutions, with the exception of the spatial phase dependence, $1-e^{i2\pi f\,x/U_0}$ term. This difference, once again, reflects the influence of premixed flame propagation on wrinkle convection speeds. In both cases, local maxima and minima arise through this term, due to interference between wrinkles generated at the x=0 boundary and disturbances excited locally as shown in our axially forced analysis in Section 3.1.1.

Additionally this expression can be compared to Eq.(3.15), which shows the corresponding explicit equation for the axially forced case. Both solutions contain the exact same low-pass filter magnitude and wave form interference terms, and although the flame angle term differs in appearance, now showing a $\cos\theta_0(x)$, it retains the same dynamical significance, showing the importance of the fluctuations normal to the mean flame surface in generating wrinkles. As the system is now transversely forced, the location where the forcing is parallel to the steady flame sheet, and hence we expect a spatial node, is at the flame base and tip.

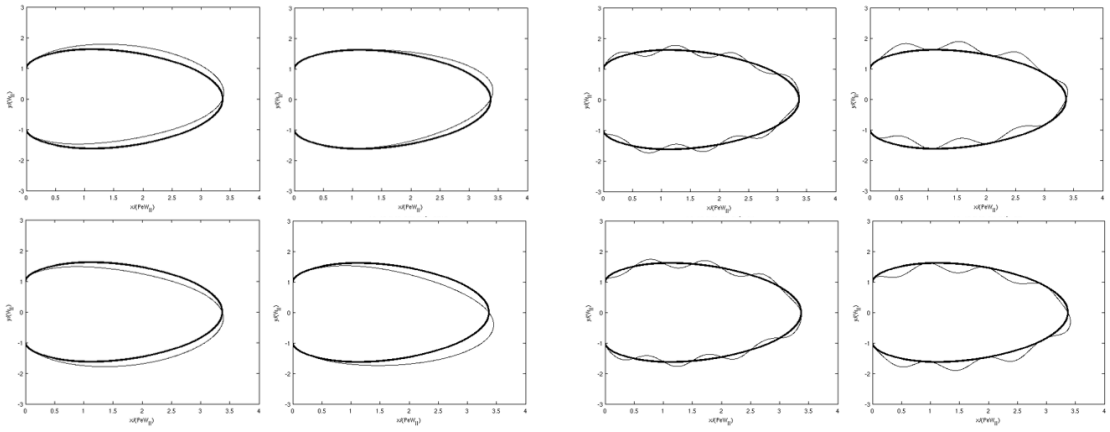

Figure 3.16. Snapshots showing the steady state (thick line) and four instantaneous (thin line) positions of a forced non-premixed flame with *Pe*=10 and $\mathcal{Z}_{St}$ = 0.3 exposed to forcing conditions of (left) $\varepsilon = 0.015$, *St*$_{Lf}$=0.337 [*St*$_R$=0.01] and (right) $\varepsilon = 0.1$, *St*$_{Lf}$=3.37 [*St*$_R$=0.1]. The instantaneous times are *t* = 0, 0.3, 0.5, 0.7 moving left to right, top to bottom.

Figure 3.16 presents several illustrative solutions of the space-time dynamics for the flame position at two Strouhal numbers, while in general, the solution is a function of the four dimensionless parameters St_{L_f} , s , Pe , and $\mathcal{Z}_{st}$. Note the bulk transverse swaying of the flame at lower Strouhal numbers, and the spatial wrinkling at higher values. Nodes occur at locations where cos θ_0 = 0 or where $\sin(\pi f\, x/U_0)=0$, as shown by Eq.(3.55) and Eq.(3.56). In comparison to the axial forcing case where the sine term in the $\xi_{1,n}$ equation caused no flame spatial fluctuations where the mean flame was horizontal, now the cosine term causes no fluctuations at the flame base and tip for the transverse forcing case, i.e. where the mean flame is vertical.

Figure 3.17 and Figure 3.18 show the magnitude and phase of $\xi_{1,n}$ for a representative low and high *St* value, respectively. Also shown are the *t*=0 instantaneous flame positions for the top and bottom branches. The nodes and local maxima and minima referred to above are clearly evident in the figures, with more nodes occurring for

the higher *St* case. The phase rolls off linearly with axial distance, again reflecting the convection process described by Eq.(3.17), and jumps 180 degrees across the nodes. The magnitude drops off sharply at the tip due to the forced spatial node by the flame angle term. This effect at the base is less evident, as a spatiotemporal node is forced here due to the attachment condition as well. As *Pe* is increased the flame length also increases, and thus the flame angle θ_0 retains small values over a greater portion of the flame, while the large flame angles are condensed to the base and tip.

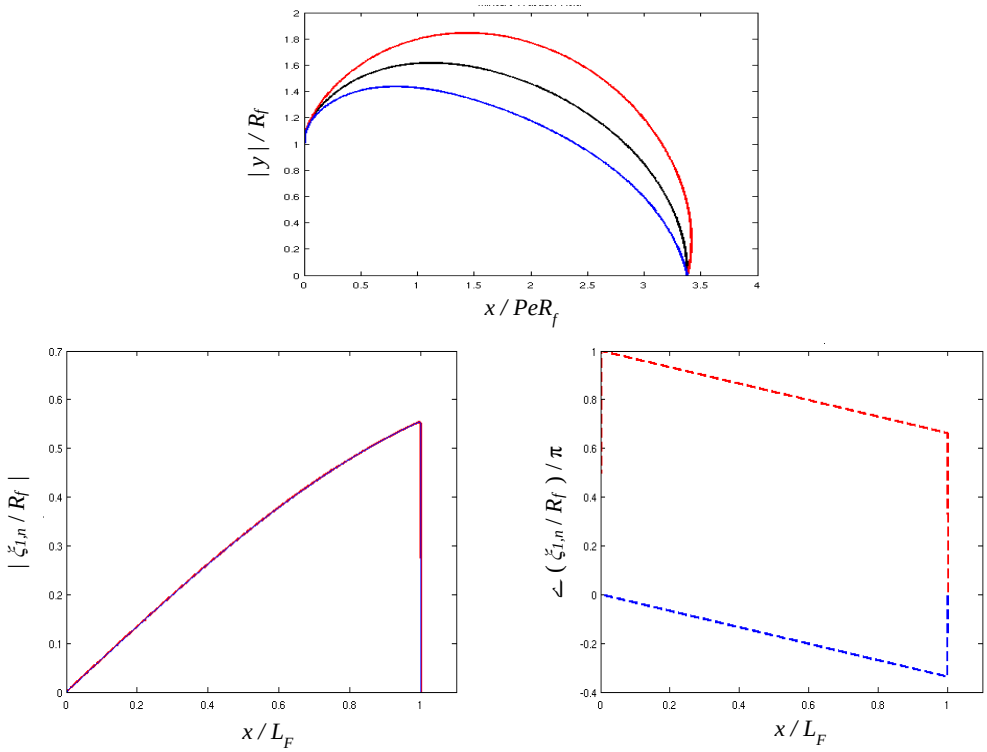

Figure 3.17. Steady (black line) and instantaneous (red:top, blue:bottom branch) flame position for *t*=0 (top), and corresponding axial dependence of (left) magnitude and (right) phase of flame response, using nominal values of $\mathcal{Z}_{st}$ =0.3 and *Pe*=10 for St_{L_f} [St_R] values of 0.337 [0.01] and ε of 0.01.

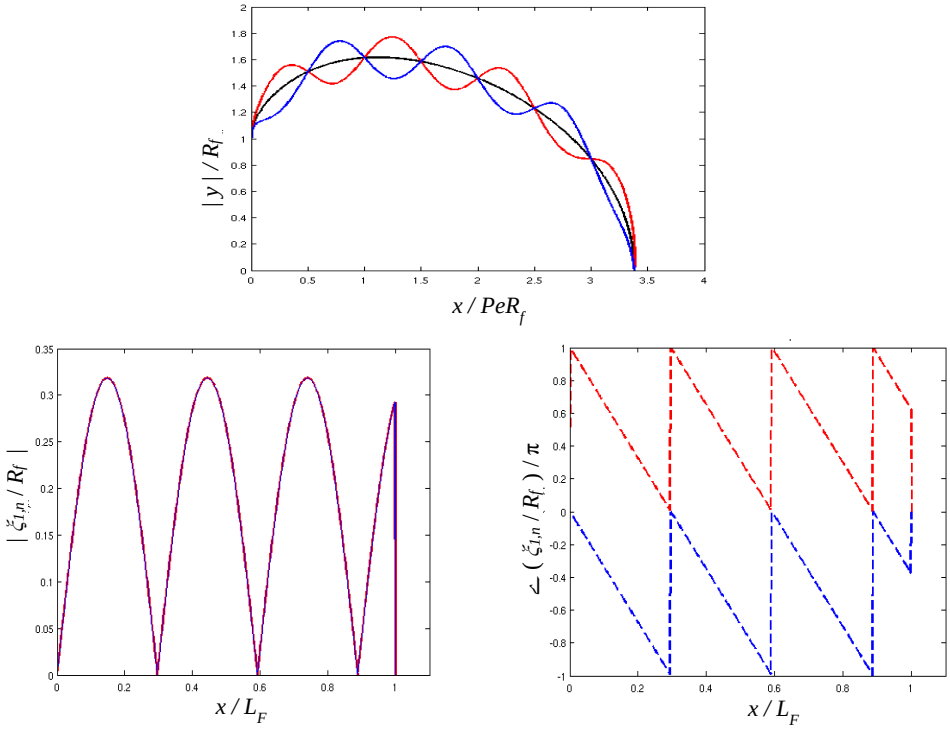

Figure 3.18. Steady (black line) and instantaneous (red:top, blue:bottom branch) flame position for *t*=0 (top), and corresponding axial dependence of (left) magnitude and (right) phase of flame response, using nominal values of $\mathcal{Z}_{st}$ =0.3 and *Pe*=10 for St_{L_f} [St_R] values of 3.37 [0.1] and ε of 0.01.

Detailed decomposition steps, as well as explicit transfer function equations, can be found in Section 2.4.3 and Section 3.1. Typical solutions, utilizing the $Pe \to \infty$ limiting results, for the unsteady heat release of one half of the non-premixed flame are shown in Figure 3.19. The left image shows the magnitude of the mass burning rate and flame area transfer functions, given by Eq.(3.29) and Eq.(3.30) respectively, for a two-dimensional non-premixed flame. The right image shows the phase of these curves (solid for mass burning rate contribution, dashed for weighted area contribution). Notice how for all *St* values the area and mass burning rate contributions from a single branch have the same magnitude (coincident in the figure) and are out of phase by 180 degrees, resulting in no unsteady heat release for one-half of the flame! As the Peclet value is reduced these

magnitudes are increased, but the contributions remain equal and out of phase, resulting in:

$$\mathcal{F}_N(St) = 0 \tag{3.57}$$

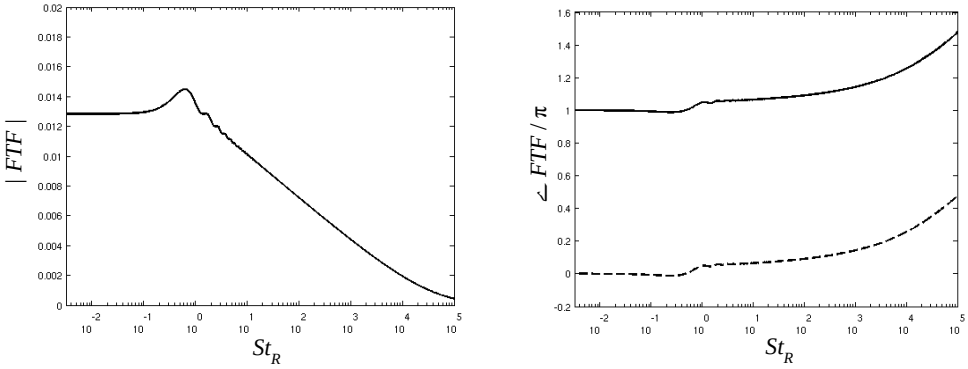

Figure 3.19. Strouhal number dependence of the (left) magnitude and (right) phase of the heat release, area, and mass burning rate transfer functions for a non-premixed flame with parameters $\mathcal{Z}_{st} = 0.3$ and $Pe = 100$.

This behavior can be analytically shown to be a result of the unique cancellation of mass burning rate transfer function terms which occurs for the transverse bulk forcing mixture fraction solutions. The total transfer function is the sum of the mass burning rate and area contributions. However, as can be seen from Eq.(3.30), the weighted area contribution cancels with one of the mass burning rate terms, resulting in a simplified form of the transfer function:

$$\mathcal{F}_N = \frac{\int_0^{L_{f,0}} \frac{\partial \mathcal{Z}_1(x,\xi_0)}{\partial y} dx + \int_0^{L_{f,0}} \xi_1(x,t) \frac{\partial^2 \mathcal{Z}_0(x,\xi_0)}{\partial y^2} dx}{\varepsilon \int_0^{L_{f,0}} \frac{\partial \mathcal{Z}_0(x,\xi_0)}{\partial y} dx} \tag{3.58}$$

By utilizing Eq.(3.54) and Eq.(3.55), this expression can be rewritten specifically for a transversely forced system:

$$\mathcal{F}_N = \frac{\int_0^{L_{f,0}} \left[\frac{-i\varepsilon U_0}{2\pi f} \right] \frac{d^2 Z_0}{dy^2} \left(1 - \cos\theta_0(x)\right) \left\{ 1 - \exp\left(2\pi i St \frac{x}{R_f} \right) \right\} \exp\left[-i2\pi ft\right] dx}{\varepsilon \int_0^{L_{f,0}} \frac{\partial Z_0(x,\xi_0)}{\partial y} dx} \tag{3.59}$$

Since in the $Pe \to \infty$ limit the flame becomes infinitely long and flat, $\cos\theta_0(x) \sim 1$ and thus the transfer function becomes zero, independent of any other parameters!

In addition, the other half of the flame branch is 180 degrees out of phase with the original branch, i.e. the phase plot contributions are switched (solid for area contribution, dashed for mass burning rate). Thus, the unsteady heat release for the independent half-flames, as well as the entire flame, is zero; a result that will be of importance in Chapter 4, where this perfect mass burning rate term cancellation does not exist for finite *Pe* value results. This result could be anticipated, at least in the low Strouhal number limit, as transverse forcing causes no fluctuation in fuel and oxidizer flow rate into the domain. Since the heat release in the quasi-steady limit is directly proportional to the fuel flow rate into the domain, transverse fluctuations consequently lead to no heat release oscillations. Similar conclusions were developed for transversely forced premixed flames by Acharya *et al.* [114].

Significantly, this section emphasizes the important distinction between local and global heat release fluctuations. This topic which will be discussed in more depth in Chapter 4, however, for now it is important to state that even though there are no global heat release fluctuations, the local heat release by each segment of flame is fluctuating, as is the instantaneous flame position.

3.4 Differential Diffusion

Throughout this section, the mixture fraction formulation and $\mathcal{Z}$-equation have been utilized to solve for explicit flame dynamics. As was discussed in Chapter 2, this formulation relies on the assumption that the mixture fraction is a conserved scalar. It was shown that a sufficient condition for the mixture fraction to be a conserved scalar is for all species to have equal diffusivity, resulting in the disappearance of the species source terms. An inconsistency, however, arises when we attempt to incorporate differential diffusion effects into this formulation.

To observe this effect, we return to Eq.(2.3), except now considering different isotropic diffusion coefficients for the various fuel, oxidizer, and product species. Utilizing a similar normalization and combination of the equations, Eq.(2.4) can be recast into the following form, once again using the existing mixture fraction definition from Eq.(2.5):

$$\rho\frac{D\mathcal{Z}}{Dt}-\nabla\cdot\left(\rho\mathscr{D}_F\nabla\mathcal{Z}\right)=\nabla\cdot\left(\rho\frac{(\mathscr{D}_{\mathrm{Pr}}-\mathscr{D}_F)}{(\varphi_{ox}+1)}\nabla Y_{\mathrm{Pr}}\right) \tag{3.60}$$

This equation reveals the presence of an additional term on the right hand side, one that becomes absent in the case of equal species diffusivities. This source term provides a direct measure of the degree to which the mixture fraction is ***not*** conserved, solely caused by differential diffusion [115]. This term can also be interpreted as the local effect of differential diffusion on the evolution of the mixture fraction.

Most existing attempts to quantify differential diffusion are based on the difference between various definitions of the mixture fraction; for example the elemental mass fractions, which has been shown to yield a measure of the differential diffusion for

each element in a reacting system, thereby forming a complete measure [115]. Other studies measured the effect by examining the differences between elemental mixture fractions based on experimental data [116, 117] and simulations [118]. For turbulent non-premixed flames, the modelling of differential diffusion has been investigated using a conditional moment closure method [119]. Additionally, recent theoretical work suggests that there may exist a refined definition of the mixture fraction variable which is conserved even in the presence of differential diffusion, however, no such definition has yet emerged [120]. Thus, the quantification of this effect has important implications for modelling approaches as well as on the fundamental understanding of non-premixed combustion.

To investigate the effects of differential diffusion on the fluctuating flame dynamics, we investigate the simplified case of a spatially developing reacting mixing layer, between pure fuel and pure oxidizer, i.e. a single planar non-premixed flame separating two semi-infinite regions containing fuel and oxidizer, shown by Figure 3.20.

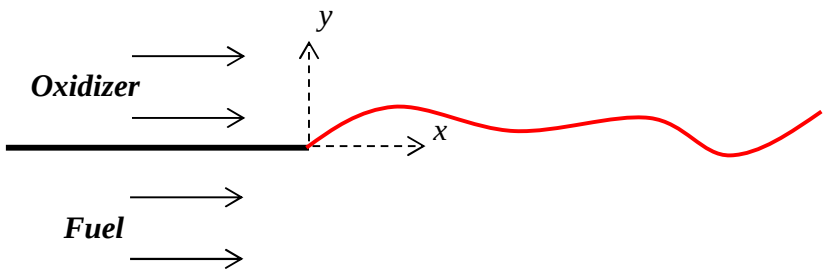

Figure 3.20. Schematic of the spatially developing mixing layer, utilized to investigate differential diffusion effects.

Considering the steady case first, as each species is originally pure, independent species equations, similar in form to Eq.(3.3), can be written for each region. Outside of the infinitesimal reaction sheet, the chemical source terms are zero, and these equations,

and corresponding boundary conditions, can be written in terms of normalized mixture fractions for the fuel and oxidizer sides as:

$$U_0 \frac{\partial \mathcal{Z}_{0,F}}{\partial x} = \mathscr{D}_F \frac{\partial^2 \mathcal{Z}_{0,F}}{\partial y^2} + b\mathscr{D}_F \frac{\partial^2 \mathcal{Z}_{0,F}}{\partial x^2} \qquad \begin{matrix} \mathcal{Z}_{0,F}(x=0, y<0) = 1 \\ \mathcal{Z}_{0,F}(x, y \to -\infty) = 1 \end{matrix} \tag{3.61}$$

$$U_0 \frac{\partial \mathcal{Z}_{0,Ox}}{\partial x} = \mathscr{D}_{Ox} \frac{\partial^2 \mathcal{Z}_{0,Ox}}{\partial y^2} + b\mathscr{D}_{Ox} \frac{\partial^2 \mathcal{Z}_{0,Ox}}{\partial x^2} \qquad \begin{matrix} \mathcal{Z}_{0,Ox}(x=0, y>0) = 0 \\ \mathcal{Z}_{0,Ox}(x, y \to \infty) = 0 \end{matrix} \tag{3.62}$$

Solutions will be considered in the absence of axial diffusion, due once again to their exclusion from the discontinuous step boundary condition utilized. Although no tractable equation exists in the combustion domain due to the discussed source term, the flame can be determined from interface conditions which couple the two equations. Respectively indicating no fuel-oxidizer interpenetration in the fast chemistry limit and stoichiometrically proportional diffusive fluxes at the flame position, these conditions can be represented as [121]:

$$\mathcal{Z}_{0,F}\Big|_f = \mathcal{Z}_{0,Ox}\Big|_f = \mathcal{Z}_{st} \tag{3.63}$$

$$\rho\mathscr{D}_F \frac{\partial \mathcal{Z}_{0,F}}{\partial y}\bigg|_f = \rho\mathscr{D}_{Ox} \frac{\partial \mathcal{Z}_{0,Ox}}{\partial y}\bigg|_f \tag{3.64}$$

Similar to the solution of a Stefan problem, a similarity transformation, $\psi = y/\sqrt{x}$, can be utilized to recast Eqs.(3.61) and (3.62) into a general form as:

$$U_0 \psi \frac{\partial \mathcal{Z}_{0,i}}{\partial \psi} + 2\mathscr{D}_i \frac{\partial^2 \mathcal{Z}_{0,i}}{\partial \psi^2} \tag{3.65}$$

with general mathematical solution:

$$\mathcal{Z}_{0,i} = C_{i,1}\sqrt{\frac{\pi\mathscr{D}_i}{U_0}}\,erf\left(\psi\sqrt{\frac{U_0}{4\mathscr{D}_i}}\right) + C_{i,2} \tag{3.66}$$

Enforcing the boundary conditions and matching conditions for our steady non-premixed mixing layer results in:

$$\frac{\exp\left(-\psi_f^2 \frac{U_0}{4\mathscr{D}_{Ox}}\right)}{\exp\left(-\psi_f^2 \frac{U_0}{4\mathscr{D}_F}\right)} = \varphi_{Ox}\sqrt{\frac{\mathscr{D}_F}{\mathscr{D}_{Ox}}}\frac{\left[1-erf\left(\psi_f\sqrt{\frac{U_0}{4\mathscr{D}_{Ox}}}\right)\right]}{\left[1+erf\left(\psi_f\sqrt{\frac{U_0}{4\mathscr{D}_F}}\right)\right]} \tag{3.67}$$

where subscript "*f*" indicates quantities evaluated at the flame location. Thus, this is an implicit equation which can be solved for ψ_f, i.e. the locus of steady flame locations. Appendix B provides the explicit fuel and oxidizer mixture fraction field solutions. Additionally, by defining a dimensionless ratio of diffusion coefficients, $\Phi = \mathscr{D}_F / \mathscr{D}_{Ox}$, and utilizing $Pe_{x,Ox}$, defined from Eq.(2.24), this flame location equation can be non-dimensionalized as:

$$\frac{\exp\left(-\tilde{\psi}_f^2 \frac{Pe_{x,Ox}}{4}\right)}{\exp\left(-\tilde{\psi}_f^2 \frac{Pe_{x,Ox}}{4\Phi}\right)} = \varphi_{Ox}\sqrt{\Phi}\frac{\left[1-erf\left(\tilde{\psi}_f\sqrt{\frac{Pe_{x,Ox}}{4}}\right)\right]}{\left[1+erf\left(\tilde{\psi}_f\sqrt{\frac{Pe_{x,Ox}}{4\Phi}}\right)\right]} \tag{3.68}$$

Figure 3.21 shows the extracted steady state flame position for various values of Φ, revealing the complex dependence upon both z_{st} and the diffusivities, both the ratio and individual magnitudes. Always displaying a "horizontal leveling" behavior, the ratio between the coefficients controls the relative position of the flame relative to the equal diffusivity case. Additionally, the $Pe_{x,Ox}$ value also alters this flame shape, an effect which is not obvious due to the normalization of the horizontal axis.

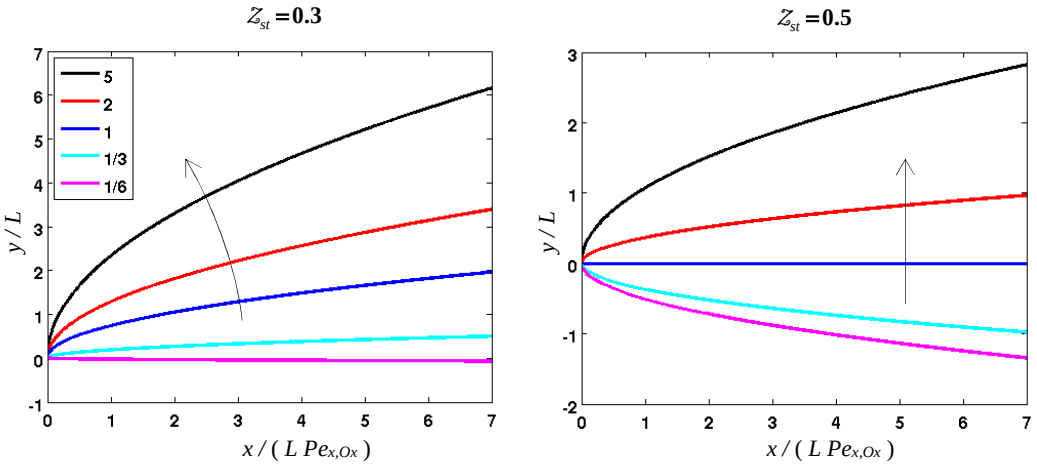

Figure 3.21. Normalized steady non-premixed reacting mixing layer position, ψ_f, extracted from Eq.(3.68), for various degrees of differential diffusion, i.e. Φ, for $\mathcal{Z}_{st}=0.3$ (left) and $\mathcal{Z}_{st}=0.5$ (right), for $Pe_{x,Ox}$=1. Arrows indicate direction of increasing Φ.

Considering once again the axially bulk forced case, boundary conditions similar to Eqs.(3.63) and (3.64) can be written for the linearized axially forced instantaneous flame position as:

$$\mathcal{Z}_{0,F}\Big|_f + \xi_1 \Big|\nabla \mathcal{Z}_{0,F}\Big\|_f + \mathcal{Z}_{1,F}\Big|_f = \mathcal{Z}_{0,Ox}\Big|_f + \xi_1 \Big|\nabla \mathcal{Z}_{0,Ox}\Big\|_f + \mathcal{Z}_{1,Ox}\Big|_f = \mathcal{Z}_{st} \tag{3.69}$$

$$\rho \mathscr{D}_F \frac{\partial\left[\mathcal{Z}_{0,F}+\mathcal{Z}_{1,F}\right]}{\partial y}\bigg|_f = \rho \mathscr{D}_{Ox} \frac{\partial\left[\mathcal{Z}_{0,Ox}+\mathcal{Z}_{1,Ox}\right]}{\partial y}\bigg|_f \tag{3.70}$$

The general mathematical solution for the forced field, governed by Eq.(3.4), can be written as:

$$\mathcal{Z}_{1,i} = C_{i,3}\frac{\varepsilon U_0}{i\omega}\frac{y}{x^{3/2}}\exp\left[\frac{-y^2}{x}\frac{U_0}{4\mathscr{D}_i}\right]\left(1-\exp\left[\frac{i\omega}{U_0}x\right]\right) \tag{3.71}$$

Enforcing the attachment boundary conditions and flame matching conditions for our non-premixed reacting mixing layer results in an implicit equation for the instantaneous flame position:

$$\varphi_{Ox}\sqrt{\frac{\mathscr{D}_F}{\mathscr{D}_{Ox}}}\frac{\left[1-erf\left(\psi_f\sqrt{\frac{U_0}{4\mathscr{D}_{Ox}}}\right)\right]}{\left[1+erf\left(\psi_f\sqrt{\frac{U_0}{4\mathscr{D}_F}}\right)\right]}=\frac{\exp\left(-\psi_f^2\frac{U_0}{4\mathscr{D}_{Ox}}\right)}{\exp\left(-\psi_f^2\frac{U_0}{4\mathscr{D}_F}\right)}\frac{\left\{\frac{2}{\sqrt{x_f}}-\frac{\varepsilon U_0}{i\omega}\left\{\frac{x_f-\frac{U_0}{2\mathscr{D}_{Ox}}y_f^2}{x_f^{5/2}}\right\}\left[1-\exp\left(\frac{i\omega}{U_0}x_f\right)\right]\exp(-i\omega t)\right\}}{\left\{\frac{2}{\sqrt{x_f}}+\frac{\varepsilon U_0}{i\omega}\left\{\frac{x_f-\frac{U_0}{2\mathscr{D}_F}y_f^2}{x_f^{5/2}}\right\}\left[1-\exp\left(\frac{i\omega}{U_0}x_f\right)\right]\exp(-i\omega t)\right\}} \tag{3.72}$$

converging to Eq.(3.67) in the limit as $\varepsilon\to 0$. Once again non-dimensionalizing and utilizing the dynamically significant parameters Φ and $Pe_{x,Ox}$, yields:

$$\varphi_{Ox}\sqrt{\Phi}\frac{\left[1-erf\left(\tilde{\psi}_f\sqrt{\frac{Pe_{x,Ox}}{4}}\right)\right]}{\left[1+erf\left(\tilde{\psi}_f\sqrt{\frac{Pe_{x,Ox}}{4\Phi}}\right)\right]}=\frac{\exp\left(-\tilde{\psi}_f^2\frac{Pe_{x,Ox}}{4}\right)}{\exp\left(-\tilde{\psi}_f^2\frac{Pe_{x,Ox}}{4\Phi}\right)}\frac{\left\{\frac{2}{\sqrt{\tilde{x}_f}}-\frac{\varepsilon}{iSt_\omega}\left\{\frac{\tilde{x}_f-\frac{Pe_{x,Ox}}{2}\tilde{y}_f^2}{\tilde{x}_f^{5/2}}\right\}\left[1-\exp\left(iSt_\omega\tilde{x}_f\right)\right]\exp(-i\omega t)\right\}}{\left\{\frac{2}{\sqrt{\tilde{x}_f}}+\frac{\varepsilon}{iSt_\omega}\left\{\frac{\tilde{x}_f-\frac{Pe_{x,Ox}}{2\Phi}\tilde{y}_f^2}{\tilde{x}_f^{5/2}}\right\}\left[1-\exp\left(iSt_\omega\tilde{x}_f\right)\right]\exp(-i\omega t)\right\}} \tag{3.73}$$

Utilizing our steady and instantaneous matching boundary conditions, and realizing that there is only one ξ_1 for the system, equations for the fluctuating fields can be related as:

$$\xi_1=\frac{-\mathcal{Z}_{1,F}\big|_f}{\left|\nabla\mathcal{Z}_{0,F}\right|_f}=\frac{-\mathcal{Z}_{1,Ox}\big|_f}{\left|\nabla\mathcal{Z}_{0,Ox}\right|_f} \tag{3.74}$$

and thus, the solution for $\xi_{1,n}\left(x,t\right)$ can be explicitly written as:

$$\xi_{1,n}\left(x,t\right)=\frac{i\varepsilon U_0}{2\pi f}\sin\theta_{0,f}(x)\left\{1-\exp\left(i2\pi St_{f,L}\frac{x}{L}\right)\right\}\exp\left[-i2\pi ft\right] \tag{3.75}$$

Significantly, this expression is identical in form to Eq.(3.15) and Eq.(3.49), reflecting the same dynamical features of the flame sheet winkles: the low-pass filter magnitude behavior, flame angle dependence, i.e. velocity fluctuations normal to the flame sheet, and wave form interference term. However, as was discussed in Section 3.2, a subtle difference lies within the flame angle term, representing the influence of the steady state flame position on the flame dynamics. The importance of the fluctuations normal to the

mean flame surface in generating wrinkles was previously shown, thus, modifications in the steady flame position due to differential diffusion would be important.

Figure 3.22 shows some representative wrinkle amplitude results, complementing the results shown in Figure 3.21. Notice the monotonic decrease of wrinkle amplitude with axial distance downstream. Different $Pe_{x,Ox}$ values would alter the relative magnitudes of these curves, due to the influence of the individual diffusion coefficient magnitudes on the steady flame position. The phase was omitted as it was the same for all the cases, showing no dependence on differential diffusion. This was expected as the convective velocity shown from Eq.(3.75) was not modified.

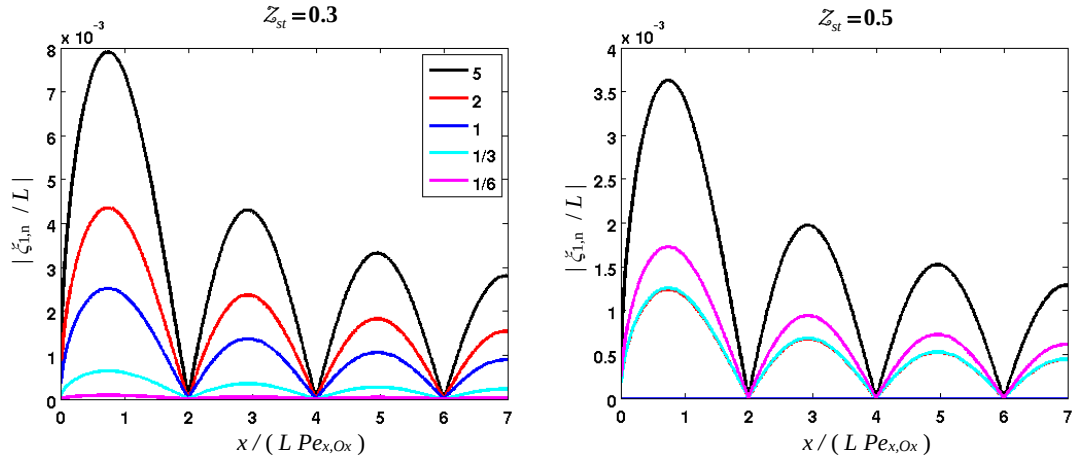

Figure 3.22. Wrinkle magnitude, $\xi_{1,n}$, plots for the forced non-premixed reacting mixing layer position, extracted from Eq.(3.75), for various degrees of differential diffusion, i.e. Φ, for $\mathcal{Z}_{st}=0.3$ (left) and $\mathcal{Z}_{st}=0.5$ (right), for $Pe_{x,Ox}$=1, $\varepsilon=0.01$, and $St_{f,L}Pe_{x,Ox}=0.5$.

As a note, analytical solutions isolating the effects of differential diffusion can be obtained for this single planar reacting mixing layer, i.e. flame, case. However, for the more advanced cases of fuel strips (which all our previous investigations were classified as, based on the inlet condition given in Eq.(3.1)), cylinders, or spheres, it is necessary to

apply a numerical method to solve the governing equations and inlet/matching boundary conditions provided in this section [121]!

CHAPTER 4

Isothermal Diffusion Flame Analysis – Advanced Dynamics

The results and analysis presented in Chapter 3 focused mainly on the $Pe \to \infty$ limit. Physically corresponding to the absence of axial diffusion, as axial convection dominated, this was done for analytical ***simplicity***, enabling the development of explicit solutions for the space-time dynamics of the flame position and unsteady heat release, and ***consistency***, since this assumption was already implicitly made when utilizing the step-inlet boundary condition. Within this limit, it was shown that forcing excited wrinkles on the flame sheet that advect axially along the flame at the mean flow speed, U_0, leading to a monotonically decreasing phase of flame wrinkles along the flame in the axial direction.

This chapter extends the previous analysis by investigating more advanced characteristics, both physics and system based, of non-premixed flames. First, being present in all real systems, we investigate the effects of finite axial diffusion on the flame dynamics. It is shown that axial diffusion influences both the flame wrinkle evolution dynamics, as well as the system inlet dynamics, each controlling specific dynamical features. The former was discussed in depth throughout Chapter 3, however, the latter was ignored, having been implicitly prescribed by our previously assumed steady and fluctuating inlet boundary conditions. As this inlet region was mentioned to be of extreme significance in the previous preliminary heat release analysis in Section 3.1.2, containing an integrable singularity, its importance will be reevaluated, along with its implications towards the heat release asymptotics (a topic which will be continued in Chapter 5). This study will be done both analytically, where tractable, and numerically, since it will be

shown that this is the proper way to completely and consistently include axial diffusion effects. Some additional intricate diffusion characteristics will also be considered, such as preferential diffusion, where the diffusion coefficient becomes anisotropic.

Lastly, multi-dimensional system and forcing configurations will be considered, as real combustion systems are inherently three-dimensional, and are often times exposed to complex multi-dimensional forcing configurations, such as helical and/or convecting disturbances.

4.1 Finite Axial Diffusion Effects – Analytical *Pe*>>1 Investigation

Our prior analysis, detailed in Chapter 3, neglected axial diffusion; while this is an important simplification in high Peclet number flames, it causes the exclusion of some important physics, such as the dissipative and dispersive nature of wrinkle propagation along the reaction sheet. Additionally, while some results regarding the various asymptotic limits for the heat release were inferred based upon computations, it is not clear how general they are. Analyses of these issues are investigated in this section, with comparisons of related features for premixed flames. An additional goal of this section is to formulate the various dynamical solutions in such a way that one general explicit solution is applicable to multiple non-premixed flame system and forcing configurations.

Once again, consider a two-dimensional flame in a uniform axial flow field, U_0, as was shown in Figure 3.1. As we are trying to generalize the final solution, we can additionally generalize the inflow ($x=0$) condition by stating that arbitrary fuel and oxidizer advect into the domain with inflow mixture fractions given by $\mathcal{Z}_{fs}^*$ and $\mathcal{Z}_{os}^*$, respectively. For compactness, we can then define the familiar "rescaled" mixture

fraction which varies between zero and unity, $\mathcal{Z} = (\mathcal{Z}^* - \mathcal{Z}_{os}^*) / (\mathcal{Z}_{fs}^* - \mathcal{Z}_{os}^*)$, as has been utilized throughout Chapter 3.

Recall that we have steady state, Eq.(3.5), and various fluctuating, Eq.(3.8) and Eq.(3.52), mixture fraction field solutions utilizing the step inlet boundary condition. Although these solutions are formally valid for arbitrary *Pe* values, it was recognized that this boundary condition implicitly assumes infinite *Pe* values, and leads to an infinite transverse gradient in mixture fraction at the burner outlet. In reality, there is some finite gradient at the burner outlet due to axial diffusion effects which become important when the convective disturbance length scale, U_0 / f , is on the order of this species concentration boundary layer. However, an interesting question is for what large, yet finite *Pe* values this inlet condition is still essentially valid. Thus, rather than looking at dynamical solutions for infinite *Pe* values, i.e. $Pe \to \infty$ limit, now we will investigate solutions for large, yet finite *Pe* values, i.e. $Pe >> 1$.

We consider the solutions for $\mathcal{Z}_1$ in cases with either spatially uniform axial or transverse velocity fluctuations, of the form Eq.(3.7) and Eq.(3.50), respectively. A general solution for the mixture fraction field, subject to the step inlet condition, Eq.(3.1), and flame attachment boundary condition, i.e. $\mathcal{Z}_1(x = 0, y, t) = 0$, at the fuel port lip, for the bounded domain is:

$$\mathcal{Z}_1 = \sum_{n=1}^{\infty} \left[\frac{2\varepsilon \sin(\mathcal{A}_n)}{n\pi i St_\omega} \right] \mathcal{M}_n \mathcal{G}(y) \exp\left(\beta_- \frac{x}{PeR_f} \right) \left[1 - \exp\left(\{\beta_{h-} - \beta_-\} \frac{x}{Pe\, R_f} \right) \right] \exp[-i\omega t] \quad (4.1)$$

where the Strouhal number based on the half-width of the fuel nozzle is defined by Eq.(2.27) ($St_\omega = St_{\omega,R}$), parameters $\mathcal{A}_n$, β_- , and β_{h-} are the same as from the bulk

forced cases (Section 3.1 and Eq.(3.9), noting $St_\omega = St / 2\pi$), s is the dimensionless ratio R_f / R_w, and the other terms, i.e. $\mathcal{M}_n$ and $\mathcal{G}(y)$, are specified in Table 4.1.

Table 4.1. Definitions used in mixture fraction solutions

	Axial Bulk Forcing	Transverse Bulk Forcing
$\mathcal{M}_n$	β_- / Pe	$-\mathcal{A}_n$
$\mathcal{M}_{xyn}$	β_{xy-} / Pe_y	$-\mathcal{A}_n$
$\mathcal{G}(y)$	$\cos(\mathcal{A}_n\, y / R_f)$	$\sin(\mathcal{A}_n\, y / R_f)$
$\mathcal{S}(x,y)$	$\partial \mathcal{Z}_0 / \partial x$	$\partial \mathcal{Z}_0 / \partial y$
$\mathcal{I}(\theta(x))$	$\sin\theta(x)$	$\pm\cos\theta(x)$

For completeness and generality, these expressions can also be written in a general form for both confined and unconfined flames in the $Pe \to \infty$ limit as:

$$\mathcal{Z}_1 = \left[\frac{-i\varepsilon R_f}{St_\omega}\right] \mathcal{S}(x,y) \left\{1 - \exp\left(i\, St_\omega \frac{x}{R_f} \right)\right\} \exp[-i\omega t] \tag{4.2}$$

4.1.1 Space-time Dynamics

An explicit expression for fluctuating flame position can be obtained in a similar manner as was done for the axial forced case in Section 3.1. Recall that $\xi_{1,n}$ is measured normal to the mean flame surface in the direction of the oxidizer. Using mixture fraction and flame geometric relations, the solution for $\xi_{1,n}(x,t)$ can be written as:

$$\frac{\xi_{1,n}(x,t)}{R_f} = -\left[\frac{\varepsilon \mathcal{I}(\theta(x)) e^{-i\omega t}}{iSt_\omega}\right] \frac{\displaystyle\sum_{n=1}^{\infty} \frac{2}{n\pi} \mathcal{M}_n \mathcal{G}(\xi_0(x)) \sin(\mathcal{A}_n) e^{\left(\beta_- \frac{x}{PeR_f}\right)} \left[1 - e^{\left(\{\beta_{h-} - \beta_-\} \frac{x}{Pe\, R_f}\right)}\right]}{\displaystyle\sum_{n=1}^{\infty} \frac{2}{n\pi} \mathcal{M}_n \mathcal{G}(\xi_0(x)) \sin(\mathcal{A}_n) e^{\left(\beta_- \frac{x}{PeR_f}\right)}} \tag{4.3}$$

where the terms $\mathscr{I}(\theta(x))$, $\mathscr{M}_n$ and $\mathscr{G}(\xi_0(x))$ are defined in Table 4.1. This is a general equation which includes the effects of axial diffusion for both axial and transverse forcing.

Insight into wave propagation, dissipation, and dispersion effects, as well as direct comparisons between the non-premixed and premixed flame wrinkle dynamics can be obtained by expanding these expressions around the $Pe \to \infty$ limit in inverse powers of *Pe*. For example, the $(\beta_{h-} - \beta_{-})/Pe$ term in Eq.(4.3) can be expanded as:

$$\frac{\{\beta_{h-} - \beta_{-}\}}{Pe} = \left\{ iSt_\omega - \frac{St_\omega^2}{Pe} - \frac{2iSt_\omega\left(\mathscr{A}_n^2 + St_\omega^2\right)}{Pe^2} + \frac{6\mathscr{A}_n^2 St_\omega^2 + 5St_\omega^4}{Pe^3} + \mathrm{O}\left(Pe^{-4}\right) \right\} \qquad (4.4)$$

and will be referred to as the $Pe >> 1$ limit. The results of Wang *et al.*[87] for the linearized response of premixed flames to bulk axial forcing (generalized here to bulk transverse forcing) can be similarly expanded for flames that are thin relative to the burner radius; i.e., where $\sigma_C << 1$, and σ_C is the scaled Markstein number, *Ma*:

$$\sigma_C = \frac{Ma}{2R_f}\left(\frac{1+\alpha^2}{\alpha^2}\right) \qquad (4.5)$$

By following this procedure to O($1/Pe^2$) and O(σ_C^2), we can develop the following general result, valid for axial or transversely forced premixed or non-premixed flames in the $Pe >> 1$ limit:

$$\frac{\xi_{1,n}^c(x,t)}{R_f} = -\left[\frac{\varepsilon\mathscr{I}(\theta(x))\exp(-i\omega t)}{iSt_\omega}\right]\left[1 - \exp\left(\frac{i\omega x}{U_c}\right)\exp\left(\frac{-\zeta x}{R_f}\right)\exp\left(\gamma St_\omega^2\frac{i\omega x}{U_c}\right)\right] + O\left(\frac{1}{Pe^3}, \sigma_C^3\right) \qquad (4.6)$$

where the waveform term is parameterized by a convection speed, U_c, axial dissipation rate, ζ, and dispersion term, γ, defined in Table 4.2. Note $\alpha = L_f / R_f = \cot\theta$ is the premixed flame aspect ratio.

Table 4.2. Propagation, dissipation, and dispersion terms

	Premixed	Non-premixed
Propagation speed, U_c	$U_0 \cos^2\theta$	$U_0 + O(1/Pe^2)$
Dissipation, ζ	$St_\omega^2 \sigma_C$	$\frac{St_\omega^2}{Pe}$
Dispersion, γ	$-2\sigma_C^2 \frac{\alpha}{\sqrt{1+\alpha^2}}$	$\frac{-2}{Pe^2}$

Consider the various terms in Eq.(4.6). The expression is led by a group of terms which describe the wave magnitude and harmonic time dependence, $\varepsilon / (iSt_\omega)\mathcal{I}\left(\theta(x)\right)\exp\left(-i\omega t\right)$. They show the familiar low-pass filter characteristic of flame wrinkle amplitude. The wave magnitude also has an axial dependence described by the term, $\mathcal{I}\left(\theta(x)\right)$, whose form depends upon whether the flame is forced axially or transversely. This shows the controlling nature of velocity fluctuations normal to the flame sheet. As shown in Table 4.1, the top and bottom flame branches are in-phase and are mirror images of each other for axial forcing, and are out-of-phase for transverse forcing. Finally, the non-premixed steady state flame angle is a function of axial coordinate, while for premixed flames with a comparable spatially uniform inflow, U_0, $\mathcal{I}\left(\theta(x)\right)$ is not.

We next consider the general wave propagation term, contained in the expression $1-\exp\left(i\omega x/U_c\right)\exp\left(-\zeta x/R_f\right)\exp\left(i\gamma St_\omega^2\omega x/U_c\right)$. The first unity term derives from the particular solution of the equation, and lacks spatial dependence because of the nature of the assumed bulk forcing. The second term describes a decaying, dispersive traveling wave generated at the boundary, $x=0$, because of the assumption of flame attachment, i.e., $\xi_{1,n}(x=0,t)=0$, or fixed mixture fraction at the burner outlet, $\mathcal{Z}_1(x=0,y,t)=0$, for the premixed and non-premixed cases, respectively.

The leading order expansion of this expression, $1-\exp\left(i\omega x/U_c\right)$, was previously presented in Section 3.1, i.e. Magina *et al.*[66]. It shows how flame wrinkles propagate without dissipation and non-dispersively in the $Pe\to\infty$ or $\sigma_C\to 0$ limits. In this limit, the major difference between the space-time dynamics of non-premixed and premixed flame dynamics comes from the U_c parameter defined in Table 4.2. In both cases, local maxima and minima in flame wrinkle amplitude arise through interference between the two terms, revealed in Eq.(3.17).

Consider next O(1/*Pe*) or O(σ_C) terms, which as shown in Table 4.2, cause wrinkles to decay exponentially with downstream distance. This causes the interference effect discussed above to become imperfect, an effect that increases quadratically with St_ω. The mechanism for wave dissipation for the two flame types are entirely different – for premixed flames, it is due to the dependence of the flame speed on the curvature, which causes positive Markstein length flames to be thermo-diffusively stable. For non-premixed flames, it is due to the progressive smoothing by diffusion of the spatial variations in the $\mathcal{Z}$ field with downstream distance.

We lastly consider O($1/Pe^2$) and O(σ_C^2) effects which, as shown in Table 4.2, introduce dispersion – i.e., a frequency dependent wave propagation speed. Explicit results for the premixed and non-premixed flames are shown in the table. An additional O($1/Pe^2$) effect for non-premixed flames is an alteration of the wave propagation speed, U_c, however, because the non-premixed result involves a ratio of two infinite sums, it is not possible to develop a simple expression for the confined case.

Illustrative solutions from Eq.(4.6) are presented for the instantaneous non-premixed flame position at several time instances in Figure 4.1, as well as the amplitude and phase of the wrinkles in Figure 4.2, for constant values of St_{L_f}. The generation and downstream propagation of flame wrinkles can be observed, with a larger number of flame wrinkles being present within the flame length for increasing frequencies. Again, the spatial variation in the amplitude comes from the $\mathcal{J}\left(\theta(x)\right)$ term, as well as the spatial interference effect in Eq.(4.6). The local maxima and minima referred to above are clearly evident in the figures for the weakly dissipative solutions. The phase rolls off linearly with axial distance, reflecting the convection process described, and jumps 180 degrees across the nodes. Note the smoothing of the wrinkles that occurs in the mid and far field with decreasing *Pe*, due to wave dissipation discussed in the context of Eq.(4.4). This effect reduces the overall peak-to-crest wrinkle amplitudes, as well as abolishing previously spatially stationary nodes, represented by the liftoff from the vertical axis. This leads to a complete loss of the spatial interference pattern for the $Pe = 5$ case relative to the $Pe \to \infty$ case. In addition, the phase does not roll-off linearly in the axial direction, and the discontinuous phase jumps are smoothed. Lastly, the steady state flame position becomes modified by axial diffusion. Both the flame tip location (i.e. overall

flame length), and the location of maximum width move downstream, as can be seen from Figure 4.2 by the movement of the flame angle forced node, an effect which was shown to impact the dynamics in Section 3.2.

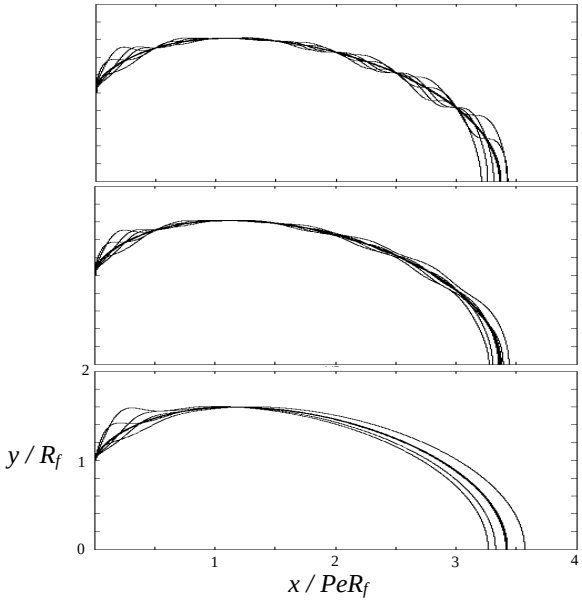

Figure 4.1. Temporal evolution of flame position for the $Pe \to \infty$ solution (top) and the general solution at two representative *Pe* values of 20 (middle), and 5 (bottom) for $PeSt_\omega = 4\pi$ and $\mathcal{Z}_{st} = 0.3$. Note *x*-axis is rescaled by *Pe*.

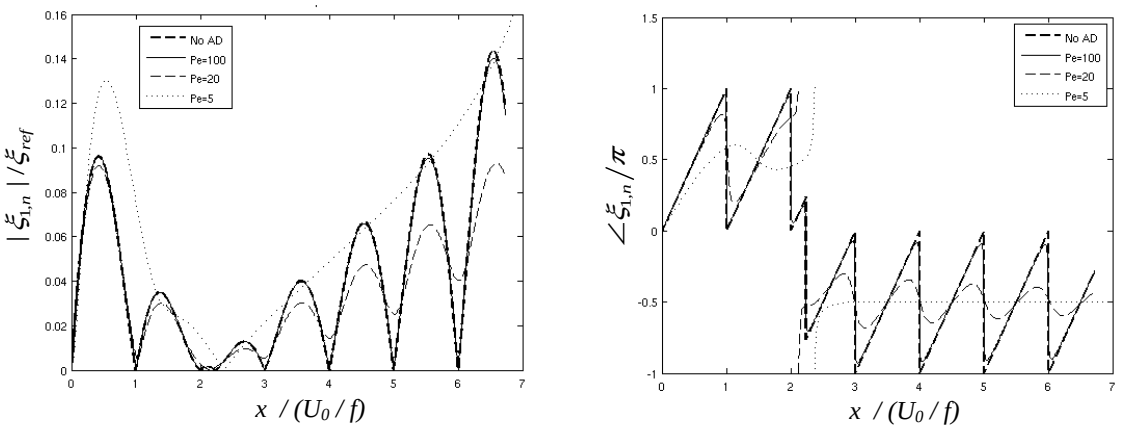

Figure 4.2. Space-time dynamics presented via the magnitude (left) and phase (right) of $\xi_{1,n}$ plotted against the ratio of axial coordinate to convective wavelength for the $Pe \to \infty$ limit and full solution at three representative *Pe* values of 100, 20, and 5 for $PeSt_\omega = 4\pi$ and $\mathcal{Z}_{st} = 0.3$.

4.1.1.1 Flame Clipping

As noted in literature, an interesting spatiotemporal behavior of long, buoyancy dominated non-premixed flames is known as “clipping”, where the upper portion of the flame becomes detached from the main body due to extreme flame flicker, and convects downstream, much like a burning droplet [122, 123]. This phenomena can also happen for momentum dominated flames due to external forcing, but only beyond critical operational parameters. The considerable corrugation of the flame front causes it to self-intersect and split, and the resulting disconnected region collapses while convecting downstream, even while the remainder of the surface enlarges near the base [59]. It has been noted in experimental and computational studies of forced coflow laminar diffusion flames that this clipping behavior only occurs *below* a certain frequency of excitation and *above* a critical amplitude for that frequency!

Significantly, recent experimental [123] and computational [122] studies of soot volume fraction in flickering CH_4/air diffusion flames have shown that for conditions in which the tip of the flame is clipped, soot production is significantly greater than similar unclipped flames, as well as being 4-5x greater than that measured for steady flames. This is due to the fact that the maximum downstream location obtained by a portion of clipped flame exceeds that for a similar conditioned, i.e. forcing frequency, unclipped flame, resulting in considerably longer soot growth times.

As mixture fraction field solutions for forced non-premixed flame systems have been obtained, we can investigate this phenomena; and although these solutions were derived in the limit of small perturbation amplitudes, some preliminary conclusions can still be drawn. Figure 4.3 shows representative clipped and un-clipped flames positions extracted from our axially forced mixture fraction field solutions.

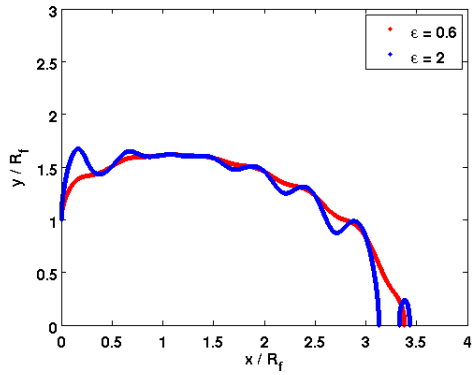

Figure 4.3. Representative clipped (ε=2; blue) and unclipped (ε=0.6; red) instantaneous flame positions, utilizing results from Section 3.1, for *Pe*=20, $St_f = 0.1$, and $\mathcal{Z}_{st} = 0.3$.

As it was noted that forcing amplitude and frequency were the two key parameters controlling clipping behavior, we investigated a two-dimensional parametric sweep over, ε and St_f, for both the axially forced mixture fraction results excluding ($Pe \to \infty$ results from Section 3.1) and including ($Pe >> 1$ results from Section 4.1) axial diffusion. The computationally extracted results are shown in Figure 4.4, denoting the regions of parametric combinations in which clipping was detected. The resulting low frequency, large fluctuation amplitude regions agree with previous works. Additionally, it can be seen that the smoothing action of axial diffusion acts to eliminate clipping behavior at higher frequencies. This result makes sense as this wrinkle dissipation effect was shown to increases quadratically with St. Also placed on these figures were curves of the form:

$$\varepsilon = 0.5 + aSt_f^b \tag{4.7}$$

indicating the critical values of ε, as a function of St, beyond which clipping would likely occur (although these curves do not capture some of the oscillatory behavior noticed computationally). The coefficients for the no axial diffusion case were, a=0.2 and b=2, and for the axial diffusion case were, a=15 and b=1, indicating how for a given forcing frequency including axial diffusion effects inhibits clipping.

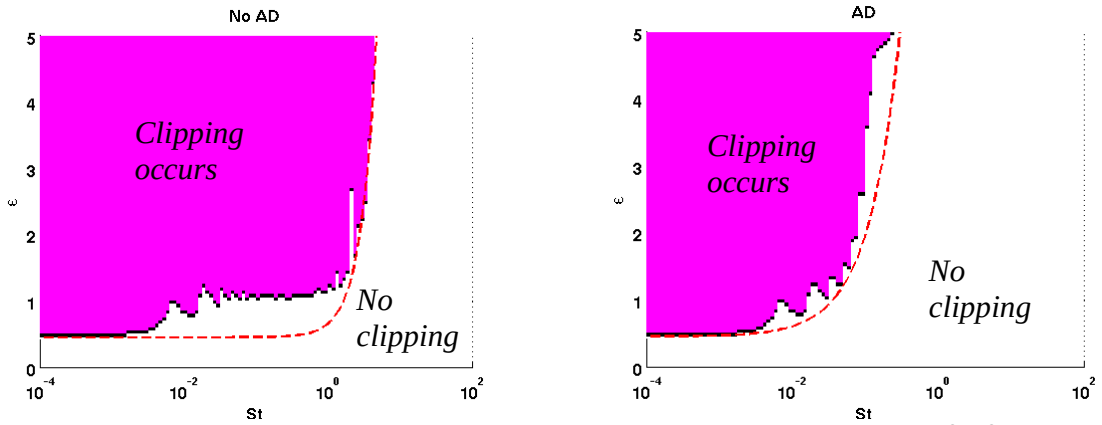

Figure 4.4. Parametric sweep over ε and St_f indicating clipping tendencies of a forced non-premixed flame excluding (left) and including (right) axial diffusion effects, for *Pe*=20 and $\mathcal{Z}_{st} = 0.3$.

4.1.2 Heat Release Analysis

Following Section 2.4.3 and Section 3.1.2, the instantaneous global heat release of the non-premixed flame, given by Eq.(2.40), and the specialized form for the two-dimensional case, given by Eq.(3.22), can be linearized and expanded (retaining the axial diffusion term) to:

$$\frac{\varphi_{Ox}}{(1+\varphi_{Ox})^2 \rho \mathscr{D} \mathscr{K}_R} \dot{Q}(t) = \int_0^{L_f^+(t)} \left[\begin{array}{l} \underbrace{\frac{\partial \mathcal{Z}_0(x,\xi_0)}{\partial x}\sin(\theta_0)dA_0}_{\text{steady state}} + \underbrace{\frac{\partial \mathcal{Z}_0(x,\xi_0)}{\partial x}\sin(\theta_0)dA_1}_{\text{area}} + \\ \underbrace{+\frac{\partial \mathcal{Z}_0(x,\xi_0)}{\partial x}\cos(\theta_0)\sin(\theta_1)dA_0 + \xi_{1,y}(x,t)\frac{\partial^2 \mathcal{Z}_0(x,\xi_0)}{\partial x \partial y}\sin(\theta_0)dA_0 + \frac{\partial \mathcal{Z}_1(x,\xi_0)}{\partial x}\sin(\theta_0)dA_0}_{\text{mass burning rate}} \end{array} \right]$$

$$- \int_0^{L_f^+(t)} \left[\begin{array}{l} \underbrace{\frac{\partial \mathcal{Z}_0(x,\xi_0)}{\partial y}\cos(\theta_0)dA_0}_{\text{steady state}} + \underbrace{\frac{\partial \mathcal{Z}_0(x,\xi_0)}{\partial y}\cos(\theta_0)dA_1}_{q_A(x,t)} + \\ \underbrace{-\frac{\partial \mathcal{Z}_0(x,\xi_0)}{\partial y}\sin(\theta_0)\sin(\theta_1)dA_0 + \xi_{1,y}(x,t)\frac{\partial^2 \mathcal{Z}_0(x,\xi_0)}{\partial y^2}\cos(\theta_0)dA_0 + \frac{\partial \mathcal{Z}_1(x,\xi_0)}{\partial y}\cos(\theta_0)dA_0}_{q_{MBR}(x,t)} \end{array} \right] \quad (4.8)$$

The terms in the top set of brackets are completely new, resulting from the inclusion of axial diffusion, i.e. the $d\mathcal{Z}/dx$ term in Eq.(3.22). For each set of brackets, the first term on the top is the steady state contribution, the second term on the top denotes the contribution of flame area fluctuating area oscillations to heat release fluctuations, and the remaining three terms the contribution of mass burning rate oscillations to heat

release fluctuations. Note the sub and superscript – and + signs on the upper integration limits $L_f(t)$, which indicate integration from 0 to L_f over the bottom and top flame branches respectively. This is important to keep in mind for forcing configurations which result in a non-axisymmetric instantaneous flame sheet. Additionally, in a rectangular coordinate system, the differential areas can be written in multiple ways, depending upon whether the integration is performed over the axial or transverse coordinate; e.g.,:

$$dA_1 = \frac{\sin\theta_0 \sin\theta_1}{\cos^2\theta_0} dx \qquad\qquad dA_1 = \frac{-\cos\theta_0 \sin\theta_1}{\sin^2\theta_0} dy \tag{4.9}$$

Representative computed transfer functions for finite *Pe* values, obtained from Eq.(4.8), are shown by the curves in Figure 4.5 and several finite *Pe* effects can be noted. First, $\mathscr{F}$ does not tend to unity for low *St* values. This is due to the fact that the instantaneous mass flux in the domain occurs not only through convection, but also diffusion. If the transfer function expression were generalized to account for both convective and diffusive flux, these transfer function values converge to unity. Second, the ripples in gain that occur near St_{Lf} ~1 are damped out at lower *Pe* values, due to dissipation mechanisms discussed previously.

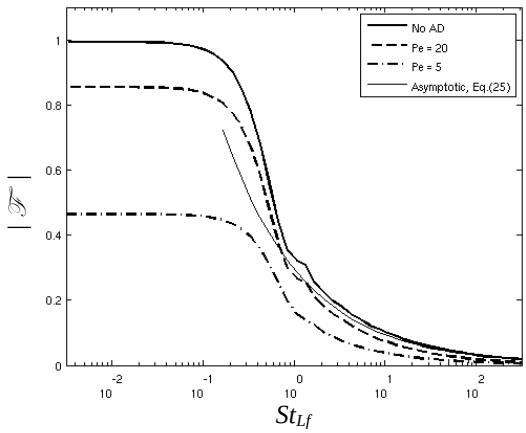

Figure 4.5. Axially forced heat release transfer function curves for the $Pe \to \infty$ limit, full solution at two representative *Pe* values of 20 and 5, and asymptotic expression plotted vs St_{L_f} for $\mathcal{Z}_{st} = 0.3$.

4.1.3 Explicit Governing Equation Validation

Recall how in Section 2.5, an explicit governing equation, Eq.(2.49), was presented for the specific case of an infinitely long, flat non-premixed flame. Additionally in Section 3.1.4, this equation was refined for a two-dimensional harmonically forced system, and an explicit solution obtained, given by Eq.(3.42), which was shown to match previous results in the $Pe \to \infty$ limit. As we now have an explicit equation for the wrinkle dynamics for large, yet finite Pe values, i.e. $Pe >> 1$, we can once again compare the solutions obtained.

The exponential inside the waveform of Eq.(3.42), can be expanded around the $Pe \to \infty$ limit as:

$$\frac{Pe - \sqrt{Pe^2 - 8\pi i PeSt}}{2} \sim iSt_\omega - \frac{St_\omega^{\,2}}{Pe} - \frac{2iSt_\omega^{\,3}}{Pe^2} + O\left(\frac{1}{Pe^3}\right) \tag{4.10}$$

Comparing this expansion to Eq.(4.4), and the resulting solution given by Eq.(4.6), reveals the exact same solutions/parameters for the wrinkle convection, dissipation, and dispersion! Hence, once again the assumption of an infinitely long, flat flame validated our $Pe >> 1$ assumption, providing the same explicit flame dynamics.

4.2 Multi-dimensional Forcing Effects

The previous Chapter and section have covered the idealistic case of two dimensional non-premixed flames exposed to unidirectional, spatially uniform, fluctuations in flow velocity. However, real combustion systems are not this simple, being inherently three-dimensional, and are often times exposed to much more advanced forcing configurations, such as helical and/or convecting disturbances. Additionally, swirl

is a common feature of many combustion designs, utilized for aerodynamic flame stabilization.

Thus, the objective of this section is to continue analysis of this problem, with several key goals. First, while two-dimensional analyses were valuable for the development of the basic suite of analysis techniques and understanding of key controlling physics, real non-premixed flames take on a more axisymmetric shape, are often embedded in swirling flows, and are subjected to three dimensional disturbances. Such three dimensional disturbances may arise from helical vortical disturbances or transverse acoustic modes. In addition, helical modes may be excited during both axial and transverse acoustic instabilities. Analyses of these problems are described in this section, with comparisons of related features for premixed flames.

Still working within the mixture fraction formulation, the instantaneous position of the three-dimensional reaction sheet, in cylindrical coordinates, is defined by $r = \xi(\theta, x, t)$, as shown in Figure 4.6.

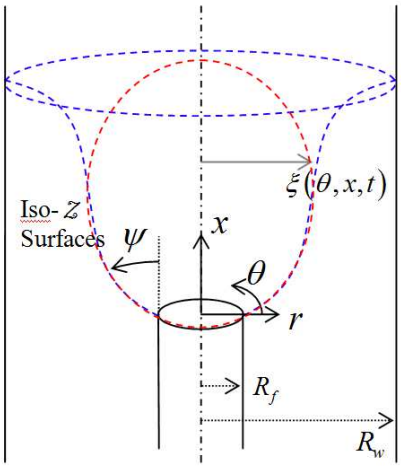

Figure 4.6. Schematic of the three-dimensional swirling non-premixed flame. Images show a steady over (red dashed line) and under (blue dashed line) ventilated flame.

Generalizing our previous inlet conditions, at the inflow ($x=0$) fuel and oxidizer advect into the domain from the central and coflowing tubes, as indicated in the figure, with inflow mixture fractions given by $\mathcal{Z}_{fs}^{*}$ and $\mathcal{Z}_{os}^{*}$, respectively. For compactness, we utilize the rescaled mixture fraction which varies between zero and unity, $\mathcal{Z}=(\mathcal{Z}^{*}-\mathcal{Z}_{os}^{*})/(\mathcal{Z}_{fs}^{*}-\mathcal{Z}_{os}^{*})$. Once again we utilize a step inlet boundary condition, formulated for the three-dimensional domain as:

$$\mathcal{Z}(r,\theta,x=0)=\begin{cases}1 & 0\le r<R_f\\ 0 & R_f\le r\end{cases} \tag{4.11}$$

No-diffusion at the side walls implies $\partial\mathcal{Z}/\partial r(r=R_w,\theta,x)=0$, and we ensure that the solution remains finite at large axial distances. Further discussion of this approximate boundary condition can be found in Section 4.3.

Once again, we derive the solution in the limit of small perturbations and so expand each variable as $(\ )(r,\theta,x,t)=(\ )_0(r,\theta,x)+(\ )_1(r,\theta,x,t)$. The solution to the zeroth order form of the $\mathcal{Z}$ -equation, Eq.(2.21), in cylindrical coordinates, subject to the boundary condition in Eq.(4.11), and the flow conditions that $u_{x,0}=U_0$, swirl velocity, $u_{\theta,0}=\Omega r$ (where Ω is the angular rate of swirl), and no radial velocity, $u_{r,0}=0$, in a bounded domain is given by:

$$\mathcal{Z}_0(r,x,\zeta)=s^2+\sum_{n=1}^{\infty}\frac{2sJ_1(r_n s)}{J_0(r_n)^2 r_n}J_0\left(r_n s\frac{r}{R_f}\right)\exp\left[\frac{\mathcal{B}}{Pe}\frac{x}{R_f}\right] \tag{4.12}$$

where r_n is the n^{th} root of the first order Bessel function of the first kind, $J_1(r_n)=0$, s is the ratio of fuel port radius to wall radius, $s=R_f/R_w$, and $\mathcal{B}$ is given by:

$$\mathcal{B}_{-} = \frac{Pe^2 - \sqrt{Pe^4 + 4\left(r_n s\right)^2 Pe^2}}{2} \tag{4.13}$$

This form of the swirl velocity represents solid body rotation, and can also be written as $u_{\theta,0} = 2\pi St\sigma(r / R_f)U_0$, where $\sigma = \Omega / \omega$ is the swirl parameter. Once again, while these solutions are formally valid for arbitrary *Pe* values, the use of the step inlet boundary condition implicitly assumes $Pe \to \infty$. This is an important point that will be utilized to elucidate dynamical features throughout this section.

The first order form of the $\mathcal{Z}$-equation, Eq.(2.22), in cylindrical coordinates takes the following form:

$$\frac{\partial \mathcal{Z}_1}{\partial t} + u_{r,0}\frac{\partial \mathcal{Z}_1}{\partial r} + \frac{u_{\theta,0}}{r}\frac{\partial \mathcal{Z}_1}{\partial \theta} + u_{x,0}\frac{\partial \mathcal{Z}_1}{\partial x} - \mathcal{D}\left[\frac{1}{r}\frac{\partial \mathcal{Z}_1}{\partial r} + \frac{\partial^2 \mathcal{Z}_1}{\partial r^2} + \frac{1}{r^2}\frac{\partial^2 \mathcal{Z}_1}{\partial \theta^2} + \frac{\partial^2 \mathcal{Z}_1}{\partial x^2}\right] = \\ = -u_{r,1}\frac{\partial \mathcal{Z}_0}{\partial r} - \frac{u_{\theta,1}}{r}\frac{\partial \mathcal{Z}_0}{\partial \theta} - u_{x,1}\frac{\partial \mathcal{Z}_0}{\partial x} \tag{4.14}$$

It is helpful to write this equation out explicitly, for in the following sections we will discuss the mixture fraction solutions and space-time dynamics for swirling non-premixed flames exposed to various forcing configurations. Each case has a unique set of forcing velocities $u_{r,1}$, $u_{\theta,1}$, and $u_{x,1}$ which produce unique solutions and dynamics. After these have all been presented, the various terms in these solutions will be examined and their influence on the flame dynamics clarified. Lastly we will compare these dynamical features to those of a three-dimensional swirling premixed flame exposed to similar forcing.

4.2.1 Bulk Axial Fluctuation Solutions

As a building block, it is useful to revisit the simplest forcing case previously considered in our two-dimensional analyses in Section 3.1, axial bulk velocity fluctuations, which is given by the forcing velocity set:

$$u_{r,1} = 0 \qquad u_{\theta,1} = 0 \qquad u_{x,1} = \varepsilon U_0 \exp\left[-i\omega t\right] \tag{4.15}$$

The general solution for the fluctuating mixture fraction field, subject to the flame attachment boundary condition, i.e. $\mathcal{Z}_1(r,\theta,x=0)=0$, at the fuel port lip is:

$$\mathcal{Z}_1(r,x,t) = \sum_{n=0}^{\infty} \frac{\mathcal{B}_- s\varepsilon J_1(r_n s)\exp\left[-i\omega t\right]}{\pi i Pe St J_0(r_n)^2 r_n} J_0\left(r_n s \frac{r}{R_f}\right) \exp\left(\frac{\mathcal{B}_-}{Pe}\frac{x}{R_f}\right)\left[1-\exp\left[\frac{\{\mathcal{B}_h - \mathcal{B}_-\}}{Pe}\frac{x}{R_f}\right]\right] \tag{4.16}$$

where

$$\mathcal{B}_h = \frac{Pe^2 - \sqrt{Pe^4 + 4Pe^2(r_n s)^2 - 8\pi i Pe^3 St}}{2} \tag{4.17}$$

Note that the solution is not a function of the angular coordinate or the swirl parameter, σ, due to the axisymmetric form of the mean flame and disturbance. Figure 4.7 shows representative instantaneous $\mathcal{Z} = \mathcal{Z}_{st}$ iso-contours for the unforced case, and each of the forced problems, for both the over- and under-ventilated non-premixed flame configurations. Notice the clear wrinkling of the flame and its azimuthal dependence in the transverse and helically forced cases, a feature that will be discussed in the following subsections.

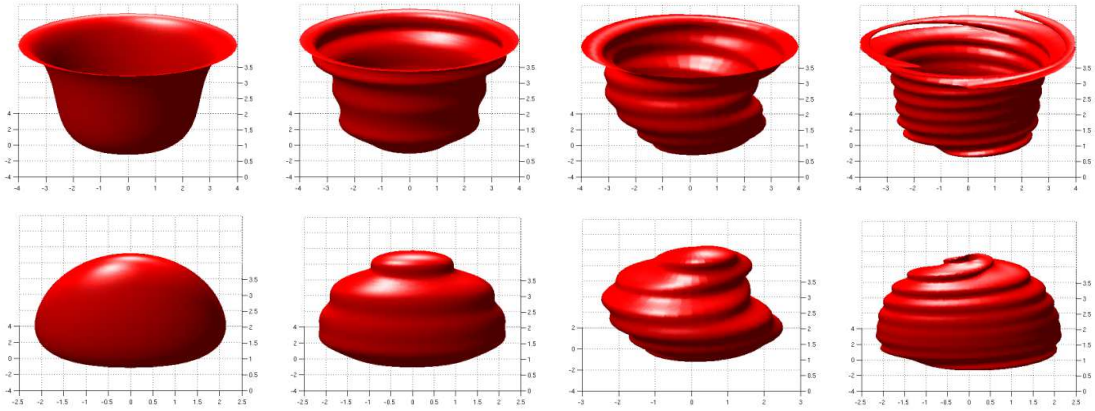

Figure 4.7. Steady state and fluctuating mixture fraction field iso-contours for an under (top row, $\mathcal{Z}_{st}$ =0.055) and over (bottom row, $\mathcal{Z}_{st}$ =0.08) ventilated non-premixed flame in a swirling convecting mean flow, subject to axial bulk disturbance, transverse bulk disturbance, and a helical disturbance with *m*= -1, k_c= 5 (from left to right) for parameters *Pe*=10, *St*=0.1, *s*=0.25.

Following the procedure outlined in Section 3.1, the first order flame position fluctuations can be extracted from this solution and written explicitly as:

$$\frac{\xi_{1,n}(x,t)}{R_f} = \sum_{n=0}^{\infty} \frac{i\varepsilon \exp[-i\omega t]}{2\pi St} \left[\frac{\partial \mathcal{Z}_{0,n} / \partial x}{|\nabla \mathcal{Z}_0|_{(r=\xi_0(x),x)}} \right] \left[1 - \exp\left[\frac{\{\mathcal{B}_h - \mathcal{B}_-\}}{Pe} \frac{x}{R_f} \right] \right] \tag{4.18}$$

where $\partial \mathcal{Z}_{0,n} / \partial x$ is the n^{th} term of the $\partial \mathcal{Z}_0 / \partial x$ summation and $\xi_{1,n}$ is the wrinkle fluctuation measured normal to the mean flame surface.

As was shown by Section 4.1, more insight into this solution in the high *Pe* limit can be obtained by formally expanding it in inverse powers of *Pe*, following Magina *et al.* [67]. Retaining terms up to order 1/*Pe* yields:

$$Pe>>1 \quad \frac{\xi_{1,n}(x,t)}{R_f} = \frac{i\varepsilon \exp[-i\omega t]}{2\pi St} \sin\psi_0(x) \left[1 - \exp\left[2\pi i St \frac{x}{R_f} \right] \exp\left[-\frac{4\pi^2 St^2}{Pe} \frac{x}{R_f} \right] \right] + O\left(\frac{1}{Pe^2} \right) \tag{4.19}$$

This solution is identical to that previously obtained for a two-dimensional flame, given by Eq.(4.6), although $\psi_0(x)$ has a different functional dependence on *x* (see Section 4.1.1

for discussion). Note, for this forcing configuration, swirl has no influence on the flame wrinkles, since the disturbance form is axisymmetric and independent of θ. Figure 4.8 shows an illustrative solution of the flame wrinkle magnitude and phase for the axial bulk forced case. The spatial variation in the amplitude, resulting from the flame angle term, as well as the spatial interference effect, can be seen. Note the clear local maxima and minima for the weakly dissipative, i.e. no axial diffusion, solution. In addition, the phase rolls off linearly with axial distance, with 180 degree jumps across the nodes. Axial diffusion acts to make this spatial interference effect imperfect, smoothing the amplitude and phase plots.

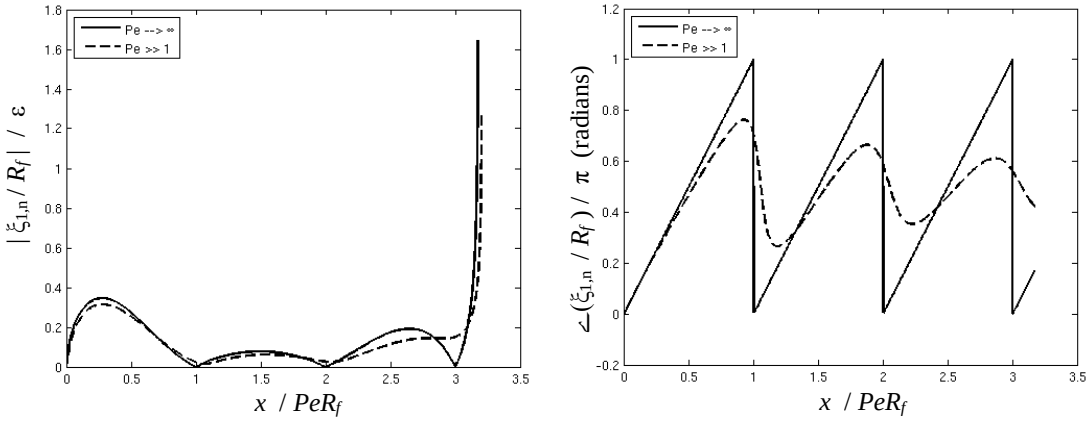

Figure 4.8. Wrinkle amplitude and phase for the axial bulk forced case for parameters *Pe*=10, *St*=0.1, ε=0.01, *s*=0.25, and $\mathcal{Z}_{st}$ =0.055.

4.2.2 Dimensionality Effects

Both Section 3.1 and Section 4.2.1 investigate axial bulk velocity oscillations of confined non-premixed flame systems, the only difference being the dimensionality of the study. Thus comparing the explicit fluctuating wrinkle equations, i.e. Eq.(3.15) and Eq.(4.19), we can isolate the effects of dimensionality on the flame dynamics.

Comparing these two equations reveals the same dynamical features of the flame sheet winkles: the low-pass filter magnitude behavior, flame angle dependence, i.e. velocity fluctuations normal to the flame sheet, and wave form interference term. However, as was the case for the study on confinement effects, a subtle difference once again lies within the flame angle term, representing the influence of the steady state flame position on the flame dynamics. When the steady flame location is altered, so is the axial dependence of the normality of the fluctuations with respect to the flame surface, influencing wrinkle generation. Figure 4.9 shows a representative over- and under-ventilated steady state flame position extracted from the two-dimensional, Eq.(3.6), and three-dimensional, Eq.(4.12), mixture fraction field solutions for two different $\mathcal{Z}_{st}$ values.

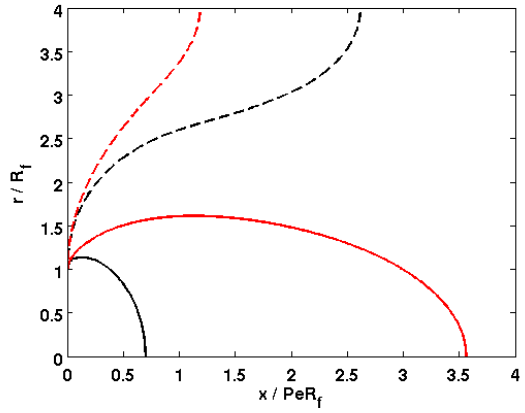

Figure 4.9. Steady flame position for representative over-ventilated, $\mathcal{Z}_{st}$ =0.3 (solid lines), and under-ventilated, $\mathcal{Z}_{st}$ =0.05 (dashed lines) for two-dimensional (red) and three-dimensional (black) non-premixed flames for parameters *Pe*=10, and, *s*=0.25.

These results make sense when we think about these two systems from a physical point of view. The two-dimensional system has a quantity of fuel proportional to $2R_f$ entering the domain, and two potential directions of diffusion thereafter (no axial diffusion case), while the three-dimensional system has a quantity of fuel proportional to πR_f^2 entering with 2π radian potential directions of diffusion. Expanding upon this, Figure

4.10 shows the corresponding flame length and width (maximum) for the same over- and under-ventilated flames considered in Figure 4.9, over a $\mathcal{Z}_{st}$ range. An additional s configuration is also shown, for a value of 0.1, hence the abrupt width cutoff at $1/s$.

However, it is difficult to draw general conclusions due to the additional dependence of these solutions upon s. The peaks in the flame lengths in Figure 4.10 result from the flame switching from over-ventilated, attaching at the centerline at y=0 (r=0), to under-ventilated, attaching at the wall at $y=R_w$ ($r= R_w$), as the $\mathcal{Z}_{st}$ value is reduced. The delineating mixture fraction value between these two flame configurations corresponds to the constant, non-spatially dependent term in each respective mixture fraction solution, i.e. $\mathcal{Z}=s$ and $\mathcal{Z}=s^2$ for the two-dimensional and three-dimensional solutions, respectively. At these delineating mixture fractions, the corresponding flames become infinitely long.

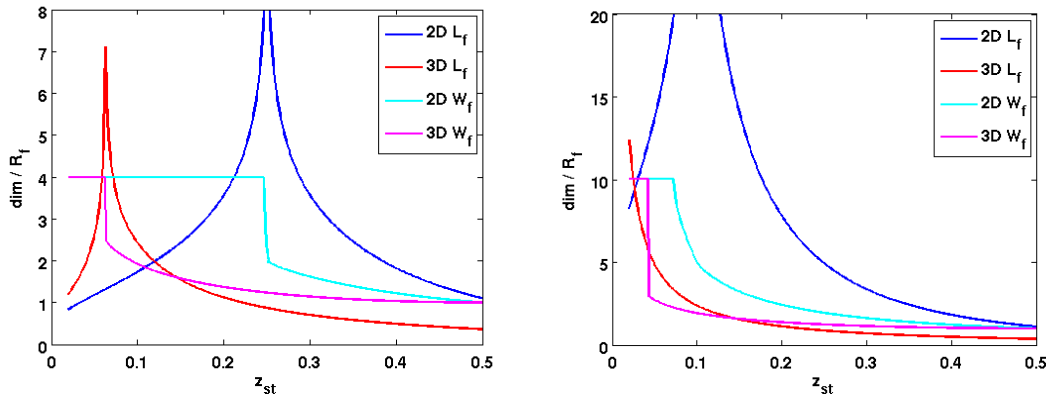

Figure 4.10. Steady flame length and width for representative two-dimensional and three-dimensional non-premixed flames for parameters *Pe*=10, *s*=0.25 (left) and *s*=0.1 (right).

4.2.3 Bulk Transverse Fluctuation Solutions

The next forcing configuration we consider is bulk transverse velocity fluctuations. In a polar coordinate system, this equates to radial and angular velocity fluctuations of the form:

$$u_{r,1} = \varepsilon U_0 \cos\theta \exp[-i\omega t] \qquad u_{\theta,1} = -\varepsilon U_0 \sin\theta \exp[-i\omega t] \qquad u_{x,1} = 0 \tag{4.20}$$

The general solution for the fluctuating mixture fraction field, subject to the flame attachment boundary condition at the fuel port lip is:

$$\mathcal{Z}_1(r,\theta,x,t) = \sum_{n=0}^{\infty} \frac{s^2 Pe\varepsilon J_1(r_n s)\exp[-i\omega t]}{-2\pi i Pe St J_0(r_n)^2} J_1\left(r_n s \frac{r}{R_f}\right) \exp\left(\frac{\mathcal{B}_-}{Pe}\frac{x}{R_f}\right) \left[\begin{array}{l} \frac{1}{(1-\sigma)}\exp(i\theta)\left\{1-\exp\left[\frac{\{\mathcal{B}_{h-}-\mathcal{B}_-\}}{Pe}\frac{x}{R_f}\right]\right\}+ \\ \frac{1}{(1+\sigma)}\exp(-i\theta)\left\{1-\exp\left[\frac{\{\mathcal{B}_{h+}-\mathcal{B}_-\}}{Pe}\frac{x}{R_f}\right]\right\} \end{array}\right] \tag{4.21}$$

where:

$$\mathcal{B}_{h\pm} = \frac{Pe^2 - \sqrt{Pe^4 + 4Pe^2(r_n s)^2 - 8\pi i Pe^3 St(1\pm\sigma)}}{2} \tag{4.22}$$

Following the same procedure as for the axial bulk case, we obtain an explicit expression for fluctuating flame position for the general and O(1/*Pe*), *Pe*>>1 expansion, respectively:

$$\frac{\xi_{1,n}(\theta,x,t)}{R_f} = \sum_{n=0}^{\infty} \frac{i\varepsilon\exp[-i\omega t]}{4\pi St}\left[\frac{\partial \mathcal{Z}_{0,n}/\partial r}{|\nabla \mathcal{Z}_0|_{(r=\xi_0(x),x)}}\right] \left[\begin{array}{l} \frac{\exp(i\theta)}{(1-\sigma)}\left\{1-\exp\left[\frac{\{\mathcal{B}_{h-}-\mathcal{B}_-\}}{Pe}\frac{x}{R_f}\right]\right\}+ \\ \frac{\exp(-i\theta)}{(1+\sigma)}\left\{1-\exp\left[\frac{\{\mathcal{B}_{h+}-\mathcal{B}_-\}}{Pe}\frac{x}{R_f}\right]\right\} \end{array}\right] \tag{4.23}$$

$$Pe>>1 \quad \frac{\xi_{1,n}(\theta,x,t)}{R_f} = \frac{i\varepsilon\exp[-i\omega t]}{4\pi St}\cos\psi_0(x) \left[\begin{array}{l} \frac{\exp(i\theta)}{(1-\sigma)}\left\{1-\exp\left[2\pi i St(1-\sigma)\frac{x}{R_f}\right]\exp\left[-\frac{4\pi^2 St^2(1-\sigma)^2}{Pe}\frac{x}{R_f}\right]\right\}+ \\ \frac{\exp(-i\theta)}{(1+\sigma)}\left\{1-\exp\left[2\pi i St(1+\sigma)\frac{x}{R_f}\right]\exp\left[-\frac{4\pi^2 St^2(1+\sigma)^2}{Pe}\frac{x}{R_f}\right]\right\} \end{array}\right] + O\left(\frac{1}{Pe^2}\right) \tag{4.24}$$

This solution has similar low-pass filter and mean flame angle axial dependence, now a $\cos\psi_0(x)$ term, as the axial bulk forced solution, and is identical to that previously obtained for a two-dimensional flame (although ψ_0(x) has a different functional dependence on *x*), *only* for the case where σ = 0. The controlling nature of velocity fluctuations normal to the flame sheet is also seen by the additional $\exp(\pm i\theta)/(1\mp\sigma)$ terms, which now accounts for direct versus glancing forcing angles. For the no-swirl case, this term demonstrates how maximum and null responses in the flame space-time dynamics are separated by 90^o in the azimuthal direction. However, in the presence of swirl, there are no azimuthal locations at which the flame is unwrinkled, due to simultaneous azimuthal and axial propagation of wrinkles by the flow. Swirl acts to azimuthally carry wrinkles around the flame to other θ angles, contributing to the imperfect nature of the spatial interference at a given angle, thus eliminating previously existing spatial nodes due to azimuthal convection.

Similar to premixed flames [114], the axial phase speed at a fixed azimuthal location can even become negative for high swirl numbers. Since we are considering azimuthal slices through the flame, it is important to note that the flame wrinkles are not actually moving backward, but rather they are moving along the characteristic curve – this will become evident when we consider a phase result for a convecting helical disturbance in the next section. Figure 4.11 shows an example image of this "slicing" as a way to visualize a three-dimensional system in two-dimensions.

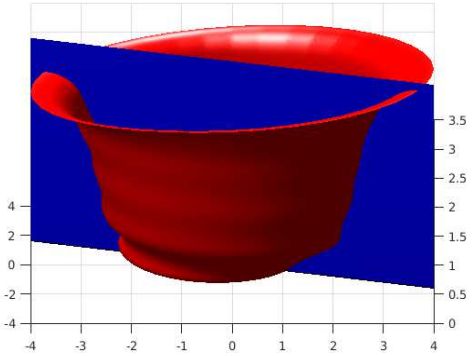

Figure 4.11. Example image of slicing plane used to visualize the three-dimensional system in two-dimensions.

Figure 4.12 shows illustrative solutions of the flame wrinkle magnitude for a case with and without swirling flow, at two perpendicular cut angles. The transverse forcing hits the θ=0 and θ=π/2 cuts at normal and grazing angles, respectively. The spatial variation in the amplitude, resulting from the flame angle term, as well as the spatial interference effect, can once again be seen, as well as the influence of the azimuthal convection of wrinkles.

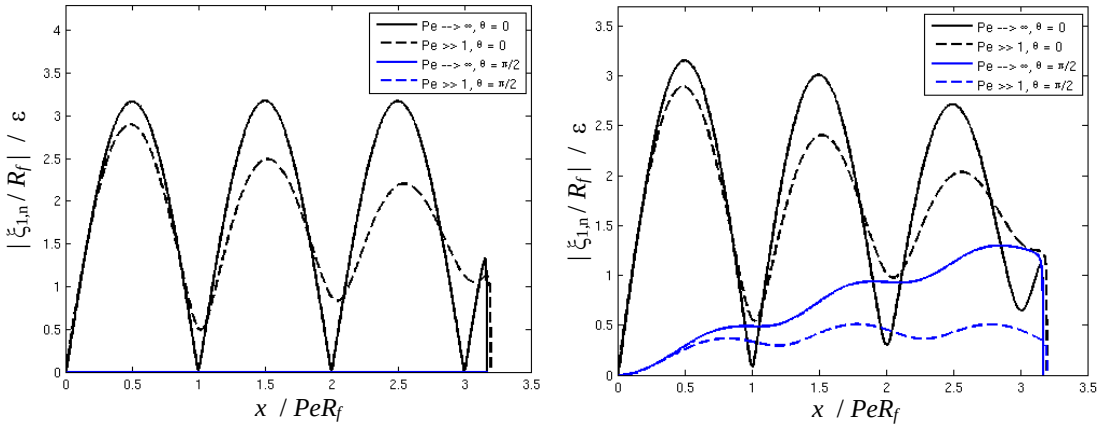

Figure 4.12. Wrinkle amplitude of two perpendicular azimuthal cuts (0 and π/2 radians) for the transverse bulk forced case for dimensionless swirl values of σ = 0 (left) and 0.05 (right) and parameters *Pe*=10, *St*=0.1, ε=0.01, *s*=0.25, and $\mathcal{Z}_{st}$ =0.055.

4.2.4 Convecting Helical Disturbance Solutions

The last forcing configuration we consider is a convecting helical disturbance of the form:

$$u_{r,1} = 0 \qquad u_{\theta,1} = 0 \qquad u_{x,1} = \varepsilon U_0 \exp\left[-i\omega t + ikx + im\theta\right] \tag{4.25}$$

where $k=\omega/U_c$ is the helical convective disturbance velocity, $k_c=U_c/U_0$ is the phase speed of the disturbance normalized by the axial flow velocity, and m is the helical mode number. Note that m=0 is the axisymmetric mode, whereas $m > 0$ and < 0 denote the co-swirling and counter-swirling modes, respectively. In both non-premixed and premixed flames, it is well known that important interference effects control the axial flame wrinkling character, as vortices disturbing the flame, and the flame wrinkles excited by these convecting vortices, do not generally travel at the same speed.

The full mixture fraction solution for this problem is quite complex. However, if we assume that radial and axial diffusion terms are much larger than the azimuthal diffusion term (an approximation which holds true in many circumstances, see Appendix C), we can neglect the azimuthal diffusion term in Eq.(4.14), significantly simplifying the solution form, making it analytically interpretable. The general solution for the fluctuating mixture fraction field, subject to the flame attachment boundary condition at the fuel port lip is:

$$\mathcal{Z}_1(r,\theta,x,t) = \sum_{n=0}^{\infty} \frac{-2\varepsilon \mathcal{B}_- s J_1(r_n s)\exp[im\theta]\exp[-i\omega t] J_0\left(r_n s \frac{r}{R_f}\right)\exp\left(\frac{\mathcal{B}_-}{Pe}\frac{x}{R_f}\right)}{J_0(r_n)^2 r_n\left(-2\pi i Pe St\left(1-\sigma m - \frac{\sqrt{Pe^4+4Pe^2(r_n s)^2}}{k_c Pe^2}\right)+\left(\frac{2\pi St}{k_c}\right)^2\right)}\left\{\exp\left[\frac{2\pi i St}{k_c}\frac{x}{R_f}\right]-\exp\left[\frac{\{\mathcal{B}_{hm}-\mathcal{B}_-\}}{Pe}\frac{x}{R_f}\right]\right\} \tag{4.26}$$

where:

$$\mathcal{B}_{hm} = \frac{Pe^2 - \sqrt{Pe^4 + 4Pe^2(r_n s)^2 - 8\pi i Pe^3 St(1-\sigma m)}}{2} \tag{4.27}$$

with the explicit expression for fluctuating flame position for the general and O(1/*Pe*), *Pe*>>1 expansion given by, respectively:

$$\frac{\xi_{1,n}(\theta,x,t)}{R_f}=\sum_{n=0}^{\infty}\frac{\varepsilon\exp[im\theta]\exp[-i\omega t]}{\left(-2\pi iSt\left(1-\sigma m-\frac{\sqrt{Pe^4+4Pe^2(r_n s)^2}}{k_c Pe^2}\right)+\frac{(2\pi St)^2}{k_c^2 Pe}\right)}\left[\frac{\partial Z_{0,n}/\partial x}{|\nabla Z_0|_{(r=\xi_0(x),x)}}\right]\left\{\exp\left[\frac{2\pi iSt}{k_c}\frac{x}{R_f}\right]-\exp\left[\frac{\{\mathcal{B}_{hm}-\mathcal{B}_{-}\}}{Pe}\frac{x}{R_f}\right]\right\} \quad (4.28)$$

Pe>>1 $$\frac{\xi_{1,n}(\theta,x,t)}{R_f}=\sum_{n=0}^{\infty}\frac{-\varepsilon\exp[im\theta]\exp[-i\omega t]}{2\pi iSt\chi-\frac{4\pi^2St^2}{k_c^2 Pe}}\sin\psi_0(x)\exp\left[\frac{2\pi iSt}{k_c}\frac{x}{R_f}\right]\left\{1-\exp\left[2\pi iSt\chi\frac{x}{R_f}\right]\exp\left[-\frac{4\pi^2St^2(1-m\sigma)^2}{Pe}\frac{x}{R_f}\right]\right\}+O\left(\frac{1}{Pe^2}\right) \quad (4.29)$$

where

$$\chi=1-m\sigma-1/k_c \quad (4.30)$$

This solution has similar low-pass filter and mean flame angle axial dependence as the previous bulk forced solutions, however, the leading wrinkle magnitude and waveform terms are more complicated due to the convective nature of the disturbance and the parameter χ. To leading order in *Pe*, the denominator shows how the complex interaction of swirl strength, helical mode, and disturbance phase speed act to alter the flame wrinkle magnitude, an interaction which produces a maximum in local spatial response for $\chi=0$, or corresponding mode number given by:

$$m_s\sigma=1-1/k_c \quad (4.31)$$

Similar criterion holds for premixed flames, and corresponds to the case where the azimuthal forcing exactly mirrors the wrinkle convection, so that no destructive interference occurs; rather they constructively superpose to cause the magnitude of flame wrinkling to grow monotonically with downstream distance. It is also important and significant to point out that for this axisymmetric mean flow, helical modes in the flow excite a corresponding helical motion in the flame response.

The two new additional parameters which emerge as significant controllers of flame wrinkle dynamics are k_c and σm, the latter of which is always grouped, indicating that swirl only influences the flame response through helical modes. Both of these alter the wrinkle interference pattern as well as the flames relative sensitivity to various co- and counter-rotating helical modes, an effect which can be more easily observed by rewriting Eq.(4.30) as, $\chi = \sigma(m_s - m)$. To leading order in *Pe*, mode numbers closer to the value m_s produce a lower value of χ and hence a higher flame motion response amplitude, and vica versa. In full, this response magnitude is a rich non-monotonic function of these controlling parameters.

An additional important point is that to leading order in *Pe*, the wrinkle magnitude is independent of the sign of χ, whereas this is important for the phase of the flame response. At a given azimuthal location, the axial phase varies linearly with downstream distance with a slope given by $\pi St(\chi - 2/k_c)$. Thus for the delineating case of $\chi = 2/k_c$, the flame response fluctuations at all axial locations, for a given azimuthal location, are in phase with each other. When $\chi > 2/k_c$, the phase rolloff is positive, indicating an apparent negative phase speed, as discussed previously.

These points are slightly modified if order 1/*Pe* terms are included, due to the additional term in the denominator of the magnitude term, and as a result, the traveling nature of the disturbance acts to alter the wrinkle magnitude and phase rolloff. In addition, the O(1/*Pe*) waveform term $(1-\sigma m)^2$ acts to alter the dissipation term non-monotonically, leading to minimum wrinkle dissipation when $\sigma m = 1$. These features can be seen in Figure 4.13 which shows illustrative solutions of the flame wrinkle magnitude

and phase for various values of χ for a near-bulk (k_c=20) and convecting disturbance (k_c=3.33) case.

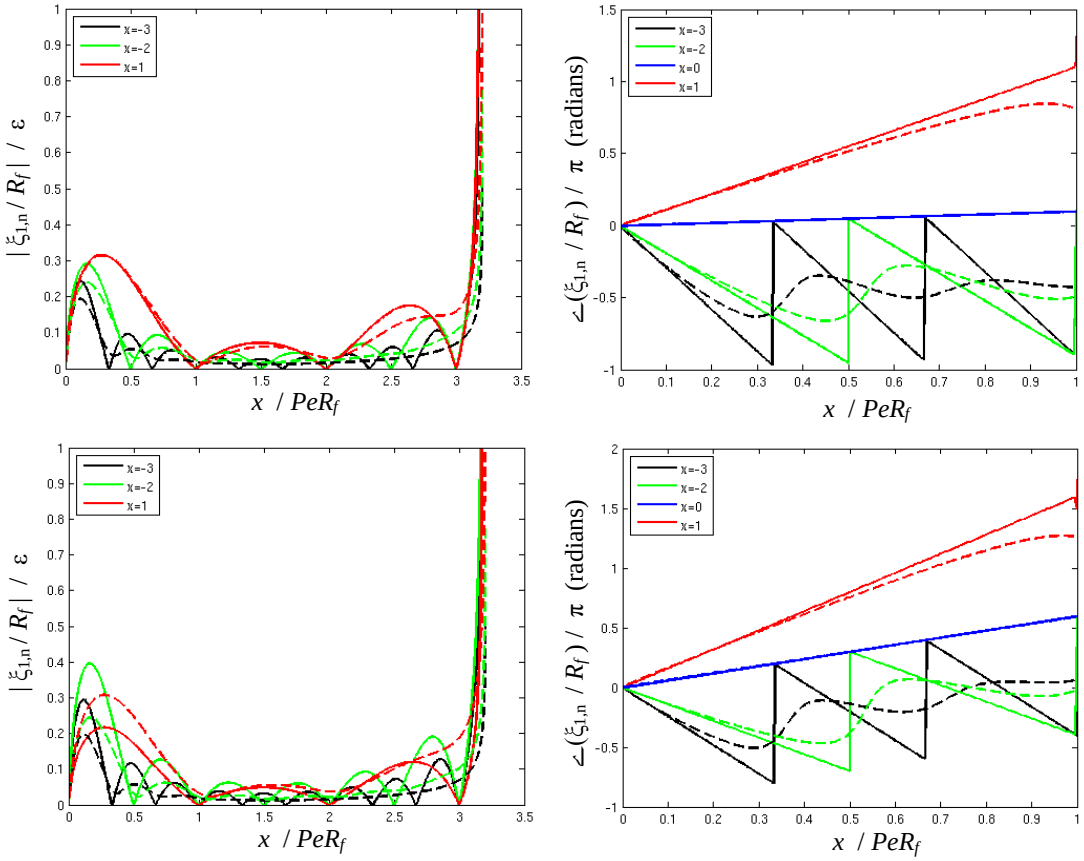

Figure 4.13. Wrinkle amplitude (left) and phase (right) for axial convecting helical disturbances case for various χ values and k_c=20 (top) and k_c=3.33 (bottom), and parameters *Pe*=10, *St*=0.1, ε=0.01, *s*=0.25, and $\mathcal{Z}_{st}$ =0.055.

Additionally, Figure 4.14 shows a surface plot of the flame response magnitude versus a parametric sweep over k_c and σ for both the first axial wrinkle, as well as the largest wrinkle on the flame sheet. The maximum in local spatial response for $\chi = 0$, is clearly evident from the red dotted line. Notice how along this ridge the wrinkle magnitude blows up.

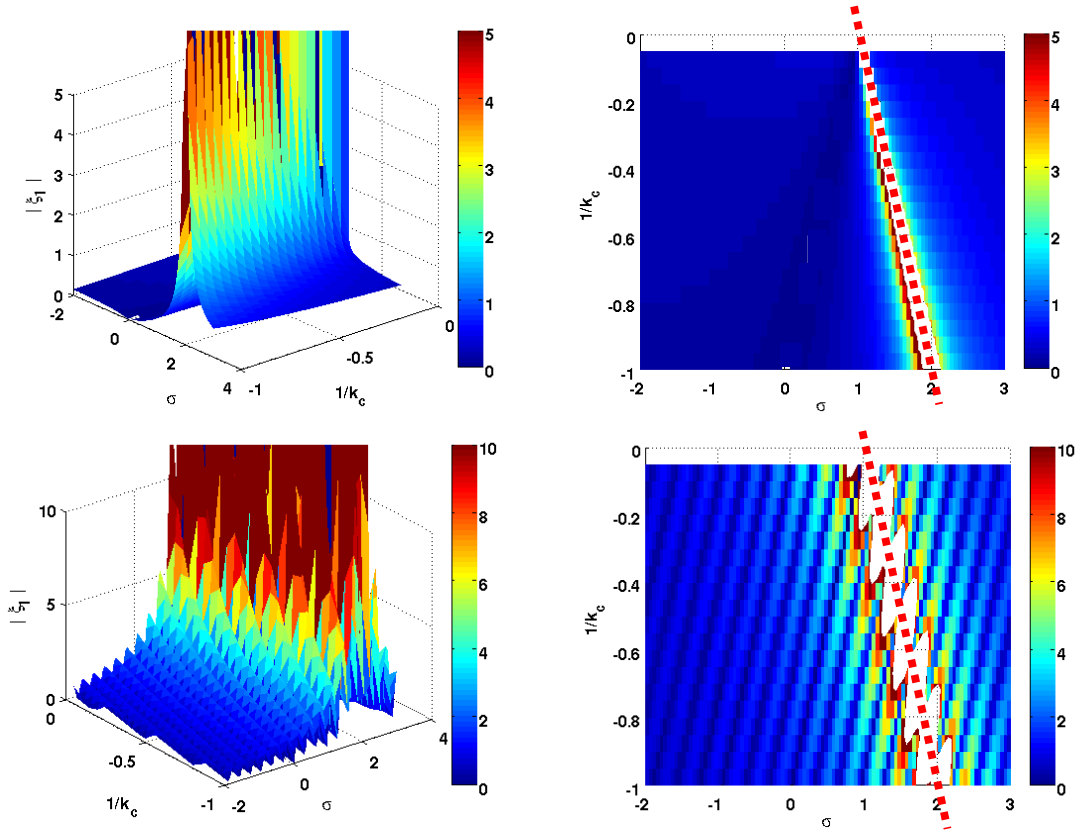

Figure 4.14. Isometric (left column) and birds-eye (right column) view of the first axial (top row) and largest overall (bottom row) wrinkle along the flame sheet, for a parametric sweep over k_c and σ for axial convecting helical disturbance parameters *Pe*=10, *St*=0.1, ε=0.01, *s*=0.25, and $\mathcal{Z}_{st}$ =0.055. The red dotted line shows Eq.(4.31), where χ=0 and thus the response is unbounded.

4.2.5 Premixed Flame Comparisons

It is useful to compare these results to those obtained for axisymmetric swirling premixed flames under similar forcing conditions. From the results of Acharya *et al.* [114, 124], flame wrinkle dynamical equations for the axial / transverse bulk and convecting helical disturbance cases can be obtained and compared to Eqs.(4.19), (4.24), and (4.29) in the $Pe \to \infty$ limit (since the premixed expressions do not include stretch effects, which was shown to relate to the inclusion of axial diffusion effects [67]). These expressions are almost identical in form to those for the non-premixed case, with a few subtle differences. First, the premixed flame angle term is independent of the axial

coordinate, owing to the flat nature of the steady state flame sheet, whereas for the non-premixed case this term is a complex function of *x*, *Pe*, $\mathcal{Z}_{st}$, and *s*. Second, the wrinkle convection parameter for the premixed case has an additional $\cos^2\psi$, due to the fact that premixed flames propagate normal to the flame surface, making their wrinkle phase speed the vector addition of the axial flow velocity and the burning velocity normal to the flame.

Although no stretch sensitive swirling premixed flame solutions exist, there is evidence showing that the disturbance decay rate is a function of the helical mode number, in addition to the forcing frequency [125], a result which Eq.(4.29) shows to be true for non-premixed flames.

4.2.6 Heat Release Discussion

By relating the fuel mass fraction and the mixture fraction gradients, the heat release, given by Eq.(2.40), can be analogously written for a three-dimensional system as:

$$\dot{Q}(t) = \int_{flame} \frac{(1+\varphi_{Ox})^2}{\varphi_{Ox}} \mathscr{D}\rho h_R \left[\frac{\partial \mathcal{Z}}{\partial x}\sin\psi - \frac{\partial \mathcal{Z}}{\partial r}\cos\theta \right] r dx d\theta \tag{4.32}$$

Notice there are no $\partial\mathcal{Z}/\partial\theta$ terms, since $\vec{e}_\theta$ is always perpendicular to $\vec{e}_n$. We will assume fixed composition fuel and oxidizer, so that the heat of reaction and mixture density are constant. The instantaneous global heat release of the non-premixed flame, given by Eq.(2.42), can be linearized and expanded to:

$$\frac{\varphi_{Ox}}{(1+\varphi_{Ox})^2\rho\mathscr{A}_R}\dot{Q}(t)=\int_0^{L_f(t)}\left[\underbrace{\frac{\partial Z_0(\xi_0,\theta,x)}{\partial x}\sin(\psi_0)\xi_0}_{\text{steady state}}+\xi_1(\theta,x,t)\frac{\partial^2 Z_0(\theta,x,\xi_0)}{\partial r\partial x}\sin(\psi_0)\xi_0+\right.$$
$$\left.+\frac{\partial Z_1(\xi_0,\theta,x)}{\partial x}\sin(\psi_0)\xi_0+\xi_1(\theta,x,t)\frac{\partial Z_0(\theta,x,\xi_0)}{\partial x}\sin(\psi_0)+\frac{\partial Z_0(\xi_0,\theta,x)}{\partial x}\cos(\psi_0)\sin(\psi_1)\xi_0\right][dx_0d\theta_0]$$
$$-\int_0^{L_f(t)}\left[\underbrace{\frac{\partial Z_0(\xi_0,\theta,x)}{\partial r}\cos(\psi_0)\xi_0}_{\text{steady state}}+\xi_1(\theta,x,t)\frac{\partial^2 Z_0(\xi_0,\theta,x)}{\partial r^2}\cos(\psi_0)\xi_0+\right.$$
$$\left.+\frac{\partial Z_1(\xi_0,\theta,x)}{\partial r}\cos(\psi_0)\xi_0+\xi_1(\theta,x,t)\frac{\partial Z_0(\xi_0,\theta,x)}{\partial r}\cos(\psi_0)-\frac{\partial Z_0(\xi_0,\theta,x)}{\partial r}\sin(\psi_0)\sin(\psi_1)\xi_0\right][dx_0d\theta_0] \quad (4.33)$$

where the top and bottom set of brackets result from the inclusion of axial and radial diffusion respectively. Within each set of brackets, the first term on the top is the steady state heat release and the remaining terms are the contributions of area and mass burning rate oscillations to heat release fluctuations.

As swirl does not influence the axial bulk forced case, the flame transfer function for the three-dimensional case takes the same form as that for our previous two-dimensional analysis, i.e. Section 3.1.2, once again keeping in mind the flame angle term has a new axial dependence. For the transversely forced case, similarly to the two-dimensional case, heat release oscillations cancel each other on opposite sides of the flame, thus resulting in no unsteady heat release. This same cancellation occurs for the helical disturbance case for all mode numbers except m=0, which corresponds to the axially forced case! Thus, as is the case for premixed flames, the m=0 mode is the sole contributor to the heat release oscillations, with k_c being the only new parameter influencing the transfer functions. Figure 4.15 shows heat release transfer function magnitude and phase for various values of k_c. For slight changes, some trends can be observed, such as reducing the *St* dropoff, decreasing the phase rolloff, and modifying the oscillatory nature of the curves. For large modifications in k_c, this final effect is so dominant in further complicating the interference effect of the disturbance wrinkles, that no real trends can be observed.

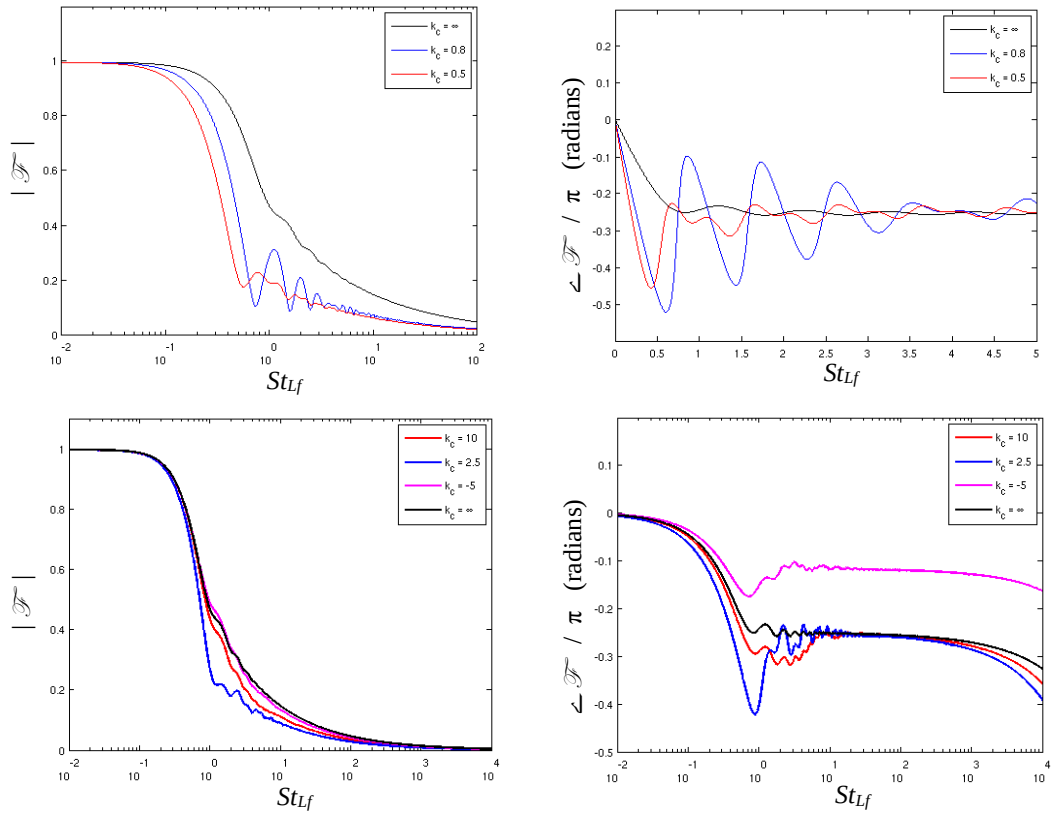

Figure 4.15. Convecting helical disturbance heat release transfer function magnitude (left) and phase (right) curves for various values of k_c and parameters Pe=100, ε=0.01, s=0.1, and $\mathcal{Z}_{st}$ =0.3. The axial bulk case corresponds to k_c=∞. Top row shows slight modifications, while bottom row shows significant modifications.

Recall from Section 4.2.4 that for a swirling flow, a non-axisymmetric mode, m_s, dominated the flame response amplitude. This is significant given the fact that only the axisymmetric mode, m=0, contributes to the global spatially integrated heat release fluctuations. Thus, different measures of the flame response, such as local wrinkling, local heat release, and global heat release, have very different sensitivities to swirl and different azimuthal modes. In fact, m and σ influence local heat release significantly, which is non-zero for various theta cuts, however cancelation on opposite sides of the flame produces no net global heat release fluctuations.

4.3 Finite Axial Diffusion Effects – Numerical Extended Inlet Study

The current work in this Chapter utilizes the same two-dimensional co-flowing fuel-oxidizer geometry, but relaxes the $Pe \rightarrow \infty$ assumption, made in Chapter 3, and discusses the implications that axial diffusion has on the mixture fraction field, space-time dynamics, and spatially integrated heat release. Sections 4.1 and 4.2 started this task by enabling axial diffusion in the governing $\mathcal{Z}$ -equation, and obtaining explicit dynamical equations for large, yet finite *Pe* values, i.e. $Pe >> 1$.

Several questions still remain about the flame position and heat release dynamics of finite Peclet number flames. In particular, axial diffusion effects manifest themselves in a variety of ways, not all of which have been captured in prior analyses. Most theoretical analyses of the problem impose inflow conditions on the mean and fluctuating conditions, even in studies that capture axial diffusion effects in the domain itself. For example, our earlier study in Section 4.1 that demonstrated how axial diffusion introduced damping of flame wrinkles utilized a prescribed step-inlet boundary condition. This simplification introduces a singularity in the solution, as there is an infinite gradient in mixture fraction at the fuel port lip. As we will show here, the high frequency characteristics of the heat release are quite sensitive to the inflow profile and the step-inflow boundary condition leads to incorrect conclusions on these asymptotic characteristics of the heat release transfer function, even in the $Pe >> 1$ limit. Stated differently, specifying an inflow step boundary conditions neglects axial diffusion effects in the region where these effects are most important – in the near-burner exit region where high transverse gradients and mass burning rates control the heat release dynamics. Thus, a key goal of the present investigation is to **completely and consistently** capture

finite *Pe* effects for the entire non-premixed flame system. This requires computational solutions of the governing equations, as explicit analytical solutions are not possible in this case.

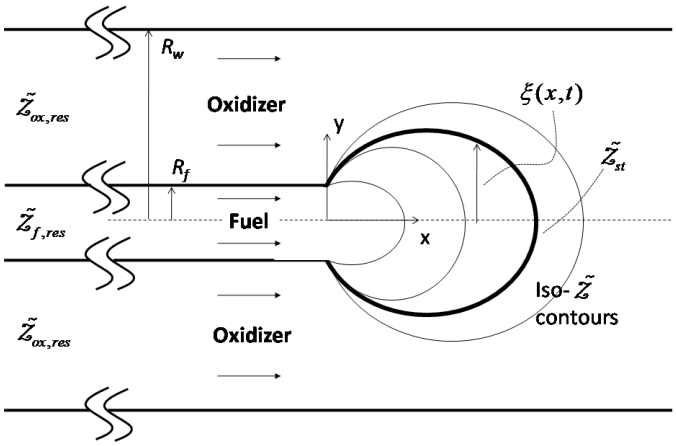

Figure 4.16. Illustration of the forced non-premixed flame model problem, referred to as the "extended inlet" geometry. The x<0 and x>0 domains are denoted the fuel/oxidizer ports and combustion region, respectively.

The new domain of interest is shown in Figure 4.16. Much like a real combustion system it is connected to two reservoirs, one fuel and one oxidizer, located at $x = -\infty$, where:

$$\mathcal{Z}^*(x=-\infty, y) = \begin{cases} \mathcal{Z}^*_{f,res} & 0 < |y| < R_f \\ \mathcal{Z}^*_{ox,res} & R_f < |y| < R_w \end{cases} \tag{4.34}$$

Previous theoretical analysis of the unsteady problem have *specified* the inflow conditions of fuel and oxidizer at x=0. However, to properly include and account for axial diffusion effects, and to properly describe the fuel/oxidizer gradients near the burner lip, we must include the x<0 fuel and oxidizer ports, since fuel can diffuse back into the oxidizer port and vice versa, altering the inlet profile. Thus we will solve the two-dimensional steady and fluctuating mixture fraction field equations, Eq.(3.3) and Eq.(3.4) respectively, utilizing the extended inlet geometry shown in Figure 4.16, subject to the

above boundary condition. In addition, no-penetration boundary conditions are applied at the side walls and fuel port walls as:

$$\frac{\partial \mathcal{Z}}{\partial y}(x, y = \pm R_w) = 0 \qquad \frac{\partial \mathcal{Z}}{\partial y}(x < 0, y = \pm R_f) = 0 \tag{4.35}$$

as well as ensuring finite mixture fraction values at large axial distances. For compactness, we explicitly define the following rescaled mixture fraction, now incorporating the reservoir rather than stream conditions, which too varies between zero and unity:

$$\mathcal{Z} = \frac{\mathcal{Z}^* - \mathcal{Z}^*_{ox,res}}{\mathcal{Z}^*_{f,res} - \mathcal{Z}^*_{ox,res}} \tag{4.36}$$

As mentioned, this problem is considered both analytically, where explicit solutions are possible in cases where the inflow boundary condition at $x = 0$ is specified, and computationally, for the general problem where the inflow conditions at $x = 0$ must be solved simultaneously with the rest of the domain of interest. As we will show next, explicitly specifying an inflow step boundary condition neglects axial diffusion effects in the region where they are most important, and imposes an artificial infinite transverse gradient in mixture fraction at the fuel port lip. Likewise, specifying a local diffusive flux boundary condition leads to a discontinuity in local mass flux between the fuel/oxidizer ports and combustion solution domains, both of whose effects will be discussed later.

The computational solutions are obtained with finite element methods, using the Comsol Multiphysics solver. The multi-frontal massively parallel sparse direct solver (MUMPS) was utilized with a convergence criterion set to 10^{-5} and relative tolerance of 0.001. This direct solver is based on LU decomposition and can take advantage of all processor cores for increased computational speed. In addition, a mapped rectangular

mesh was utilized with increasing resolution closer to the fuel port lip where high transverse gradients occur. The maximum element size, occurring near the exit plane was on the order of R_f, while the minimum element size, occurring near the fuel port lip, was on the order of $R_f / 10^3$. Dirichlet and Neumann boundary conditions were utilized at the inlet/outlet and at the port/walls, respectively.

4.3.1 Inflow and Inlet Conditions

This section considers system inflow and inlet conditions. Previous investigations into non-premixed flame dynamics were performed in the large *Pe* limit, although this assumption was not always explicitly stated. For example, most studies utilized a step inlet boundary condition for inflow mixture fraction at x=0. However, when we start considering finite/lower *Pe* value effects and, thus, axial diffusion effects, this inlet boundary condition, as well as simple rectangular domain of interest, becomes invalid due to time varying back diffusion of fuel into the oxidizer port and vice versa. Thus, now we further discuss the inflow conditions and their relation to the inlet (defined as the x=0 plane) conditions, denoted as:

$$\mathcal{Z}_0(x=0,y) = \mathcal{f}_0(y) \qquad \mathcal{Z}_1(x=0,y) = \mathcal{f}_1(y) \tag{4.37}$$

Standard solution techniques can be used to solve Eq.(3.3) and Eq.(3.4) for a given steady and fluctuating inflow profile, $\mathcal{f}_0(y)$ and $\mathcal{f}_1(y)$, respectively, for spatially uniform forcing. Once again, defining our forcing to be spatially uniform axial velocity fluctuations, represented by Eq.(3.7), and including axial diffusion in the governing equations by setting b=1, mixture fraction field solutions for the combustion region, i.e. $x > 0$ can be obtained:

$$\mathcal{Z}_0 = A_0 + \sum_{n=1}^{\infty} A_n \cos\left(\mathcal{A}_n \frac{y}{R_f}\right) \exp\left(\beta_- \frac{x}{PeR_f}\right) \tag{4.38}$$

$$\hat{\mathcal{Z}}_1 = \sum_{n=1}^{\infty} \frac{\varepsilon A_n \beta_-}{2\pi i PeSt} \cos\left(\mathcal{A}_n \frac{y}{R_f}\right) \exp\left[\beta_- \frac{x}{PeR_f}\right] + \sum_{n=1}^{\infty} B_n \cos\left(\mathcal{A}_n \frac{y}{R_f}\right) \exp\left[\beta_{h-} \frac{x}{PeR_f}\right] \tag{4.39}$$

where $\mathcal{A}_n$ are the eigenvalues previously defined in Section 3.1 ($\mathcal{A}_n = n\pi s$) and A_0, A_n, and, B_n are given by:

$$A_0 = \frac{1}{R_w} \int_0^{R_w} \mathcal{F}_0(y) dy \tag{4.40}$$

$$A_n = \frac{2}{R_w} \int_0^{R_w} \mathcal{F}_0(y) \cos\left(\mathcal{A}_n \frac{y}{R_f}\right) dy \qquad B_n = \frac{2}{R_w} \int_0^{R_w} \mathcal{F}_1(y) \cos\left(\mathcal{A}_n \frac{y}{R_f}\right) dy - \frac{\varepsilon A_n \beta_-}{2\pi i PeSt} \tag{4.41}$$

and the Strouhal number, defined by Eq.(2.27), parameters s, β_-, and β_{h-} are the same as from the bulk forced cases (Section 3.1 and Eq.(3.9)).

The b=0 solutions can be obtained by taking the $Pe \to \infty$ limit of these solutions. As noted above, most studies have previously considered the following inflow condition, generalized from previous sections, given by:

$$\mathcal{F}_0(y) = \begin{cases} 1 & 0 \le |y| < R_f \\ 0 & R_f \le |y| < R_w \end{cases} \tag{4.42}$$

$$\mathcal{F}_1(y) = \{0 \qquad \forall y \tag{4.43}$$

This boundary condition implies that $\mathcal{Z}_1(x=0, y) = 0$, eliminating the need for simultaneously solving for the port regions, i.e. $x < 0$. The steady state and fluctuating mixture fraction field solutions for this step inlet boundary condition were treated in previous sections. However, this boundary condition creates a non-physical infinite transverse gradient in mixture fraction at the fuel port lip, a singularity that dominates

certain solution characteristics such as the flame attachment and asymptotic heat release characteristics – a key motivator for this study. In reality, axial diffusion smoothes out this step boundary condition, as fuel diffuses upstream into the oxidizer "port" and vice versa. Thus, applying the inlet boundary condition, given by Eq.(4.42), to the geometry in Figure 4.16 implicitly neglects axial diffusion effects and, in reality, $\mathcal{f}_0(y)$ and $\mathcal{f}_1(y)$, cannot be imposed on the problem but must be solved as part of the problem.

Insight into the "correct and consistent" x=0 inlet condition can be obtained by integrating the $\mathcal{Z}$-equation, Eq.(2.7), from known values at the x=-∞ reservoirs to the inflow plane. This leads to the following expressions relating the values at the reservoir and inlet:

$$\int_{-\infty}^{0} \frac{\partial \mathcal{Z}}{\partial t} dx + \bar{u}_x \mathcal{Z}\big|_{x=0} = \bar{u}_x \mathcal{Z}\big|_{x=-\infty} + \mathscr{D} \int_{-\infty}^{0} \frac{\partial^2 \mathcal{Z}}{\partial y^2} dx + b\mathscr{D} \left.\frac{\partial \mathcal{Z}}{\partial x}\right|_{x=0} \tag{4.44}$$

where $\bar{u}_x$ is the instantaneous axial velocity. Note that, as the reservoirs are pure fuel and oxidizer respectively, $\partial \mathcal{Z} / \partial x(x = -\infty, y) = \mathcal{Z}_1(x = -\infty, y) = 0$. In addition, due to our no-flux boundary conditions at the solid duct walls, $\partial \mathcal{Z} / \partial y(-\infty < x < 0, y = R_f, R_w) = 0$. Utilizing these boundary conditions and expanding Eq.(4.44) into nominal and fluctuating values, leads to:

$$U_0 \mathcal{Z}_0\big|_{x=0} = U_0 \mathcal{Z}_0\big|_{x=-\infty} + \mathscr{D} \int_{-\infty}^{0} \frac{\partial^2 \mathcal{Z}_0}{\partial y^2} dx + b\mathscr{D} \left.\frac{\partial \mathcal{Z}_0}{\partial x}\right|_{x=0} \tag{4.45}$$

$$\int_{-\infty}^{0} \frac{\partial \mathcal{Z}_1}{\partial t} dx + U_0 \mathcal{Z}_1\big|_{x=0} + u_1 \mathcal{Z}_0\big|_{x=0} = u_1 \mathcal{Z}_0\big|_{x=-\infty} + \mathscr{D} \int_{-\infty}^{0} \frac{\partial^2 \mathcal{Z}_1}{\partial y^2} dx + b\mathscr{D} \left.\frac{\partial \mathcal{Z}_1}{\partial x}\right|_{x=0} \tag{4.46}$$

Note the existence of the second derivative term in y, on the right hand side of these equations. While this term is zero at the centerline (for symmetric axial forcing),

this transverse gradient will be quite high in some regions, particularly near the nozzle edges. We can also obtain a transversely averaged expression by integrating Eq.(4.45) transversely in the fuel and oxidizer domains, respectively, resulting in:

$$\frac{1}{R_f}\int_0^{R_f} \mathcal{Z}_0\big|_{x=0} dy - \int_0^{R_f}\left(\frac{1}{Pe}\int_{-\infty}^{0}\frac{\partial^2 \mathcal{Z}_0}{\partial y^2}dx\right)dy - \int_0^{R_f}\left(\frac{b}{Pe}\frac{\partial \mathcal{Z}_0}{\partial x}\bigg|_{x=0}\right)dy = \mathcal{Z}_{f,res} \qquad 0<|y|<R_f \tag{4.47}$$

$$\frac{1}{R_f}\int_{R_f}^{R_w} \mathcal{Z}_0\big|_{x=0} dy - \int_{R_f}^{R_w}\left(\frac{1}{Pe}\int_{-\infty}^{0}\frac{\partial^2 \mathcal{Z}_0}{\partial y^2}dx\right)dy - \int_{R_f}^{R_w}\left(\frac{b}{Pe}\frac{\partial \mathcal{Z}_0}{\partial x}\bigg|_{x=0}\right)dy = \mathcal{Z}_{ox,res}\frac{(R_w-R_f)}{R_f} \qquad R_f<|y|<R_w \tag{4.48}$$

Defining the transversely averaged mixture fractions with a superscript " * ", and taking advantage of our no-flux boundary conditions at the centerline and solid duct walls, $\partial \mathcal{Z} / \partial y(-\infty < x < 0, y = 0, R_f, R_w) = 0$, these expressions can be represented as:

$$\mathcal{Z}_0\big|_{x=0}^{\ *} - \frac{bR_f}{Pe}\left(\frac{\partial \mathcal{Z}_0}{\partial x}\bigg|_{x=0}\right)^{*} = \mathcal{Z}_{f,res} \qquad 0<|y|<R_f \tag{4.49}$$

$$\mathcal{Z}_0\big|_{x=0}^{\ *} - \frac{bR_f}{Pe}\left(\frac{\partial \mathcal{Z}_0}{\partial x}\bigg|_{x=0}\right)^{*} = \mathcal{Z}_{ox,res} \qquad R_f<|y|<R_w \tag{4.50}$$

This expression is identical to the inflow conditions used by Tyagi *et al.* [64] who utilized the following condition *locally*:

$$\mathcal{Z}_0\big|_{x=0} - \frac{R_f}{Pe}\frac{\partial \mathcal{Z}_0}{\partial x}\bigg|_{x=0} = \mathcal{Z}_{f,res} \qquad 0<|y|<R_f \tag{4.51}$$

$$\mathcal{Z}_0\big|_{x=0} - \frac{R_f}{Pe}\frac{\partial \mathcal{Z}_0}{\partial x}\bigg|_{x=0} = \mathcal{Z}_{ox,res} \qquad R_f<|y|<R_w \tag{4.52}$$

Physically, these latter two expressions state that the instantaneous mass flux associated with both convection and diffusion at the inlet equals the value at the reservoir, ***locally*** (i.e., at every *y* station). Comparing Tyagi *et al.*'s inflow conditions with Eq.(4.45) shows that they are correct as integral expressions, but not locally.

Transverse averaging allows for the elimination of the second derivative with respect to the y term by taking advantage of the no-flux boundary condition. Significantly, Eq.(4.49) and (4.50) are not recovered as leading order corrections to Eq.(4.47) and (4.48) with a formal asymptotic expansion of the boundary condition in Eq.(4.45) in powers of $1/Pe$, as is shown in Appendix D. Additionally, replacing Eq.(4.42) with Eqs.(4.51) and (4.52) as an inlet boundary condition and using it to solve for the mixture fraction field solutions in regions $x<0$ and $x>0$ leads to a discontinuity in local mass flux at $x=0$ at each y location. These solutions, along with accompanying discussion are provided in Appendix E.

In general, the distributions of $\mathscr{f}(y)$ must be determined computationally by simultaneously solving for the flow in the $x<0$ and $x>0$ domains. Figure 4.17 illustrates the results of such a computation for various values of Pe. Note that the inlet mixture fraction distribution tends to the step profile, given by Eq.(4.42) for $Pe>>1$, but $\mathscr{f}_0(y)$ is significantly smoothed in the y direction with decreasing Pe.

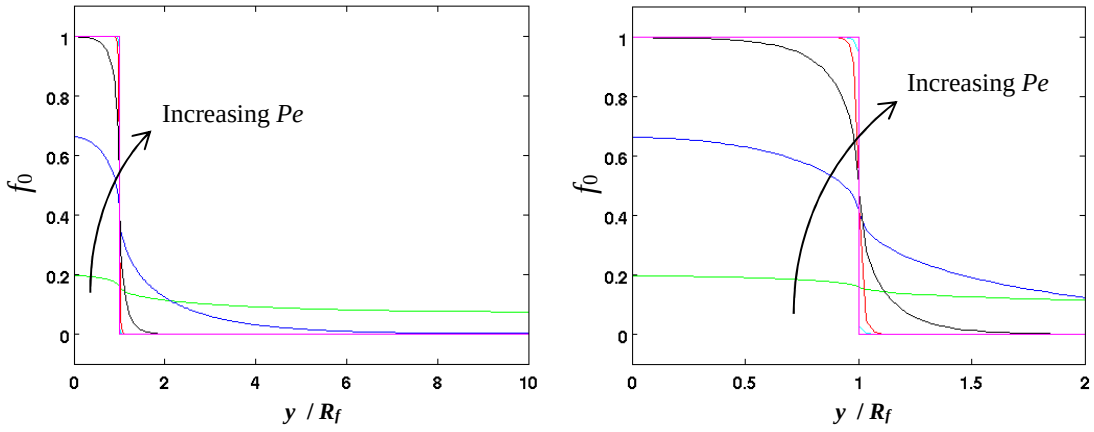

Figure 4.17. Computed steady state inlet mixture fraction profiles, $\mathscr{f}_0(y)$, as a function of Peclet value with axial diffusion effects, for a geometry defined by R_w/R_f = 10. Right image shows the same result, but focused on the y/R_f=1 region. Curves are shown for Pe values of 0.1, 1, 10, 100, 1000, and 10000 respectively.

4.3.2 Flame Attachment Point

This section considers the location of the flame at the burner and discusses the oscillatory attachment point induced by axial diffusion effects. The inclusion of axial diffusion influences the instantaneous flame attachment point, i.e. the location where the reaction sheet intersects with the fuel port wall. In the $Pe \to \infty$ limit, this location is stationary and always at the fuel port lip, $x=0$ and $y=R_f$, valid for all values of Pe and $\mathcal{Z}_{st}$, directly resulting from our inlet condition, i.e. $\mathcal{Z}_1(x=0,y,t)=0$. However, coupled axial and transverse diffusion effects move the flame attachment point away from the outlet and into the fuel or oxidizer ports (depending on $\mathcal{Z}_{st}$ and Pe values); i.e., into the $x<0$ domain. A detail of the unforced flame position near the burner exit is illustrated in Figure 4.18 for various values of $\mathcal{Z}_{st}$ and Pe. Notice how, for large Pe values, the attachment points for all the iso-contours are relatively close to the fuel port tip (all converging to a single point in the $Pe \to \infty$ limit). As Pe is decreased these positions move upstream, either into the fuel or oxidizer port depending upon $\mathcal{Z}_{st}$.

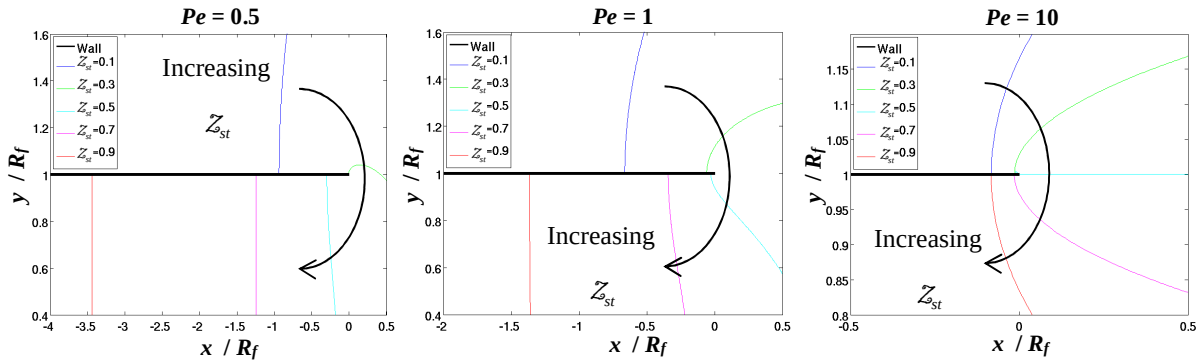

Figure 4.18. Steady state flame attachment point and near-wall position at several values of Pe and $\mathcal{Z}_{st}$. The curves shown are for $\mathcal{Z}_{st}$ values of 0.1, 0.3, 0.5, 0.7, and 0.9 respectively, where the arrow indicates the direction of increasing $\mathcal{Z}_{st}$. Note the unique x-axis for each figure.

Figure 4.19 shows a summary plot of the steady state attachment point vs $\mathcal{Z}_{st}$ for various *Pe* values. Positive values represent attachment locations inside the oxidizer port on the top side of the fuel port lip, whereas negative values represent attachment locations inside the fuel port on the bottom side of the fuel port lip. The large *Pe* values show near independence of attachment point on $\mathcal{Z}_{st}$, while the smaller values show large alterations in attachment point location with $\mathcal{Z}_{st}$. Additionally, it can be shown computationally that the $\mathcal{Z}_{st}$ value required for steady state flame attachment at the burner lip follows the trend:

$$\mathcal{Z}_{st}\Big|_{x_{\text{attach}}=0} = -\frac{R_f}{R_w} Pe^{-1} + 0.5 \tag{4.53}$$

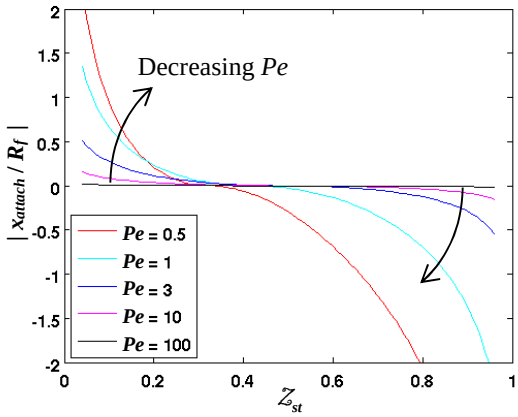

Figure 4.19. Steady state flame attachment point summary plot of x_{attach} / R_f (location where $x<0$ and $y=R_f$) vs $\mathcal{Z}_{st}$ for several different *Pe* values. The curves shown are for *Pe* values of 0.5, 1, 3, 10, and 100 respectively, where the arrows indicate the direction of decreasing *Pe*. Positive and negative values represent attachment locations inside the oxidizer port on the top side of the fuel port lip, and inside the fuel port on the bottom side of the fuel port lip, respectively.

In addition, the instantaneous attachment point moves over a forcing period, as shown in Figure 4.20. Notice how the magnitude of this axial motion depends upon the forcing frequency. This is due to the low-pass filter characteristic of the flame position, as the time derivative of the flame position is related to the local flow velocity through

Eq.(2.7). Figure 4.21 shows this more clearly through magnitude and phase plots of the instantaneous flame attachment point transfer function for various dimensionless frequency values. The transfer function, defined as (x_{attach}/R_f) / (u_1/U_0) quantifies the input-output relation between forcing and flame attachment point motion. In addition to the low pass filter characteristic, the increased motion at low *Pe* values as shown by the previous figures can also be seen. The $\mathcal{Z}_{st}$ value also has an influence upon the transfer functions, an effect which is coupled to *Pe*, whose degree can be deduced from Figure 4.19. For example, very low and very high $\mathcal{Z}_{st}$ values have larger transfer function amplitudes than intermediate values.

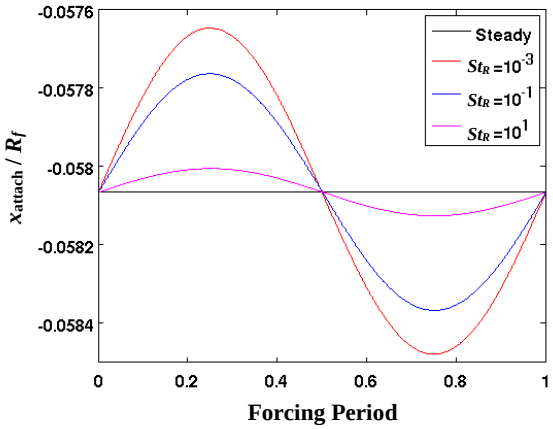

Figure 4.20. Instantaneous flame attachment point motion for *Pe* = 1, $\mathcal{Z}_{st}$ = 0.3, and ε = 0.01 for various St_R values.

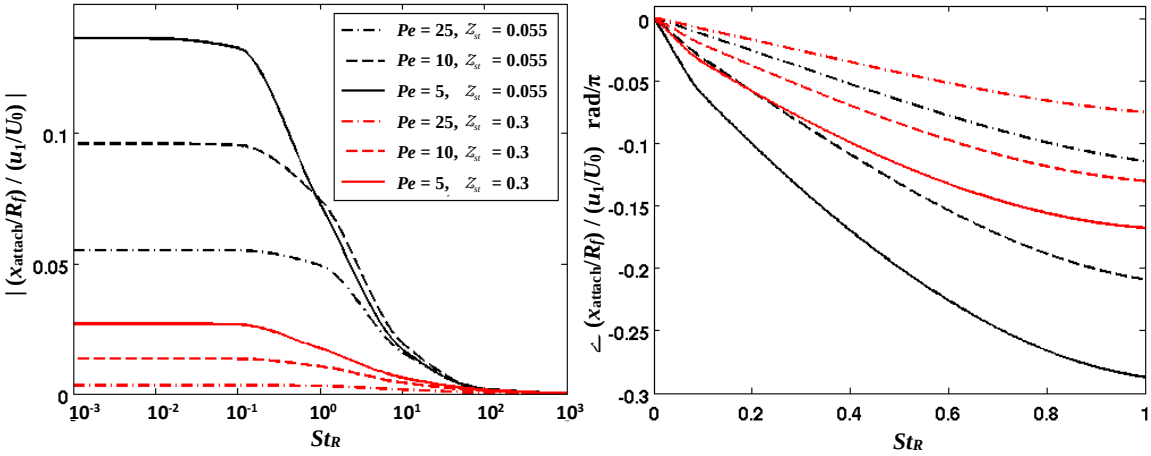

Figure 4.21. Magnitude (left) and phase (right) of the instantaneous attachment point transfer function.

4.3.3 Space-time Dynamics of the Reaction Sheet

As before, we are interested in the reaction sheet location, specifically the position of the fluctuating flame, which can be determined from the explicit expression given by Eq.(2.33) for many cases. Although no analytical expression for $\xi_{1,n}$ has been obtained for the extended inlet axial diffusion case, it can be extracted from the numerical solution results. Additionally, in order to aid in the interpretation of the computations, it is helpful to revisit the analytical solution obtained using the step inlet boundary condition, derived previously in Section 4.1, in the *Pe* >> 1 limit for axial bulk forcing, specifically Eq.(4.6).

The $Pe \to \infty$ analytical solutions, along with various extended inlet numerically computed results are shown in Figure 4.22, which depicts the axial dependence of the flame response magnitude for various forcing frequencies and *Pe* values. It can be seen from the plots that the results incorporating axial diffusion have many similarities, but clearly the node/anti-node behavior discussed above is smoothed out by the action of axial diffusion, as expected based upon the discussion in Section 4.1.1. This flame wrinkle smoothing leads to imperfect interference between the terms, as previously

mentioned, and abolishes previous spatiotemporal magnitude nodes. This effect becomes more pronounced at higher forcing frequencies, where more spatial wrinkles exist, and also at larger axial distances downstream. Note also that the magnitude of flame movement is nonzero at x=0 in the smaller Peclet number cases, as explained in Section 4.3.2.

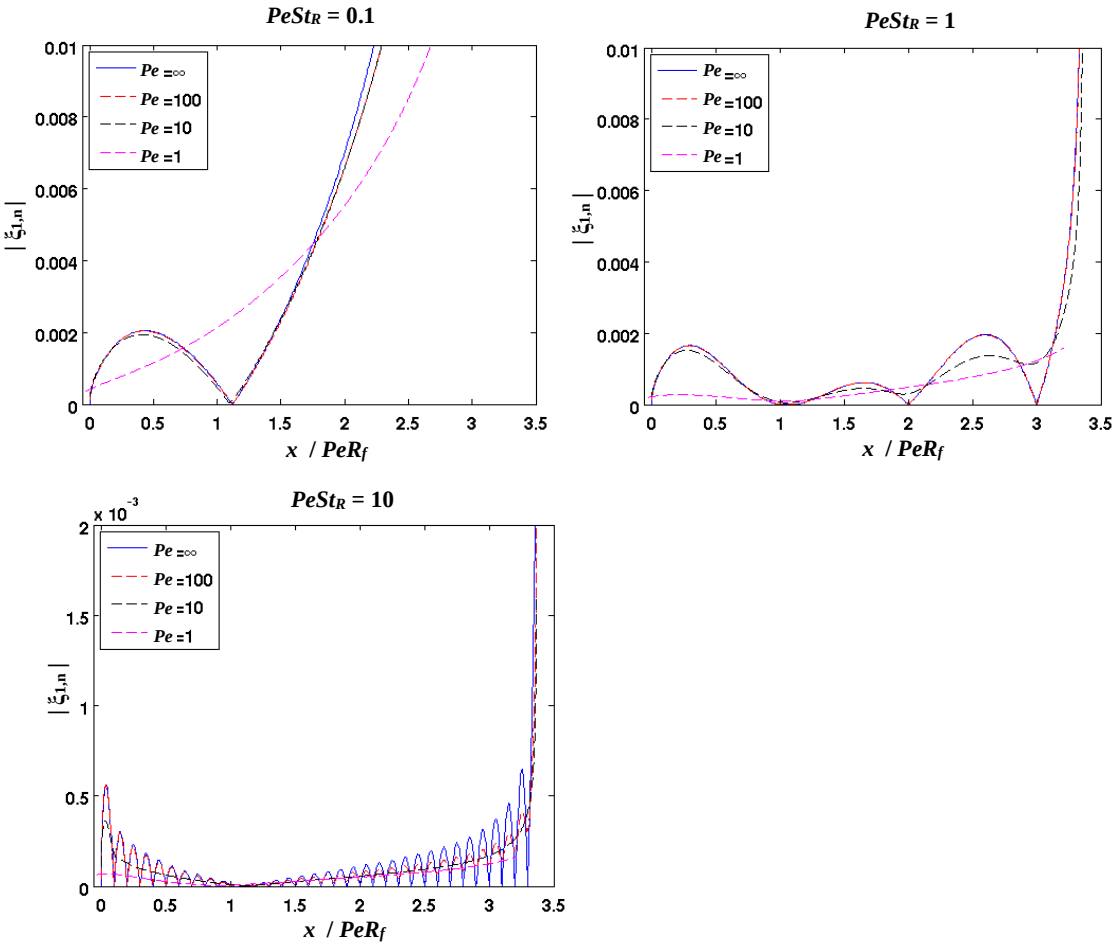

Figure 4.22. Axial dependence of the magnitude of flame response using nominal values of $\mathcal{Z}_{st}$ =0.3 for various degrees of axial diffusion for three forcing frequencies *PeSt*$_R$ = 0.1, 1.0, and 10.

4.3.4 Spatially Integrated Heat Release

Our previous investigations into non-premixed flame heat release dynamics have focused solely on the spatially integrated quantity, due to its utility for combustion instability or noise problems where the flame is small relative to the acoustic wavelength [4]. However, the heat release per unit area, $\dot{q}(\bar{x},t)$, is also an interesting quantity worth of some attention due to its relation to the heat release asymptotics (to be discussed in Chapter 5). Additionally, for axisymmetric single-valued flames, the heat release per unit area can be simplified and expressed as a function of only the axial coordinate, i.e. $\dot{q}(x,t)$. Its relation to the spatially integrated quantity is given by the following surface integral over the reaction sheet:

$$\dot{Q}(t) = \int_A \dot{q}(t)\, dA = \int_A \dot{m}_F'' \, \mathcal{h}_R \, dA \tag{4.54}$$

where as before $\dot{m}_F$" is the reactant mass burning rate per unit area, and $\mathcal{h}_R$ is the heat release per unit mass of reactant consumed. The next few sections analyze various important features of this equation. The distributions of the mean and fluctuating heat release will be investigated along with how they influence the heat release transfer function trends and asymptotics.

4.3.4.1 Distribution of the Mean and Fluctuating Heat Release

In two-dimensional premixed flames, the axial distribution of heat release does not vary strongly, as the mass burning rate per unit area is directly proportional to the laminar burning velocity, which is not usually a strong function of the axial position. For this reason, premixed flame heat release oscillations are closely correlated with oscillations in flame surface area. In contrast, the axial distribution of heat release in non-

premixed flames can vary by several orders of magnitude, as the strong transverse gradients that drive fuel/oxidizer flux near the burner outlet are smoothed with downstream distance. To illustrate, Figure 4.23 shows the steady state distribution of heat release per unit area, $q_0(x)$, along the flame sheet, for various *Pe* values. The cumulative heat release distribution, $q_{0,c}$, is also plotted, defined as:

$$q_{0,c}(x) = \frac{\int_0^x q_0(x)\,dx}{Q_0} \tag{4.55}$$

where Q_0 is the steady state heat release defined as:

$$Q_0 = \int_0^{L_{f,0}} q_0(x)\,dx \tag{4.56}$$

Also plotted for reference is the axial distribution for a constant burning velocity premixed flame, indicated by "PM Flame" in the legend. This abbreviation will be used throughout to denote the values for a corresponding premixed flame.

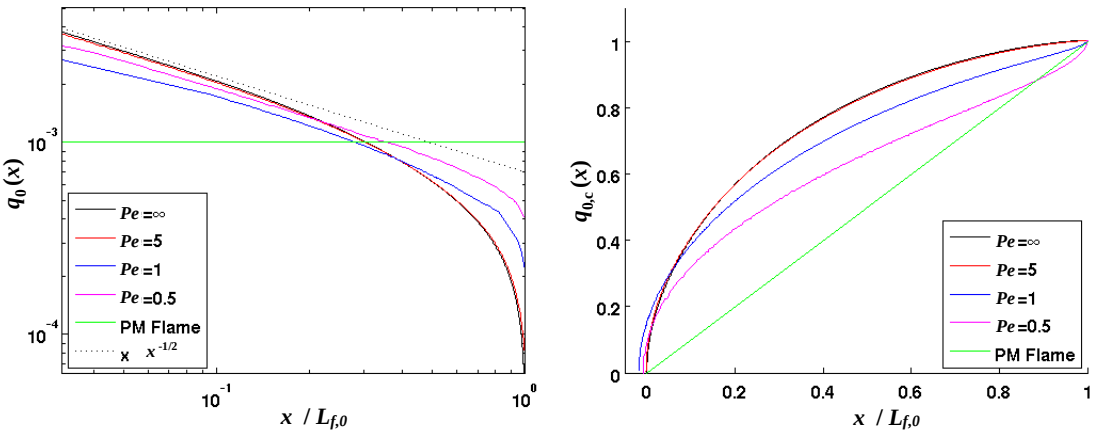

Figure 4.23. Axial dependence of steady state heat release, both distributed (left) and cumulative (right), for $\mathcal{Z}_{st}$ = 0.3 and various *Pe* values.

For the steady state distribution, the *Pe*→∞ limiting case has an integrable singularity at the inlet that can be shown analytically to scale as $\dot{m}_F'' \sim x^{-1/2}$, as also shown in Figure 4.23. With finite *Pe* values, the inlet profile is smoothed and the peak value at

x=0 is reduced. In addition, the heat release contribution from the tip increases with decreasing *Pe* value. Comparing and contrasting the premixed and non-premixed flame curves shows that half of the average heat release occurs in roughly the first 15-20% of the non-premixed flame, while it occurs at the 50% flame midpoint for the premixed flame. This result clearly shows the need for particular care in accounting for inflow conditions that influence the x/R_f<<1 region for non-premixed flame problems.

Figure 4.24 shows the corresponding unsteady heat release distribution, $\hat{q}_1(x)$, for various *Pe* and *St* values. The cumulative heat release distribution is plotted in Figure 4.25 with two different normalizations, defined as:

$$q_{1,c_1} = \frac{\int_0^x \hat{q}_1(x)\,dx}{\varepsilon Q_0} \qquad q_{1,c_2} = \frac{\int_0^x \hat{q}_1(x)\,dx}{\int_0^{L_{f,0}} \hat{q}_1(x)\,dx} \tag{4.57}$$

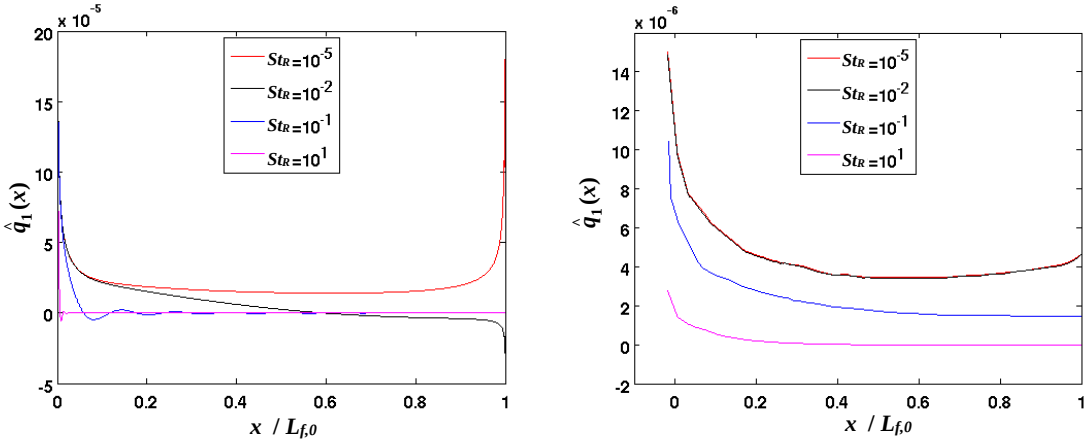

Figure 4.24. Axial dependence of fluctuating heat release distributions for *Pe* values of 25 (left) and 1 (right) and various values *St*.

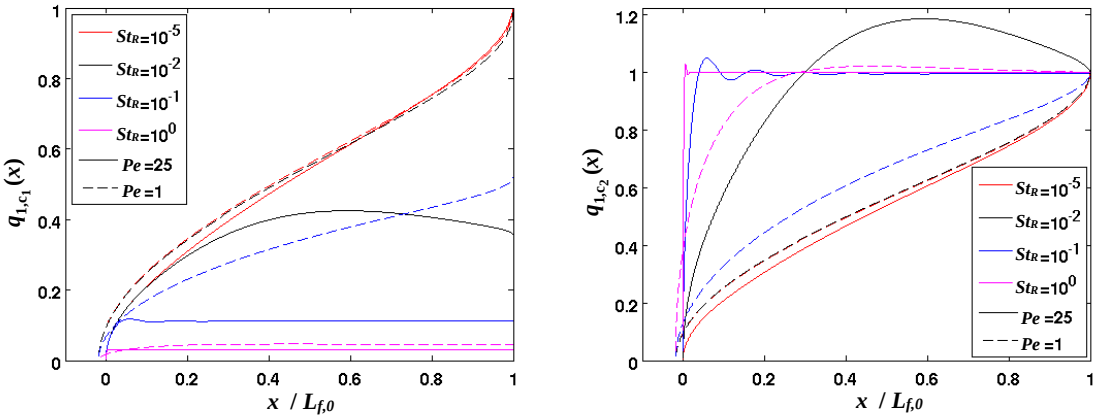

Figure 4.25. Axial dependence of fluctuating cumulative heat release distributions normalized by q_{1,c_1}(left) and q_{1,c_2} (right) for various values of *Pe* and *St.*

The first normalization definition, given by Eq.(4.57), uses the steady state heat release for normalization so that its value at $x/L_{f,0} = 1$ corresponds to the flame transfer function's value (discussed later). The second normalization uses the spatially integrated unsteady heat release, so that its value at $x/L_{f,0} = 1$ goes to unity, thus allowing one to visualize which parts of the flame contribute to its unsteady heat release. Figure 4.24 shows that, for $Pe >> 1$ and $St << 1$, the largest values of local fluctuating heat release occur at both the flame base, due to the sharp inlet gradient, and at the flame tip, due to the pulsing flame length. However, neither of these regions contributions to the cumulative heat release are dominant, as shown in Figure 4.25.

For $Pe >> 1$ and $St \sim O(1)$ or $>> 1$, the local heat release at the tip diminishes, and the largest local values occur at the flame base. Moreover, the cumulative distributions show that the majority of the unsteady heat release occurs at the flame base – a fact which enables the development of simple asymptotic expressions for the $St >> 1$ heat release, to be discussed in the next Chapter. The same *St* trends hold for lower finite *Pe*

values, yet the base and tip (for low *St* values), contributions are reduced and the middle length of flame has a larger contribution due to axial diffusion.

4.3.4.2 Heat Release TF – General Results

Having considered the spatial distributions of the heat release, we next consider its spatially integrated value and the flame transfer function, $\mathscr{F}$, previously defined by Eq.(3.28). Figure 4.26 plots the computed amplitude and phase of $\mathscr{F}$ as a function of *St* for various *Pe* values, utilizing Eq.(4.8), as well as the *Pe*→∞ result previously obtained, given by Eq.(3.58). For the amplitude, the most prominent difference between the results which include and neglect axial diffusion are the asymptotic characteristics; the *Pe*→∞ result having a two-zone structure, while the results with axial diffusion show a three zone asymptotic structure. These asymptotic roll off values, along with the transitional *St* values (some of which are dependent upon *Pe*) will be focused upon in Chapter 5. The phase plot also shows some differences between the results, although they all appear qualitatively similar.

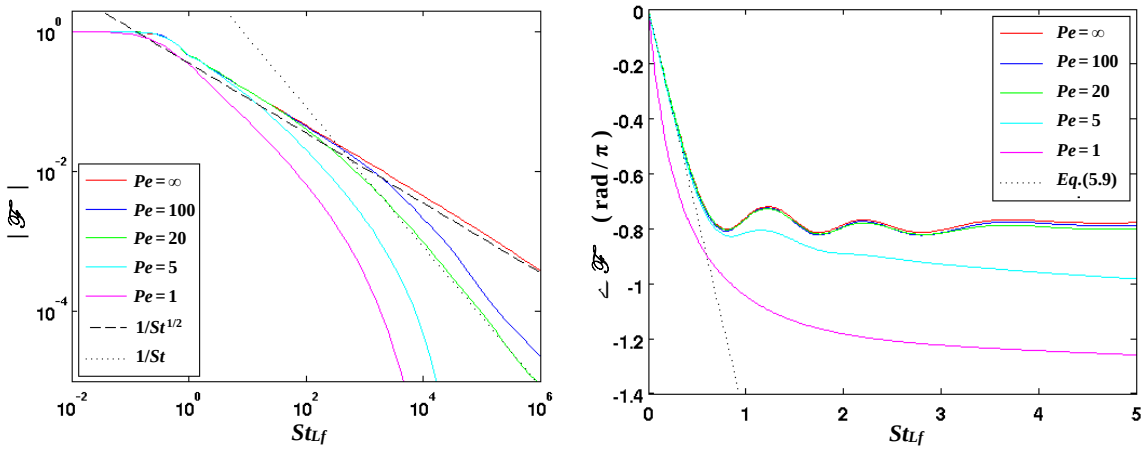

Figure 4.26. Heat release transfer function amplitude (left) and phase (right) as a function of St_{Lf} for $\mathcal{Z}_{st}$ = 0.3 for various *Pe* values.

Detailed discussions regarding the heat release asymptotic characteristics, and accompanying elucidating model problems, are left for Chapter 5. However, preliminary observation of the computed results show that three different *St* ranges exist, each with a well defined *St* roll off; transitioning from St^0 roll off, at low *St* values, to $1/(St^{1/2})$, for intermediate *St* values, to $1/St$, for high *St* values. Additionally, these transitional *St* values appear to have some functional dependence upon *Pe*.

4.4 Anisotropic Diffusion

This section considers the topic of anisotropic, i.e. preferential, diffusion, where the diffusion coefficient is the same for all species, enabling use of the mixture fraction formulation, however is anisotropic for each. Treating this as a mathematical exercise, we can return to Eq.(2.24) and define a $Pe_{x,y}$ and $Pe_{x,x}$ representing the different degrees of diffusion in the various directions. For compactness and since we only consider the case of axial flow, we will denote $Pe_{x,x} \equiv Pe_x$ and $Pe_{x,y} \equiv Pe_y$.

The resulting full solution (b=1) for the steady state mixture fraction field can be obtained by solving a modified form of Eq.(3.3) (one differentiating between $\mathscr{D}_x$ and $\mathscr{D}_y$), and utilizing Eqs.(3.2) and (3.1) as boundary and inlet conditions, respectively, and is given by:

$$\mathcal{Z}_0 = \frac{R_f}{R_w} + \sum_{n=1}^{\infty} \frac{2}{n\pi} \sin\left(\mathscr{A}_n\right) \cos\left(\mathscr{A}_n \frac{y}{R_f}\right) \exp\left(\frac{x}{Pe_y R_f} \beta_{xy-}\right) \tag{4.58}$$

where $\mathscr{A}_n = n\pi(R_f / R_w)$ and β_{xy-} is a modified form of Eq.(3.9), defined as:

$$\beta_{xy-} = \frac{Pe_y Pe_x - \sqrt{Pe_y^2 Pe_x^2 + 4Pe_y Pe_x \mathcal{A}_n^2}}{2}$$

$$\beta_{xy\,\mathrm{h}-} = \frac{Pe_y Pe_x - \sqrt{Pe_y^2 Pe_x^2 + 4Pe_y Pe_x \mathcal{A}_n^2 - 8\pi i Pe_x\, Pe_y^2 St}}{2} \tag{4.59}$$

Similarly, the resulting full solution for the fluctuating mixture fraction field, $\mathcal{Z}_1$, exposed to axial or transverse bulk forcing, is:

$$\mathcal{Z}_1 = \sum_{n=1}^{\infty}\left[\frac{2\varepsilon \sin(\mathcal{A}_n)}{n\pi i St_\omega}\right]\mathcal{M}_{xyn}\mathcal{G}(y)\exp\left(\frac{x}{Pe_y R_f}\beta_{xy-}\right)\left\{1-\exp\left(\left\{\beta_{xy\,\mathrm{h}-}-\beta_{xy-}\right\}\frac{x}{Pe_y R_f}\right)\right\}\exp[-i\omega t] \tag{4.60}$$

utilizing terms defined in Table 4.1 for each configuration.

Insight into the effects of anisotropic diffusion can be obtained by expanding these expressions around the $Pe_x, Pe_y \to \infty$ limit in inverse powers of *Pe*, as was done previously. Thus, the $\left(\beta_{xy\,\mathrm{h}-}-\beta_{xy-}\right)/Pe$ term can be expanded as:

$$\frac{\left\{\beta_{xy\,\mathrm{h}-}-\beta_{xy-}\right\}}{Pe_y} = \left\{iSt_\omega - \frac{St_\omega^2}{Pe_x} - \frac{2iSt_\omega^3}{Pe_x^2} - \frac{2iSt_\omega \mathcal{A}_n^2}{Pe_x Pe_y} + \mathrm{O}\left(Pe^{-3}\right)\right\} \tag{4.61}$$

Interestingly, an explicit equation for flame wrinkle dynamics can be expressed in the **exact** same form as Eq.(4.6), with different propagation, dissipation, and dispersion terms shown in Table 4.3. This table also shows the terms for the isotropic diffusion case, considered in Section 4.1.

Table 4.3. Preferential diffusion propagation, dissipation, and dispersion terms

	$Pe_x \neq Pe_y$	$Pe = Pe_x = Pe_y$
Propagation speed, U_c	$U_0 + O(1/Pe_x Pe_y)$	$U_0 + O(1/Pe^2)$
Dissipation, ζ	$\frac{St_\omega^2}{Pe_x}$	$\frac{St_\omega^2}{Pe}$
Dispersion, γ	$\frac{-2}{Pe_x^2}$	$\frac{-2}{Pe^2}$

Based on the discussion in Section 4.1, this result makes sense. It is the magnitude of the diffusion coefficient in the axial direction which controls the dominant features of the waveform term, i.e. wrinkle dissipation and dispersion as the wrinkles convect downstream. The transverse diffusion only coming into effect with the modification to the wrinkle convection term. However, the transverse diffusion magnitude dominates the flame angle term, governing the shape of the steady state flame, an effect which can be seen by expanding the β_{xy-} term around $Pe_x, Pe_y >> 1$ as:

$$\frac{\beta_{xy-}}{Pe_y} = \left\{ \frac{-\mathcal{A}_n^2}{Pe_y} + \frac{\mathcal{A}_n^4}{Pe_y^2 Pe_x} + \mathrm{O}\left(Pe^{-3}\right) \right\} \tag{4.62}$$

CHAPTER 5

Heat Release Asymptotics

This chapter describes numerical and theoretical analyses of the heat release dynamics and asymptotics of harmonically forced, non-premixed flames. A key objective of this work is to analyze and understand the interesting heat release transfer function results from the various studies in the previous Chapters. It was observed that some system/forcing configurations yielded rich complex heat release and transfer function results, dependent upon numerous dynamical parameters, while others yielded bland conclusions. The assumptions made during the analyses were also shown to influence the results. Solutions excluding axial diffusion, i.e. the $Pe \to \infty$ limiting results, showed a two-zone transfer function asymptotic structure, while the results with axial diffusion showed three zones. Additionally, whether axial diffusion was included in only the combustion domain, $Pe >> 1$ analytical results in Section 4.1, or in the fuel and oxidizer ports too, computational results in Section 4.3, impacted the zone transition *St* values. These asymptotic rolloff values, along with the transitional *St* values (some of which are dependent upon *Pe*) will be focused upon here. The relative contributions of the mass burning rate and area fluctuations to the overall unsteady heat release will also be investigated.

5.1 General Asymptotics

While we will discuss more advanced analytical and computed results later, it is useful to first set the stage by studying the solution characteristics in the $Pe \to \infty$ limit

where analytical progress is possible and the asymptotic structure lucid. As stated in Section 3.1.2, in this limit, two important simplifications can be made; first, only the $\partial \mathcal{Z} / \partial y \cos\theta$ terms remain in Eq.(3.22) and second, the weighted area contribution cancels out the first mass burning rate term, analytically shown by Eq.(3.30), resulting in Eq.(3.58).

By utilizing previous expressions for mixture fraction and fluctuating flame position for the spatially uniform forced case, this transfer function can be written as:

$$\mathcal{T}_N = \frac{\int_0^{L_{f,0-}^{+}} \left[\frac{-iR_f}{2\pi St} \right] g(x,\xi_0) \left\{ 1 - \exp\left(i 2\pi St \frac{x}{R_f} \right) \right\} dx}{\varepsilon \int_0^{L_{f,0-}^{+}} \frac{\partial \mathcal{Z}_0(x,\xi_0)}{\partial y} dx} \tag{5.1}$$

where $g(x,\xi_0)$ is an axial distribution function, which will be utilized extensively in the next sections, defined as:

$$g(x,\xi_0) = \tan(\theta_0) \frac{\partial^2 \mathcal{Z}_0(x,\xi_0)}{\partial y^2} + \frac{d^2 \mathcal{Z}_0(x,\xi_0)}{dxdy} \tag{5.2}$$

For transverse forcing, it was explicitly shown by Eq.(3.59) that the two mass burning rate contributions in $g(x,\xi_0)$, are of equal amplitude and are out of phase by 180 degrees for **all** *St* values, thus resulting in no unsteady heat release for *each flame branch*. As was discussed in Section 3.3, this result could be anticipated, at least in the low Strouhal number limit, as transverse forcing causes no fluctuation in fuel and oxidizer flow rate into the domain – thus, transverse fluctuations consequently lead to no heat release oscillations. A similar result, no unsteady global heat release, was also obtained for transversely forced premixed flames [114].

No such mutual cancelation occurs for the axial bulk forced configuration. Explicit expressions for $\dot{Q}$ cannot be developed in general, because only an implicit expression for the time average flame position, $\xi_0(x)$ and, consequently, $g(x,\xi_0)$, are available. However, approximate expressions can be developed in the high *Pe* limit, by taking advantage of the fact that $\mathcal{Z}_0(x)$ becomes nearly independent of *x* as the flame becomes infinitely flat and long (see Figure 3.11 and corresponding discussion), and thus the flame position can be approximated by $\xi_0(x) \sim R_f(1+O(1/Pe))$ except near the flame tip. However, near the tip the heat release is proportional to axial diffusive fluxes (because the flame is normal to the flow at this location), which also is of O(1/*Pe*). The solution obtained by applying these approximations to Eq.(5.2) is indicated in Figure 5.1.

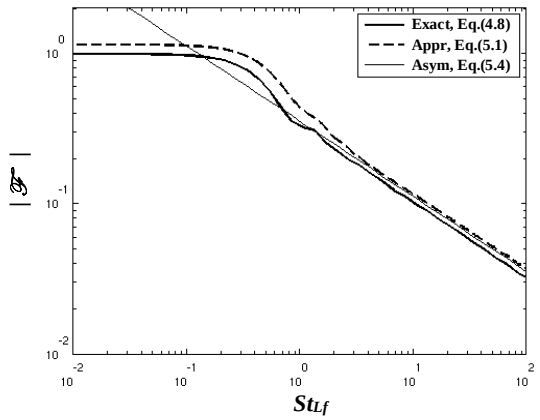

Figure 5.1. Axially forced heat release transfer function curves for the $Pe \to \infty$ (Eq.(4.8)) and approximate $\xi_0(x) = R_f$ (Eq.(5.1)) solutions, along with asymptotic expression plotted vs St_{L_f} for $\mathcal{Z}_{st} = 0.3$.

It can be seen, and will be proven in the upcoming sections, that the transfer function, $\mathcal{F}$, has a value of unity for low *St* values. Furthermore, it was shown in Section 4.3.4 that the high *St* limit of Eq.(5.1) is controlled by the features of $g(x,\xi_0)$ near $x = 0$, which to leading order is given by (a result derived in Appendix F):

$$g(x,\xi_0)=\frac{1}{4\sqrt{R\pi/Pe}\;x^{3/2}} \tag{5.3}$$

Substituting this expression into Eq.(5.1) reveals that in the limit of large *St* (also indicated in the figure):

$$\mathcal{F}\approx\frac{-(1+i)}{4\sqrt{St_{L_f}}} \tag{5.4}$$

Figure 5.1 presents illustrative exact (Eq.(4.8)), approximate (Eq.(5.1) where $\xi_0(x)=R_f$), and asymptotic (Eq.(5.4)) expressions for $\mathcal{F}$ at $Pe=100$ and $\mathcal{Z}_{st}=0.3$. $\mathcal{F}$ has a value of unity at low *St* values and rolls-off as $1/(St^{1/2})$ at high *St* values. The transition between these two zones can be observed to occur at $St_{L_f}\sim O(1)$.

Note that oscillatory integrals of the following form:

$$\int_{x_1}^{x_2} f(x)\exp(iStx)dx \tag{5.5}$$

are controlled by the values of the integrand at the boundary, i.e., at $f(x_1)$ and $f(x_2)$, and generally lead to a $1/St$ asymptotic behavior. However, the mass burning rate has an integrable singularity at the $x=0$ inlet boundary in the $Pe\to\infty$ limit due to the infinite transverse gradient in $\mathcal{Z}$ imposed by the step-inlet boundary condition, a singularity that ends up controlling the heat release asymptotics and leads to the indicated $1/(St^{1/2})$ behavior. When axial diffusion is included, this $1/(St^{1/2})$ behavior persists for a range of Strouhal numbers where the convective wrinkle wavelength is much longer than the thickness of the transition zone of fuel/oxidizer profiles at $x=0$. However, once the convective wavelength becomes of the order of this layer, the standard $1/St$ behavior should occur, as expected for oscillatory integrals. Thus, as will be derived in the

following sections, the Strouhal number at which the $1/St^{1/2}$ to $1/St$ transition occurs is a function of the thickness of this layer that, which in turn, is a function of *Pe*. As we have so far assumed a discontinuous profile at $x = 0$, no such $1/St$ behavior occurs at high *St* for Eq.(5.2), however. Significantly, the $1/(St^{1/2})$ behavior in the heat release transfer function is a much slower roll-off than the $1/St$ roll-off that occurs to leading order σ_C in premixed flames, causing the heat release response of non-premixed flames to exceed that of premixed flames at high Strouhal numbers for this problem.

As previously pointed out in Section 3.1.2, another significant difference between the transfer function of axial bulk forced premixed and non-premixed flames is the relative significance of area and mass burning rate terms. Premixed flames are dominated by area fluctuations, whereas non-premixed flames are mass burning rate fluctuation dominated; the ratio of these contributions will be analyzed further in the next section.

5.2 Heat Release TF - Low *St* Asymptotic Results

Expanding $\mathscr{T}$, as given by Eq.(5.1), in powers of St (see Appendix G), leads to:

$$St << 1 \qquad \mathscr{T} = 1 + iSt_{Lf} \frac{2\pi \int_0^{L_{f,0}} x \frac{\partial Z_0(x, \xi_0(x))}{\partial y} \cdot dx}{L_{f,0} \int_0^{L_{f,0}} \frac{\partial Z_0(x, \xi_0(x))}{\partial y} \cdot dx} + O(St_{Lf}^2) \tag{5.6}$$

Thus, $|\mathscr{T}| = 1 + O(St^2)$ for $St << 1$. This value of unity can be understood physically from the fact that in the quasi-steady limit, the instantaneous heat release is proportional to the instantaneous mass flow rate of fuel and oxidizer into the combustion domain, i.e. across the inlet plane; in other words, a 1% fluctuation in velocity induces a 1% fluctuation in heat release [4]. The low *St* phase behavior can also be extracted from this

expression, since $\angle\mathcal{F}$ = $\tan^{-1}(\mathrm{Im}(\mathcal{F})/\mathrm{Re}(\mathcal{F}))$. This can then be cast in terms of a n-τ model as [126]:

$$\mathcal{F} = \eta \exp\left[i\omega\tau\right] \tag{5.7}$$

or likewise, represented in the time domain as:

$$\frac{\dot{Q}_1}{\dot{Q}_0} = \eta \frac{u_1(t-\tau)}{U_0} \tag{5.8}$$

where the gain is unity, i.e. η =1, and the time delay is given by:

$$\tau = \left[\frac{\int_0^{L_{f,0}} x \frac{\partial \mathcal{Z}_0(x,\xi_0(x))}{\partial y} \cdot dx}{L_{f,0} \int_0^{L_{f,0}} \frac{\partial \mathcal{Z}_0(x,\xi_0(x))}{\partial y} \cdot dx} \right] \frac{L_{f,0}}{U_0} \tag{5.9}$$

This time delay is equivalent to replacing the distributed flame by a concentrated source at some fractional distance of the flame length. While the gain is straightforward, the time delay is a complex function of parameters such as *Pe* and $\mathcal{Z}_{st}$. These parametric dependencies of τ cannot be calculated analytically but must be extracted from the computations due to the implicit nature of the mean flame position, at which these integrand values are evaluated. This value (normalized by $L_{f,0}$ / U_0), for example, is around 0.2 for a methane-air, non-premixed system, which has a $\mathcal{Z}_{st}$ value of 0.055. For reference, the constant burning velocity two-dimensional bulk axially forced premixed flame result is $\tau/(L_{f,0}/U_0) \approx 0.5$ (assuming the flow velocity is much greater than the flame speed), showing that the non-premixed flame time delay is about a factor of two smaller than a premixed flame with the same length. This result directly follows from the heat release distributions shown in Figure 4.23. Figure 5.2 plots calculations of $\tau/(L_{f,0}/U_0)$ as a function of *Pe* for several $\mathcal{Z}_{st}$ values, representative of positive and

negative (nomenclature defined in Section 4.3.2) fuel port attachment location diffusion flame configurations. The corresponding premixed flame value is also plotted for reference. The solid lines indicate the numerical extended inlet results, while the dashed lines show the corresponding $Pe \to \infty$ analytical results, given by Eq.(5.9). The deviation of the asymptotic results from the computed ones for lower *Pe* values is due to both axial diffusion effects upon this effective time delay, but also reflects the importance of how flame length is defined; i.e., the flames base moves upstream into the fuel/oxidizer ports with decreasing *Pe*, see Figure 4.18, while $L_{f,0}$ used in the figure is defined as the distance of the flame tip from the burner outlet.

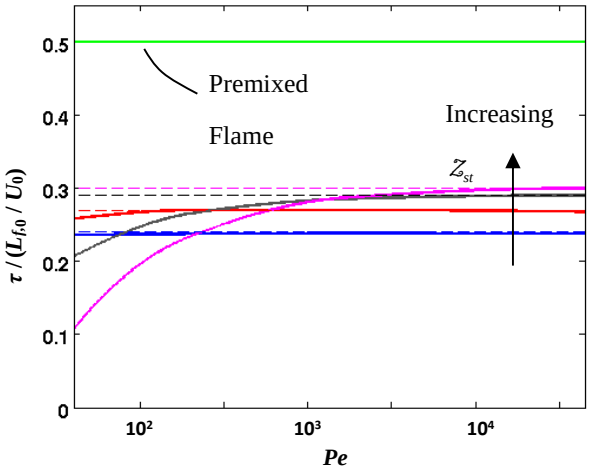

Figure 5.2. Normalized time delay parameter, $\tau / (L_{f,0} / U_0)$, shown as a function of *Pe* for various Z_{st} values (0.3, 0.6, 0.8, 0.9). The corresponding (based on geometry, assumptions, and configuration) premixed flame value is also displayed. For each Z_{st} value, the corresponding *Pe*→∞ solution is shown by a dashed line.

As noted in the context of Eq.(2.42), the heat release fluctuations can be decomposed into contributions associated with burning rate and flame area. However, non-premixed flame heat release oscillations are dominated by mass flux oscillations near the burner outlet, where these gradients are the sharpest. The flame surface area

oscillations have little influence on the overall heat release because the local burning rate is so low over most of the flame.

In the absence of axial diffusion, some analytical progress can be made about the ratio of these unsteady heat release contributions in the low *St* limit. The ratio of the mass burning rate, Eq.(3.29), and weighted area, Eq.(3.30), transfer functions is given by:

$$\frac{\mathcal{T}_{N,mbr}}{\mathcal{T}_{N,wa}} = \frac{\int_0^{L_{f,0}} \frac{\partial Z_1(x,\xi_0)}{\partial y} dx + \int_0^{L_{f,0}} \frac{\partial Z_0(x,\xi_0)}{\partial x} \sin(\theta_1) dx + \int_0^{L_{f,0}} \xi_1(x,t) \frac{\partial^2 Z_0(x,\xi_0)}{\partial y^2} dx}{\int_0^{L_{f,0}} \frac{\partial Z_0(x,\xi_0)}{\partial y} \cos(\theta_0) dA_1} \tag{5.10}$$

Utilizing the mixture fraction and fluctuating wrinkle explicit solutions given in Section 3.1, in the low *St* limit these terms scale as:

$$\frac{\mathcal{T}_{N,mbr}}{\mathcal{T}_{N,wa}} \sim \frac{\mathrm{O}(Pe) + \mathrm{O}(Pe^{-1}) + \mathrm{O}(Pe)}{\mathrm{O}(Pe^{-1})} \sim \mathrm{O}(Pe^2) \tag{5.11}$$

Thus, in the absence of axial diffusion, the ratio of mass burning rate to area contributions from the unsteady heat release is revealed to be of order O(Pe^2) in the low *St* limit. However, there is still a functional dependence of this ratio upon Z_{st}.

More generally, Figure 5.3 plots the ratio of the magnitudes of the spatially integrated mass burning rate and area terms, for a representative low *St* value, as a function of *Pe*, defined as:

$$Q_{MBR} = \int_0^{L_{f,0}} \hat{q}_{MBR}(x) dx \qquad Q_A = \int_0^{L_{f,0}} \hat{q}_A(x) dx \tag{5.12}$$

where $\hat{q}_{MBR}$ and $\hat{q}_A$ were previously denoted in Eq.(4.8). Note the excellent agreement of the computed and $Pe \to \infty$ results at large *Pe* values, both with each other and to the analytically obtained scaling. At higher Strouhal numbers, the mass burning rate

continues to dominate relative to area fluctuations, but has a more complex dependency on *St* and *Pe*.

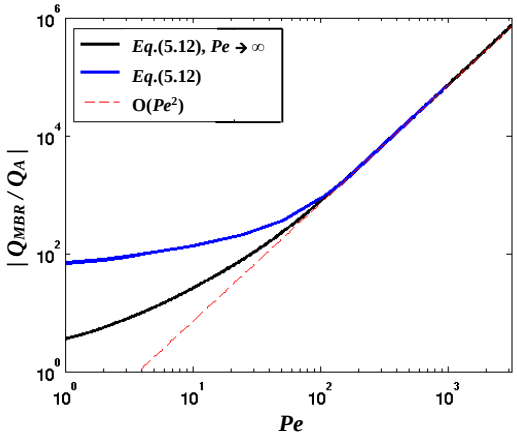

Figure 5.3. Ratio of mass burning rate to area terms in the unsteady heat release expression for the computed extended inlet and $Pe\rightarrow\infty$ limiting solution cases; showing the ratio for a fixed value of $St_R=10^{-5}$.

Figure 5.4 attempts to comment on this complex behavior by showing plots with additional dependence upon other parameters. The left plot shows various *Pe* value curves as a function of *St* for a representative $\mathcal{Z}_{st}$ value of 0.055. Notice the convergence to unity (*y*-axis being normalized by Pe^2) at low *St* values for the high *Pe* curves, with increased divergence as *Pe* is reduced. There is also increased modulation at higher *St* values. The right plot brings in the additional $\mathcal{Z}_{st}$ dependence for completeness, revealing the slightly modified low *St* value trends, and drastically altered high *St* modulation.

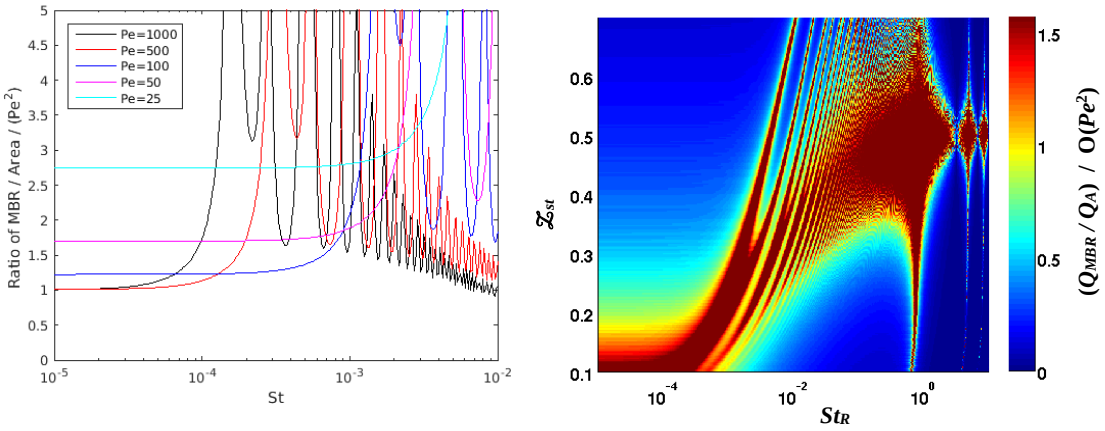

Figure 5.4. Ratio of mass burning rate to area terms in the unsteady heat release expression, showing the ratio normalized by O(Pe^2) and its complex dependence upon (left) St_R in two-dimensional *Pe* cuts for $\mathcal{Z}_{st}$ =0.055 and (right) for the *Pe*→∞ limiting solution case upon St_R and $\mathcal{Z}_{st}$.

As a final comment, consider the quantitative heat release in the quasi-steady limit. Under these conditions, the quantity of fuel-bound-energy which travels (via both convection and diffusion) across the inlet plane (x=0), must equal that which diffuses normally across the flame sheet. As was discussed in Section 4.3.1, and specifically in Appendix D and Appendix E, the inclusion of axial diffusion greatly complicates this issue, thus for our simplified $Pe\to\infty$ case, this balance can be expressed mathematically, utilizing Eq.(2.40), as:

$$\dot{Q}(t) = \int_{flame} \frac{-(1+\varphi_{Ox})^2}{\varphi_{Ox}} \rho \mathscr{D} \mathscr{h}_R \frac{\partial \mathcal{Z}(x,\xi_0)}{\partial n} dA = \int_0^{R_f} \rho \mathscr{h}_R u_x dy \qquad (5.13)$$

Transforming our integration limits and simplifying, an equation for the steady state heat release balance, utilizing Eq.(3.26), can be written as:

$$\dot{Q}_0 = \frac{-(1+\varphi_{Ox})^2}{\varphi_{Ox}} \int_0^{L_{f,0}} \frac{\partial \mathcal{Z}_0(x,\xi_0)}{\partial y} dx = Pe \qquad (5.14)$$

The corresponding value for spatially uniform velocity fluctuations can be obtained utilizing Eq.(3.27) and Eq.(3.7), and realizing that transverse fluctuations move no fluid across the inlet plane, and is given by:

$$\hat{\dot{Q}}_1 = \frac{-(1+\varphi_{Ox})^2}{\varphi_{Ox}} \int_0^{L_{f,0}} \left[\frac{\partial \hat{Z}_1}{\partial y} + \xi_1 \frac{\partial^2 \hat{Z}_0}{\partial y^2} \right] dx = \varepsilon Pe \qquad (5.15)$$

Utilizing these results, along with Eq.(2.41), the unity low *St* limit can also be observed and validated.

5.3 Heat Release TF - High *St* Asymptotic Results

Having considered the low *St* results, we next consider higher frequency transfer function characteristics. As was previously shown by the cumulative unsteady heat release distribution results in Figure 4.25, in this limit the unsteady heat release is dominated by its value at $x/L_{f,0}<<1$. It is common for highly oscillatory integrals, similar in form to Eq.(5.5), to be controlled by the values of the integrand at the boundaries (i.e. $x=0$ and $x=L_{f,0}$), and generally lead to a $1/St$ asymptotic behavior. However, as is shown in Figure 4.26, the transfer function has a $1/(St^{1/2})$ behavior for the $Pe\rightarrow\infty$ case, and only for finite *Pe* values does it transition to $1/St$ at some sufficiently high *St*.

For a step inflow profile, the mass burning rate has an integrable singularity at the $x=0$ inlet boundary in the $Pe\rightarrow\infty$ limit, a singularity which controls the heat release asymptotics. It was shown previously that the $St>>1$ transfer function is given by Eq.(5.4); i.e., $|\mathscr{T}|\sim 1/(St^{1/2})$, as indicated in Figure 4.26. Since we have shown in Section 5.2, the flame transfer function amplitude is unity in the limit of low *St* values, the Strouhal number at which this first transition occurs, from O(1) to $O(St^{-1/2})$, will be denoted St_1 and can be obtained from the following expression, representing the intersection of limits:

$$\left| \frac{i+1}{4\sqrt{St_1}} \right| = 1 \qquad \longrightarrow \qquad St_1 = \frac{1}{8} \qquad (5.16)$$

Even for more realistic inflow profiles that are smooth but very thin relative to the convective wavelength at x=0 (i.e., the finite Pe case), $|\mathcal{F}|$ still has a $1/St^{1/2}$ character, for the same reasons as the step inlet, for some range of St values. However, for disturbances with length scales that are on the order of the inflow profile thickness, different asymptotic considerations apply which ultimately cause the non-premixed flame to exhibit a $1/St$ asymptotic behavior that one would expect of highly oscillatory integrals.

At this point, it is important that we differentiate and isolate the various effects of axial diffusion, discussed in Chapter 4, on the heat release fluctuations, i.e., inflow boundary effects and dynamical effects. By "dynamical effects", we are referring to the inclusion of axial diffusion in the unsteady mixture fraction equation, i.e. setting b=1 in Eq.(3.4). These effects upon the space-time dynamics were noted previously in Section 4.1, resulting in dissipation and dispersion of flame wrinkles. By "inflow boundary effects", we are referring to the inclusion of axial diffusion in the steady mixture fraction equation, i.e., by setting b=1 in Eq.(3.3), effects previously discussed in Section 4.3.

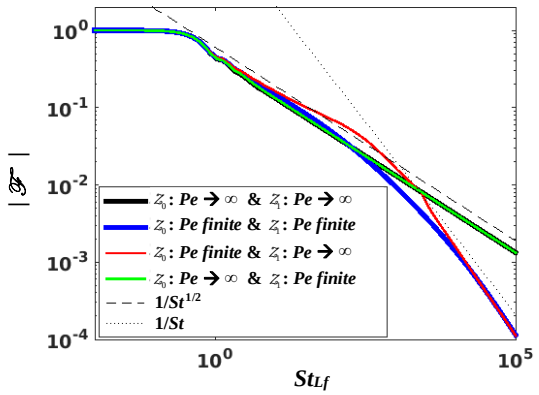

Figure 5.5. Flame transfer function amplitude curves isolating dynamical and inflow boundary effects on high *St* asymptotic trends.

These two effects can be isolated and the resulting transfer function magnitudes are plotted in Figure 5.5. These results were generated by repeating the calculations by including or neglecting axial diffusion in the steady and unsteady mixture fraction equations. To isolate the dynamical effects, axial diffusion was not included in the steady governing equation, thus retaining the sharp step inlet boundary condition, and was included in the dynamical fluctuating equation; this solution is indicated by "$\mathcal{Z}_0$: $Pe \to \infty$ & $\mathcal{Z}_1$: Pe finite" in the figure. To isolate the inlet effects, axial diffusion was included in the steady governing equation, allowing the smoothing of the inlet profile, and was excluded from the dynamical fluctuating equation, denoted as "$\mathcal{Z}_0$: Pe finite & $\mathcal{Z}_1$: $Pe \to \infty$" in the figure. Also shown are cases where axial diffusion is excluded in both equations and included in both.

5.3.1 Piecewise Linear Inlet Boundary Condition Model Problem

The figure clearly shows that it is the smoothed inflow profile that controls the high St asymptotic features. In other words, the key effect of axial diffusion on the asymptotic characteristics of $\mathscr{T}$ is on the time averaged profiles of $\mathcal{Z}$, specifically the inlet profile – i.e., axial diffusion effects on the unsteady dynamics of $\mathcal{Z}$ have minor influences on $\mathscr{T}$, although they have important influences on the downstream evolution of the flame position, as shown by Eq.(4.6).

To demonstrate this point explicitly, it is useful to consider solution properties of a model problem with a finite thickness $\mathcal{Z}_0$ transition layer, parameterized by δ, shown in Figure 5.6. In reality, the non-dimensional profile thickness parameter, δ, simulates the extent to which axial diffusion has altered the inlet boundary condition, and is

proportional to the inverse of *Pe*. In this model problem, however, we decouple this dependence of δ upon *Pe*.

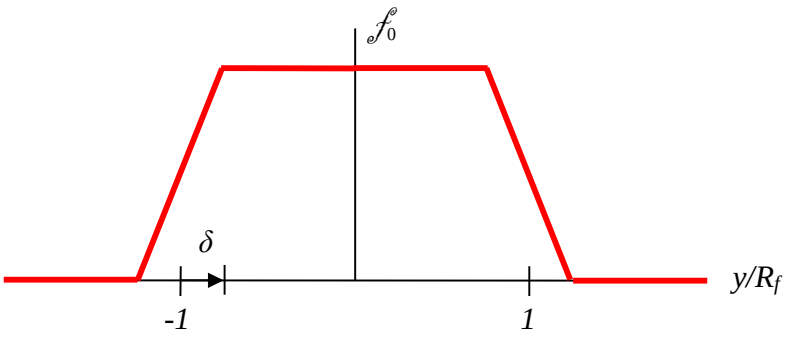

Figure 5.6. Piecewise linear inlet mixture fraction boundary condition utilized to analytically evaluate the effects of a smoothed inflow profile on high *St* asymptotic trends.

Utilizing this inflow boundary condition for the unconfined system (the lack of infinite summations making the math more tractable), and the governing equation given by Eq.(3.3), with *b*=0 (thus isolating the inflow boundary effect), the full steady state mixture fraction solution can be solved and is provided in Appendix H. In order to make analytical progress, we consider the limiting characteristics of this solution for large, but finite, *Pe* values (small δ values) and small axial locations. Tending towards a step-profile as $Pe\rightarrow\infty$ or $\delta\rightarrow 0$ enables comparisons to previous results, while the latter limit is of interest as the majority of unsteady heat release occurs near the burner lip, as was shown in Figure 4.23 and Figure 4.25. This simplified mixture fraction solution is provided below:

$$Pe \gg 1 \;\&\; x \ll 1 \qquad \mathcal{Z}_0(\tilde{x},\tilde{y}) = \frac{-1}{4\delta}\left[\begin{array}{l} \exp\left(-\frac{(-1+\tilde{y})^2}{4\tilde{x}}\right)\left[2\tilde{x}+\frac{4\sqrt{\tilde{x}}}{\sqrt{\pi}}\right]\left\{\frac{\delta(-1+\tilde{y})}{\tilde{x}}\right\}+ \\ -\exp\left(-\frac{(1+\tilde{y})^2}{4\tilde{x}}\right)\left[2\tilde{x}+\frac{4\sqrt{\tilde{x}}}{\sqrt{\pi}}\right]\left\{\frac{\delta(1+\tilde{y})}{\tilde{x}}\right\}+ \\ -\sqrt{Pe(\delta+1-\tilde{y})^2}-\sqrt{Pe(\delta+1+\tilde{y})^2}+\sqrt{Pe(\delta-1-\tilde{y})^2}+\sqrt{Pe(\delta-1+\tilde{y})^2} \end{array}\right] \tag{5.17}$$

Since as was discussed, the key effect of axial diffusion on the asymptotic characteristics of $\mathcal{F}$ is on the time averaged profiles of $\mathcal{Z}$, rather than the unsteady dynamics, it is useful to consider the $Pe\rightarrow\infty$ solution shown in Eq.(5.1) utilizing these smoothed, time average inflow profiles. Inclusion of finite *Pe* effects in the solution for the flame position, such as dissipation, into the heat release transfer function would not alter these high *St* asymptotics. This is because in the high *St* limit all the exponential terms tend towards zero and it is the unity constant that results in the highest *St* asymptotic region rolling off as 1/*St*. Further exponential terms, such as $\exp[-4\pi^2 St_R^2 x / (Pe^* R_f)]$, would just drive this term to zero sooner. Thus, this model problem simulates the smoothing effect of axial diffusion on the inlet boundary condition, eliminating the singularity caused by the step inlet boundary condition, while maintaining the $Pe\rightarrow\infty$ limit for the unsteady governing equation. Returning to Eq.(5.1), the function $g(x,\xi_0)$ is given for the smoothed profile as:

$$g(x,\xi_0) = \frac{\sqrt{Pe}}{2x^{3/2}\sqrt{R_f \pi}} + \frac{1}{4\delta x} \tag{5.18}$$

Substituting this expression into Eq.(5.1) revealss that in the limit of large *St* :

$$Pe \rightarrow \infty \text{ , } St >> 1 \qquad \mathcal{F} = \frac{C_1}{\sqrt{St_{L_f}}} + \frac{C_2}{St_{L_f}} \frac{1}{Pe\delta}\sqrt{\frac{PeL_f}{R_f}} \tag{5.19}$$

where

$$C_1 = \frac{(i+1)}{4} \qquad C_2 = \frac{i\left[\lambda - 4\sqrt{\pi}\right]}{16\sqrt{\pi}} \tag{5.20}$$

and λ is Euler's constant, with numerical value $\lambda \simeq 0.577216$. Note how the leading order *St*>>1 term is O($St^{-1/2}$), while the next term is of O(St^{-1}). Thus, while a $St^{-1/2}$

behavior occurs for the step inlet function profiles, a smooth mixture fraction at the base of the flame (resulting from finite *Pe* values) leads to the 1/*St* asymptotic behavior that one would expect of highly oscillatory integrals. For this model problem we can develop an explicit expression for the Strouhal number at which $St^{-1/2}$ to St^{-1} transition occurs, denoted as St_2, by equating these two terms:

$$\left|\frac{C_1}{\sqrt{St_2}}\right| = \left|\frac{C_2}{St_2}\frac{1}{Pe\delta}\sqrt{\frac{PeL_f}{R_f}}\right| \quad \longrightarrow \quad St_2 = \left(\frac{|C_2|}{|C_1|}\right)^2 \frac{1}{Pe^2\delta^2}\frac{PeL_f}{R_f} \tag{5.21}$$

Physically, this transition Strouhal number coincides with conditions where the convective disturbance wavelength is on the order of the axial extent required for fuel/oxidizer to diffuse across the inlet transition layer, i.e:

$$\frac{U_0}{f} \sim \frac{U_0\left(R_f\delta\right)^2}{\mathscr{D}} \tag{5.22}$$

However, in reality (and our computational world), *Pe* and δ are not independent. As was stated previously, the profile thickness parameter, δ, is proportional to the inverse of *Pe* under these conditions, a point which should make sense as the inlet profile steepens, and becomes thinner, as *Pe* is increased, converging to a step function in the $Pe\rightarrow\infty$ limit. Figure 5.7 demonstrates this point explicitly by showing computed profile thicknesses, based on the computations detailed in Section 4.3.1 and Figure 4.17, for various *Pe* value computational cases, where δ is defined as the distance from $0.95\times \mathscr{f}_0^{\circ}(y=0)$ to $0.05\times \mathscr{f}_0^{\circ}(y=R_w)$. Note the agreement with the O($1/Pe$) curve. Also shown is a plot of the slope of the inlet profile evaluated at the fuel port lip, i.e. $\partial \mathscr{f}_0^{\circ}/\partial y\big|_{x=0,y=R_f}$, for various

Pe value computational cases. Notice the multi-zonal structure, and corresponding high $Pe^{1/2}$ scaling.

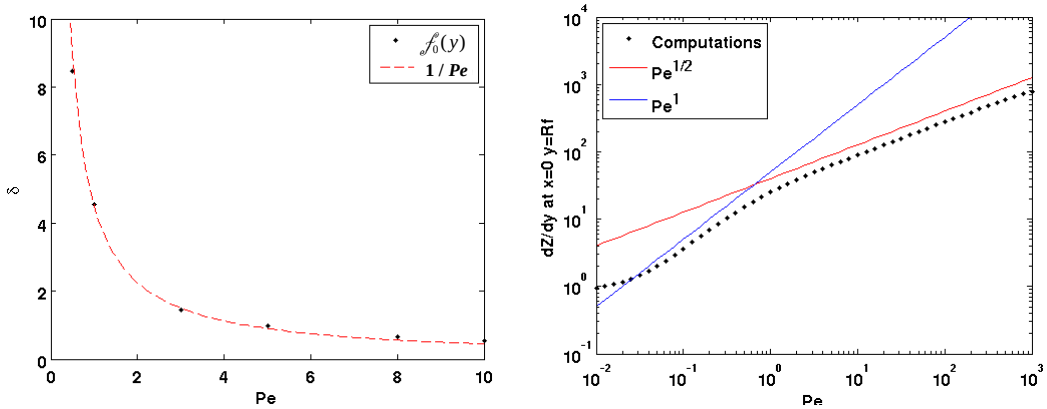

Figure 5.7. Computed inlet profile thicknesses (left) and inlet profile slope at the fuel port lip (right) for the extended inlet geometry considered in Section 4.3, for R_f=1 and R_w=10.

The resulting relation between fuel port lip inlet slope and inlet thickness can then be obtained for large *Pe* values (*Pe*>>1) as:

$$\left.\frac{\partial \mathscr{f}_0}{\partial y}\right|_{x=0,\, y=R_f} \propto \frac{1}{\sqrt{Pe}} \propto \frac{1}{\sqrt{\delta}} \tag{5.23}$$

Keep in mind the difference in shape between the computational inlet profiles, shown in Figure 4.17, from the piecewise linear model. Figure 5.8 shows some representative inlet profile slope values evaluated at the fuel port lip. The un-normalized plot shows how the magnitude of this slope monotonically increases with increasing *Pe*, while the normalized plot shows the broadening effect influencing the profile thickness.

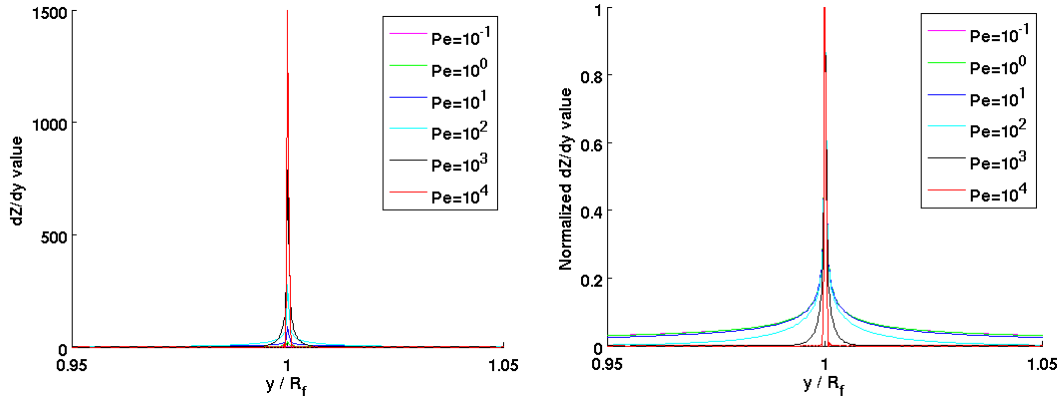

Figure 5.8. Computed un-normalized (left) and normalized (right) inlet profile slope for the extended inlet geometry considered in Section 4.3, for R_f=1 and R_w=10.

Thus, if we substitute in $\delta \sim 1/Pe$ into Eq.(5.21), this shows that:

$$St_2 = \left(\frac{|C_2|}{|C_1|} \right)^2 \frac{PeL_f}{R_f} \tag{5.24}$$

As St_2 is a function of Pe and L_f, the St transition points previously discussed in Section 4.3.4 and specifically Figure 4.26, are more easily observed by rescaling the axes. Figure 5.9 replots the data shown in Figure 4.26 by normalizing the horizontal axis by St_2 and the vertical axis by $C_1 / (St_2)^{1/2}$. The figure shows how this scaling properly and efficiently collapses the high St results at the different Pe values.

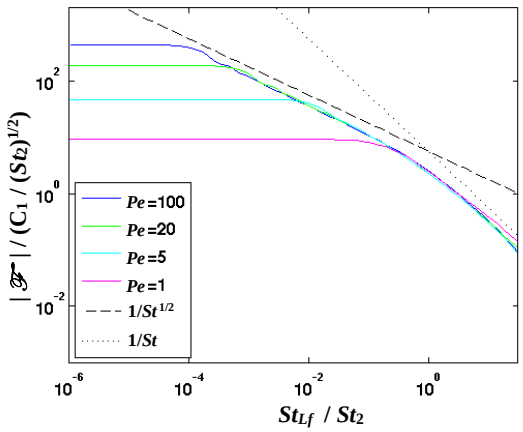

Figure 5.9. Normalized heat release transfer function amplitude plot for various degrees of axial diffusion, i.e. *Pe* values. The original horizontal axis, St_{Lf}, and vertical axis, $|\mathcal{T}|$, have been normalized so as to collapse the high *St* results. The $1/St^{1/2}$ and $1/St$ lines are the asymptotic values for the *Pe*=20 case for visual representation.

CHAPTER 6

Non-isothermal Diffusion Flame Analysis – Experimental Efforts

This chapter analyzes the dynamics of harmonically forced, non-premixed flames, both experimentally and computationally, and compares the measured space/time dynamics of the flame to that predicted from the forced mixture fraction equation, i.e. the $\mathcal{Z}$ -equation, Eq.(2.7). By investigating tangible, i.e. real-life, flames absent of mathematical assumptions for simplicity and tractability, insight can be gained into non-premixed flame response, as well as the validity and impact of various assumptions made in previous analyses. Additionally, enhanced predictive capabilities could result from utilizing measured velocity field data as model inputs. Thus, high speed PIV data was taken on a coflowing methane-air diffusion flame, equipped with speakers for harmonic forcing, over a variety of flow velocities, forcing frequencies, and forcing amplitudes. These measured velocity fields were used as inputs to a $\mathcal{Z}$ -equation solver, and the resulting space-time dynamics of iso-$\mathcal{Z}$ surfaces were extracted from the $\mathcal{Z}$ field solutions.

6.1 Introduction

This chapter describes measurements and analysis of the space-time evolution of disturbances on ***real*** harmonically forced, laminar, non-premixed flames. A significant experimental and modeling literature exists on the response of premixed flames to harmonic flow disturbances [4, 21-27]. Measurements have experimentally characterized both the local space-time dynamics of wrinkles on laminar flames [41, 127-129], as well

as the spatially integrated heat release [130]. These measurements show that wrinkles are excited at the flame stabilization point and locations of spatial non-uniformities in disturbance velocity, and subsequently convect down the flame. The response of the flame at a given point in space and time is non-local – i.e., it is not only a function of the local disturbance, but is, rather, a convolution of disturbances excited at upstream locations at appropriate convective time delays. For these reasons, a variety of interference behaviors and spatially non-monotonic variations in flame wrinkle magnitude occur [92]. Similar analytical studies of flame wrinkling behavior have also been performed in harmonically excited turbulent flames. In this case, the flame's local wrinkling and heat release consists of both the narrowband excitation, as well as broadband turbulent fluctuations – additionally these two types of disturbances nonlinearly interact with each other. For example, the harmonic forcing modulates the phase-averaged turbulent burning velocity, and the turbulent flame disturbances increase the rate of destruction of harmonic flame wrinkles [131, 132]. A particularly large literature has developed for global heat release response of turbulent flames to harmonic forcing, referred to as the heat release transfer function [37, 133]. Indeed, many industrial companies now possess capabilities for measuring flame transfer functions in high pressure, high flow facilities in order to screen their designs for instabilities [28, 134, 135].

Once again, there is significantly less literature on forced, non-premixed flames. Experimental efforts have elucidated some of the natural flame dynamics, such as flicker characteristics or buoyancy-related instabilities, and flow field characterization [44, 48, 49, 51, 58, 136, 137]. The impact of forcing on the flames emissive properties,

specifically soot generation and suppression, has also been investigated [53, 138, 139]. One study reported on the flame wrinkle evolution characteristics of non-premixed flames, including wrinkle magnitude as a function of axial position for unforced flickering flames [140]. We are not aware of any experimental studies of the space-time dynamics of flame wrinkles on forced, non-premixed flames. Additionally, some work has reported the spatially integrated heat release and flame transfer function dynamics of non-premixed flames [52, 141, 142].

A number of recent analytical studies have also been reported for forced, non-premixing flames, considering the space-time wrinkle dynamics, the space-time heat release dynamics, and the thermoacoustic system behavior which the non-premixed flame is part of [59, 62-64, 66, 67, 93, 143]. These studies have analyzed this problem within the infinite reaction rate, $\mathcal{Z}$ -equation formulation for the mixture fraction. This problem admits analytical solutions for certain types of imposed mean and fluctuating velocity fields (e.g., bulk forcing, convecting disturbance fields, and so forth), and constant diffusion coefficients. For example, Chapter 3 and Chapter 4 developed various explicit solutions, such as Eq.(3.15) and Eq.(4.6), for the fluctuating flame position, $\xi_{1,n}(x,t)$, of a non-premixed flame exposed to spatially uniform, axial flow oscillations.

In real flames with temperature gradients, more complex shear flows, and convecting vortical disturbances, it can be anticipated that the evolution of flame wrinkles will be more complex, as wrinkles excited at one location and convecting downstream, and those excited further downstream by a spatially varying disturbing field, will set up more complex interference fields. Motivated by the above studies, the objective of this chapter is to experimentally characterize the gain and phase

characteristics of the flame wrinkle behavior, as well as to use actual measured mean and disturbance velocities as inputs to the governing flame dynamics equations in order to predict the flame response. Due to the spatially varying nature of the velocity and diffusivity, these problems must be solved computationally; however, the analytical work presented in prior chapters provides useful interpretive insight into these results. Specifically, experimental measurements of the flame response allow us to determine the spatial evolution of the amplitude and phase of induced flame wrinkles. In addition, simultaneous particle image velocimetry (PIV) measurements enable characterization of the velocity field disturbances, showing both the disturbance field that is exciting the flame, as well as the influence of the flame on the disturbance field, a physical feature that was previously intractable. Finally, by substituting these measured velocity disturbances into the species equation (or $\mathcal{Z}$ -equation), we also can predict the response of the flame and compare these measurements to the actual flame wrinkling. While a similar modeling effort has been done for premixed flames that used measured velocity fields as inputs to the flame dynamics equations [127, 128, 144], we are not aware of a prior study of this nature for the non-premixed flame case.

6.2 Experimental Facilities and Diagnostics

Figure 6.1 shows the experimental facility and diagnostic setup used in this study. Appendix I shows additional images of the tangible equipment. The key components of the facility are the fuel and air conditioning sections, combustor section, forcing section, and exhaust. Natural gas, ~98% CH_4 with the balance consisting of higher hydrocarbons and inerts, passes through an 25*psi* system regulator and flows up the central fuel tube, of inner radius R_f = 4.50*mm* and 0.254*mm* wall thickness. Non-preheated air passes through

a 75*psi* line regulator/filter and flows up a coflowing annular passage, of inner radius R_w = 4.0*cm* and 5.0*mm* wall thickness, that surrounds the fuel tube port outside diameter. The air passes through a hexagonal honeycomb flow straightener, with 4.78*mm* apothem and nominal wall thickness of 0.8*mm*, 1.10*m* upstream of the burner outlet. Time-averaged air and fuel volumetric fluxes (i.e., spatially averaged velocities) were matched to within 1% in order to minimize shear layer strength, so that the dominant source of excitation of the flame was from the acoustic forcing, and not the acoustically excited shear layers. The facility was operated at velocities of 20-90*cm/s*. This velocity range and fuel (air) diameter correspond to Froude numbers in the range of 0.95-4.3, based upon $Fr = U_x / \sqrt{gR_f}$.

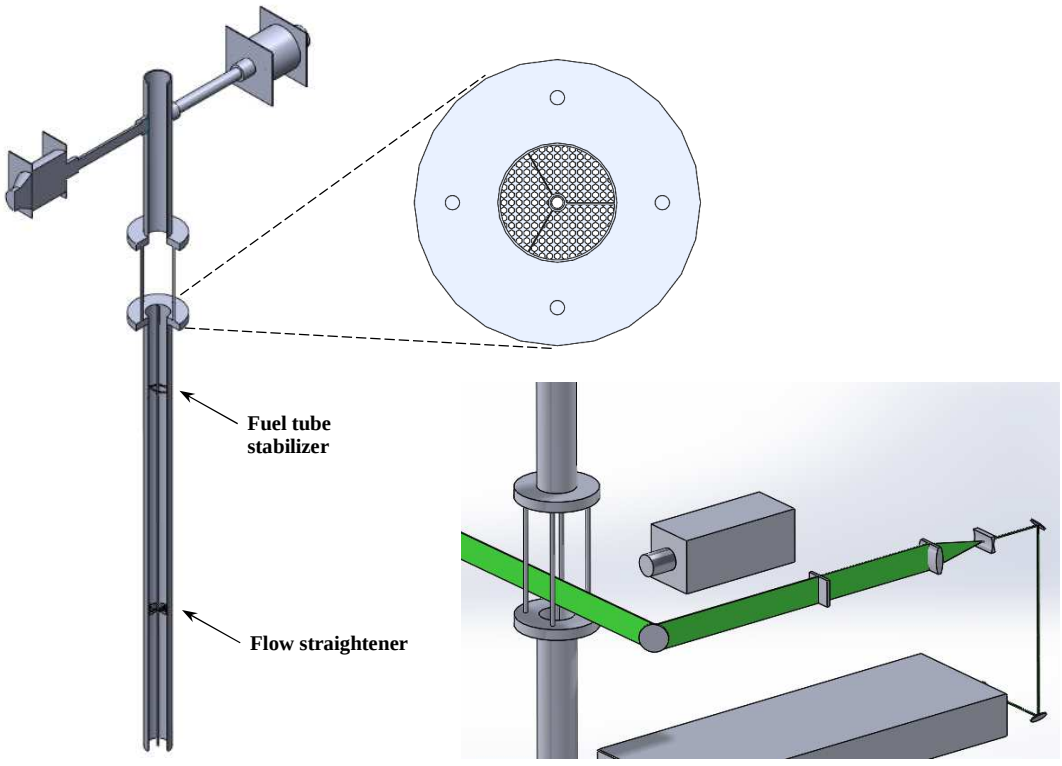

Figure 6.1. Picture of the vertical co-flowing non-premixed flame experimental facility (left), a detailed view of the burner (top-right), and a model showing the PIV laser diagnostic setup and the beam path (bottom-right).

It is known that, for low Froude numbers, i.e. the buoyancy dominated regime, non-premixed flames are globally unstable and exhibit narrowband oscillations at a low frequency on the order of f_b ~10 Hz [42, 43]. When present in this facility, these instabilities were quite evident from the presence of a low frequency peak in the luminosity spectrum images. All data presented in this paper were obtained from conditions where this peak was at least 20 times smaller than the spectral peak at the forcing frequency, over a large axial extent. Figure 6.2 shows representative spectra of the flame position, ξ, for an unforced and forced system. Note the absence of the flicker frequency, and the dominance of the forcing frequency at f_f for the forced system. The burner tube diameter was chosen as large as possible, with the constraint of having a ratio of $R_f/R_w << 1$ (to minimize confinement effects) and a momentum-dominated flame. The flow velocities were set by balancing between the competing requirements of a laminar flow and a momentum dominated flame. For reference, a flow velocity of 40*cm/s* corresponds to Reynolds numbers on the order of ~200 and 2000, based upon fuel and oxidizer port diameters, respectively.

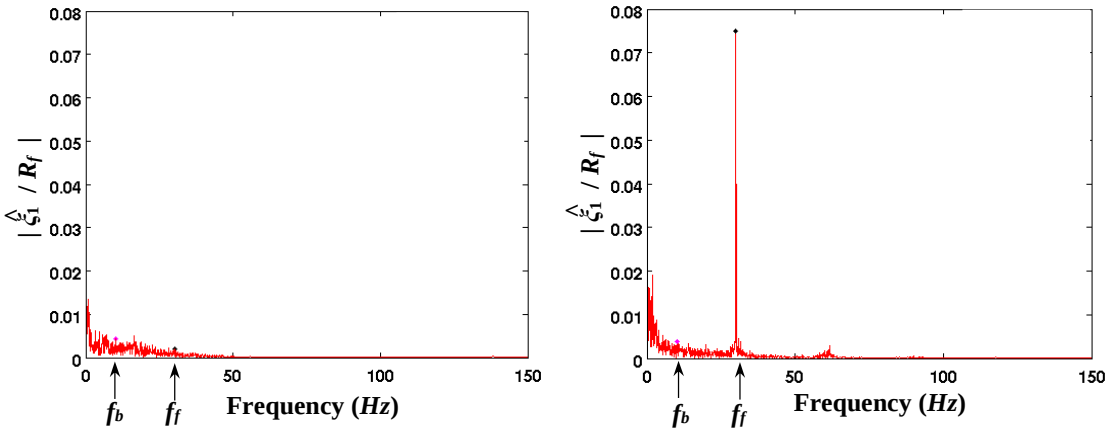

Figure 6.2. Frequency spectra of the transverse flame location, ξ_1, at x/R_f=5.13 for the U_0=0.4*m/s* case for the unforced (left) and forced at 30*Hz* (right) configurations. Vertical arrows indicate the forcing frequency, f_f, and the buoyant instability frequency, f_b.

Moving into the combustor section, the fuel and air tubes terminate into a 30.5*cm* long cylindrical quartz tube of inner radius R_w = 3.75*cm* and 2.0*mm* wall thickness, that provides confinement and minimizes the influence of ambient disturbances on the flame, whilst allowing optical access from all sides. The combustion products then flow into an exhaust section, which consists of a 0.6*m* long tube of inner radius R_w = 4.0*cm* and 5.0*mm* wall thickness. Connected perpendicular to this exhaust, 0.46*m* above the termination of the combustor section, are two antipodal 30.5*cm* long tubes of inner radius 1.75*cm* and 3.55*mm* wall thickness, which are attached to loudspeakers. These loudspeakers are driven by a harmonic function generator and amplifier, in order to obtain desired forcing amplitudes, i.e. $\varepsilon = \hat{u}_1 / U_{x,0}$ values, between 0.05-0.3. In general, this forcing configuration excites both axial (i.e., one-dimensional) acoustic disturbances and transverse, multidimensional duct modes. However, the 10-100*Hz* forcing frequency range used for this study is well below the ~4930*Hz* cut-off frequency, defined by $f_c = 0.58\, c / R_w$, of the exhaust section [4]. Consequently, multi-dimensional disturbances are evanescent and decay quickly in the axial direction. As such, the acoustic excitation source utilized here is essentially one-dimensional. For reference, the first transverse duct mode decays as $\exp\left[-\sqrt{m^2\pi^2 - (kR_w)^2}\,\frac{x}{R_w}\right]$ [4], where $k = \sqrt{\omega^2 / c^2}$, so that its value is less than 1.4×10^{-6} % of its original value once it reaches the combustor section.

The primary experimental diagnostics consisted of high speed, line of sight integrated, imaging of flame luminosity, and high speed particle image velocimetry (PIV), see Figure 6.1. High speed imaging was performed with a Photron SA5 camera, operating at a 1000*Hz* frame rate, with 0.2*ms* exposure time, and 1024 × 1024 pixel resolution. The camera was outfitted with a f/2.8, 135*mm* lens, such that a physical

window of $90mm \times 90mm$ region of the test section was imaged. This imaging region spanned from the burner lip to $15R_f$ downstream. The flame was imaged through a bandpass optical filter, centered at $527nm$, with greater than 93% transmission between $517nm$ and $537nm$. A total of 10,918 images were acquired in each run. Figure 6.3 shows two representative luminosity images of the forced non-premixed flame, along with an image of a forced premixed flame for comparison. Notice the clear presence of wrinkles along the flame surface. However, the premixed flame develops a prominent cusp downstream, a manifestation of flame propagation, which is absent in non-premixed flames.

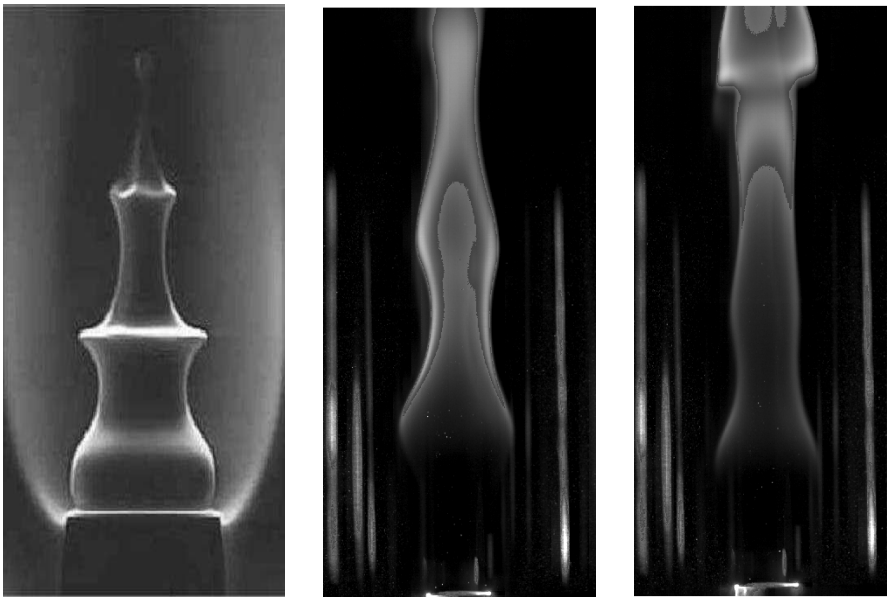

Figure 6.3. Schlieren image of a conical methane-air forced premixed flame at 150Hz (left) (reproduced from Ducruix *et al.* [145]) along with line of sight luminosity images of forced methane-air non-premixed flames at $30Hz$ (middle) and $50Hz$ (right) forcing frequency.

Mie scattering images for high speed PIV were also obtained. A dual-flow seeder was utilized to independently seed both the fuel and air flows with $0.3\text{-}1\mu m$ Al_2O_3 particles, chosen due to their durability in reacting flows and their high refractive index

[146]. This particle size was chosen due to the relatively low flow velocities used in this testing, so that the particles could accurately track the flow at the frequencies of interest. For reference, the Stokes number, representing a characteristic non-dimensional frequency of the particle response, for the largest excitation frequency considered (100*Hz*) is *Sk*=0.004, from the definition $Sk = d_p\sqrt{\omega/\upsilon}$ [146], utilizing a nominal particle size of $0.7\mu m$ and a viscosity of υ=1.72 × $10^{-5}m^2/s$, calculated at 298K. The Stokes number is 4 times smaller, *Sk*=0.001, when calculated at the approximate product temperature, 1800 K. The seed was dried in an oven for an excess of 24 hours, then placed into the two separate vertical seed holders. During operation, the fuel and air flows passed thru supercritical orifices, directly below the seed holders, before passing through the seed. A pneumatic shaker was attached adjacent to both seed holders, to ensure continued seed pickup.

The particle-laden flow then passed through the respective passages to the combustor, where they were illuminated with a double-pulsed Nd:YAG laser, with wavelength of 532*nm*, pulse duration of 100*ns*, and 4*mJ*/pulse energy. Each of the two lasers in the double-pulsed system is operated at 500*Hz*. The laser beams were expanded with a -50*mm* cylindrical lens into an expanding sheet, which was then shaped with a 750*mm* cylindrical lens. The time-delay between the two illuminating laser pulses of a given pair was 1*ms*, chosen such that for our intended flow velocity range, seed particles would move roughly 1/4th of the PIV (final pass) interrogation window (to be discussed next). This is a significant enough spatial change to ensure good velocity calculations, while reducing loss of pairs. The measurement plane was located through the concentric central axis of the fuel and oxidizer ports, as shown by Figure 6.3. Defocusing introduces

challenges due to the high curvature of the non-premixed flame sheet as will be discussed later in the experimental results.

Data was obtained over a parametric grid of experimental input variables, specifically flow velocity, forcing frequency, and forcing amplitude, all of which have been shown to be dynamically significant factors for non-premixed (as well as premixed flames). These conditions are summarized in Table 6.1.

Table 6.1. Range of experimental input parameters. "*" indicates forcing frequency data sets where only limited flow velocity and forcing amplitude combinations were obtainable.

Input parameter	Value set
Fuel/Air flow velocity, $U_{0,\mathrm{des}}$ (m/s)	0.1, 0.2, 0.4, 0.7
Forcing Frequency, f_f (Hz)	10, 20, 30, 40, 50, 70*, 100*
Forcing Amplitude, ε	0.05, 0.15

6.3 Data Analysis

The two key experimental observables are the instantaneous flame position, and instantaneous velocity field at the flame. The processing methods for extracting these data are described in this section. A representative luminosity/Mie image of a wrinkled non-premixed flame, obtained from the experimental setup, is shown in Figure 6.4(a). These images are used to characterize the space-time dynamics of the flame sheet, which requires determining the instantaneous flame edge.

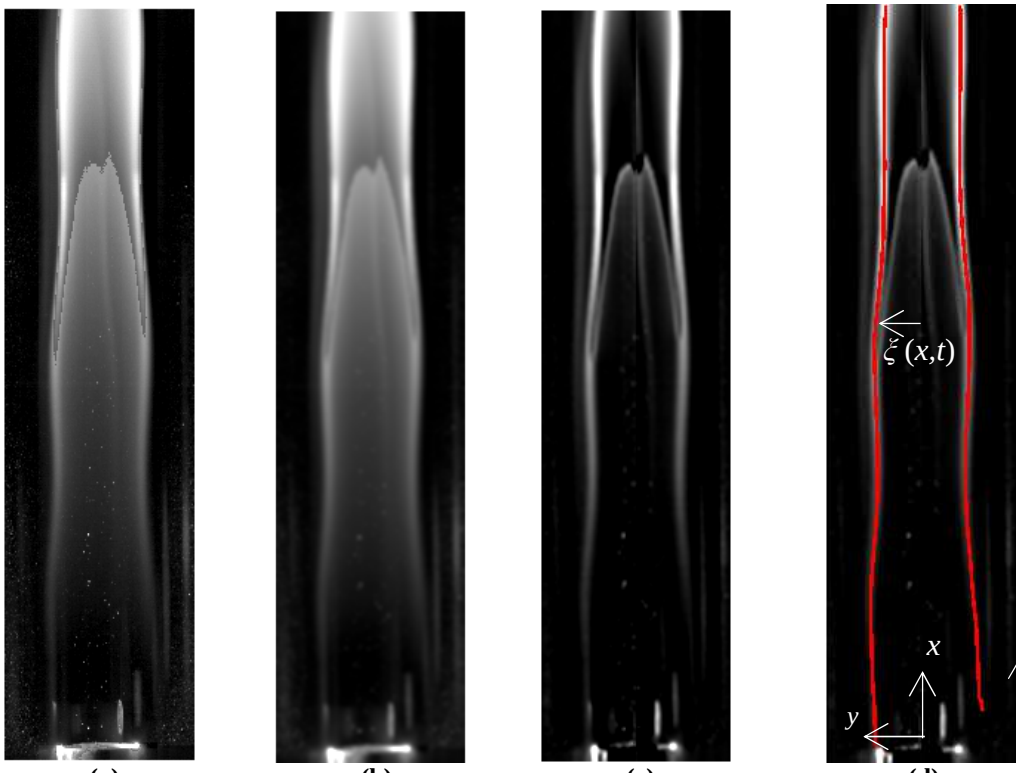

Figure 6.4. (a) Raw luminosity image of a forced non-premixed flame (b) bilateral filtered image (c) inverse Abel transformed image (d) and edge detected image.

To reduce noise without blurring edges, a bilateral filter was used. Implementing this spatially varying nonlinear filter, the intensity value at each spatial location was replaced by a weighted average of the intensity values from nearby locations. The weights, based on a Gaussian distribution, are dependent upon both spatial orientation as well as quantitative intensity differences. Systematically looping through each location and modifying the weights accordingly makes this procedure edge preserving, as can be seen from Figure 6.4(b). An inverse Abel transform was then used on the left and right halves of the images, independently (being a symmetric operator), in order to estimate an intensity slice from the line-of-sight integrated image. The combination of these procedures is shown in Figure 6.4(c). The flame edge, defined as the instantaneous transverse location of the calculated edge and denoted $\xi(x,t)$, was then determined from

the intensity peak, shown in Figure 6.4(d). Note that an edge is calculated separately for the left and right transformed images – these two values would coincide if the images were perfectly axisymmetric, and for our results they generally agree to within 5% (comparisons are shown later; see Figure 6.13). The Fourier transform of the fluctuating component $\xi_1(x,t)$, denoted $\hat{\xi}_1(x)$, then quantifies the wrinkle amplitude and phase (with respect to its value at the left flame branch base) as a function of axial location.

We next describe the velocity calculations, obtained from the PIV measurements. Velocity vectors were computed from the Mie scattering image pairs using a cross-correlation algorithm [147] with a multi-pass approach [148] and two-dimensional Gaussian sub-pixel interpolation [147]. Image preprocessing was implemented with a particle intensity normalization of 3 pixels. The multi-pass analysis consisted of two preliminary passes with 64 × 64 pixel interrogation windows and 75% overlap between interrogation windows, followed by 2 passes with 24 × 24 pixel interrogation windows and 50% overlap between the interrogation windows, resulting in velocity vectors calculated at $0.8mm \times 0.8mm$ spatial intervals. Post-processing algorithms were used to discard a small number of spurious vectors, defined as points with 1.7 times the root mean square (rms) values of the neighbors. In addition, a local validation method discarded neighboring vectors whose ratio of difference-to-average velocity magnitude was greater than 1.9 times the rms of the nearest neighbors. These post-processing techniques resulted in less than 1% of the total velocity vectors being discarded. Discarded values were replaced with the instantaneous average of neighboring vectors.

The PIV measurement was calibrated by imaging a black anodized aluminum calibration plate with a laser etched pattern, which was located in-plane with the laser

light sheet. The laser etched pattern consisted of a regularly spaced grid of crosses, composed of 0.3*mm* thick lines, with spacing of 6*mm* and with positional uncertainty of 0.004%. The spatial coordinates of the Mie scattering images and resultant velocity fields were mapped to this grid. The worst-case calibration error was estimated to be 1 pixel over the large 160 mm calibration plate.

Near the flame tip, the highly curved flame defocuses the cameras view of the Mie particles, sometimes blurring them. When compounded with the luminosity emissions that partially saturate the signal at flame tip, these effects lead to highly spurious results. An example image displaying this effect is shown in Figure 6.5, showing the spurious velocity data near the upper portion of the image.

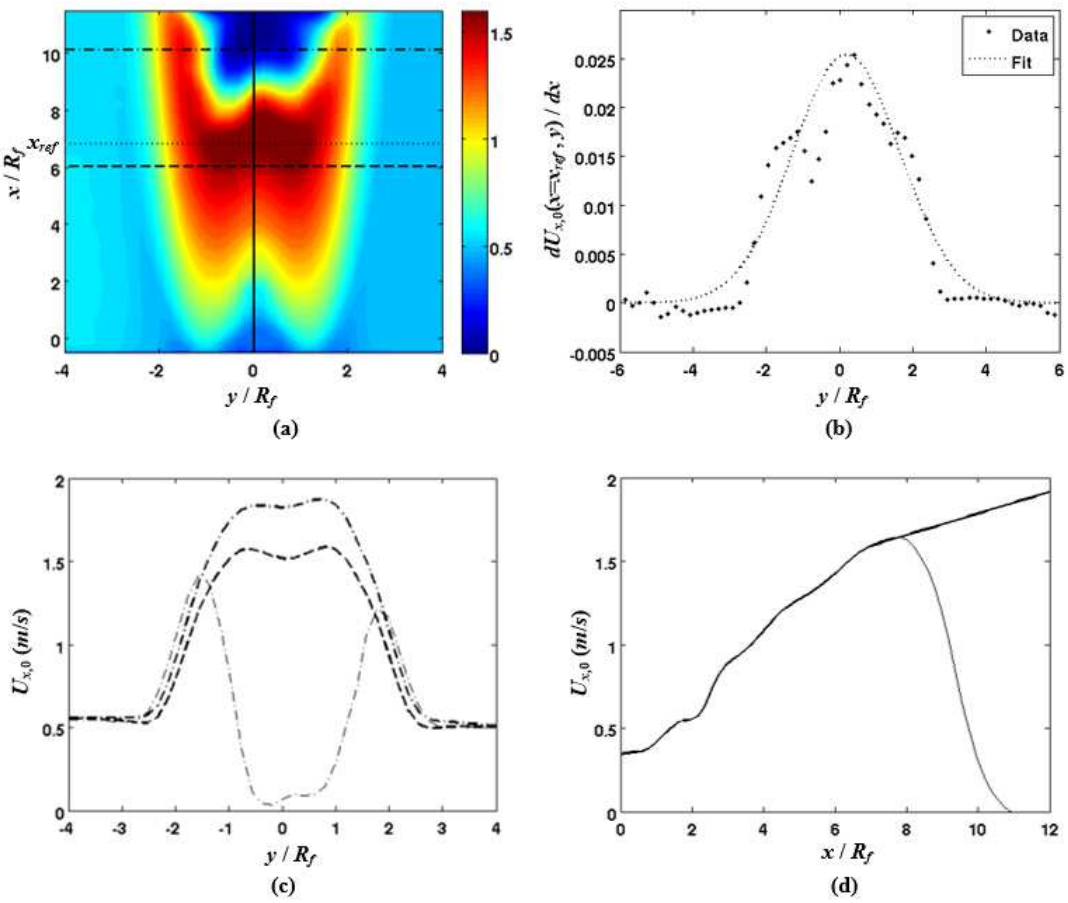

Figure 6.5. Representative PIV data showing spurious result near upper edge of image due to intensity saturation and flame curvature distortion (a). The void filling procedure is also depicted by the axial velocity gradient, d$U_{x,0}$/dx at a representative axial location below the void, x_{ref} (b), along with transverse (c) and axial (d) cuts of the raw velocity data (thin lines) and extrapolated data (thick lines). The line styles correspond to the various traverses show in top left image.

In these regions, the velocity is extrapolated from upstream locations of good data. This is done by looking at the axial velocity gradient, i.e. $dU_{x,0}/dx$ at an axial location upstream (below the void), where valid data exists, denoted x_{ref}. A Gaussian curve is fit to this gradient profile, shown in Figure 6.5, and the downstream velocity values are then extrapolated at locations $x > x_{ref}$. Representative transverse and axial cuts are also shown in Figure 6.5, showing both the raw and extrapolated data. The calculation results shown later will indicate the regions of actual and extrapolated data.

6.4 Experimental Results

Having the ability to track the instantaneous flame edge, characteristics of the experimental flame wrinkle dynamics can be investigated. We will refer to four representative conditions throughout the rest of this paper, shown in Table 6.2.

Table 6.2. Representative operational condition sets.

Case Set	$U_{0,des}$ **(*m*/*s*)**	f_f **(*Hz*)**	ε
Case A	0.1	50	0.15
Case B	0.2	20	0.05
Case C	0.4	30	0.05
Case D	0.4	40	0.05

Representative results showing the instantaneous spatial dependence of $\xi(x,t)$ at different time instances over a forcing period is shown in Figure 6.6. Notice the clear downstream axial convection of the flame wrinkle crests with time, a result predicted by the waveform portion of the various explicit equations. Flame wrinkle convection can also be directly inferred from the phase of $\hat{\xi}(x, f = f_f)$. Note that a wrinkle convecting axially at a constant speed, U_c, leads to a linear phase-axial location dependence, with a slope given by:

$$U_c = \left| \frac{2\pi f_f}{\partial \angle \hat{\xi}(x, f = f_f) / \partial x} \right| \tag{6.1}$$

Figure 6.6 also plots the axial dependence of U_c calculated using this formula, overlaid upon measured steady velocity results along various three axial profiles through the domain. Note the very close correspondence of the wrinkle velocity to the mean flow velocity. This result is consistent with prior analytical work that used simpler model velocity profiles, and showed that to leading order in *Pe*, $U_c = U_{x,0}$. Note that this is not

the case in premixed flames, where the flame wrinkle speed is the vector superposition of the flow velocity and flame speed projected normal to the flame front.

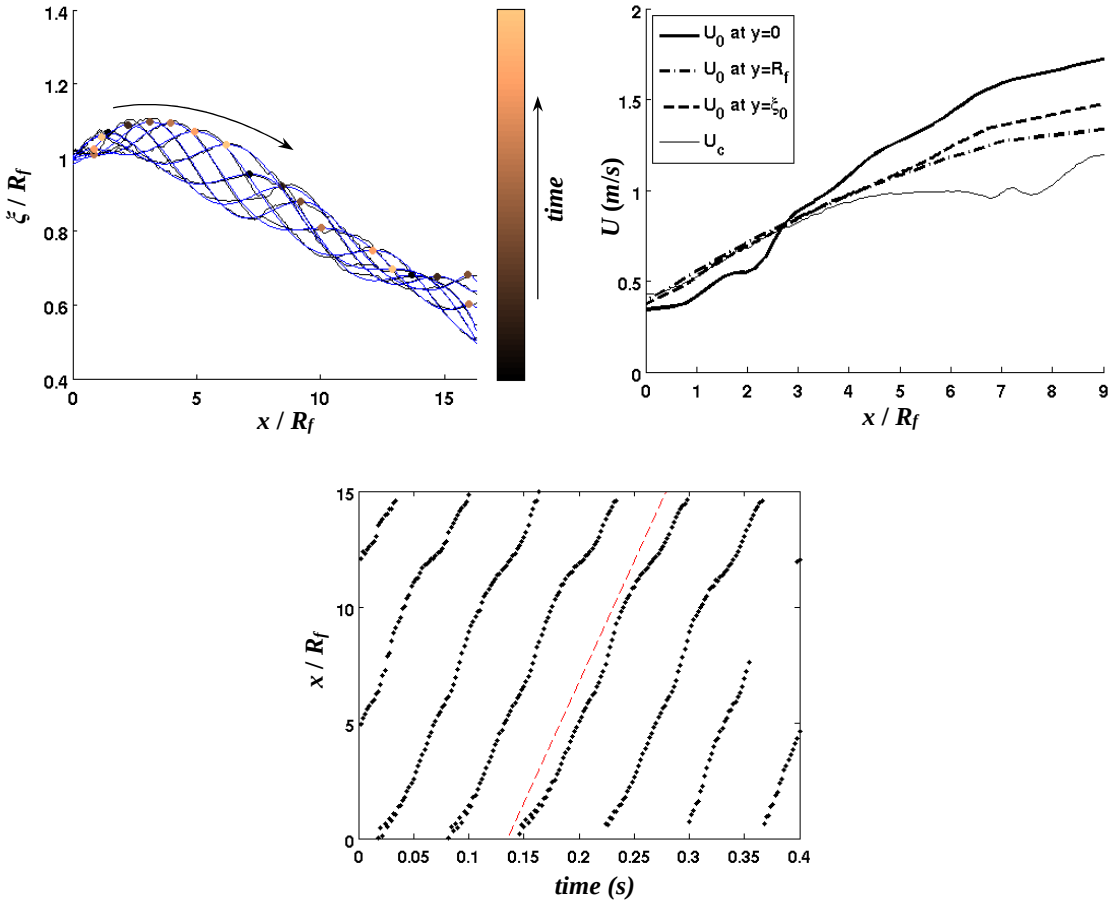

Figure 6.6. (top-left) Instantaneous flame positions at various time instances over a forcing period (left; black and blue lines indicate raw and smoothed experimental data, respectively, while arrows indicate increasing time), (top-right) steady flow velocity cuts, at the centerline [y=0], burner lip [y=R_f], and mean flame position [y=$\xi_0(x)$], and wrinkle convection speed (right) results for Case C, and (bottom) representative axial evolution of the wrinkle crests for Case C, where the line indicates a convective velocity of 0.6 *m*/s.

The fluctuating flame position, $\xi_1(x,t)$ is calculated as the transverse distance of the instantaneous flame position from the average; i.e., $\xi_1(x,t)=\xi(x,t)-\xi_0(x)$. The fluctuating response can then be extracted from the Fourier transform at the forcing frequency, $\hat{\xi}(x, f = f_f)$. Representative results for the magnitude and phase of the flame wrinkle are shown in Figure 6.7 for Case C.

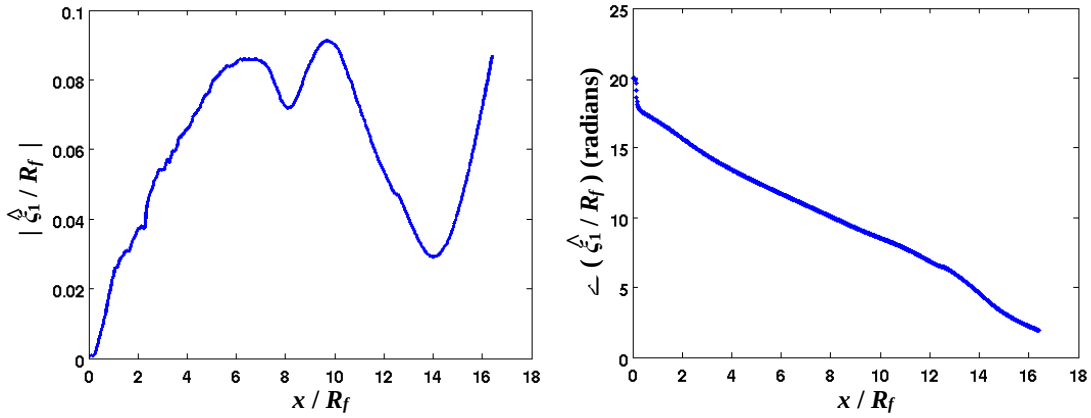

Figure 6.7. Representative experimental flame wrinkle amplitude (left) and phase (right) results for Case C.

Note the nearly stationary behavior of the flame at the base near the burner lip, i.e. $\hat{\xi}_1(x \sim 0, f = f_f) \sim 0$, indicative of flame attachment – these results are consistent with prior theoretical results developed for non-premixed flames in the fast chemistry, *Pe*>>1 limit, see Chapter 4. Additionally in this near base region, the response magnitude grows with downstream distance. This characteristic has been previously attributed to the amplification of the disturbances in the convectively unstable shear layer [127]. Further downstream the magnitude of flame wrinkling peaks at x/R_f = 6 and oscillates. This behavior is suggestive of an interference phenomenon and is consistent with the predictions of prior calculations of forced non-premixed flames from previous Chapters. Similar interference results have been observed for axially forced premixed flame systems [149]. The phase rolls off nearly linearly with axial distance, for the reasons discussed earlier in the context of Figure 6.6. Additional flame wrinkle results will be shown in Section 6.6 where we compare results with modeling predictions.

We next show representative velocity results. The time averaged axial $U_{x,0}$ and radial $U_{r,0}$ velocity component fields are shown in Figure 6.8 for the same conditions

shown in Figure 6.5 thru Figure 6.7. The time averaged centerline of the flame, extracted from the procedure outlined in Figure 6.4 and demonstrated instantaneously in Figure 6.6, is also indicated. The figure clearly shows the axial flow acceleration. In addition, the radial velocity result shows the induced radially expanding (both inflowing and outflowing) velocities inside and outside the flame, respectively, an expected result based on the gas expansion occurring on both sides of the flame sheet.

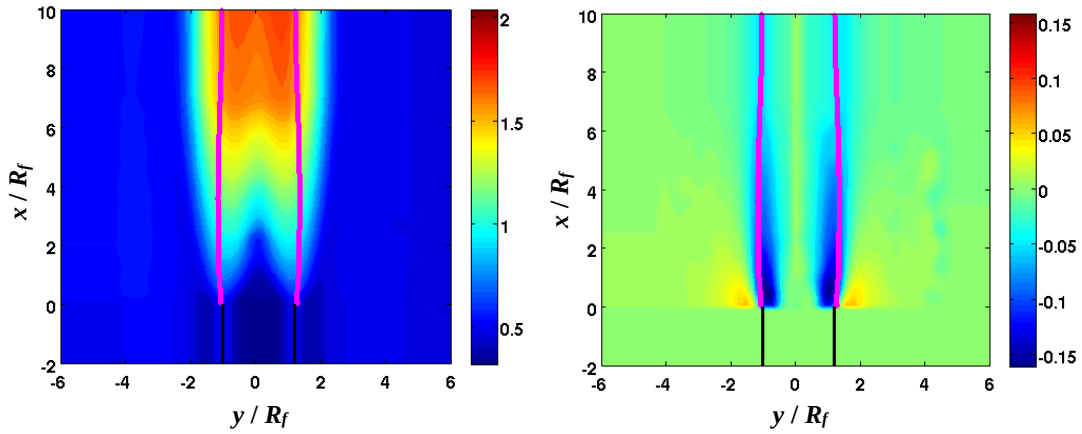

Figure 6.8. Representative experimental velocity fields (using corrections described in the context of Figure 6.5) showing the time averaged axial, $U_{x,0}$ (left), and radial, $U_{r,0}$ (right; positive direction being radially outward), velocity fields for Case C, along with overlaid steady flame position (line). Fuel port walls are shown in black and the colorbars show velocity in *m/s*.

Figure 6.9 shows the axial and radial magnitude and phase values of the velocity fluctuations at $\xi_0(x)$ for Case C. The phase of the radial velocity disturbance shows clear signs of downstream convection (the phase slope corresponds to a value of ~0.6 *m*/*s*), suggesting that it is dominated by vortical disturbances. Being convectively unstable in its own right [150], harmonic excitation causes the shear layer to roll up into vortices at the frequency of excitation [151]. The axial velocity phase is more complex, but its general flatness with respect to axial distance is more suggestive of it being dominated by an acoustic standing wave. Also, the complex axial disturbance magnitude distribution is perhaps due to the influence of the flame density jump upon the acoustic field.

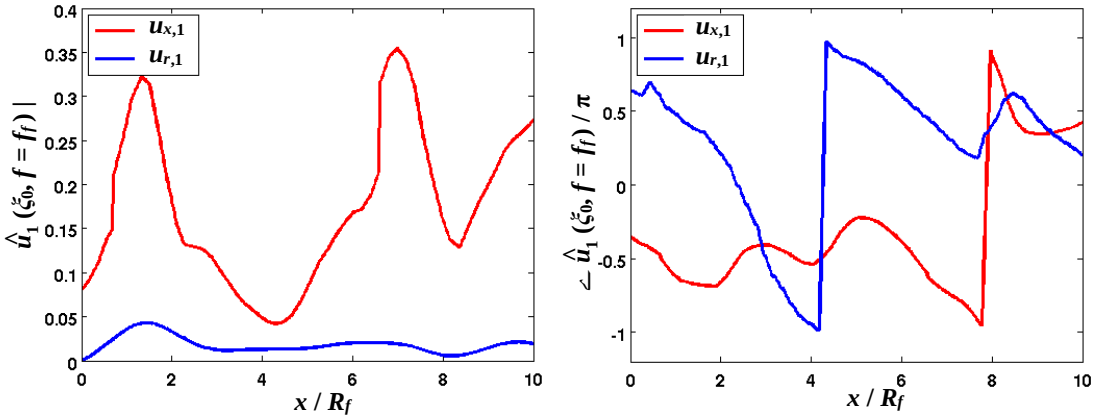

Figure 6.9. Representative experimental axial, $\hat{u}_{x,1}$, and radial, $\hat{u}_{r,1}$, disturbance velocity magnitude (left) and phase (right) curves extracted along the mean flame for Case C.

This data can also be interpreted through the use of a joint progress variable field, as shown by Figure 6.10, which indicates the spatiotemporal likelihood of the instantaneously tracked flame edge existing throughout the domain. Shown is the variable field for Case C, along with fields obtained utilizing analytical results both in the $Pe \to \infty$ limit and $Pe >> 1$ limit (Eq.(4.18)) for similar conditions for comparison of nodal locations. The experimental flame brush is also marked.

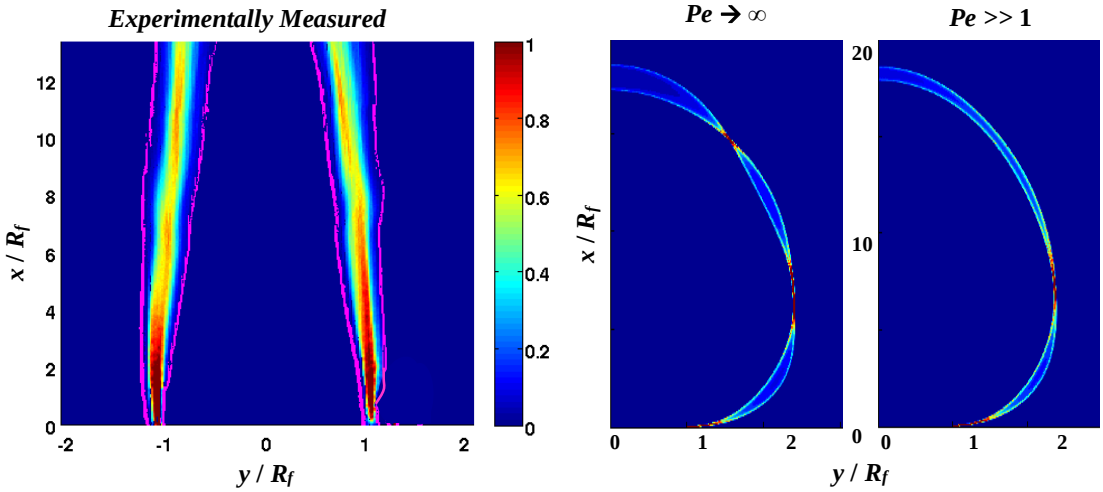

Figure 6.10. Joint progress variable field for (left) experimentally measured instantaneous flame edges for Case C with marked flame brush and (right) analytical mixture fraction field solutions for *Pe*=10, f_f=30*Hz*, and $\mathcal{Z}_{st} = 0.055$.

6.5 Modeling

This section presents the flame dynamics modeling approach, which utilizes the experimentally measured mean and fluctuating velocity fields as inputs to the mixture fraction equation. The predicted space-time dynamics of the reaction sheet are extracted from these calculations and compared to the actual measured flame positions for various flow velocities and forcing frequencies.

6.5.1 Equation Formulation

This section presents the background equations and corresponding assumptions fundamental to this analysis. The key assumptions of this analysis are (1) infinitely fast chemistry, wherein the flame sheet collapses to the stoichiometric surface of the mixture fraction field, $\mathcal{Z}_{st}$, (2) all species have equal diffusivities, (3) negligible radiative heat loss effects, (4) small perturbation amplitudes so that the products of disturbances can be neglected, (5) unity Lewis number, and (6) local diffusivity is only a function of temperature and determined from the Hirschfelder-Bird-Spotz equation [152].

Unique to this analysis, the velocity and diffusion coefficient terms are completely general and vary in space and time. Note that prior analytical treatments of this problem have prescribed these profiles, generally using relatively simple spatial profiles to enable analytical tractability. As this equation is solved computationally in this study, no such assumption is necessary.

Following assumptions (1) and (4), and working in cylindrical coordinates, the resulting steady and fluctuating mixture fraction field governing equations are:

$$\left[U_{r,0}-\frac{\partial \mathscr{D}_0}{\partial r}\right]\frac{\partial Z_0}{\partial r}+\frac{1}{r}\left[U_{\theta,0}-\frac{1}{r}\frac{\partial \mathscr{D}_0}{\partial \theta}\right]\frac{\partial Z_0}{\partial \theta}+\left[U_{x,0}-\frac{\partial \mathscr{D}_0}{\partial x}\right]\frac{\partial Z_0}{\partial x}+ \\ -\mathscr{D}_0\left[\frac{1}{r}\frac{\partial Z_0}{\partial r}+\frac{\partial^2 Z_0}{\partial r^2}+\frac{1}{r^2}\frac{\partial^2 Z_0}{\partial \theta^2}+\frac{\partial^2 Z_0}{\partial x^2}\right]=0 \tag{6.2}$$

$$\frac{\partial Z_1}{\partial t}+\left[U_{r,0}-\frac{\partial \mathscr{D}_0}{\partial r}\right]\frac{\partial Z_1}{\partial r}+\left[\frac{U_{\theta,0}}{r}-\frac{1}{r^2}\frac{\partial \mathscr{D}_0}{\partial \theta}\right]\frac{\partial Z_1}{\partial \theta}+\left[U_{x,0}-\frac{\partial \mathscr{D}_0}{\partial x}\right]\frac{\partial Z_1}{\partial x}+ \\ -\mathscr{D}_0\left[\frac{1}{r}\frac{\partial Z_1}{\partial r}+\frac{\partial^2 Z_1}{\partial r^2}+\frac{1}{r^2}\frac{\partial^2 Z_1}{\partial \theta^2}+\frac{\partial^2 Z_1}{\partial x^2}\right]=\left[-u_{r,1}+\frac{\partial \mathscr{D}_1}{\partial r}\right]\frac{\partial Z_0}{\partial r}+\left[-\frac{u_{\theta,1}}{r}+\frac{1}{r^2}\frac{\partial \mathscr{D}_1}{\partial \theta}\right]\frac{\partial Z_0}{\partial \theta}+ \\ +\left[-u_{x,1}+\frac{\partial \mathscr{D}_1}{\partial x}\right]\frac{\partial Z_0}{\partial x}+\mathscr{D}_1\left[\frac{1}{r}\frac{\partial Z_0}{\partial r}+\frac{\partial^2 Z_0}{\partial r^2}+\frac{1}{r^2}\frac{\partial^2 Z_0}{\partial \theta^2}+\frac{\partial^2 Z_0}{\partial x^2}\right] \tag{6.3}$$

Thus, provided adequate inputs, such as prescribed diffusion coefficient and velocity fields over the ***entire*** computational domain, along with boundary conditions, the steady and fluctuating mixture fraction fields can be solved for over the domain of interest.

Part of these necessary inputs, i.e. the prescribed steady and fluctuating velocity fields, were experimentally obtained and presented in Section 6.4, while others, such as the boundary conditions, will be discussed in the next subsection. The sole remaining quantity of concern is the spatially variant diffusion coefficient, which can be re-written using the chain rule as:

$$\frac{\partial \mathscr{D}}{\partial x_i}=\frac{\partial \mathscr{D}}{\partial \mathscr{T}}\frac{\partial \mathscr{T}}{\partial Z}\frac{\partial Z}{\partial x_i} \tag{6.4}$$

The specification of $\partial \mathscr{D} / \partial \mathscr{T}$, following assumption (6), was calculated via the Hirschfelder-Bird-Spotz equation, with empirical correlation coefficients developed by Fuller specifically for methane air systems as [153]:

$$\mathscr{D}_{CH_4-Air}\left[cm^2/s\right]=\frac{10^{-3}\mathscr{T}^{1.75}\left(\frac{1}{M_{CH_4}}+\frac{1}{M_{Air}}\right)^{1/2}}{P\left[\left(V_{CH_4}\right)^{1/3}+\left(V_{Air}\right)^{1/3}\right]^2} \tag{6.5}$$

where P, M, and V are the absolute pressure in atmospheres, molecular weights, and atomic diffusion volumes [154] of the various species, i.e. methane and air. The pressure is assumed to be ambient along with the reference values for the molecular weights and diffusion volumes. Similarly, $\partial\mathscr{T}/\partial\mathcal{Z}$ is determined using assumption (5) of unity Lewis number, where the temperature dependence can be related to the mixture fraction by:

$$\begin{aligned} \mathcal{Z}<\mathcal{Z}_{st} \qquad & \mathscr{T}\left(\mathcal{Z}\right)=\frac{\mathscr{T}_a-\mathscr{T}_f}{\left(-\mathcal{Z}_{st}\right)}\left(\mathcal{Z}-\mathcal{Z}_{st}\right)+\mathscr{T}_f \\ \mathcal{Z}>\mathcal{Z}_{st} \qquad & \mathscr{T}\left(\mathcal{Z}\right)=\frac{\mathscr{T}_a-\mathscr{T}_f}{\left(1-\mathcal{Z}_{st}\right)}\left(\mathcal{Z}-\mathcal{Z}_{st}\right)+\mathscr{T}_f \end{aligned} \tag{6.6}$$

6.5.2 Boundary Conditions and Inflow Mixture Fraction Specification

There are a number of complications in comparing experimental and numerical data for the non-premixed problem, which are not present in the premixed flame problem. In prior related studies for premixed flame dynamics, all modeling inputs can be directly obtained from measurements – these are the velocity field at the flame (i.e., the mean and fluctuating velocity field upstream over the entire experimental domain is not required, as it is for the non-premixed problem) and the time averaged position of the flame [128]. In contrast, due to the elliptic nature of the mixture fraction equations, it is not sufficient to only specify the time averaged flame position and fluctuating velocity field at the flame.

Rather, as shown by the $\mathcal{Z}$-equation, the mixture fraction field, its gradient, and the fluctuating velocity field in the whole domain must be specified. This section describes the boundary conditions and approach used to specify the velocity field in regions outside of the measurement window, as well as the time averaged mixture fraction field, which was not measured.

A physical window of $90mm \times 90mm$ region of the test section was imaged, oriented symmetrically above the fuel port, spanning from the burner lip to $15R_f$ downstream, with PIV velocity data available as far as $12R_f$ downstream. Figure 6.11 shows these various regions schematically. As the transverse extent of the PIV camera capture region, $\sim 7.5R_f$, was smaller than the total experimental region, $\sim 10R_f$, the velocity field in the exterior radial region, i.e. $r>7.5R_f$, was determined by extrapolation of the measurements in the viewing window. Figure 6.5 shows how these values become constant far into the oxidizer domain, and thus $U_0(x,r>R_f)$ was set equal to $U_0(x,r=7.5R_f)$, for both the axial and radial components, respectively. The radial velocity was also set to zero at the walls, $U_{r,0}(x>0,r=R_w)=0$. Similarly, the velocity field was extrapolated downstream, i.e $x>12R_f$, utilizing the procedure previously described in Section 6.3 and Figure 6.5. Finally, the velocity in the fuel and oxidizer inflow regions, $x<0$, were set equal to their value at the inlet plane (the velocity field in this region was used to compute the inflow mixture fraction profile, described next); i.e. $U_{x,0}(x<0,r) = U_{x,0}(x=0,r)$ was utilized, with no radial component. No penetration boundary conditions were once again utilized at the fuel and oxidizer port walls, i.e. $U_{r,0}(x<0,r=R_f)=0$. Figure 6.11 also shows the various regions of actual (textured) and extrapolated (blank space) velocity

data. The same extrapolation procedure was utilized on the corresponding fluctuating velocity fields, which are also used as model inputs.

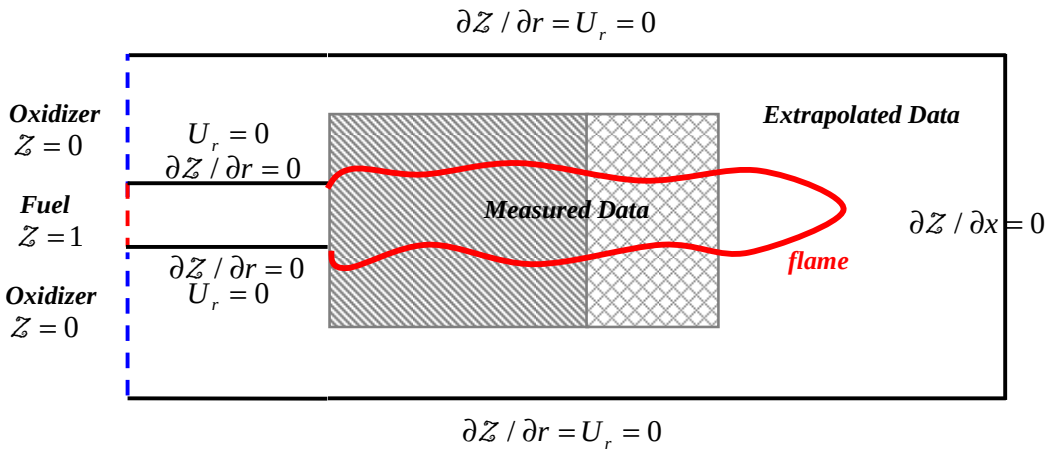

Figure 6.11. Schematic of the computational/experimental domain and the regions of various data types, boundary conditions, and inflow conditions. The white, diagonal texture, and cross-hatched textured regions indicate areas of no data, both luminosity and PIV, and only luminosity, respectively.

Consistent with the procedure followed in Section 4.3 ,the mixture fraction inlet profiles, and corresponding field, were determined by assuming pure, i.e. transversely uniform, fuel ($\mathcal{Z} = 1$) and oxidizer ($\mathcal{Z} = 0$) reservoirs, also shown in Figure 6.11, far upstream of the inflow (we used x=-50R_f). The mixture fraction inflow profile at x=0 was not specified, but rather computed as part of the problem, and extracted from the resulting computed mixture fraction field solutions, Eq.(6.2) and (6.3). Figure 6.12 shows various computed time-averaged inflow mixture fraction profiles extracted for a representative $U_{0,\mathrm{des}}$ span. An alternative, more analytically tractable and less computationally expensive approach, is to simply assume that at the x=0 inlet plane, $\mathcal{Z}$ =1 for $r \le R_f$ and $\mathcal{Z}$ =0 for $r > R_f$. However, axial diffusion of fuel and oxidizer modifies these results near the tube outlet, which was shown to have several dynamically significant effects in Chapter 4. Consequently, this computational approach was used, which smoothes the mixture

fraction profile at x=0, an effect which decreases with increasing $U_{0,des}$; i.e., increasing Pe value. Dirichlet boundary conditions were utilized at the upstream reservoir location as, $\mathcal{Z}$ =1 for $r \le R_f$ and $\mathcal{Z}$ =0 for $r > R_f$, while Neumann boundary conditions were utilized at the various port and side walls as, $\partial \mathcal{Z} / \partial r = 0$, as well as far downstream, $\partial \mathcal{Z} / \partial x = 0$.

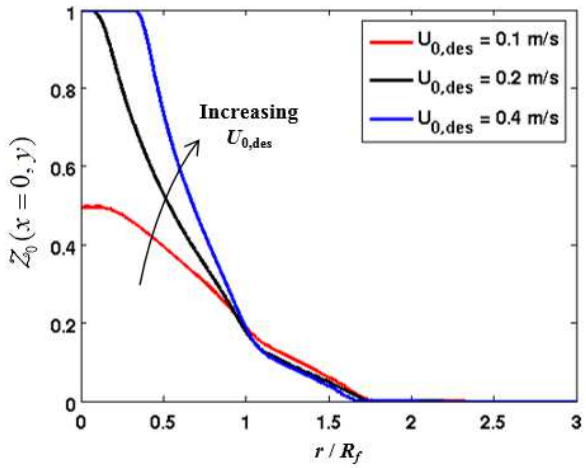

Figure 6.12. Computational time-averaged inflow mixture fraction profiles extracted for various experimental cases with $U_{0,des}$ values of 0.1 *m/s*, 0.2 *m/s*, and 0.4 *m/s* and f_f = 30*Hz*.

6.5.3 Computational Approach

Solutions of Eq.(6.2) and (6.3) were obtained with finite element methods, using the Comsol Multiphysics solver due to its balance of computational freedom and efficiency. The multifrontal massively parallel sparse direct solver, denoted MUMPS, was utilized with a convergence criterion set to 10^{-5} and relative tolerance of 0.001. This direct solver is based on LU decomposition and can take advantage of all processor cores for increased computational speed. Also, since our previous studies revealed large spatial gradients in the near burner lip region, a mapped rectangular mesh was employed, containing increased grid resolution closer to the fuel port lip. The maximum element

size, occurring near the exit plane at x=18R_f was on the order of R_f /10, while the minimum element size, occurring near the fuel port lip, was on the order of R_f / 10^3. Grid sensitivity studies were performed which showed that a uniform increase in mesh density by 9, yielded less than 2% modification in field and contour results.

As the inflow was experimentally designed and controlled to be non-swirling and laminar, the mean and fluctuating azimuthal velocity was set to zero, resulting in a simplified steady field equation:

$$\left[U_{r,0}-\frac{\partial \mathscr{D}_0}{\partial r}\right]\frac{\partial \mathcal{Z}_0}{\partial r}+\left[U_{x,0}-\frac{\partial \mathscr{D}_0}{\partial x}\right]\frac{\partial \mathcal{Z}_0}{\partial x}-\mathscr{D}_0\left[\frac{1}{r}\frac{\partial \mathcal{Z}_0}{\partial r}+\frac{\partial^2 \mathcal{Z}_0}{\partial r^2}+\frac{\partial^2 \mathcal{Z}_0}{\partial x^2}\right]=0 \tag{6.7}$$

while the fluctuating equation, Eq.(6.3), can be cast into spectral space as:

$$\begin{aligned}&\left[U_{r,0}-\frac{\partial \mathscr{D}_0}{\partial r}\right]\frac{\partial \hat{\mathcal{Z}}_1}{\partial r}+\left[U_{x,0}-\frac{\partial \mathscr{D}_0}{\partial x}\right]\frac{\partial \hat{\mathcal{Z}}_1}{\partial x}-\mathscr{D}_0\left[\frac{1}{r}\frac{\partial \hat{\mathcal{Z}}_1}{\partial r}+\frac{\partial^2 \hat{\mathcal{Z}}_1}{\partial r^2}+\frac{\partial^2 \hat{\mathcal{Z}}_1}{\partial x^2}\right]=\\&=i\omega\hat{\mathcal{Z}}_1+\left[-u_{r,1}+\frac{\partial \mathscr{D}_1}{\partial r}\right]\frac{\partial \mathcal{Z}_0}{\partial r}+\left[-u_{x,1}+\frac{\partial \mathscr{D}_1}{\partial x}\right]\frac{\partial \mathcal{Z}_0}{\partial x}+\mathscr{D}_1\left[\frac{1}{r}\frac{\partial \mathcal{Z}_0}{\partial r}+\frac{\partial^2 \mathcal{Z}_0}{\partial r^2}+\frac{\partial^2 \mathcal{Z}_0}{\partial x^2}\right]\end{aligned} \tag{6.8}$$

6.5.4 Time-averaged Flame Shapes and Model Comparisons

Once Eq.(6.7) and (6.8) are solved, iso-$\mathcal{Z}$ contours can be extracted from the resulting steady and forced field solutions which, following assumption (1), are utilized to denote the flame sheet position. Figure 6.13 shows representative results of the $\mathcal{Z}_0$ fields, where the time averaged flame position is also indicated. If the $\mathcal{Z}_0$ field were calculated perfectly, the measured flame shape would lie on the $\mathcal{Z}_0 = \mathcal{Z}_{st} = 0.055$ contour. Clearly it does not – rather, in the mid and far-field, i.e. x / R_f>3, the flame more

closely follows the $\mathcal{Z}_0 = \mathcal{Z}^* = 0.11$ contour, while near the burner lip it follows a lower valued iso-contour, dependent upon the specific case. Note how the case on the left shows much better near-field agreement with the experimental results than the case on the right. This difference in near field characteristics is likely a result of errors in the computed $\mathcal{Z}_0(x=0,r)$ inflow profile. Additionally, the nature of the mixture fraction boundary condition contributes to this discrepancy, requiring the computed flame sheet to attach normally to the fuel port wall, thru use of the no penetration mixture fraction condition, i.e. $\partial\mathcal{Z}(x<0, r=R_f)/\partial r = 0$. In reality attachment occurs at some finite angle, hence lengthening the steady flame shape, and pushing the location of maximum width downstream. Nozzle heating has been shown to significantly influence the nozzle exit region [155], while body force and gravitational effects have been shown to influence the entire mixture fraction field and resulting flame shape [156].

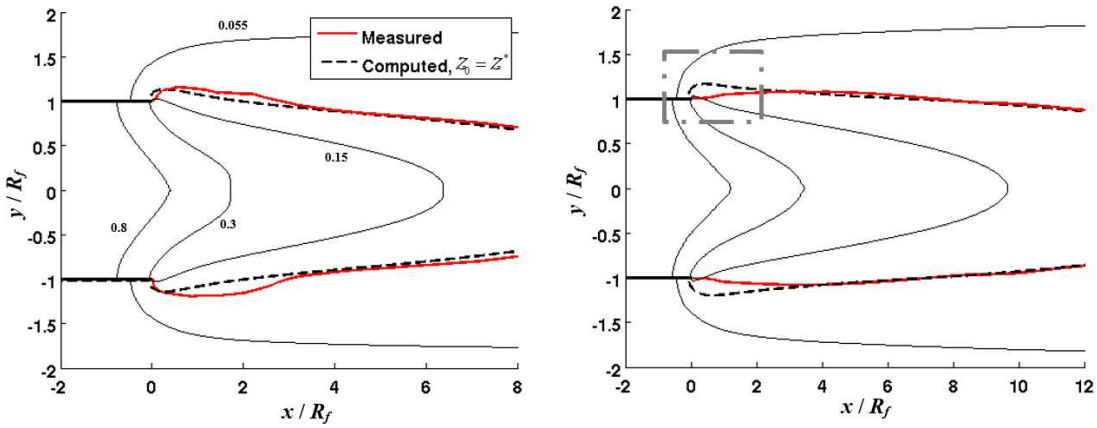

Figure 6.13. Experimental and modeled steady state flame position for two representative results for (left) Case B and (right) Case C. Also plotted are various computed iso-mixture fraction contours (thin lines) for iso-$\mathcal{Z}$ values of 0.055, 0.11, 0.15, 0.3, and 0.8. Note the difference in *x*-axis between figures.

Further downstream, the fact that the flame does not lie on the $\mathcal{Z}_0 = \mathcal{Z}_{st}$ line may reflect some of the other model assumptions; e.g., neglecting radiation effects (which would influence temperature distributions and, therefore the assumed diffusion coefficient field), and differential diffusion effects. Other studies have also shown occasional significant differences in mean flame shape between experimental results and computationally extracted iso-contour methods [157, 158]. A comprehensive study further investigating the various influencing factors on the steady flame shape is deferred to, and presented in Appendix J.

Again, as mentioned in the opening comments of Section 6.3, these issues do not create challenges for prediction of premixed flame wrinkle dynamics, as one can simply specify the time averaged flame shape, which is measured. Given these issues, we adopted the following approach for prediction of the fluctuating flame position – a modified flame identifying mixture fraction value, i.e. $\mathcal{Z} = \mathcal{Z}^*$, was utilized for the temperature-diffusion coefficient-mixture fraction relationship, needed for Eq.(6.6). The steady, $\mathcal{Z}_0$, and fluctuating, $\mathcal{Z}_1$, mixture fraction fields were then calculated via, Eq.(6.7) and Eq.(6.8), with the use of the spatially varying diffusion coefficient, Eq.(6.5). Then the mixture fraction properties were determined along the $\mathcal{Z}_0 = \mathcal{Z}^*$ iso-contour. Of particular interest, which can be seen from Eq.(2.33) and will be discussed in the next section, is the value of $\partial \mathcal{Z}_0 / \partial y$ needed to relate $\mathcal{Z}_1$ and ξ_1. By following this procedure, we use a consistent approach for calculating $\mathcal{Z}_0$ and $\mathcal{Z}_1$, and relating mixture fraction, temperature, and diffusivity. Given the lack of general near-field agreement between the measured flame slope, denoted $\partial \xi_0 / \partial x$, and that of the $\mathcal{Z}_0 = \mathcal{Z}^*$ iso-contour shown in

Figure 6.13 near x=0, we can anticipate discrepancies in the comparison of flame dynamics near x=0, an issue we will return to in the next section.

6.6 Space-time Dynamic Result Comparisons

This section presents comparisons of the measured flame response characteristics to those predicted from the mixture fraction equation using the measured velocity field as model inputs. While these previously discussed expressions, or computational fields, for $\mathcal{Z}_0$ and $\mathcal{Z}_1$ provide solutions for the mixture fraction values over the entire domain, we are particularly interested in the reaction sheet location, which is still given by the implicit equation $\mathcal{Z}(x,\xi(x,t)) = \mathcal{Z}_{st}$. Following the discussion in Section 6.5.4, an implicit expression for the time averaged flame sheet position, $\xi_0(x)$, can be determined from the coordinates where $\mathcal{Z}_0(x,\xi(x)) = \mathcal{Z}^*$. Following the procedure outlined in earlier chapters, in the limit of small disturbances, an explicit expression for fluctuating flame position can be obtained, given by Eq.(2.33), where ξ_1 is measured in the radial direction, as indicated in Figure 6.4. Utilizing this expression, flame wrinkle magnitude and phase results can be obtained utilizing the modeled mixture fraction fields, and can be compared to the experimental results for both the left and right flame branches. Some representative comparisons are shown in Figure 6.14 for various flow and forcing conditions, given in Table 6.2, representative of the range of operational parameters. Additional results are provided in Appendix K, for additional operational conditions, listed in Table 6.1. Note results are only shown for axial extents where measured data exists ***and*** the experimental flame was located, hence the shorter axial extent for the lower flow velocity cases.

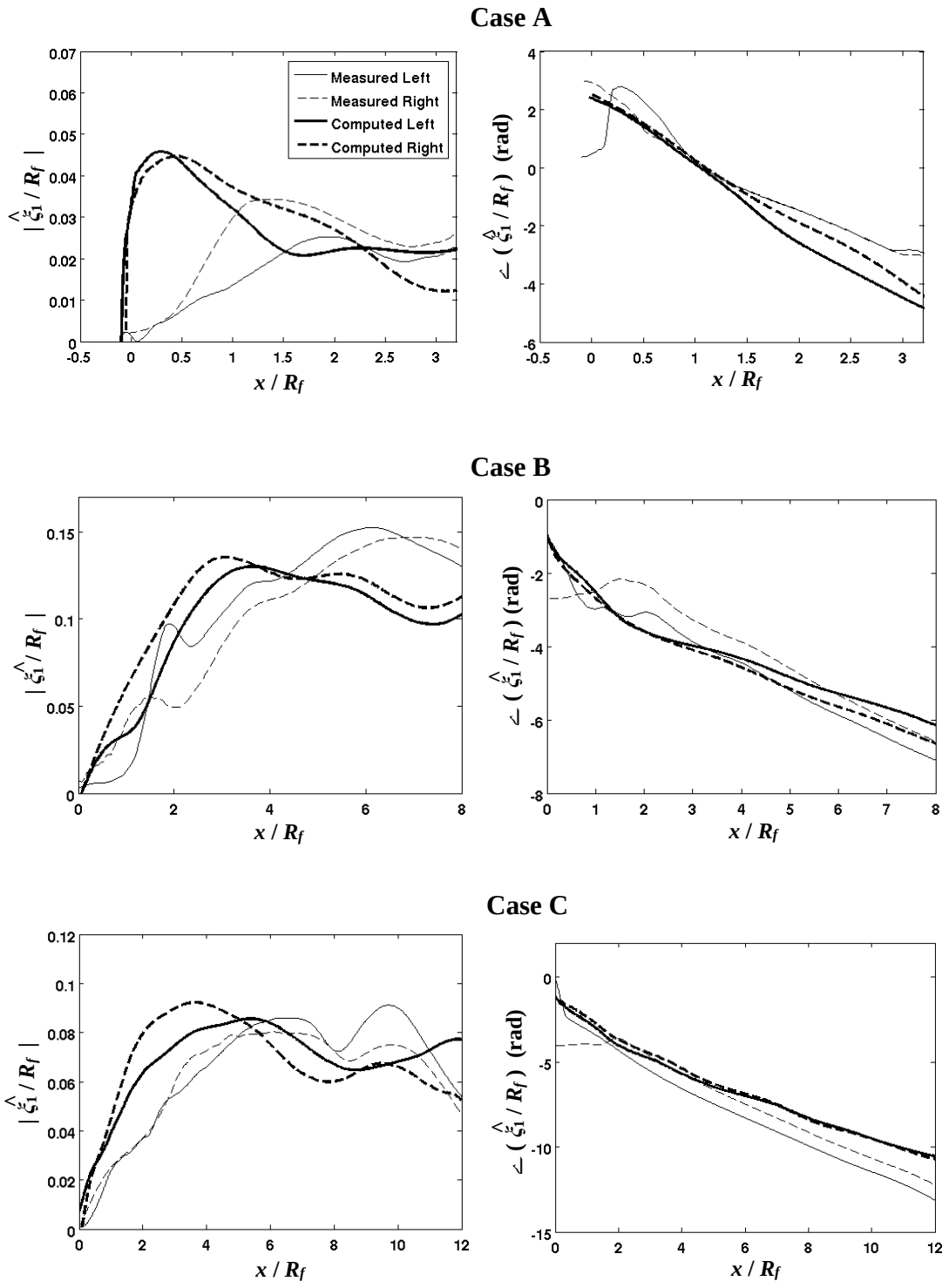

Figure 6.14. Representative space-time dynamic magnitude (left column) and phase (right column) comparisons between experimental (measured) and modeling (computed) results for a representative set of data for various $U_{0,des}$ and f_f values. Note: axial velocity extrapolation occurs downstream of presented results, i.e. $x / R_f > 12$.

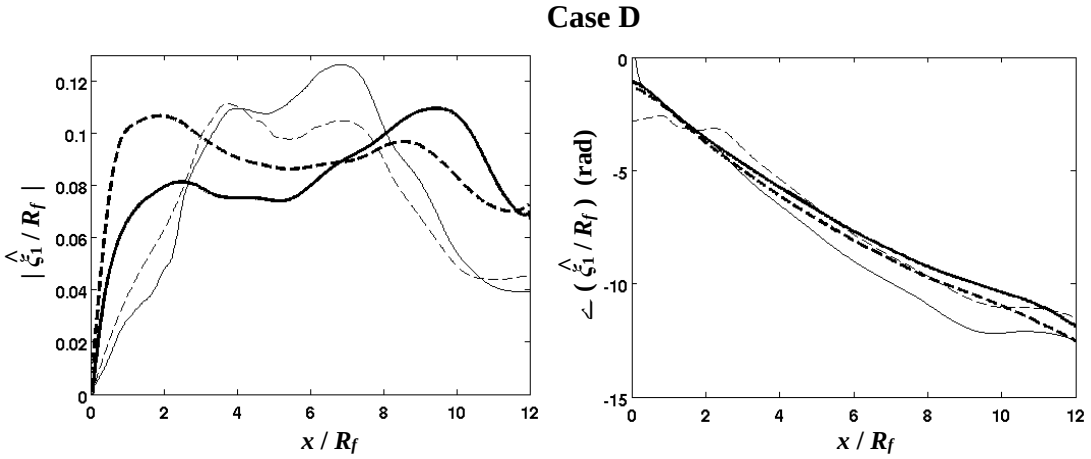

Figure 6.14 continued.

First, note the qualitative similarities between the experimental and computational results. Specifically, both results predict the rise, peaking and then falloff (possibly accompanied by some modulation) of the amplitude. The values of the peak wrinkle amplitudes are always in good agreement with the predictions. Additionally, the phase results also show the near linear rolloff with axial distance, with extremely comparable slopes. However, while the modeled result always captures the general trend of the wrinkle amplitude, the predicted slope of the initial magnitude rise, along with the axial location of the first peaks, does not always compare well to the experiments; for example, in Figure 6.14, Case B compares much better than Case C in terms of both initial amplitude rise and peak locations. We will consider this deviation in more detail at the end of this section.

Further downstream, the amplitude shows a maxima/minima pattern caused by wrinkle interference, between flame sheet wrinkles generated at the x=0 boundary and disturbances excited locally. The spatial length scale of these maxima depend upon the forcing frequency, with more modulations occurring for higher forcing frequencies, as

both expected from the physics and predicted by the calculations. With regards to the phase, the calculated curves tend to have more non-linearity than the purely experimental curves, with similar qualitative trends.

The difference in near field dependence of $|\xi_1|$ upon x could be expected from the discussion in Section 6.5.4, where it was noted that the predicted and measured flame shape also differed near x=0. Referring back to Eq.(4.6) (derived for a much simpler, bulk velocity field), note that this equation can be expanded about x in the near field, and to leading order in *Pe* results in:

$$\left.\frac{d\,|\hat{\xi}_{1,n}\,|}{dx}\right|_{x\sim 0} = \varepsilon \sin\theta_0(x) \tag{6.9}$$

Note how this equation directly shows the relationship between the slope of $|\xi_1|$ and $\sin\theta_0(x)$ for small x. Figure 6.15 shows how this flame angle quantity was defined, capturing a representative value for the near base region, x~0, rather than simply the attachment location (which would result in $\sin\theta_0(\min(x)) \sim 1$ for all computational cases via normal attachment). In order to evaluate the effect of these near field flame position prediction errors, we define a discrepancy parameter as:

$$\Delta_{x\sim 0}^{\exp-\mathrm{comp}} \equiv \left(\exp \text{parameter}\right)\Big|_{x\sim 0} - \left(\text{comp parameter}\right)\Big|_{x\sim 0} \tag{6.10}$$

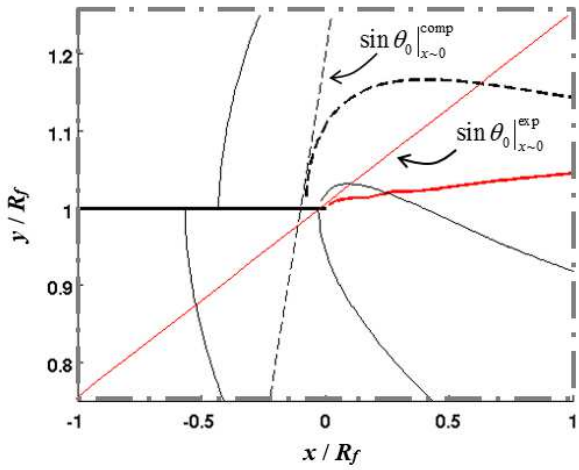

Figure 6.15. Zoomed view of boxed region of Figure 6.13, for Case C, explicitly denoting the *x*~0 computed and experimentally measured flame slopes.

Figure 6.16 plots the difference in the experimental and computed wrinkle amplitude rise in the near-base region, $|\Delta_{x\sim0}^{exp-comp} d(|\hat{\xi}_1 / R_f|)/dx|$, as a function of the difference in the experimentally extracted and computed time-averaged flame slope, $|\Delta_{x\sim0}^{exp-comp} \sin\theta_0(x)|$, for the majority of the experimental cases noted in Table 6.1. Notice, how for the cases where the initial flame slope is captured more accurately computationally, the resulting amplitude slope is also more accurate. The two cases previously utilized in Figure 6.13 and Figure 6.14 are explicitly noted on Figure 6.16 for reference. This result shows the importance in capturing the true near-field mixture fraction field characteristics, and how they are essential to accurately predicting the flame dynamics.

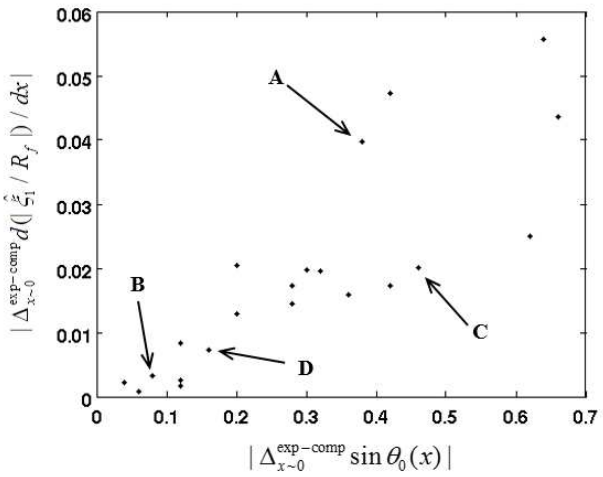

Figure 6.16. Plot showing the relation between the difference in the near-base experimental and computed (denoted utilizing $\Delta_{x\sim 0}^{\exp-\mathrm{comp}}$) flame slope, i.e. $\sin\theta_0(x)$, and wrinkle amplitude slope, i.e. $d(|\hat{\xi}_1 / R_f|)/dx$, for all edge tractable experimental cases (see Table 6.1). Cases from Table 6.2 are explicitly marked.

6.7 Revised Analytical Model – Accelerating U_0

As the above PIV results have shown, the steady state axial velocity can vary greatly in the non-premixed system, in contrast to the analytical models presented in Chapters 3 and 4, which utilized a constant, spatially invariant steady axial flow velocity. Thus, this final section addresses that issue by reinvestigating the dynamics, exposed to an axially varying steady flow velocity. The revised $\mathcal{Z}$ -equation can be represented as:

$$\frac{\partial \mathcal{Z}(x,t)}{\partial t} + \vec{u}(x,t)\cdot\nabla\mathcal{Z}(x,t) = \nabla\cdot\left(\mathscr{D}\nabla\mathcal{Z}(x,t)\right) \qquad (6.11)$$

Once again utilizing the simplified case of a two-dimensional system in the absence of axial diffusion, a form of the steady state mixture fraction field, governed by Eq.(3.3), with axially varying steady flow velocity, i.e. $U_0(x)$, can be solved for utilizing the familiar step inlet boundary condition and no-wall diffusive flux condition. The resulting solution is given by:

$$Z_0 = \frac{R_f}{R_w} + \sum_{n=1}^{\infty} \frac{2}{n\pi} \sin(\mathcal{A}_n) \cos\left(\mathcal{A}_n \frac{y}{R_f} \right) \exp\left[\int_0^{x/R_f} \frac{-\mathcal{A}_n^2}{Pe(\psi)} d\psi \right] \qquad (6.12)$$

Notice how *Pe* still retains the previous definition, given by Eq.(2.25), however is now a function of axial location due to the varying steady flow velocity. Insight into this modified axial dependence term can be gained by looking at various approximations for the axial dependence of $U_0(x)$, i.e. $Pe(x)$, several of which are shown in Table 6.3.

Table 6.3. Example axial dependencies of the steady mixture fraction solution

	exp[ ]
$Pe(x) = Pe$	$\exp\left[-\mathcal{A}_n^2 \frac{x}{PeR_f} \right]$
$Pe(x) = Pe + \widehat{Pe}x$	$\left[Pe + \widehat{Pe}x \right]^{-\mathcal{A}_n^2/\widehat{Pe}}$
$Pe(x) = Pe + \widehat{Pe}x^2$	$\exp\left[-\frac{\mathcal{A}_n^2}{\sqrt{Pe\widehat{Pe}}} \tan^{-1}\left(\sqrt{\frac{\widehat{Pe}}{Pe}} \frac{x}{R_f} \right) \right]$

The corresponding axially forced solution is also obtainable, however, it is dependent upon the definition of the fluctuation magnitude, ε. For example, if this term is a function of the axial location downstream as well, i.e. $\hat{u}_{x,1}(x) = \varepsilon U_0(x)$, the solution is different from if the term is a constant, i.e. $\hat{u}_{x,1}(x) = \varepsilon U_0$. Although for physical systems the latter is more realistic, both solutions can be considered simultaneously by considering the fluctuating mixture fraction field equation, similar to Eq.(3.4), in non-dimensional form as:

$$-2\pi i Pe(\eta) St \hat{Z}_1 + Pe(\eta)\frac{\partial \hat{Z}_1}{\partial \eta} - \frac{\partial^2 \hat{Z}_1}{\partial \zeta^2} = -Pe(\eta)\frac{\varepsilon}{\mathscr{U}(\eta)}\frac{\partial Z_0}{\partial \eta} \tag{6.13}$$

where

$$\mathscr{U}(\eta) = \frac{\varepsilon U_0(\eta)}{\hat{u}_{x,1}} \tag{6.14}$$

Utilizing this representation, no further restrictions need to be made on the form of $\hat{u}_{x,1}(x)$. The Leibniz integration rule must be utilized on the right hand side of Eq.(6.13) due to the differentiation of $\mathscr{Z}_0$, which contains an integral with variable bounds. The corresponding fluctuating mixture fraction field solution can be obtained as:

$$\hat{\mathscr{Z}}_1 = \sum_{n=1}^{\infty} \frac{2\varepsilon \mathscr{A}_n^{\,2} \sin(\mathscr{A}_n)}{n\pi} \cos\left(\mathscr{A}_n \frac{y}{R_f}\right) \exp\left[2\pi i St \frac{x}{R_f}\right] \exp\left[\int_0^{x/R_f} \left(\frac{-\mathscr{A}_n^{\,2}}{Pe(\psi)}\right) d\psi_1\right] \left[\int_0^{x/R_f} \frac{\exp[-2\pi i St \psi_2]}{\mathscr{U}(\psi_2) Pe(\psi_2)} d\psi_2\right] \tag{6.15}$$

Similarly, utilizing Eq.(2.33), an explicit equation for the flame wrinkle can be obtained as:

$$\frac{\xi_{1,n}}{R_f} = \varepsilon \sin\theta_0(x) Pe(\eta) \exp[2\pi i St \eta] \left[\int_0^{\eta} \frac{\exp[-2\pi i St \psi]}{\mathscr{U}(\psi_2) Pe(\psi)} d\psi\right] \exp[-i\omega t] \tag{6.16}$$

Comparing this expression with the corresponding one for the steady mean axial flow solution, Eq.(3.15), reveals similar features. The familiar flame angle term dependence is evident, along with the magnitude / low-pass filter characteristic, which is now built into the integrated quantity. The major difference comes with the waveform term, which is altered by the spatially varying flow velocity, resulting in a modified oscillatory mixture fraction interference pattern.

CHAPTER 7

Conclusions and Future Work

This chapter summarizes the results of this thesis and illustrates the key contributions of this work on the combustion research community, related industries, and the world. Then, several suggestions are made for future work, manifesting as both continuation studies, building upon results presented here, as well as new topics of investigation, discovered to be relevant based on results and lessons learned from this work. These investigations would continue to further our understanding of flame dynamics and lead to enhanced predictive capabilities.

7.1 Concluding Remarks

Overall, this thesis focuses on the spatiotemporal dynamics of flame response, comparing the relatively unexplored topic of non-premixed flames to the well-established set of premixed flame results. Utilizing the research trifecta, analytical, numerical/computational, and experimental analyses were employed to study the excitation, convection, and dissipation of wrinkles on the flame front. These analyses identified key controlling physics, many of which could be identified explicitly, along with key dimensionless parameters and investigatory techniques, providing insight into the complex topic of flame dynamics. Chapter 2 introduced the arsenal of exploratory tools utilized throughout, while new findings were presented from Chapter 3 through Chapter 6.

Chapter 3 presented results demonstrating the fundamental dynamics for the flame sheet motion and unsteady heat release of a harmonically forced isothermal diffusion flame. Significantly, an ***explicit*** expression for the space-time dynamics of the flame sheet was developed, along with an expression for the heat release transfer function, for bulk forced non-premixed systems. This expression demonstrated the role of axial convection in propagating flame wrinkles downstream, leading to nodes and anti-nodes in the flame response, similar to premixed flames. Additionally, the controlling nature of velocity fluctuations normal to the mean flame was demonstrated through influencing factors, such as forcing direction, confinement, and differential diffusion effects; the latter two of which altered the mean flame shape, and hence the unsteady dynamics. While the space-time dynamics were shown to be similar to premixed flames, their heat release dynamics were revealed to be quite different, premixed flames being dominated by area fluctuations and non-premixed flames by mass burning rate fluctuations. Their gain sensitivities both tend towards unity at low *St* values, but the non-premixed flame response is larger than premixed flames for $St \sim O(1)$.

Chapter 4 built upon these results, introducing more advanced system physics and configurations, and as a result, dynamical features. Some physical effects, such as system dimensionality and anisotropic diffusion, were shown to influence wrinkle dynamics only through modifications in the steady flame position. Others, such as multi-dimensional forcing and finite axial diffusion effects, resulted in more entwined modifications of the dynamics.

Swirl was shown to influence three-dimensional diffusion flames differently depending upon the forcing configuration. Only influential on the flame dynamics when

the forcing was non-axisymmetric, such as transverse bulk and helical disturbances, the effect of swirl influenced the flame spatial wrinkling and heat release fluctuations differently. Whereas these two quantities are related, they exhibit different sensitivities to frequency, dimensionless swirl number, and other flame parameters. Starting with flame wrinkling characteristics, the simultaneous azimuthal and axial propagation of wrinkles by the flow greatly altered the wrinkle structure at a given azimuthal location. For an axisymmetric flame, the helical modes in the fluctuating flow field generated an identical azimuthal dependence in the flame wrinkling behavior. In addition, it was shown that a given helical mode, m_s, dominated the amplitude of flame wrinkling, whose value was a function of swirl number, flow velocity, forcing frequency, and disturbance phase speed. In general it was shown that this mode was non-axisymmetric and could be either co- or counter- rotating relative to the mean swirl. Contrary to this rich modal behavior, for the unsteady heat release, only the axisymmetric contribution of the flame wrinkling behavior, *i.e.* the m=0 mode, contributed to the global heat release fluctuations of these axisymmetric flames, a result in accordance with premixed flame results. Although the non-axisymmetric modes produce local heat release oscillations, the contributions on opposite sides of the flame cancel, due to the 2π periodicity of these modes, leading to no global heat release fluctuations.

Numerical computations revealed that axial diffusion smoothed out the flame wrinkles as they moved downstream, eliminating spatially invariant nodes that occurred in the $Pe \rightarrow \infty$ limit. This effect was verified analytically, along with a dispersive convecting nature, when $O(Pe^{-1})$ and $O(Pe^{-2})$ terms were included, respectively, at large yet finite Pe values for simplified mixture fraction field solutions. The inlet boundary

condition was also discussed. Although several approximate forms exist in the literature, it was shown that in general, the distributions of the inlet boundary profile, must be determined computationally by simultaneously solving for the flow in the $x<0$ and $x>0$ domains. In addition the influence of axial diffusion on both the steady state and instantaneous flame positions was discussed. It was observed that with this additional physics, the instantaneous flame attachment point was a function of both Pe and $\mathcal{Z}_{st}$, as opposed to remaining fixed at the fuel port lip.

Chapter 5 focused more on the unsteady heat release dynamics of non-premixed flames, utilizing various asymptotic analyses to isolate and identify general results and limiting roll-off values. Preliminary results performed in the $Pe\rightarrow\infty$ limit showed that the transfer function curves exhibited St^0 and $St^{-1/2}$ dependencies in the low and high St limits respectively, while axial diffusion effects were shown to smooth the transfer function curves. An n-τ model was obtained for the low St asymptotics of the heat release transfer functions, while finite axial diffusion effects were shown to alter the corresponding high St asymptotics, producing an additional St roll off region of $1/St$ at large values, due to the smoothing action of the mixture fraction gradient at the fuel port lip. Significantly, these high Strouhal number solution characteristics were shown to be controlled by the gradients in the fuel/oxidizer composition at the burner outlet. While a $St^{-1/2}$ behavior occurred for the step function exit profiles, a smooth mixture fraction at the base of the flame was demonstrated to cause the non-premixed flame to exhibit a $1/St$ asymptotic behavior that one would expect of the integral with a non-singular kernel, and no points of stationary phase.

Lastly, Chapter 6 discusses the non-isothermal diffusion flame analysis and corresponding experimental efforts associated with this work. A vertical coflowing non-premixed flame facility was developed with axial forcing capabilities. Various diagnostic techniques, such as luminosity and PIV were utilized to experimentally investigate and characterize the spatiotemporal dynamics of the forced non-premixed flame. Utilizing the experimentally measured spatially variant velocity field, along with computed spatially variant diffusion coefficient as model inputs, a revised model was developed for predicting the space-time dynamics of forced diffusion flames. Good qualitative agreement was demonstrated between the experimental and modeled results with regards to flame wrinkle magnitude and phase. Near-base wrinkle amplitude growth, followed by downstream modulatory interference patterns, were captured along with general far-field trends and phase rolloff values. However, not measuring the mixture fraction field as a model input resulted in some computational limitations, specifically in the near-base region, where the largest differences occurred in terms of the axial dependence of $|\xi_1|$. Arising from discrepancies between the modeled and experimental time-averaged flame position, these results emphasize the importance of capturing the appropriate physics essential to the development of a spatio-temporally accurate mixture fraction field, if predictive dynamics are desired. These results could be further enhanced with additional experimentation by broadening the operational velocity range, as the results presented here were primarily axial convection dominated, extending the axial extent containing PIV data, and with better mitigation of the shear layer through sub-inlet velocity uniformity and matching.

7.2 Summary of Key Contributions

This thesis describes local and global response characteristics of non-premixed flames subject to harmonic velocity disturbances. The analyses were approached from various directions and utilized multiple techniques, each containing distinct strengths, limitations, and enabling a unique perspective into the flame dynamics. The problems investigated followed a logical progression, each one building upon the previous, with either increasing complexity, additional included physics, or enhanced accuracy. When tractable, separation of variables was utilized to provide analytical mixture fraction field solutions, enabling the (implicit via its own accord) investigation of non-premixed flame dynamics. For problems where analytical approaches were shown to be inadequate in consistently and completely capturing the desired physics, computational approaches were implemented for field solutions. Furthermore, experimental investigations were undertaken to reveal the various dynamical features, still obscured by mathematical simplifications. Additionally, measurements were utilized to validate, as well as, improve established models. These solution techniques, along with asymptotic analyses, provide comprehensive insights to the dynamics of non-premixed flames.

The first key finding is the establishment of a technique for obtaining explicit solutions for unsteady non-premixed flame dynamic problems. Beneficial to both space-time and heat release dynamics, the non-premixed flame realm is an inherently different problem from the premixed case, being controlled by different fundamental physics, and as such, obtaining explicit equations is not analogous or straightforward. Linearization techniques, along with intricate parametric and mathematical manipulation had to be implemented.

The second key finding is identifying and explaining the fundamental relationship between the velocity excitation and the flame response. Various elements of the dynamics were observable explicitly, such as the low-pass filter characteristic, controlling nature of locally normal velocity fluctuations, and the waveform interference behavior. Some problem conditions (boundary or assumptions) altered the wrinkle interference effects and introduced new physics to the problem, while others modified the dynamics through altering the mean flame location. The importance of accurately capturing the core physics of the problem was reinforced with experimental efforts.

The last key finding is the development of results, consistent in form although different in acquisition, which allowed for the direct comparison between established premixed and unexplored non-premixed flame dynamics. It was revealed how the overall space-time dynamics are similar, having the same dynamically relevant features. However, the heat release characteristics are fundamentally different, being dominated by different physics and having different asymptotic trends. Significantly, the resulting tri-zonal asymptotic structure demonstrates the fact that non-premixed flames are more sensitive to velocity fluctuations than premixed flames at most disturbance frequencies of relevance.

The results and findings presented here have a wide range of beneficiaries. To the research and academic realm, this work has identified and begun to fill a void present in the intellectual domain, regarding non-premixed flame dynamics; one which had become extremely lopsided in favor of premixed flame dynamics. To the combustion harnessing industries, a better understanding of fundamental flame dynamics allows for better products, systems, and, procedures. Enhanced predictive capabilities, instability

screening procedures, proactive hardware life extension, and increased efficiency are all feasible outcomes, saving time and money. To the world, these results can help make devices, big and small, which help people achieve tasks, goals, and dreams safely, efficiently, eco-friendly, and cost-effectively.

7.3 Reflections

The earliest non-premixed flame response dynamics results presented in this thesis were derived from a rather substantial list of assumptions, desiring mathematical simplicity and analytical tractability. Throughout this work, these restrictions were systematically alleviated, making the results presented more inclusive and complete, amid discussing the manner in which specific assumptions modified the system physics and flame dynamics. However, due to mathematical tractability of this physical system, some assumptions could not be lifted. It is important that we reflect back on some of these key assumptions and mention how they would potentially alter the results.

Central to the interpretation of flames, especially mathematically and computationally, the infinitely fast chemistry, i.e. thin flamelet, assumption imposed provided a compact and complete definition of the spatial flame location. In reality, finite chemistry and rate effects exist, which muddle this definition [159]. Previous studies have found that finite rate effect have little to no effect on the natural flickering dynamics of non-premixed flames [160]. Thus, the wrinkle dynamic characteristics presented here, i.e. convection, dissipation, dispersion, are still expected to hold. However, it is known that the internal structure of the flame front strongly depends on the flame thickness, which as is discussed in Appendix L, is dependent upon the imposed forcing. Thus, slight

alterations in wrinkle magnitude and convection velocity could be anticipated since as the flame thickness becomes finite, the gradients in mixture fraction are expected to diminish.

Radiation and heat loss effects were also excluded. Previous studies have assessed these effects, for both steady and unsteady non-premixed flames, and observed that the effect of radiation on the flame response and extinction becomes important only for weakly strained diffusion flames, characterized by large thicknesses (coupling in the above discussion) [161, 162]. Resulting from the competition between the mechanisms of reactant leakage and radiative loss with reducing strain rate, this effect could be potentially large near the dynamically significant flame base and flame tip. These radiative effects have also been shown to trigger nonlinear diffusion flame oscillation evolution. Nonlinear effects have been studied for both premixed and non-premixed flames, potentially introducing additional wrinkle destruction processes [62, 92].

Lastly, the results presented here have utilized flame base attachment conditions, both analytically and numerically. Even though the experimental results show this to be qualitatively true, this near base region is still somewhat ambiguous, potentially being lifted by multiple flame thicknesses. In turn, some discrepancy between the near base experimental flame angle and the imposed normal fuel port attachment due to the no-penetration boundary condition, discussed in Section 6.6 and Figure 6.16, could be altered by near base/port heat loss effects and flame extinction [47]. Additionally, the configuration of the flame attaching here could be fundamentally different, adopting more a triple flame or edge flame structure [163, 164]. This would alter the entire flame shape, and impact both the space-time dynamics, as they are a function of the steady

flame location, as well as the heat release dynamics, which revealed the significance of the near-base region.

7.4 Recommendations for Future Work

Firstly, there needs to be a stronger link between the mathematical tools and solutions available to the combustion systems of interest. A plethora of mathematical solutions exist, however, linking ones correspondence to a physical system or problem of interest and relevance (simplified or not) is where true progress is made. Accurate capturing of the mixture fraction field was shown to be of key importance throughout this thesis. Thus, a modified form of the mixture fraction equation, or even a new conserved scalar and corresponding governing equation, must be developed, one which includes a larger set of essential physics to the general non-premixed system. For example, an expression capable of providing analytical solutions for multi-dimensional anisotropic problems, completely and consistently, with body force effects, is needed..

Of similar accord, additional studies related to the general dynamics of surfaces should be pursued. A key contribution of this work was dealing with how to extract meaningful and explicit iso-surface dynamics from field equations. Being vastly applicable to various academic and industrial applications, enhanced understanding of these general dynamics would be helpful.

The next suggestion is to follow the logical flow of the results presented here, and to take some of these studies a step or two further. For example, an explicit expression was presented for the second order fluctuating flame response in terms of the mixture fraction fields, however, these were not transformed into interpretable explicit analytical expressions from which response characteristics could be extracted.

Additionally, made feasible through the various tools and techniques established here, other new and challenging problems can now be embarked upon. The non-premixed jet-in-crossflow problem, being one of extreme relevance, should be tackled with similar mixture fraction equations and analyses. Furthermore, turbulence should be introduced into the non-premixed flame problem, through the development of an ensemble averaged $\mathcal{Z}$ -equation, in order to get insight as to the effects of turbulence on the iso-surface dynamics, wrinkle evolution characteristics, and, heat release. Additionally, through proper merging with premixed flame dynamics, a governing equation for partially premixed combustion dynamics should be investigated.

Lastly, a comprehensive investigation of forced non-premixed flame dynamics through computational fluid dynamic would be a valuable study. With the ability to omnipotently control various features of the systems physics and boundary conditions, various ambiguous response characteristics could be linked to controlling system features. Additionally, more complex geometries, flows, and forcing configurations could be investigated.

Appendix A

The general fluctuating mixture fraction field solution, Eq.(3.46), presented in Section 3.2 analyzed an unconfined non-premixed flame exposed to bulk axial flow oscillations, with the inclusion of axial diffusion. The variables utilized in this solution are defined here:

$$c = \frac{Pe^2 - \sqrt{Pe^4 + 4Pe^2 w^2}}{2} \tag{A.1}$$

$$d = \frac{4\pi PeSt \dfrac{\sin(wR)}{w}\left[1 - \dfrac{\varepsilon c}{\dfrac{c^2}{Pe^2} - c + 2\pi i PeSt - w^2}\right]}{\dfrac{-2gh}{Pe^2} + h} \tag{A.2}$$

$$g = \frac{Pe^2 - Pe\sqrt{\dfrac{Pe^2 + 4w^2 + \sqrt{\left\{Pe^2 + 4w^2\right\}^2 + \left\{8\pi PeSt\right\}^2}}{2}}}{2} \tag{A.3}$$

$$h = \frac{Pe}{2}\sqrt{\frac{-Pe^2 - 4w^2 + \sqrt{\left\{Pe^2 + 4w^2\right\}^2 + \left\{8\pi PeSt\right\}^2}}{2}} \tag{A.4}$$

$$k = \frac{2\varepsilon \sin(wR)c}{w\left(\dfrac{c^2}{Pe^2} - c + 2\pi i PeSt - w^2\right)} \tag{A.5}$$

Additionally, the high *Pe* series expansions of these variables are also provided:

$$c \sim -w^2 + \frac{w^4}{Pe^2} - \frac{2w^6}{Pe^4} + O\left[\frac{1}{Pe^5}\right] \tag{A.6}$$

$$d \sim \frac{2\sin(Rw)}{w} - \frac{i\varepsilon w \sin(Rw)}{\pi StPe} + \frac{i\varepsilon w^3 \sin(Rw)}{\pi StPe^3} + O\left[\frac{1}{Pe^5}\right] \tag{A.7}$$

$$g \sim \left(-4\pi^2 St^2 - w^2\right) + \frac{80\pi^4 St^4 + 24\pi^2 St^2 w^2 + w^4}{Pe^2} + \ldots$$
$$\ldots - \frac{2688\pi^6 St^6 + 1120\pi^4 St^4 w^2 + 120\pi^2 St^2 w^4 + 2w^6}{Pe^4} + O\left[\frac{1}{Pe^5}\right] \tag{A.8}$$

$$h \sim 2\pi StPe - \frac{16\pi^3 St^3 + 4\pi Stw^2}{Pe} + \frac{448\pi^5 St^5 + 160\pi^3 St^3 w^2 + 12\pi Stw^4}{Pe^3} + O\left[\frac{1}{Pe^5}\right] \tag{A.9}$$

$$k \sim \frac{i\varepsilon w \sin(Rw)}{\pi StPe} - \frac{i\varepsilon w^3 \sin(Rw)}{\pi StPe^3} + O\left[\frac{1}{Pe^5}\right] \tag{A.10}$$

Appendix B

Here we present the explicit fuel and oxidizer mixture fraction field solutions for the example problem in Section 3.4 of the reacting mixing layer. The steady state and fluctuating field solutions are provided below, where subscript "*f*" indicates quantities evaluated at the flame sheet:

$$\mathcal{Z}_{0,Ox}(\psi) = \mathcal{Z}_{st}\frac{\left[erf\left(\psi\sqrt{\frac{U_0}{4\mathscr{D}_{Ox}}}\right)-1\right]}{\left[erf\left(\psi_f\sqrt{\frac{U_0}{4\mathscr{D}_{Ox}}}\right)-1\right]} \tag{B.1}$$

$$\mathcal{Z}_{0,F}(\psi) = 1+\left(\mathcal{Z}_{st}-1\right)\frac{\left[erf\left(\psi\sqrt{\frac{U_0}{4\mathscr{D}_{F}}}\right)+1\right]}{\left[erf\left(\psi_f\sqrt{\frac{U_0}{4\mathscr{D}_{F}}}\right)+1\right]} \tag{B.2}$$

$$\mathcal{Z}_{1,Ox} = \frac{-\mathcal{Z}_{st}\sqrt{\frac{U_0}{4\pi\mathscr{D}_{Ox}}}\frac{\varepsilon U_0}{i\omega}}{\left[erf\left(\psi_f\sqrt{\frac{U_0}{4\mathscr{D}_{Ox}}}\right)-1\right]}\frac{y}{x^{3/2}}\exp\left[\frac{-y^2}{x}\frac{U_0}{4\mathscr{D}_{Ox}}\right]\left(1-\exp\left[\frac{i\omega}{U_0}x\right]\right) \tag{B.3}$$

$$\mathcal{Z}_{1,F} = \frac{\left(1-\mathcal{Z}_{st}\right)\sqrt{\frac{U_0}{4\pi\mathscr{D}_{F}}}\frac{\varepsilon U_0}{i\omega}}{\left[erf\left(\psi_f\sqrt{\frac{U_0}{4\mathscr{D}_{F}}}\right)+1\right]}\frac{y}{x^{3/2}}\exp\left[\frac{-y^2}{x}\frac{U_0}{4\mathscr{D}_{F}}\right]\left(1-\exp\left[\frac{i\omega}{U_0}x\right]\right) \tag{B.4}$$

Appendix C

Returning to the assumption made in Section 4.2.4 of negligible azimuthal diffusion for the convecting helical disturbance solution, Figure C0.1 shows the magnitudes of the various diffusion terms along an instantaneous flame branch for a representative θ value, for a moderate level of swirl. The continual dominance of radial and axial diffusion along the length of the flame, compared to that of azimuthal diffusion, is evident.

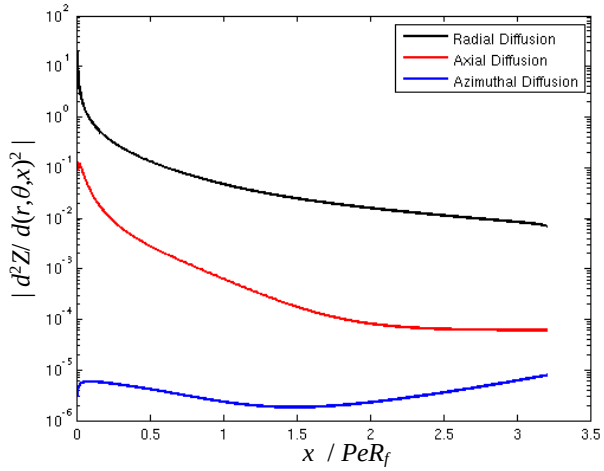

Figure C0.1. Representative plots of the instantaneous comparisons of the diffusion terms along the flame sheet for an axial convecting helical disturbance for parameters m= -1, σ=0.1, k_c=20, *Pe*=10, *St*=0.001, ε=0.01, *s*=0.25, and $\tilde{Z}_{st}$ =0.055.

Appendix D

Regarding the various proposed inlet boundary conditions discussed in Section 4.3.1, an interesting question is whether, Eq.(4.49) and (4.50) are recovered as leading order corrections to Eq.(4.47) and (4.48) with a formal asymptotic expansion of the boundary condition in Eq.(4.45) in powers of 1/*Pe*. Utilizing the general inlet mixture fraction solutions from Section 4.1, this condition can be expressed as:

$$U_0 Z_0\big|_{x=0} = U_0 Z_0\big|_{x=-\infty} - \mathscr{D}\int_{-\infty}^{0}\left[\sum_{n=1}^{\infty} A_n\left(\frac{\mathscr{A}_n}{R_f}\right)^2 \cos\left(\mathscr{A}_n \frac{y}{R_f}\right)\exp\left(\frac{x}{PeR_f}\left[\frac{Pe^2 - \sqrt{Pe^4 + 4Pe^2\mathscr{A}_n^2}}{2}\right]\right)\right]dx + \tag{D.1}$$
$$+b\mathscr{D}\left.\frac{\partial Z_0}{\partial x}\right|_{x=0}$$

Note that as the convergence is uniform, we can differentiate/integrate this infinite summation term-by-term. Simplifying and evaluating the integral and limiting bounds:

$$U_0 Z_0\big|_{x=0} = U_0 Z_{0,res} - \mathscr{D}\left[\sum_{n=1}^{\infty} A_n\left(\frac{\mathscr{A}_n}{R_f}\right)^2 \cos\left(\mathscr{A}_n \frac{y}{R_f}\right)\left[\frac{2PeR_f}{Pe^2 - \sqrt{Pe^4 + 4Pe^2\mathscr{A}_n^2}}\right]\right] + \tag{D.2}$$
$$+b\mathscr{D}\left.\frac{\partial Z_0}{\partial x}\right|_{x=0}$$

Finally expanding these terms in orders of 1/*Pe*, similar to Eq.(4.4), and rearranging yields:

$$Z_0\big|_{x=0} - \frac{bR_f}{Pe}\left.\frac{\partial Z_0}{\partial x}\right|_{x=0} = Z_{0,res} + \sum_{n=1}^{\infty} A_n \cos\left(\mathscr{A}_n \frac{y}{R_f}\right)\left[1 + \frac{\mathscr{A}_n^2}{Pe^2} - \frac{\mathscr{A}_n^4}{Pe^4} + O(Pe^{-5})\right] + \tag{D.3}$$

Notice how, to leading order, Eq.(4.49) and (4.50) are not recovered due to the presence of the last term, which is actually O(*Pe*) larger!

Appendix E

A series of analytic steady state mixture fraction field solutions can be obtained for the extended inlet geometry discussed in Section 4.3 by replacing Eq.(4.42) with Eqs.(4.51) and (4.52) as an inlet boundary condition, and using it to solve Eq.(3.3), with axial diffusion included (b=1), in the fuel/oxidizer port (x<0) and combustion regions (x>0). The new combustion region solution, valid for $x \geq 0$ & $0 \leq y \leq R_w$ and denoted $\mathcal{Z}_0^+$, can be obtained utilizing the same symmetry and no penetration boundary conditions as before, given by Eq.(3.2). Additionally, fuel and oxidizer port solutions, valid for $x < 0$ & $0 \leq y \leq R_f$ and $x < 0$ & $R_f < y \leq R_w$, respectively, and denoted $\mathcal{Z}_0^f$ and $\mathcal{Z}_0^{ox}$ can be obtained. Additional no penetration at the fuel port wall, finite mixture fraction values, and mixture fraction matching boundary conditions, must be applied to get meaningful solutions, given respectively:

$$\partial \mathcal{Z}_0 / \partial y\big|_{x<0,\, y=R_f} = 0 \tag{E.1}$$

$$\mathcal{Z}_0\big|_{x\to-\infty,\, y} = Finite \tag{E.2}$$

$$\mathcal{Z}_0^f\big|_{x=0,\,0\leq y\leq R_f} = \mathcal{Z}_0^+\big|_{x=0,\,0\leq y\leq R_f} \quad \& \quad \mathcal{Z}_0^{ox}\big|_{x=0,\,R_f<y\leq R_w} = \mathcal{Z}_0^+\big|_{x=0,\,R_f<y\leq R_w} \tag{E.3}$$

These mixture fraction solutions are shown below, along with Figure E0.1 which shows the various solution domains:

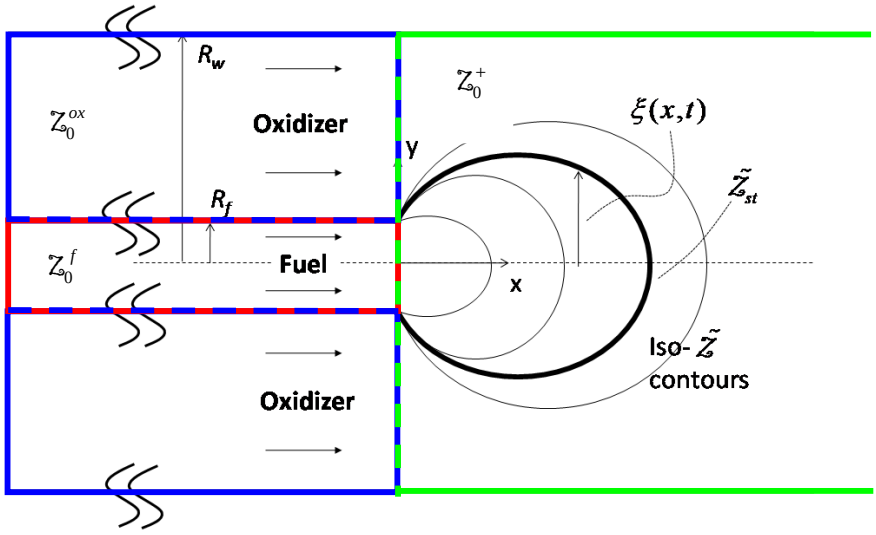

Figure E0.1. Illustration of the extended inlet geometry with the various solution domains utilized for the modified inlet boundary condition case denoted. The fuel port, oxidizer port, and original domains are enclosed by red, blue, and green boundaries, respectively.

$$\mathcal{Z}_0^{+} = s + \sum_{n=1}^{\infty} \frac{\frac{2}{n\pi}\sin(\mathcal{A}_n)}{1-\frac{r_-}{Pe^2}} \cos\left(\mathcal{A}_n \frac{y}{R_f}\right) \exp\left(r_- \frac{x}{PeR_f}\right) \tag{E.4}$$

$$\begin{aligned} \mathcal{Z}_0^{f} &= 1 + A_{0,F} \exp\left(\frac{x}{R_f} Pe\right) + \\ &+ \sum_{m=1}^{\infty} A_{m,F} \cos\left(k_{m,F} \frac{y}{R_f}\right) \exp\left(\frac{x}{PeR_f}\left[\frac{Pe^2 + \sqrt{Pe^4 + 4Pe^2 k_{m,F}{}^2}}{2}\right]\right) \end{aligned} \tag{E.5}$$

$$\begin{aligned} \mathcal{Z}_0^{ox} &= B_{0,O} \exp\left(\frac{x}{R_f} Pe\right) + \\ &+ \sum_{m=1}^{\infty}\left[A_{m,O} \sin\left(k_{m,O} \frac{y}{R_f}\right) + B_{m,O} \cos\left(k_{m,O} \frac{y}{R_f}\right)\right] \exp\left(\frac{x}{PeR_f}\left[\frac{Pe^2 + \sqrt{Pe^4 + 4Pe^2 k_{m,O}{}^2}}{2}\right]\right) \end{aligned} \tag{E.6}$$

where the various eigenvalues are:

$$r_- = \frac{Pe^2 - \sqrt{Pe^4 + 4Pe^2 \mathcal{A}_n{}^2}}{2} \tag{E.7}$$

$$\mathcal{A}_n = n\pi s \tag{E.8}$$

$$k_{m,F} = m\pi \tag{E.9}$$

$$k_{m,O} = \frac{\pi m}{\frac{1}{s}-1} \tag{E.10}$$

and the various coefficients are:

$$A_{0,F} = (s-1) + \sum_{n=1}^{\infty} \frac{2s}{\left[1-\frac{r_-}{Pe^2}\right]} \frac{\sin^2(\mathcal{A}_n)}{\mathcal{A}_n^2} \tag{E.11}$$

$$A_{m,F} = \sum_{n=1}^{\infty} \frac{4s}{\left[1-\frac{r_-}{Pe^2}\right]} \left\{ \frac{\sin^2(\mathcal{A}_n)\cos(k_{m,F})}{\mathcal{A}_n^2 - k_{m,F}^2} \right\} \tag{E.12}$$

$$B_{0,O} = s - \sum_{n=1}^{\infty} \frac{2s}{\left(\frac{1}{s}-1\right)\left[1-\frac{r_-}{Pe^2}\right]} \frac{\sin^2(\mathcal{A}_n)}{\mathcal{A}_n^2} \tag{E.13}$$

$$B_{m,O} = \frac{1}{\left(\frac{1}{s}-1\right)} \sum_{n=1}^{\infty} \frac{\frac{2}{n\pi}\sin(\mathcal{A}_n)}{\left[1-\frac{r_-}{Pe^2}\right]} \left\{ \frac{\left[\begin{array}{l} \mathcal{A}_n \sin\left(\mathcal{A}_n\left[\frac{2}{s}-1\right]\right)\cos(k_{m,O}\left[\frac{2}{s}-1\right]) - \mathcal{A}_n \sin(\mathcal{A}_n)\cos(k_{m,O}) + \\ -k_{m,O}\cos\left(\mathcal{A}_n\left[\frac{2}{s}-1\right]\right)\sin(k_{m,O}\left[\frac{2}{s}-1\right]) + k_{m,O}\cos(\mathcal{A}_n)\sin(k_{m,O}) \end{array}\right]}{\mathcal{A}_n^2 - k_{m,O}^2} \right\} \tag{E.14}$$

$$A_{m,O} = \frac{1}{\left(\frac{1}{s}-1\right)} \sum_{n=1}^{\infty} \frac{\frac{2}{n\pi}\sin(\mathcal{A}_n)}{\left[1-\frac{r_-}{Pe^2}\right]} \left\{ \frac{\left[\begin{array}{l} \mathcal{A}_n \sin\left(\mathcal{A}_n\left[\frac{2}{s}-1\right]\right)\sin(k_{m,O}\left[\frac{2}{s}-1\right]) - \mathcal{A}_n \sin(\mathcal{A}_n)\sin(k_{m,O}) + \\ +k_{m,O}\cos\left(\mathcal{A}_n\left[\frac{2}{s}-1\right]\right)\cos(k_{m,O}\left[\frac{2}{s}-1\right]) - k_{m,O}\cos(\mathcal{A}_n)\cos(k_{m,O}) \end{array}\right]}{\mathcal{A}_n^2 - k_{m,O}^2} \right\} \tag{E.15}$$

Physically, the two new inlet boundary condition expressions state that the mass flux associated with both convection and diffusion at the inlet equals the value at the reservoir, locally (i.e., at every *y* station). Comparing these proposed inflow conditions with Eq.(4.42) shows that Eqs.(4.51) and (4.52) are correct as an integral expression, but not locally, and in fact, utilizing them leads to a discontinuity in local

mass flux at x=0 at each y location. This is shown in Figure E0.2 (top-left) which plots iso-$\mathcal{Z}_0$ contours of this extended inlet domain. Note that three analytical solutions had to be obtained for the fuel port, oxidizer port, and combustion zone and solutions matched between these domains utilizing continuous mixture fraction values. Figure E0.2 (top-right) shows the slope of a representative iso-contour at the inlet for the various solutions. Note the large discontinuity in solutions at the fuel port lip, an artifact which is elucidated in Figure E0.2 (bottom) which shows the value of $\partial \mathcal{Z}_0 / \partial x$ for these solutions across the inlet.

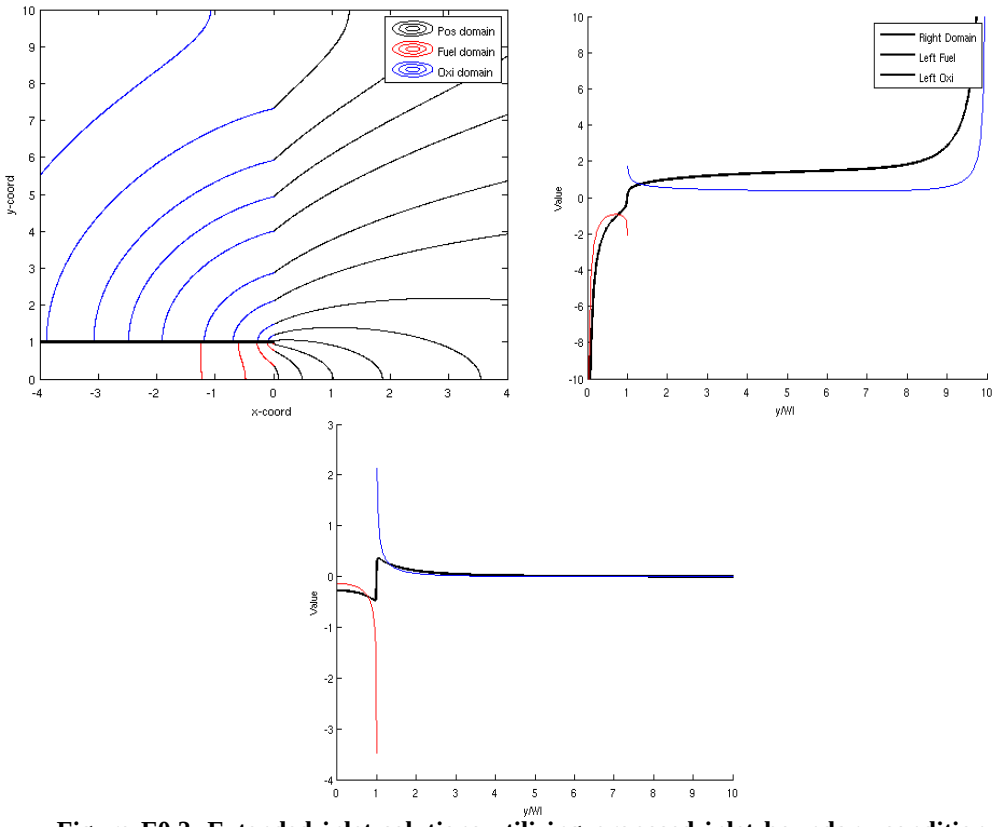

Figure E0.2. Extended inlet solutions utilizing proposed inlet boundary condition for (top left) iso-contours of mixture fraction, (top right) iso-contour of slope at the inlet, and (bottom) diffusive flux at the inlet.

Appendix F

Presented are the details of the heat release transfer function high *St* asymptotics, mainly Eq.(5.3). This expression can be obtained by simplifying Eq.(5.2), utilizing various physical features present in the $Pe\to\infty$ and high *St* limits. It is helpful to note that Eq.(5.2) can be recast utilizing geometric relations between the flame angle and the mixture fraction fields as:

$$g(x,\xi_0)=\frac{-\dfrac{\partial Z_0(x,\xi_0)}{\partial x}}{\dfrac{\partial Z_0(x,\xi_0)}{\partial y}}\frac{\partial^2 Z_0(x,\xi_0)}{\partial y^2}+\frac{d^2 Z_0(x,\xi_0)}{dxdy} \tag{F.1}$$

First, in the high *Pe* limit, Figure 3.11 and the corresponding discussion showed that $Z_0(x)$ becomes nearly independent of *x* as the flame becomes infinitely flat and long, and thus the flame position can be approximated by $\xi_0(x)\sim R_f(1+O(1/Pe))$ except at the tip (a point which will be made irrelevant soon). Utilizing the unconfined $Pe\to\infty$ mixture fraction field solutions from Section 3.2 for analytical clarity (same results obtainable from the confined solutions, requiring various infinite summation limit evaluations), substituting $\xi_0(x)=R_f$ into Eq.(F.1) and simplifying yields:

$$g(x,\xi_0)=\frac{-\exp\left(-\dfrac{1}{\left(\dfrac{x}{PeR_f}\right)}\right)^2}{2\sqrt{\pi}xR\left(\dfrac{x}{PeR_f}\right)^{3/2}\left[\exp\left(-\dfrac{1}{\left(\dfrac{x}{PeR_f}\right)}\right)-1\right]}+\frac{\left[1+\left(\dfrac{2PeR_f}{x}-1\right)\exp\left(-\dfrac{1}{\left(\dfrac{x}{PeR_f}\right)}\right)\right]}{4Pe\sqrt{\pi}R_f{}^2\left(\dfrac{x}{PeR_f}\right)^{3/2}} \tag{F.2}$$

Next, as was shown in Section 4.3 (specifically Section 4.3.4.1), in the high *St* limit, the global heat release is controlled by the features of $g(x,\xi_0)$ near $x=0$. Thus, expanding Eq.(F.2) around small values of *x*, yields:

$$g(x,\xi_0)=\frac{1}{4Pe\sqrt{\pi}R_f{}^2\left(\frac{x}{PeR_f}\right)^{3/2}}+HOTs \tag{F.3}$$

which can be rearranged to match the form of Eq.(5.3).

Appendix G

Presented are the details of the heat release transfer function low *St* asymptotics. Starting with an expansion of $\mathcal{Z}_1$ in the *Pe*→∞, low *St* limit:

$$\mathcal{Z}_1(x,y,t) = -\varepsilon x \frac{\partial \mathcal{Z}_0}{\partial x}\exp(-i\omega t) - \frac{i\pi\varepsilon St x^2}{R_f}\frac{\partial \mathcal{Z}_0}{\partial x}\exp(-i\omega t) + O(St^2) \tag{G.1}$$

Using Eq.(2.33) and the geometric relation, $\tan\theta_0 \equiv d\xi_0 / dx$, it can be shown that in the low *St* limit, the flame position fluctuation can be expressed in terms of the steady flame position as:

$$\xi_{1,n} = -\left[1 + \frac{i\pi St x}{R_f}\right]\varepsilon \cdot \frac{d\xi_0}{dx} \cdot x \cdot \exp(-i\omega t) + O(St) \tag{G.2}$$

Noting that:

$$\frac{\partial}{\partial x}\left[\frac{\partial \mathcal{Z}_0(x,\xi_0(x))}{\partial y}\right] = \frac{\partial^2 \mathcal{Z}_0(x,\xi_0(x))}{\partial x \partial y} + \frac{d\xi_0}{dx}\frac{\partial^2 \mathcal{Z}_0(x,\xi_0(x))}{\partial y^2} \tag{G.3}$$

And utilizing these expressions, Eq.(3.27) can be rewritten in the low *St* limit as:

$$\frac{-\varphi_{ox}}{(1+\varphi_{ox})^2 \rho \mathscr{D} \mathscr{h}_R}\dot{Q}_1(t) = -\int_0^{L_{f,0^-}^+} x \frac{\partial}{\partial x}\left(\frac{\partial \mathcal{Z}_0(x,\xi_0(x))}{\partial y}\right)\left[1 + \frac{i\pi St x}{R_R}\right]\varepsilon \exp(-i\omega t)dx \tag{G.4}$$

This integral can be simplified using integration by parts, and results in:

$$\begin{aligned}\frac{-\varphi_{ox}}{(1+\varphi_{ox})^2 \rho \mathscr{D} \mathscr{h}_R}\dot{Q}_1(t) = &\int_0^{L_{f,0^-}^+} \frac{\partial \mathcal{Z}_0(x,\xi_0(x))}{\partial y}\varepsilon \exp(-i\omega t)dx + \\ &+ \int_0^{L_{f,0^-}^+} \frac{2\pi i St}{R_f} x \frac{\partial \mathcal{Z}_0(x,\xi_0(x))}{\partial y}\varepsilon \exp(-i\omega t)dx\end{aligned} \tag{G.5}$$

Notice how the leading order term resembles the steady state heat release, Q_0, given by Eq.(3.26). Thus putting this in terms of the transfer function, i.e. Eq.(3.29):

$$\mathcal{F} = 1 + iSt_{Lf} \frac{2\pi \int_0^{L_{f,0}} x \frac{\partial Z_0(x, \xi_0(x))}{\partial y} \cdot dx}{L_{f,0} \int_0^{L_{f,0}} \frac{\partial Z_0(x, \xi_0(x))}{\partial y} \cdot dx} + O(St_{Lf}^2) \qquad \text{(G.6)}$$

Appendix H

Presented is the steady state mixture fraction solution for an unconfined system, that excludes axial diffusion (i.e. setting b=0 in the governing equation given by Eq.(3.3)), and utilizes the piecewise linear inlet boundary condition shown in Figure 5.6.

$$Z_0(\tilde{x},\tilde{y}) = \frac{1}{2}\left[\begin{array}{l} \left[\frac{\tilde{y}+1+\delta}{2\delta}\right] erf\left(\frac{(-1+\delta-\tilde{y})}{2\sqrt{\tilde{x}}}\right) - \frac{\tilde{x}}{\delta}\exp\left(-\frac{(\tilde{y}+1+\delta)^2}{4\tilde{x}}\right) + \\ -\left[\frac{\tilde{y}+1+\delta}{2\delta}\right] erf\left(\frac{(-1-\delta-\tilde{y})}{2\sqrt{\tilde{x}}}\right) + \frac{\tilde{x}}{\delta}\exp\left(-\frac{(\tilde{y}+1-\delta)^2}{4\tilde{x}}\right) + \\ +\left(erf\left(\frac{1-\delta-\tilde{y}}{\sqrt{4\tilde{x}}}\right) - erf\left(\frac{-1+\delta-\tilde{y}}{\sqrt{4\tilde{x}}}\right)\right) + \\ +\left[\frac{-\tilde{y}+1+\delta}{2\delta}\right] erf\left(\frac{(1+\delta-\tilde{y})}{2\sqrt{\tilde{x}}}\right) + \frac{\tilde{x}}{\delta}\exp\left(-\frac{(\tilde{y}-1+\delta)^2}{4\tilde{x}}\right) + \\ -\left[\frac{-\tilde{y}+1+\delta}{2\delta}\right] erf\left(\frac{(1-\delta-\tilde{y})}{2\sqrt{\tilde{x}}}\right) - \frac{\tilde{x}}{\delta}\exp\left(-\frac{(\tilde{y}-1-\delta)^2}{4\tilde{x}}\right) \end{array}\right] \quad \text{(H.1)}$$

where non-dimensional coordinates are being utilized for compactness and were previously defined by Eq.(2.23).

Appendix I

Presented are various additional views and images of the forced non-premixed experimental facility.

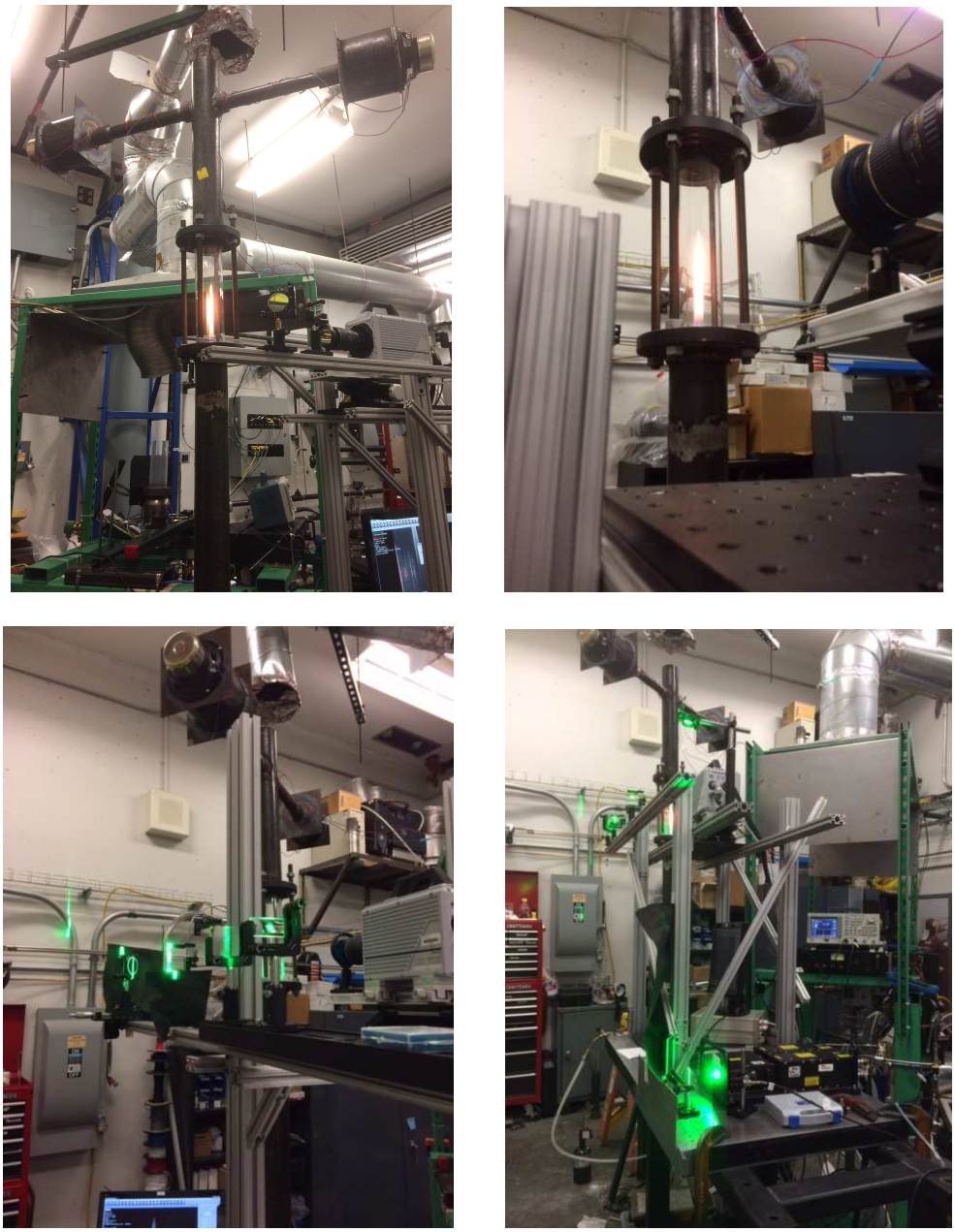

Figure I0.1. Pictures of the experimental rig facility.

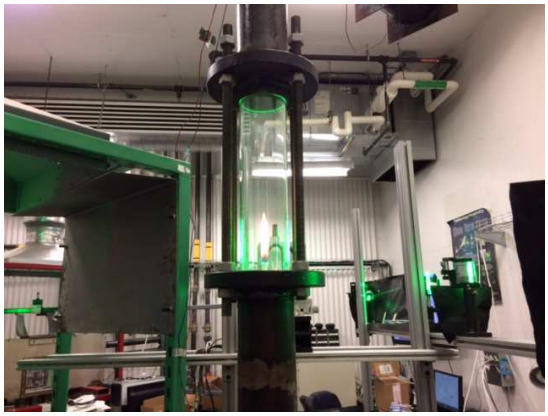

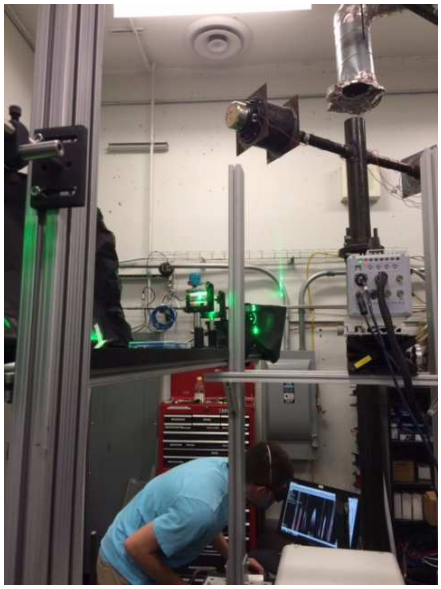

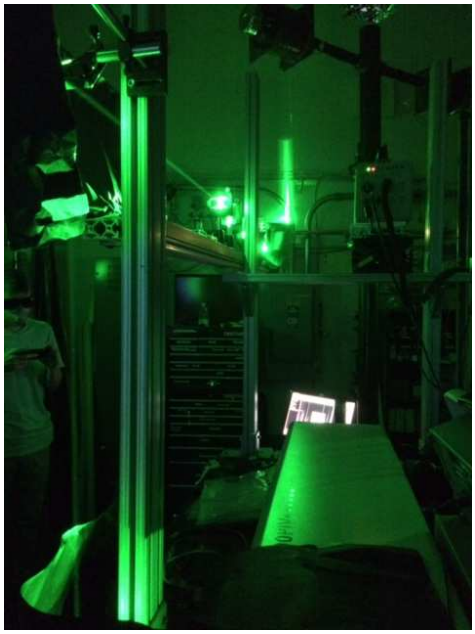

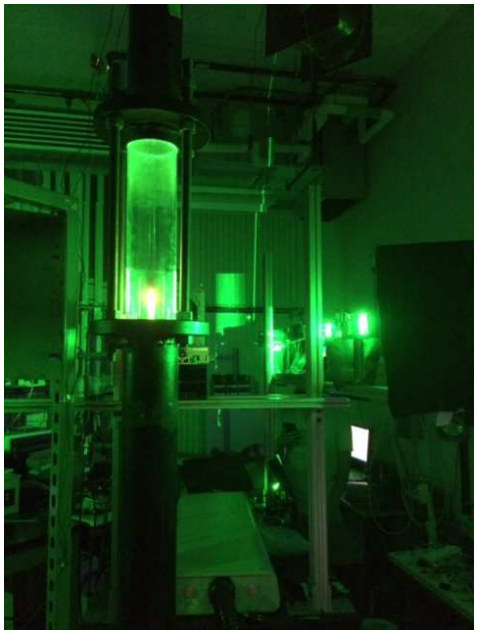

Figure I0.1 continued.

Appendix J

This appendix describes the computational fluid dynamic (CFD) efforts taken in order to broaden our understanding of non-premixed flame dynamics. The results, both analytical and numerical, from previous chapters revealed the importance of the steady flame location on the unsteady flame dynamics. Chapter 6 revealed the extreme sensitivity of accurate spatiotemporal dynamic predictions/modeling on accurately capturing the steady field and flame location, while Section 6.5.4 identified various limitations and discrepancies of the mixture fraction model approach and experimental results. Thus, here we present a through investigating of the influencing factors on the steady flame shape.

Additionally, the various results presented have utilized varying degrees of restrictive assumptions. These have been from as brash as ignoring the flames heat release, to as reserved as the thin flamelet assumption. A secondary objective of this work extension is to examine the effects of these various assumptions on the flame dynamics. Chapter 6 started on this endeavor by examining experimental non-premixed flame systems, however, due to the uncontrollability of real life systems, it was difficult to isolate the various “realistic” effects, such as viscous effects from flame heat release effects, as everything was coupled within the results obtained. Thus, this study also seeks to answer these questions by utilizing computational fluid dynamics, and the ANSYS Fluent solver, to methodically investigate the influence of various restrictive assumptions imposed.

J.1 Overview

The key to obtaining meaningful results from CFD for combustion related applications is the use of an appropriate combustion model within the solver. The choice of a particular model should be based on the capability of the model to capture the essential and characteristic physics of the problem considered. For example, the characteristics of many industrially relevant flame problems involve lifted, swirl-stabilized flames, and if the turbulent combustion model does not contain the physics essential to capturing the flame lift-off, it will not have any subsequent predictive capability for features such as space-time dynamics or pollutant emissions. In other words, the basic physics and relevant tools must be right. Fluent has proven to excel at thermal fluid flow and heat transfer combustion problems, containing advanced, flamelet-based combustion models which have proven to yield substantial improvements as compared to default models available in other CFD software packages.

Specifically, we will take advantage of Fluent's non-premixed combustion model, which uses a modelling approach that solves transport equations for one or two conserved scalars and the mixture fractions. Multiple chemical species, including radicals and intermediate species, may be included in the problem definition, and their concentrations can be derived from the predicted mixture fraction distribution. Thus, combustion is simplified to a mixing problem, and the difficulties associated with closing non-linear mean reaction rates are avoided. Once mixed, the chemistry can be modeled as being in chemical equilibrium with the equilibrium model, or being near chemical equilibrium with the steady laminar flamelet model. Additionally, to use this model, turbulence must be enabled in the viscous model.

J.2 Meshing

As for all computational solvers, the computational domain needs to be divided into small finite volume elements, i.e. meshing. Utilized here is a mesh of structured hexahedral elements, although other polyhedrals may also be used, meaning that each element connects to as many elements as it has faces and the mesh is arranged in an orderly topological fashion. With eight vertices necessary for a single block of mesh, these points were defined for our various combustion and port regions, and the interior hexagonal mesh was built with OpenFOAMs blockmesh utility, utilizing evenly spaced elements, i.e. simple-grading. Specifically, domain extents were divided into 0.01m segments. Blockmesh was utilized due to its fast, efficient, and easily dynamic mesh construction excelling for simple geometries, specifically this inverse wedge flow. A wire-frame view of the mesh domain is shown in Figure J0.1, consisting of 280,224 cells, 563563 faces, and 283340 nodes with minimum orthogonal quality and max aspect ratio of 0.99998 and 2.97, respectively. Inflow, wall, and outflow conditions were then imposed on the respective faces. Lastly, note the finite thickness of the fuel port wall, having a value of 0.001m at the far upstream “reservoir” location.

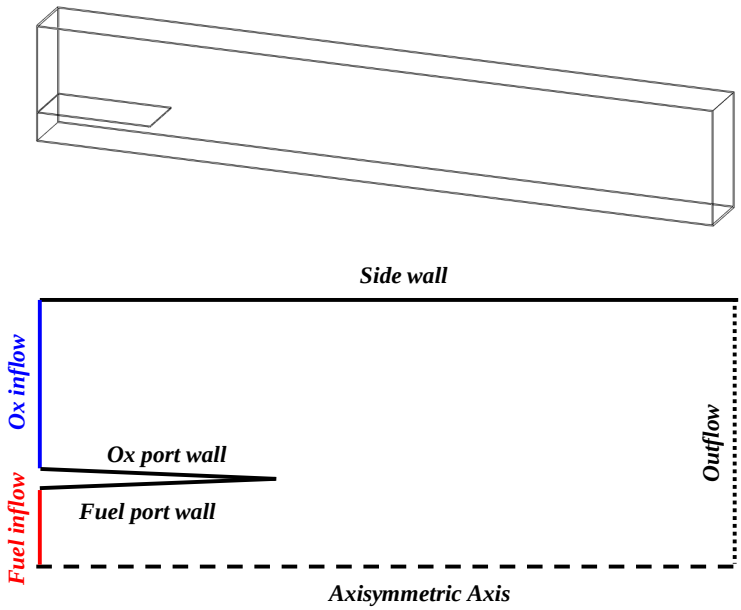

Figure J0.1. Fluent axi-symmetric computational domain depicted by a (top) wire-frame view and (bottom) schematically labeled side view.

J.3 Details of Schemes

The specific solver utilized was an axisymmetric three-dimensional pressure-based solver, with absolute velocity formulation, including the energy equation, viscous standard k-epsilon equation, and species non-premixed combustion model in Fluent, and utilizing Chemical Equilibrium state relation and non-adiabatic energy treatment. Gravitational effects could be turned on and off in the axial direction as pleased. When studying steady-state problems, the SIMPLE (semi-implicit method for pressure-linked equations) pressure-velocity coupling algorithm was utilized, as it was not necessary to fully resolve the linear pressure-velocity coupling, since changes between consecutive solutions were no longer small. The gradient was computed utilizing a least squares cell based method, while second order spatial discretization was used for all species and parameters, with second order upwind schemes.

J.4 Equations and Solver Sets

A list of all the equations utilized throughout this study (in various combinations) is provided, for reference throughout this appendix:

E1) user defined scalar (mixture fraction equation) with unity and nil inflow boundary conditions at the fuel and oxidizer inflow faces, respectively

E2) flow equations with specified inflow velocities and outlet fluxes

E3) turbulence k-epsilon equations with set turbulence intensity and viscosity ratios to model laminar flow

E4) energy equation with set inflow reactant temperatures

E5) species non-premixed combustion model with probability density function (PDF) mixture fraction model

E6) species transport model.

Preliminary axisymmetric results were validated with a similar configuration three-dimensional cylindrical mesh, to ensure axisymmetric solver validity.

One major advantage of using a solver such as Fluent is the flexibility to solve our non-premixed flame system with various physical flame characteristics included or excluded. This allows for the comparison of the various analytical and computational results presented throughout this work, with the experimental results. We will also be able to isolate which assumptions were the most important and impactful on the various solution characteristics.

To do this requires various solver sets to be defined. The first, denoted "**Z**" (solving *E1*), solves over the solution domain for a conserved scalar (with diffusive properties similar to methane), with inflow conditions given similar to Eq.(4.34). This

solver utilizes a prescribed steady flow velocity and correlates to the solvers previously utilized throughout Chapter 4 and 5, utilized primarily for validation and as a control. The next solver, denoted "**ZF**" (solving *E1* and *E2*), introduces viscous effects by solving the flow equations, along with the conserved scalar equation, thus modifying the velocity fields. The next solver, denoted "**ZFS**" (solving *E1*, *E2*, *E3*, *E4*, *E6*), introduces multi-species transport effects to the previous solver, by solving the species transport equations along with the flow and conserved scalar equations. This will allow for differential diffusion effects to occur. The next solver, denoted "**ZFR**" (solving *E1*, *E2*, *E3*, *E4*, *E5*), introduces heat release effects by solving for non-premixed reacting flow equations, utilizing the described non-premixed combustion model (rather than the species transport equations). These latter two solvers are also taken one step further by the inclusion of body force and gravitational effects, and will be denoted "**ZFSG**" and "**ZFRG**", respectively.

J.5 Steady Results

Figure J0.2 shows various computationally extracted steady state flame position solutions, utilizing these various solvers. When applicable, we track both stoichiometric contours of the conserved scalar, as well as those of the CH_4 field. The conserved scalar profiles are modified due to the impact of the various species transport and reaction equations on the flow fields, which in turn modify the conserved scalar.

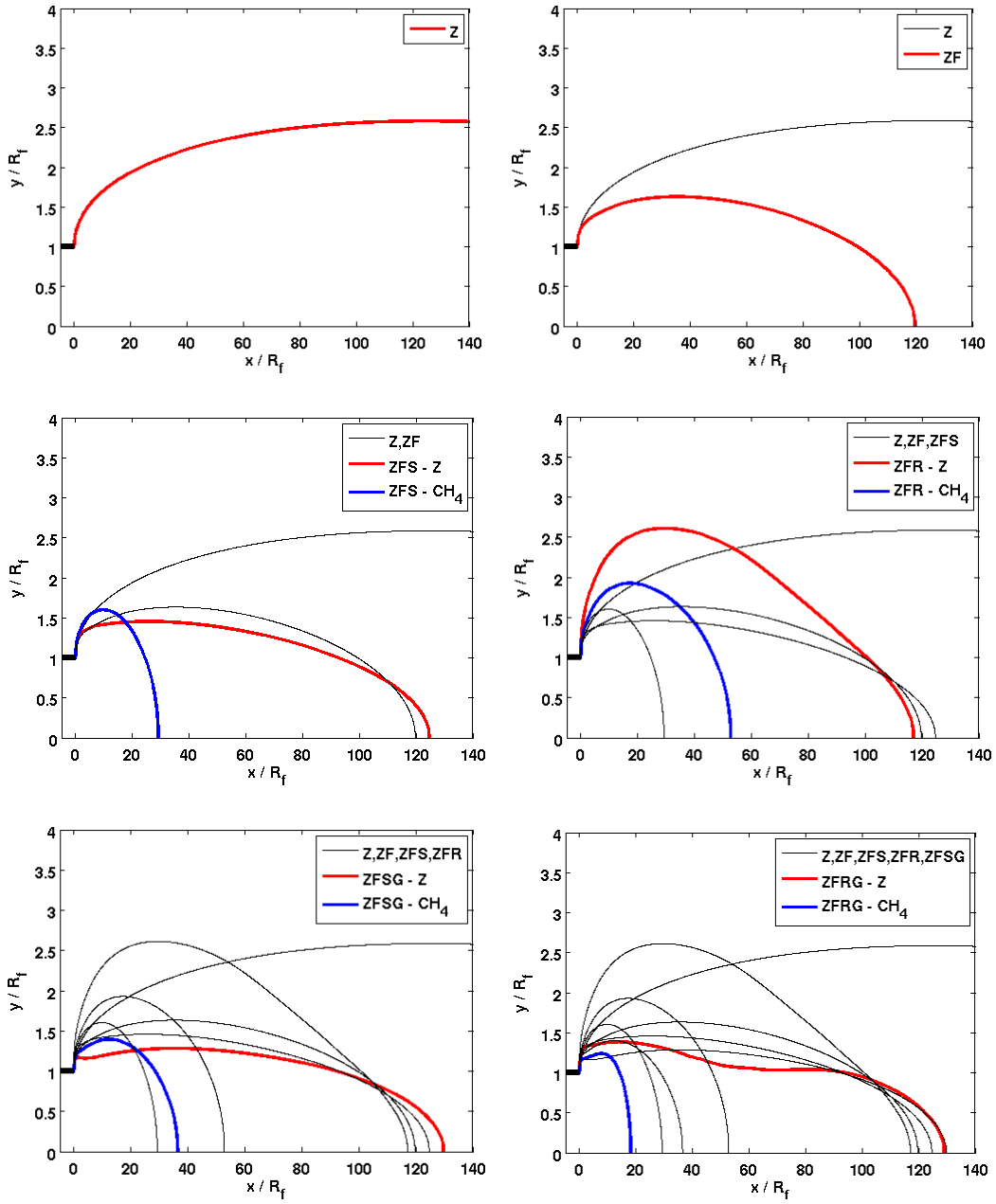

Figure J0.2. Various fluent solution sets for the axi-symmetric non-premixed flame model problem, for fuel and oxidizer inflow velocities of 0.4 *m/s* for a system consisting of pure methane and air reservoirs for the fuel and oxidizer streams, respectively.

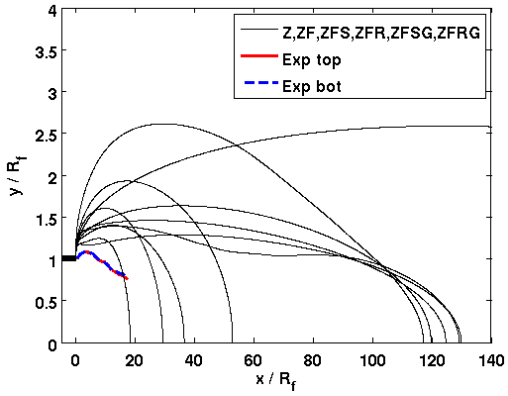

Figure J0.2 continued.

Some key effects can be noted from Figure J0.2. The inclusion of viscous/flow effects drastically reduces the overall flame length and width, presumably due to modifications to the inlet mixture fraction profile. Heat release effects, generating flow expansion on both sides of the flame sheet, act to widen the flame position. Differential diffusion acts to alter the shape slightly, however, it is not until gravitational effects are included, that the flame shape begins to resemble tangible diffusion flames, such as candles. Significant narrowing of the flame is evident, even with flame lift-off attachment required. Previous studies have also observed the significant influence of body forces on the steady flame shape [156, 165-167]. For example, Figure J0.3 shows the effects of gravity on the steady candle diffusion flame shape. Notice how the flame in microgravity (absent of co-flow however) resembles many of the steady iso-$\mathcal{Z}_0$ contours from the various analytical studies, while the flame in standard Earth gravity resembles many of the experimentally extracted edges!

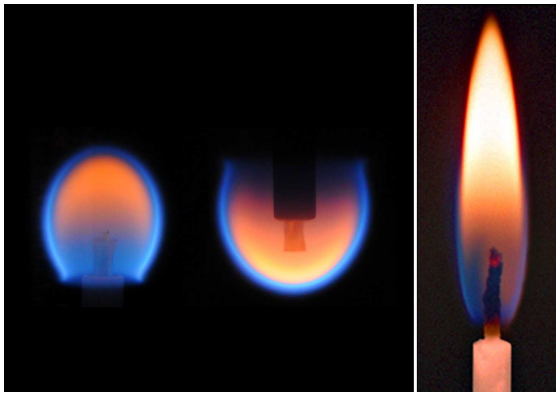

Figure J0.3. Images of a candle diffusion flame (left) in microgravity and (right) normal earth gravity [168].

A final subtlety of this study involves the various potential flame location defining definitions. Previously restricted to iso-mixture fraction contours, we are now able to investigate alternate mathematical definitions, such as individual species or maximum property contours. Figure J0.4 shows various different flame position definitions, compared to the experimentally measured values for the diffusion flame rig, discussed in Section 6.2, operated at $U_{0,des}$=0.4 *m/s*, in the absence of forcing. Interestingly, the temperature and OH species contours show the best agreement to the experimentally observed shapes.

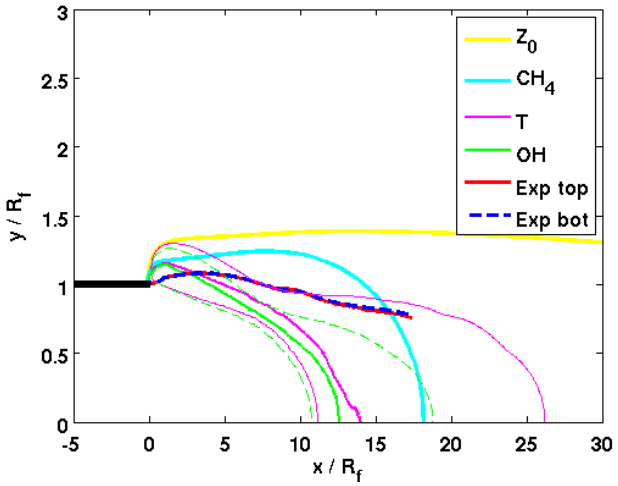

Figure J0.4. Fluent solution sets for the axi-symmetric non-premixed flame model problem showing the various steady flame position definitions, for fuel and oxidizer inflow velocities of 0.4 *m/s* and consisting of pure methane and air reservoirs for the fuel and oxidizer streams, respectively. For the temperature and OH species curves, the thin lines indicate 90% maximum iso-contours, while the thick lines indicate the axial dependence of the transverse maximums.

Appendix K

Presented are additional results, extending the discussion in Section 6.6 regarding Figure 6.14, for additional operational conditions, listed in Table 6.1. Note results are only shown for axial extents where measured data exists ***and*** the experimental flame was located, hence the shorter axial extent for the lower flow velocity cases.

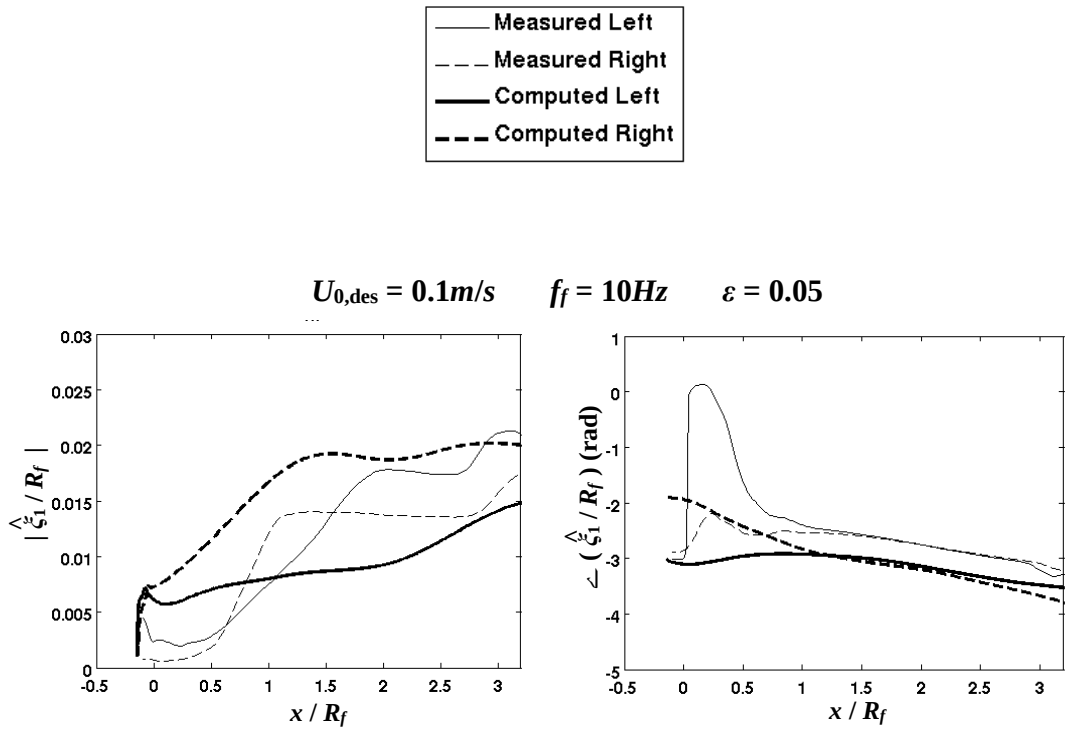

Figure K0.1. Additional space-time dynamic magnitude (left column) and phase (right column) comparisons between experimental (measured) and modeling (computed) results for an expanded set of data for $U_{0,des}$ = 0.1*m/s* and various f_f values. Note: axial velocity extrapolation occurs downstream of presented results, i.e. $x / R_f > 12$.

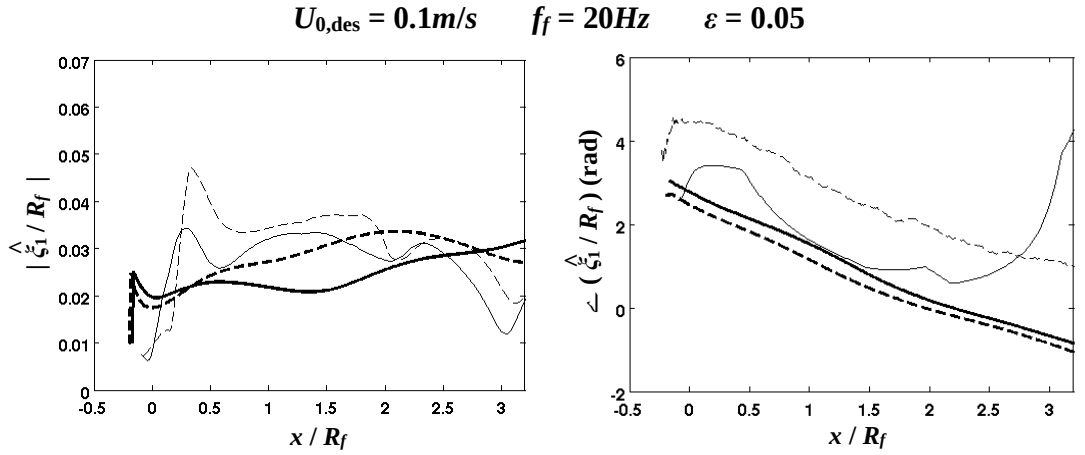

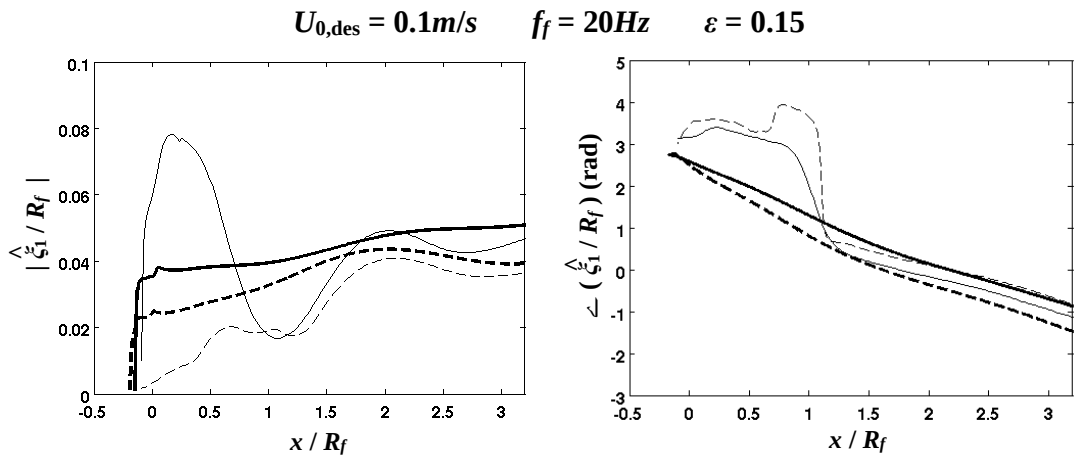

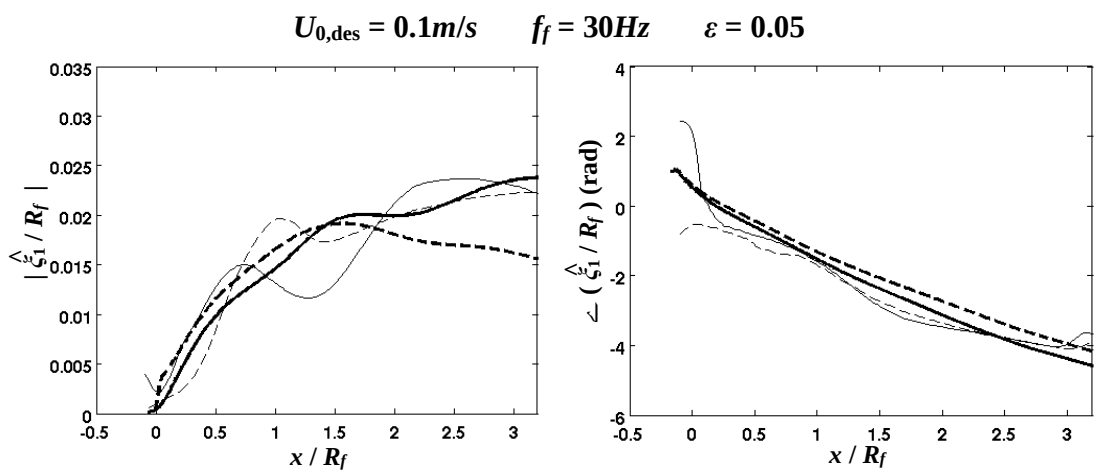

Figure K0.1 continued.

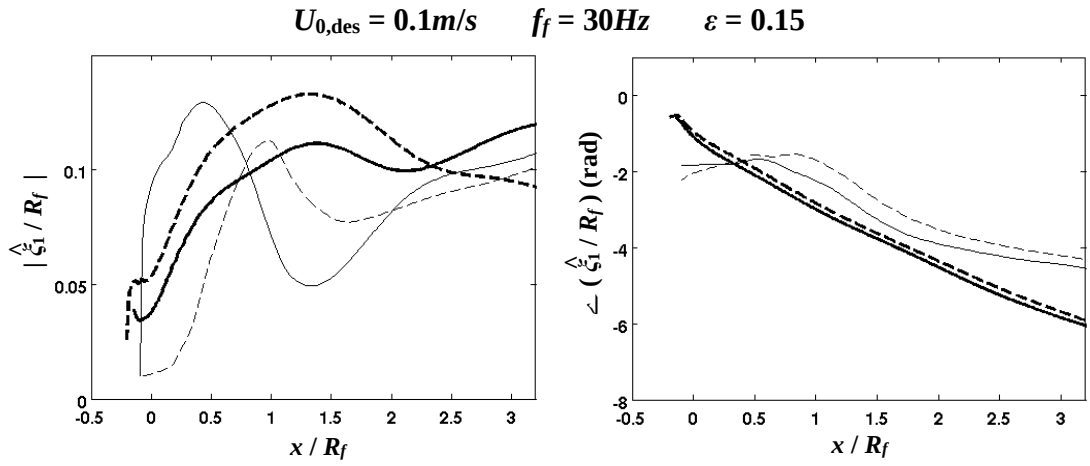

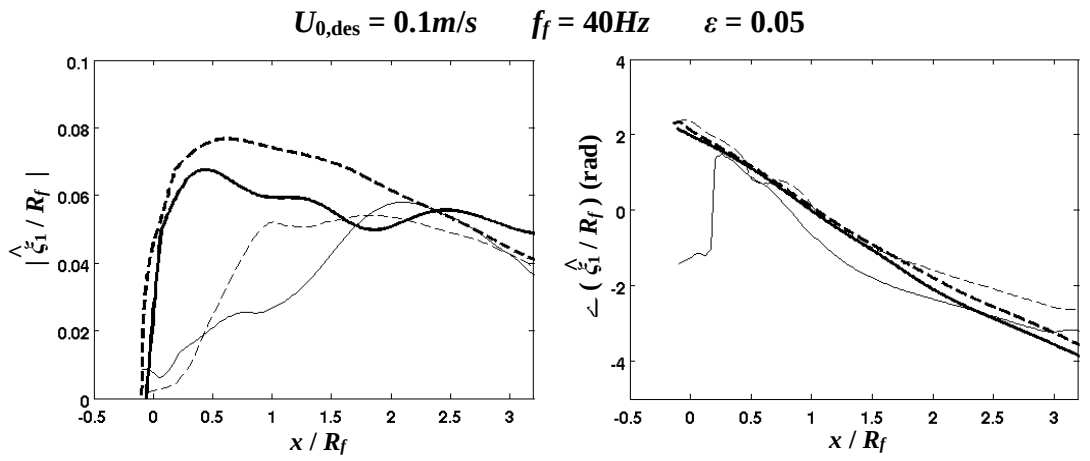

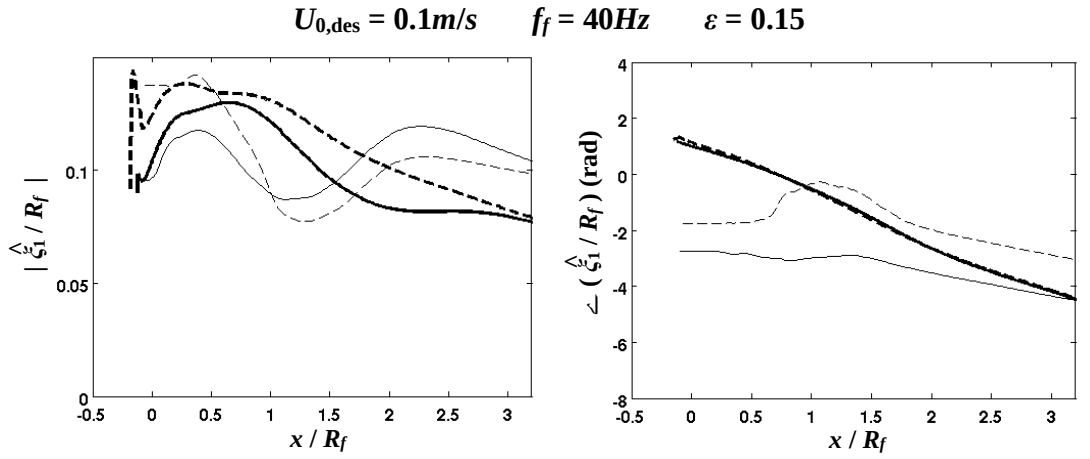

Figure K0.1 continued.

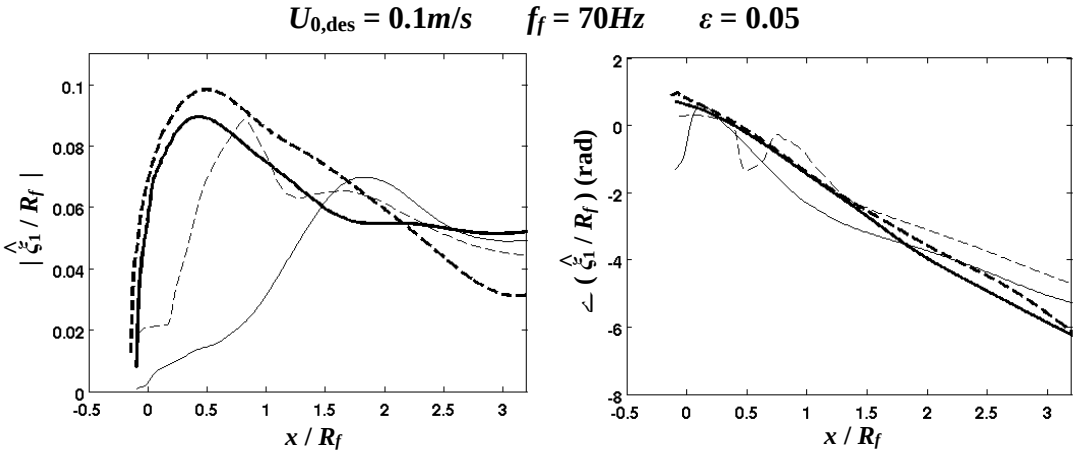

Figure K0.1 continued.

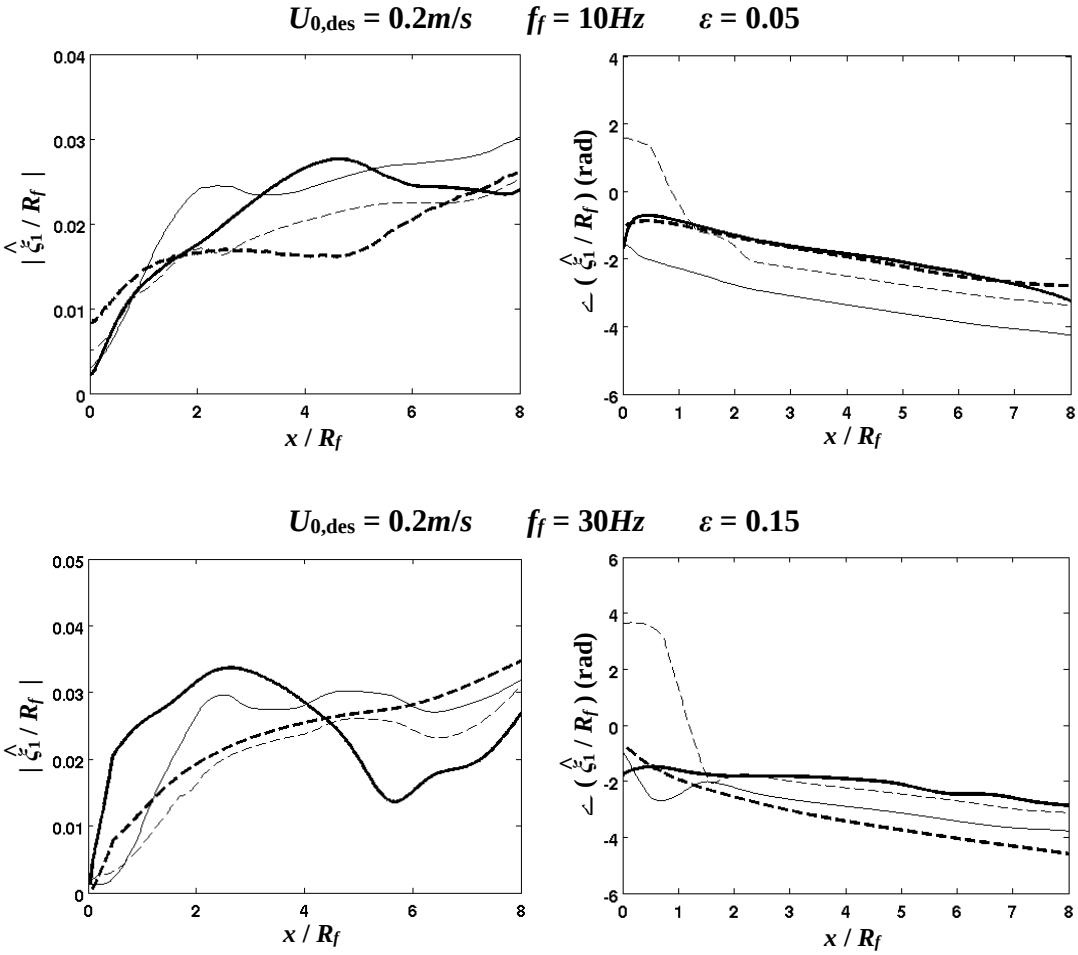

Figure K0.2. Additional space-time dynamic magnitude (left column) and phase (right column) comparisons between experimental (measured) and modeling (computed) results for an expanded set of data for $U_{0,des}$ = 0.2*m/s* and various f_f values. Note: axial velocity extrapolation occurs downstream of presented results, i.e. $x / R_f > 12$.

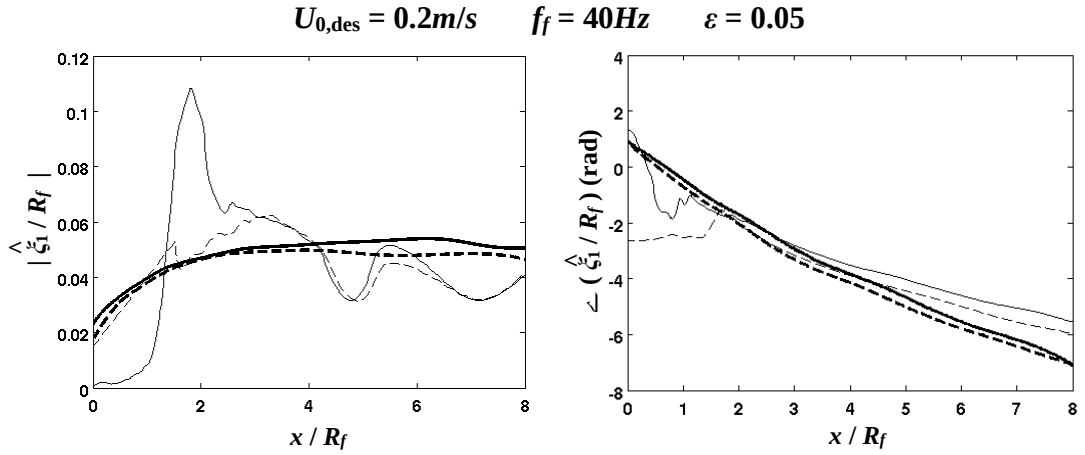

Figure K0.2 continued.

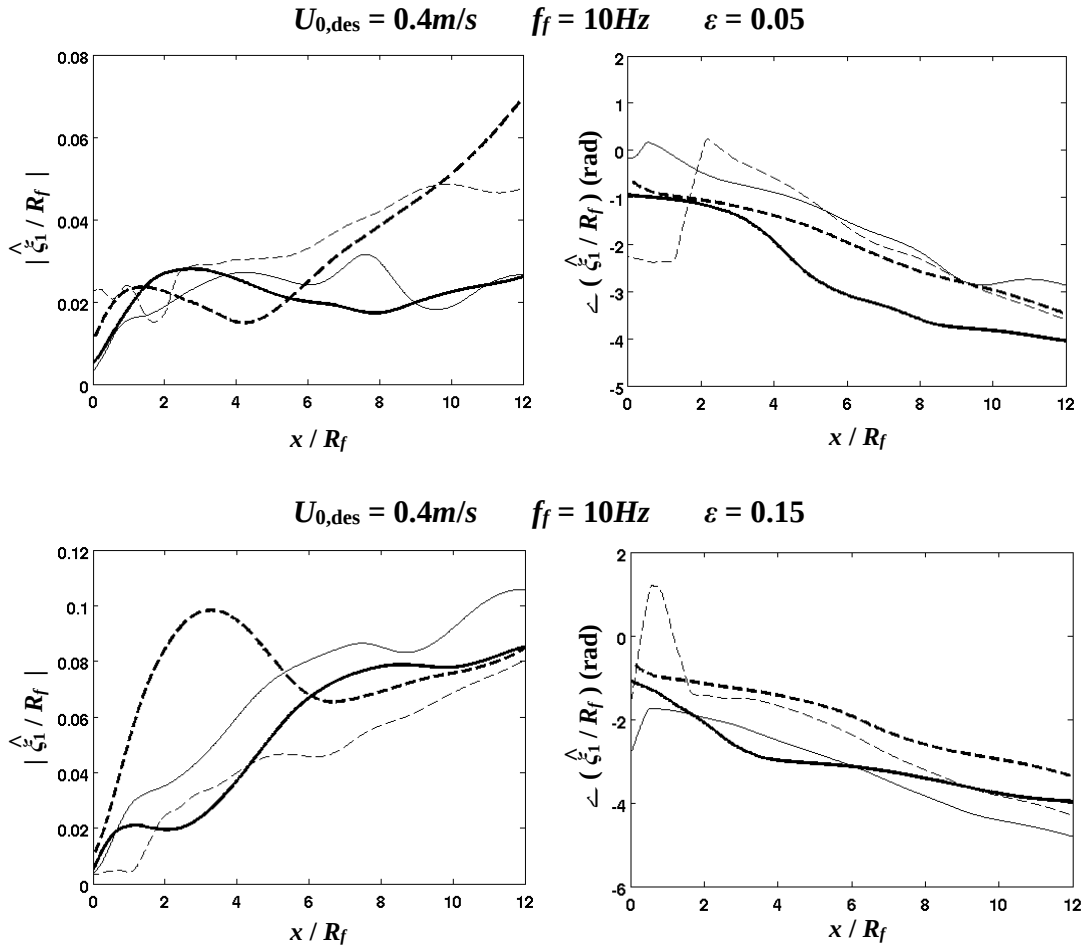

Figure K0.3. Additional space-time dynamic magnitude (left column) and phase (right column) comparisons between experimental (measured) and modeling (computed) results for an expanded set of data for $U_{0,des}$ = 0.4*m/s* and various f_f values. Note: axial velocity extrapolation occurs downstream of presented results, i.e. $x / R_f > 12$.

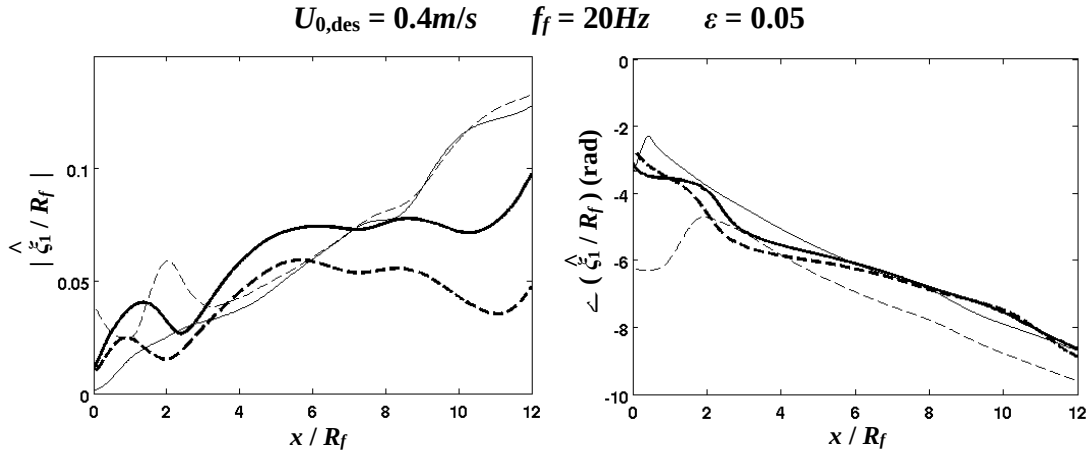

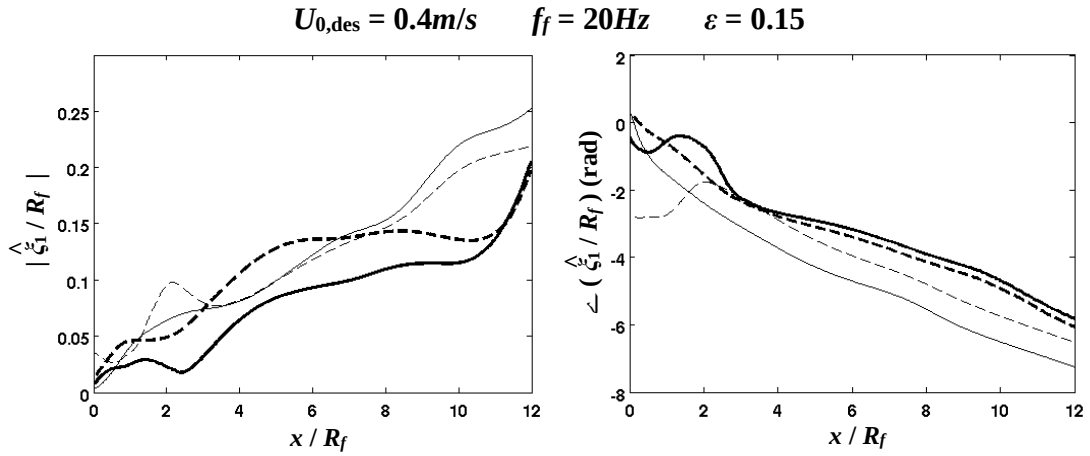

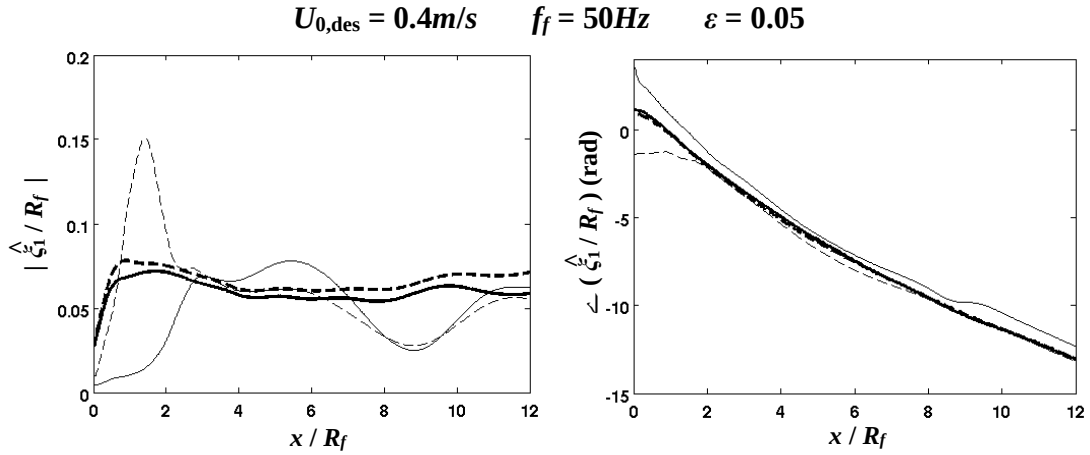

Figure K0.3 continued.

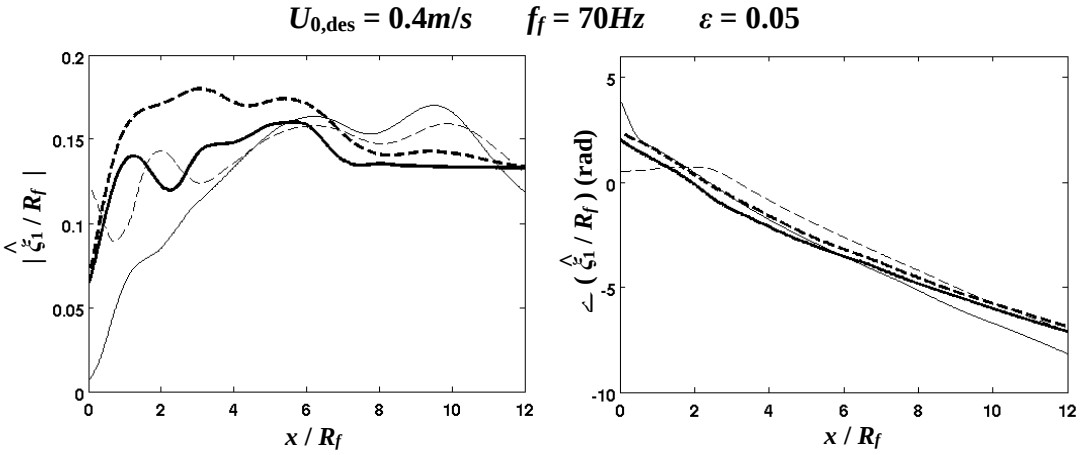

Figure K0.3 continued.

Appendix L

Section 7.4 discussed the limitations of the infinitely fast chemistry assumption. The modification of the flame thickness with velocity fluctuations was also discussed. Here we show a representative experimentally extracted fluctuating flame thickness, δ_f, amplitude as a function of axial location for Case C (listed in Table 6.2). To obtain the flame thickness, transverse cuts were taken from the filtered and transformed luminosity images, described in Figure 6.4. For each flame branch, the thickness was defined as the distance between the 80% max-branch luminosity intensity locations, as shown in the left plot of Figure L0.1. Computed at each axial location, results describing the fluctuating thickness amplitude as a function of axial location are shown on the right. A clear modulatory behavior can be observed, indicating that velocity fluctuations do in fact influence the flame thickness. Thus, the degree of finite rate effects, which are dependent upon flame thickness, would also be altered.

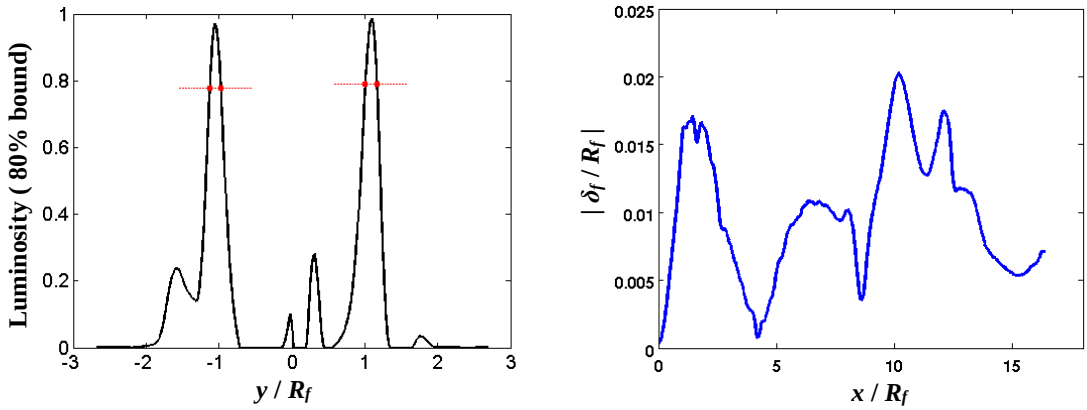

Figure L0.1. Representative results for Case C, describing (left) the experimental flame thickness extraction technique at an axial location of $x / R_f = 4$, and (right) the fluctuating flame thickness amplitude.

References

1. *First Flames: Earliest Man-Made Fire Found?* Evoanth.

2. *Combustion: Chemical Reactions.* Encyclopedia Britannica.

3. *http://www3.epa.gov/ttn/naaqs/criteria.html.*

4. Lieuwen, T., *Unsteady Combustor Physics*. 2013: Cambridge Press.

5. Lieuwen, T.C. and V. Yang, *Gas turbine emissions*. Vol. 38. 2013: Cambridge University Press.

6. Lieuwen, T.C. and V. Yang, *Combustion instabilities in gas turbine engines: operational experience, fundamental mechanisms and modeling*. 2005.

7. Tyndall, J., *Sound*. Vol. 3. 1877: D. Appleton.

8. Le Conte, J., Philosophical Magazine HP, (235).

9. Putnam, A.A., *Combustion-driven oscillations in industry*. 1971, New York : American Elsevier.

10. Larsen, C.E., *NASA Experience with Pogo in Human Spaceflight Vehicles*. 2008, NASA Engineering and Safety Center.

11. Denison, M.R., *A simplified model of unstable burning in solid propellants.* ARS Journal, 1961. **31**(8): p. 1112-1122.

12. Blomshield, F.S. *Historical Perspective of Combustion Instability in Motors: Case Studies*. in *37th AIAA Propulsion Conference*. July 2001. Salt Lake City, UT.

13. Rayleigh, J., *The Theory of Sound*. 1945, New York: Dover Publication.

14. Fureby, C., *A computational study of combustion instabilities due to vortex shedding.* Proceedings of the Combustion Institute, 2000. **28**(1): p. 783-791.

15. Bai, T., X.C. Cheng, B.R. Daniel, J.I. Jagoda, and B.T. Zinn, *Vortex shedding and periodic combustion processes in a Rijke type pulse combustor*. Combustion Science and Technology, 1993. **94**(1-6): p. 245-258.

16. Dowling, A.P., *Thermoacoustic Sources and Instabilities,* in *Modern Methods in Analytical Acoustics*, D.G. Crighton, et al., Editors. 1994, Springer-Verlag. p. 378-405.

17. Dowling, A.P., *A kinematic model of a ducted flame.* Journal of Fluid Mechanics, 1999. **394**: p. 51-72.

18. Barron, A.R., *Physical methods in chemistry and nano science.* Connexions: Houston, TX, 2012: p. 365.

19. Cowell, L., *Combustion and Fuels - Solar Turbines Incorporated.*

20. Khosravy el_Hossaini, M., *Review of the New Combustion Technologies in Modern Gas Turbines.* 2014.

21. Lieuwen, T., *Modeling premixed combustion-acoustic wave interactions: A review.* Journal of Propulsion and Power, 2003. **19**(5): p. 765-781.

22. Baillot, F., D. Durox, and R. Prud'Homme, *Experimental and theoretical study of a premixed vibrating flame.* Combustion and flame, 1992. **88**(2): p. 149-152, IN1, 153-168.

23. Huang, Y. and V. Yang, *Dynamics and Stability of Lean-Premixed Swirl-Stabilized Combustion.* Progress in Energy and Combustion Science, 2009. **35**: p. 293-364.

24. Preetham, S.H. and T. Lieuwen, *Dynamics of laminar premixed flames forced by harmonic velocity disturbances.* Journal of Propulsion and Power, 2008. **24**(6): p. 1390-1402.

25. Schuller, T., D. Durox, and S. Candel, *A unified model for the prediction of laminar flame transfer functions: comparisons between conical and V-flame dynamics.* Combustion and Flame, 2003. **134**(1-2): p. 21-34.

26. Boyer, L. and J. Quinard, *On the dynamics of anchored flames.* Combustion and flame, 1990. **82**(1): p. 51-65.

27. Fleifil, M., A.M. Annaswamy, Z.A. Ghoneim, and A.F. Ghoneim, *Response of a laminar premixed flame to flow oscillations: A kinematic model and thermoacoustic instability results.* Combustion and flame, 1996. **106**: p. 487-510.

28. Lee, J.G. and D.A. Santavicca, *Experimental diagnostics for the study of combustion instabilities in lean premixed combustors.* Journal of Propulsion and Power, 2003. **19**(5): p. 735-750.

29. Lee, J.G., K. Kim, and D.A. Santavicca, *Measurement of equivalence ratio fluctuation and its effect on heat release during unstable combustion.* Proceedings of the Combustion Institute, 2000. **28**(1): p. 415-421.

30. Palies, P., D. Durox, T. Schuller, and S. Candel, *The combined dynamics of swirler and turbulent premixed swirling flames.* Combustion and Flame, 2010. **157**(9): p. 1698-1717.

31. Durox, D., T. Schuller, N. Noiray, and S. Candel, *Experimental analysis of nonlinear flame transfer functions for different flame geometries.* Proceedings of the Combustion Institute, 2009. **32**(1): p. 1391-1398.

32. Kornilov, V.N., R. Rook, J.H.M. ten Thije Boonkkamp, and L.P.H. de Goey, *Experimental and numerical investigation of the acoustic response of multi-slit Bunsen burners.* Combustion and Flame, 2009. **156**(10): p. 1957-1970.

33. Giauque, A., L. Selle, L. Gicquel, T. Poinsot, H. Buechner, P. Kaufmann, and W. Krebs, *System identification of a large-scale swirled partially premixed combustor using LES and measurements.* Journal of Turbulence, 2005: p. N21.

34. Truffin, K. and T. Poinsot, *Comparison and extension of methods for acoustic identification of burners.* Combustion and Flame, 2005. **142**(4): p. 388-400.

35. Shreekrishna, S. Hemchandra, and T. Lieuwen, *Premixed flame response to equivalence ratio perturbations.* Combustion Theory and Modelling, 2010. **14**(5): p. 681-714.

36. Preetham, S.K. Thumuluru, H. Santosh, and T. Lieuwen, *Linear Response of Laminar Premixed Flames to Flow Oscillations: Unsteady Stretch Effects.* Journal of Propulsion and Power, 2010. **26**(3).

37. Hemchandra, S., N. Peters, and T. Lieuwen, *Heat release response of acoustically forced turbulent premixed flames—role of kinematic restoration.* Proceedings of the Combustion Institute, 2011. **33**(1): p. 1609-1617.

38. Shreekrishna and T. Lieuwen, *High Frequency Response of Premixed Flames to Acoustic Disturbances*, in *15th AIAA/CEAS Aeroacoustics Conference*. 2009: Miami, FL.

39. Palies, P., T. Schuller, D. Durox, and S. Candel, *Modeling of premixed swirling flames transfer functions.* Proceedings of the Combustion Institute, 2011. **33**(2): p. 2967-2974.

40. Ducruix, S., T. Schuller, D. Durox, and S. Candel, eds. *Combustion instability mechanism in premixed combustors*. Combustion instabilities in gas turbine engines: operational experience, fundamental mechanisms and modeling, ed. T. Lieuwen and V. Yang. Vol. 210. 2005, American Institute of Aeronautics and Astronautics.

41. Acharya, V., B. Emerson, U. Mondragon, C. Brown, D.H. Shin, V. McDonell, and T. Lieuwen, *Measurements and analysis of bluff-body flame response to transverse excitation.* ASME Turbo Expo, 2011.

42. Chamberlin, D. and A. Rose, *The flicker of luminous flames.* Industrial & Engineering Chemistry, 1928. **20**(10): p. 1013-1016.

43. Buckmaster, J. and N. Peters. *The infinite candle and its stability—a paradigm for flickering diffusion flames*. in *Symposium (International) on Combustion*. 1988. Elsevier.

44. Boulanger, J., *Laminar round jet diffusion flame buoyant instabilities: Study on the disappearance of varicose structures at ultra-low Froude number*. Combustion and flame, 2010. **157**(4): p. 757-768.

45. Kukuck, S. and M. Matalon, *The onset of oscillations in diffusion flames.* Combustion Theory and Modelling, 2001. **5**(2): p. 217-240.

46. Matalon, M., *Intrinsic flame instabilities in premixed and nonpremixed combustion.* Annu. Rev. Fluid Mech., 2007. **39**: p. 163-191.

47. Matalon, M., G. Ludford, and J. Buckmaster, *Diffusion flames in a chamber*. Acta Astronautica, 1979. **6**(7): p. 943-959.

48. Chen, L.-W., Q. Wang, and Y. Zhang, *Flow characterisation of diffusion flame under non-resonant acoustic excitation.* Experimental Thermal and Fluid Science, 2013. **45**: p. 227-233.

49. Huang, H.W., Q. Wang, H.J. Tang, M. Zhu, and Y. Zhang, *Characterisation of external acoustic excitation on diffusion flames using digital colour image processing.* Fuel, 2012. **94**: p. 102-109.

50. Wang, Q., H.W. Huang, H.J. Tang, M. Zhu, and Y. Zhang, *Nonlinear response of buoyant diffusion flame under acoustic excitation.* Fuel, 2013. **103**: p. 364-372.

51. Chrystie, R. and S.H. Chung, *Response to Acoustic Forcing of Laminar Coflow Jet Diffusion Flames.* Combustion Science and Technology, 2014. **186**(4-5): p. 409-420.

52. Williams, T.C., C.R. Shaddix, R.W. Schefer, and P. Desgroux, *The response of buoyant laminar diffusion flames to low-frequency forcing.* Combustion and Flame, 2007. **151**(4): p. 676-684.

53. Saito, M., M. Sato, and A. Nishimura, *Soot suppression by acoustic oscillated combustion.* Fuel, 1998. **77**(9): p. 973-978.

54. Ferreira, D., P. Lacava, M. Ferreira, and J. de Carvalho, JA, *NOx and CO emissions and soot presence in partially premixed acoustically excited flames.* Journal of the Energy Institute, 2009. **82**(3): p. 123-132.

55. Chung, S. and C. Law, *Burke–Schumann flame with streamwise and preferential diffusion.* Combustion Science and Technology, 1984. **37**(1-2): p. 21-46.

56. Mohammed, R.K., M.A. Tanoff, M.D. Smooke, A.M. Schaffer, and M.B. Long. *Computational and experimental study of a forced, timevarying, axisymmetric, laminar diffusion flame*. in *Proceedings of the Combustion Institute*. 1998. Elsevier.

57. Siwatch, V., B. Lawrence, S. Kuchibhatla, K. Annamalai, and D. Ranjan, *Excess Air, Schmidt Number, and NOx Formation in Laminar Jet Flames.* Combustion Science and Technology, 2014. **186**(12): p. 1936-1953.

58. Dworkin, S., B. Connelly, A. Schaffer, B. Bennett, M. Long, M. Smooke, M. Puccio, B. McAndrews, and J. Miller, *Computational and experimental study of a forced, time-dependent, methane–air coflow diffusion flame.* Proceedings of the Combustion Institute, 2007. **31**(1): p. 971-978.

59. Tyagi, M., N. Jamadar, and S. Chakravarthy, *Oscillatory response of an idealized two-dimensional diffusion flame: Analytical and numerical study.* Combustion and flame, 2007. **149**(3): p. 271-285.

60. Law, C. and S. Chung, *Steady state diffusion flame structure with Lewis number variations.* Combustion Science and Technology, 1982. **29**(3-6): p. 129-145.

61. Burke, S. and T. Schumann, *Diffusion flames.* Industrial & Engineering Chemistry, 1928. **20**(10): p. 998-1004.

62. Balasubramanian, K. and R. Sujith, *Nonlinear response of diffusion flames to uniform velocity disturbances.* Combustion science and technology, 2008. **180**(1-3): p. 418-436.

63. Balasubramanian, K. and R. Sujith, *Non-normality and nonlinearity in combustion-acoustic interaction in diffusion flames.* Journal of Fluid Mechanics, 2008. **594**: p. 29-58.

64. Tyagi, M., S. Chakravarthy, and R. Sujith, *Unsteady combustion response of a ducted non-premixed flame and acoustic coupling.* Combustion Theory and Modelling, 2007. **11**(2): p. 205-226.

65. Magri, L., K. Balasubramanian, R. Sujith, and M.P. Juniper, *Non-normality in combustion-acoustic interaction in diffusion flames: a critical revision.* arXiv preprint arXiv:1310.0238, 2013.

66. Magina, N., D.-H. Shin, V. Acharya, and T. Lieuwen, *Response of non-premixed flames to bulk flow perturbations.* Proceedings of the Combustion Institute, 2013. **34**(1): p. 963-971.

67. Magina, N., V. Acharya, T. Sun, and T. Lieuwen, *Propagation, dissipation, and dispersion of disturbances on harmonically forced, non-premixed flames.* Proceedings of the Combustion Institute, 2015. **35**(1): p. 1097-1105.

68. *http://achatespower.com/why-internal-combustion-engine/.*

69. *http://www.edmunds.com/car-reviews/features/why-the-internal-combustion-engine-is-the-future.html.*

70. *https://en.wikipedia.org/wiki/Energy_density.*

71. Williams, F.A., *Combustion theory*. 2nd ed. 1985, Menlo Park, Ca: Benjamin/Cummings Publishing Co.

72. Hirschfelder, J.O., C.F. Curtiss, R.B. Bird, and M.G. Mayer, *Molecular theory of gases and liquids*. Vol. 26. 1954: Wiley New York.

73. Law, C.K., *Combustion physics*. 2006: Cambridge Univ Pr.

74. Markstein, G., *Nonsteady flame propagation*. 1964: Published for and on behalf of Advisory Group for Aeronautical Research and Development, North Atlantic Treaty Organization by Pergamon Press.

75. Aldredge, R., *The speed of isothermal-front propagation in isotropic, weakly turbulent flows.* Combustion Science and Technology, 2006. **178**(7): p. 1201-1215.

76. Pitsch, H. and L. Duchamp de Lageneste, *Large-eddy simulation of premixed turbulent combustion using a level-set approach.* Proceedings of the Combustion Institute, 2002. **29**(2): p. 2001-2008.

77. Menon, S. and W.-H. Jou, *Large-Eddy Simulations of Combustion Instability in an Axisymmetric Ramjet Combustor*. Combustion Science and Technology, 1991. **75**(1-3): p. 53-72.

78. Vervisch, L., E. Bidaux, K. Bray, and W. Kollmann, *Surface density function in premixed turbulent combustion modeling, similarities between probability density function and flame surface approaches.* Physics of Fluids (1994-present), 1995. **7**(10): p. 2496-2503.

79. Pope, S., *The evolution of surfaces in turbulence.* International journal of engineering science, 1988. **26**(5): p. 445-469.

80. Trouvé, A. and T. Poinsot, *The evolution equation for the flame surface density in turbulent premixed combustion.* Journal of Fluid Mechanics, 1994. **278**: p. 1-31.

81. Candel, S.M. and T.J. Poinsot, *Flame stretch and the balance equation for the flame area*. Combustion Science and Technology, 1990. **70**(1-3): p. 1-15.

82. Marble, F.E. and J.E. Broadwell, *The coherent flame model for turbulent chemical reactions*. 1977, DTIC Document.

83. Kerstein, A.R., W.T. Ashurst, and F.A. Williams, *Field equation for interface propagation in an unsteady homogeneous flow field.* Physical Review A, 1988. **37**(7): p. 2728.

84. Do Carmo, M.P. and M.P. Do Carmo, *Differential geometry of curves and surfaces*. Vol. 2. 1976: Prentice-hall Englewood Cliffs.

85. Kollmann, W. and J. Chen. *Dynamics of the flame surface area in turbulent non-premixed combustion*. in *Symposium (International) on Combustion*. 1994. Elsevier.

86. Preetham, T., K. Sai, H. Santosh, and T. Lieuwen, *Linear Response of Laminar Premixed Flames to Flow Oscillations: Unsteady Stretch Effects.* Journal of Propulsion and Power, 2010. **26**(3): p. 524-532.

87. Wang, H.Y., C.K. Law, and T. Lieuwen, *Linear Response of Stretch-affected Premixed Flames to Flow Oscillations.* Combustion and flame, 2009: p. 889-895.

88. Shin, D.H., *Premixed flame kinematics in harmonically oscillating velocity field*, in *Aerospace engineering*. 2011, Georgia Institute of Technology: Atlanta.

89. Whitham, G., *A general approach to linear and non-linear dispersive waves using a Lagrangian.* Journal of Fluid Mechanics, 1965. **22**(02): p. 273-283.

90. Whitham, G., *Linear and nonlinear waves*. Vol. 226. 1974: Wiley New York.

91. Whitham, G. *Non-linear dispersive waves*. in *Proceedings of the Royal Society of London A: Mathematical, Physical and Engineering Sciences*. 1965. The Royal Society.

92. Shin, D.-H. and T. Lieuwen, *Flame wrinkle destruction processes in harmonically forced, laminar premixed flames.* Combustion and Flame, 2012. **159**(11): p. 3312-3322.

93. Magri, L. and M.P. Juniper, *Sensitivity analysis of a time-delayed thermo-acoustic system via an adjoint-based approach.* Journal of Fluid Mechanics, 2013. **719**: p. 183-202.

94. Blackstock, D.T., *Fundamentals of physical acoustics*. 2000: John Wiley & Sons.

95. O'Connor, J., V. Acharya, and T. Lieuwen, *Transverse combustion instabilities: Acoustic, fluid mechanic, and flame processes.* Progress in Energy and Combustion Science, 2015. **49**: p. 1-39.

96. Mongia, H., T. Held, G. Hsiao, and R. Pandalai, *Incorporation of combustion instability issues into design process: GE aeroderivative and aero engines experience.* Progress in astronautics and aeronautics, 2005. **210**: p. 43.

97. Cohen, J., G. Hagen, A. Banaszuk, S. Becz, and P. Mehta, *Attenuation of combustor pressure oscillations using symmetry breaking.* AIAA Paper No. GT2011-0060, 2011.

98. Smith, K.O. and J. Blust, *Combustion instabilities in industrial gas turbines: solar turbines' experience.* Progress in Astronautics and Aeronautics, 2005. **210**: p. 29.

99. Krebs, W., S. Bethke, J. Lepers, P. Flohr, B. Prade, C. Johnson, and S. Sattinger, *Thermoacoustic design tools and passive control: Siemens power generation approaches.* Progress in Astronautics and Aeronautics, 2005. **210**: p. 89.

100. Zellhuber, M., C. Meraner, R. Kulkarni, W. Polifke, and B. Schuermans, *Large eddy simulation of flame response to transverse acoustic excitation in a model reheat combustor*. Journal of Engineering for Gas Turbines and Power, 2013. **135**(9): p. 091508.

101. Elias, I., *Acoustical Resonances Produced by Combustion of a Fuel-Air Mixture in a Rectangular Duct.* The Journal of the Acoustical Society of America, 1959. **31**(3): p. 296-304.

102. Kaskan, W. and A. Noreen, *High-frequency oscillations of a flame held by a bluff body.* ASME Transactions, 1955. **77**(6): p. 855-891.

103. Macquisten, M., *Combustion oscillations in a twin-stream afterburner*. Journal of sound and vibration, 1995. **188**(4): p. 545-560.

104. Rogers, D.E., *A mechanism for high-frequency oscillation in ramjet combustors and afterburners.* Journal of Jet Propulsion, 1956. **26**(6): p. 456-462.

105. Karnesky, A. and S. Colucci, *Recent occurrences of combustion instability in solid rocket motors-An overview*. Journal of Spacecraft and Rockets, 1975. **12**(1): p. 33-38.

106. Price, E., *Solid Rocket Combustion Instability—An American Historical Account*. Nonsteady Burning and Combustion Stability of Solid Propellants, 1992. **143**: p. 1-16.

107. Berman, K., *Combustion studies with a rocket motor having a full-length observation window*. Journal of the American Rocket Society, 1952. **22**(2): p. 78-85.

108. Davis, D.W. and B. Chehroudi, *Shear-coaxial jets from a rocket-like injector in a transverse acoustic field at high pressures.* AIAA Paper, 2006(2006-758).

109. Ellis, M., G. Xia, V. Sankaran, W. Anderson, and C. Merkle. *Acoustic mode simulations in experimental rocket combustors*. in *41st Joint Propulsoin Conference and Exhibit*. 2005.

110. Harrje, D.T. and F.H. Reardon, *Liquid propellant rocket combustion instability. nasa sp-194.* NASA Special Publication, 1972. **194**.

111. Marshall, W., S. Pal, R. Woodward, R. Santoro, R. Smith, G. Xia, V. Sankaran, and C. Merkle. *Experimental and computational investigation of combustor acoustics and instabilities, Part II: Transverse modes*. in *44th aerospace sciences meeting and exhibit*. 2006.

112. Richecoeur, F., P. Scouflaire, S. Ducruix, and S. Candel, *High-frequency transverse acoustic coupling in a multiple-injector cryogenic combustor*. Journal of Propulsion and Power, 2006. **22**(4): p. 790-799.

113. O'Connor, J. and T. Lieuwen, *Disturbance field characteristics of a transversely excited burner.* Combustion Science and Technology, 2011. **183**(5): p. 427-443.

114. Acharya, V., D.-H. Shin, and T. Lieuwen, *Swirl effects on harmonically excited, premixed flame kinematics.* Combustion and flame, 2012. **159**(3): p. 1139-1150.

115. Sutherland, J., P. Smith, and J. Chen, *Quantification of differential diffusion in nonpremixed systems.* Combustion Theory and Modelling, 2005. **9**(2): p. 365-383.

116. Smith, L., R. Dibble, L. Talbot, R. Barlow, and C. Carter, *Laser Raman scattering measurements of differential molecular diffusion in nonreacting turbulent jets of H2/CO2 mixing with air.* Physics of Fluids (1994-present), 1995. **7**(6): p. 1455-1466.

117. Smith, L., R. Dibble, L. Talbot, R. Barlow, and C. Carter, *Laser Raman scattering measurements of differential molecular diffusion in turbulent nonpremixed jet flames of H2CO2 fuel.* Combustion and flame, 1995. **100**(1): p. 153-160.

118. Chen, Y.-c. and J.-Y. Chen, *Fuel-dilution effect on differential molecular diffusion in laminar hydrogen diffusion flames.* Combustion Theory and Modelling, 1998. **2**(4): p. 497-514.

119. Kronenburg, A. and R. Bilger, *Modelling of differential diffusion effects in nonpremixed nonreacting turbulent flow.* Physics of Fluids (1994-present), 1997. **9**(5): p. 1435-1447.

120. Lam, S. and J. Bellan, *On de-coupling of Shvab-Zel'dovich variables in the presence of diffusion.* Combustion and flame, 2003. **132**(4): p. 691-696.

121. Costa, F.d.S., *Effects of differential diffusion on unsteady diffusion flames.* International communications in heat and mass transfer, 1998. **25**(2): p. 237-244.

122. Shaddix, C.R., J.E. Harrington, and K.C. Smyth, *Quantitative measurements of enhanced soot production in a flickering methane/air diffusion flame.* Combustion and Flame, 1994. **99**(3): p. 723-732.

123. Kaplan, C.R., C.R. Shaddix, and K.C. Smyth, *Computations of enhanced soot production in time-varying CH 4/air diffusion flames.* Combustion and Flame, 1996. **106**(4): p. 392-405.

124. Acharya, V.S., D.-H. Shin, and T. Lieuwen, *Premixed flames excited by helical disturbances: Flame wrinkling and heat release oscillations.* Journal of Propulsion and Power, 2013. **29**(6): p. 1282-1291.

125. Michalke, A., *Survey on jet instability theory.* Progress in Aerospace Sciences, 1984. **21**: p. 159-199.

126. Crocco, L. and S.-I. Cheng, *Theory of combustion instability in liquid propellant rocket motors*. 1956: Cambridge Univ Press.

127. Emerson, B., U. Mondragon, V. Acharya, D.-H. Shin, C. Brown, V. McDonell, and T. Lieuwen, *Velocity and flame wrinkling characteristics of a transversely forced, bluff-body stabilized flame, part I: experiments and data analysis.* Combustion Science and Technology, 2013. **185**(7): p. 1056-1076.

128. Acharya, V., B. Emerson, U. Mondragon, D.-H. Shin, C. Brown, V. McDonell, and T. Lieuwen, *Velocity and flame wrinkling characteristics of a transversely forced, bluff-body stabilized flame, Part II: Flame response modeling and comparison with measurements.* Combustion Science and Technology, 2013. **185**(7): p. 1077-1097.

129. Malanoski, M., M. Aguilar, V. Acharya, and T. Lieuwen. *Dynamics of a Transversely Excited Swirling, Lifted Flame: Part I—Experiments and Data Analysis*. in *ASME Turbo Expo 2013: Turbine Technical Conference and Exposition*. 2013. American Society of Mechanical Engineers.

130. Kim, K., J. Lee, B. Quay, and D. Santavicca, *Spatially distributed flame transfer functions for predicting combustion dynamics in lean premixed gas turbine combustors.* Combustion and Flame, 2010. **157**(9): p. 1718-1730.

131. Balachandran, R., B. Ayoola, C. Kaminski, A. Dowling, and E. Mastorakos, *Experimental investigation of the nonlinear response of turbulent premixed flames to imposed inlet velocity oscillations.* Combustion and Flame, 2005. **143**(1-2): p. 37-55.

132. Armitage, C., R. Balachandran, E. Mastorakos, and R. Cant, *Investigation of the nonlinear response of turbulent premixed flames to imposed inlet velocity oscillations.* Combustion and Flame, 2006. **146**(3): p. 419-436.

133. Swaminathan, N., R. Balachandran, G. Xu, and A. Dowling, *On the correlation of heat release rate in turbulent premixed flames.* Proceedings of the Combustion Institute, 2010.

134. Cheung, W., G. Sims, R. Copplestone, J. Tilston, C. Wilson, S.R. Stow, and A.P. Dowling. *Measurement and analysis of flame transfer function in a sector combustor under high pressure conditions*. in *ASME Turbo Expo 2003, collocated with the 2003 International Joint Power Generation Conference*. 2003. American Society of Mechanical Engineers.

135. Freitag, E., H. Konle, M. Lauer, C. Hirsch, and T. Sattelmayer. *Pressure influence on the flame transfer function of a premixed swirling flame*. in *ASME Turbo Expo 2006: Power for Land, Sea, and Air*. 2006. American Society of Mechanical Engineers.

136. Chen, L.-W., Q. Wang, and Y. Zhang, *Flow characterisation of diffusion flame in a standing wave.* Experimental Thermal and Fluid Science, 2012. **41**: p. 84-93.

137. Davis, M. and L.H. Lin, *Structures induced by periodic acoustic excitation of a diffusion flame.* Combustion and flame, 1995. **103**(3): p. 151-160.

138. Cetegen, B.M. and S. Basu, *Soot topography in a planar diffusion flame wrapped by a line vortex.* Combustion and Flame, 2006. **146**(4): p. 687-697.

139. Barve, V.V., N.T. Clemens, O.A. Ezekoye, and V. Katta, *Soot production rates in strongly forced methane-air laminar diffusion flames.* 2006.

140. Wang, Q., J. Yang, H.W. Huang, Y. Zhang, and C. Zhao, *Three-dimensional investigation of the dynamics of a propane diffusion flame.* Fuel, 2014. **116**: p. 448-454.

141. Chen, T., U. Hegde, B. Daniel, and B. Zinn, *Flame radiation and acoustic intensity measurements in acoustically excited diffusion flames.* Journal of Propulsion and Power, 1993. **9**(2): p. 210-216.

142. Idahosa, U., A. Saha, C. Xu, and S. Basu, *Non-premixed acoustically perturbed swirling flame dynamics.* Combustion and Flame, 2010. **157**(9): p. 1800-1814.

143. Magina, N.A. and T.C. Lieuwen. *Effect of axial diffusion on the response of over-ventilated diffusion flames to axial flow perturbations*. in *52nd Aerospace Science Meeting*. 2014.

144. Shanbhogue, S., D.H. Shin, S. Hemchandra, D. Plaks, and T. Lieuwen, *Flame sheet dynamics of bluff-body stabilized flames during longitudinal acoustic forcing.* Proceedings of the Combustion Institute, 2009. **32**(2): p. 1787-1794.

145. Ducruix, S., T. Schuller, D. Durox, and S. Candel, *Combustion dynamics and instabilities: Elementary coupling and driving mechanisms.* Journal of propulsion and power, 2003. **19**(5): p. 722-734.

146. Melling, A., *Tracer particles and seeding for particle image velocimetry.* Measurement Science and Technology, 1997. **8**(12): p. 1406.

147. Willert, C.E. and M. Gharib, *Digital particle image velocimetry.* Experiments in fluids, 1991. **10**(4): p. 181-193.

148. Soria, J., A. Masri, and D. Honnery. *An adaptive cross-correlation digital PIV technique for unsteady flow investigations*. in *Proceedings of the 1st Australian Conference on Laser Diagnostics in Fluid Mechanics and Combustion, Sydney, NSW, Australia*. 1996.

149. Shin, D., S. Shanbhogue, and T. Lieuwen. *Premixed Flame Kinematics in an Axially Decaying, Harmonically Oscillating Vorticity Field*. 2008.

150. Monkewitz, P.A., *A note on vortex shedding from axisymmetric bluff bodies.* Journal of Fluid Mechanics, 1988. **192**: p. 561-575.

151. Sheridan, J., J. Soria, W. Jie, and M. Welsh, *The Kelvin-Helmholtz instability of the separated shear layer from a circular cylinder*, in *Bluff-Body Wakes, Dynamics and Instabilities*. 1993, Springer. p. 115-118.

152. Hirschfelder, J.O., R.B. Bird, and E.L. Spotz, *The Transport Properties for Non-Polar Gases.* The Journal of Chemical Physics, 1948. **16**(10): p. 968-981.

153. Bird, R.B., W.E. Stewart, and E.N. Lightfoot, *Transport phenomena. 1960.* Madison, USA, 1960.

154. Fuller, E.N., P.D. Schettler, and J.C. Giddings, *New method for prediction of binary gas-phase diffusion coefficients.* Industrial & Engineering Chemistry, 1966. **58**(5): p. 18-27.

155. Xiong, Y., M.S. Cha, and S.H. Chung, *Fuel density effect on near nozzle flow field in small laminar coflow diffusion flames.* Proceedings of the Combustion Institute, 2015. **35**(1): p. 873-880.

156. Ellzey, J. and E. Oran. *Effects of heat release and gravity on an unsteady diffusion flame*. in *Symposium (International) on Combustion*. 1991. Elsevier.

157. Mitchell, R.E., A.F. Sarofim, and L. Clomburg, *Experimental and numerical investigation of confined laminar diffusion flames.* Combustion and flame, 1980. **37**: p. 227-244.

158. Norton, T.S., K.C. Smyth, H.J. Miller, and M.D. Smooke, *Comparison of experimental and computed species concentration and temperature profiles in laminar, two-dimensional methane/air diffusion flames.* Combustion Science and Technology, 1993. **90**(1-4): p. 1-34.

159. Buckmaster, J., P. Clavin, A. Linan, M. Matalon, N. Peters, G. Sivashinsky, and F. Williams, *Combustion theory and modeling.* Proceedings of the Combustion Institute, 2005. **30**(1): p. 1-19.

160. Katta, V., L. Goss, and W. Roquemore, *Effect of nonunity Lewis number and finite-rate chemistry on the dynamics of a hydrogen-air jet diffusion flame.* Combustion and Flame, 1994. **96**(1): p. 60-74.

161. Egolfopoulos, F. *Geometric and radiation effects on steady and unsteady strained laminar flames*. in *Symposium (International) on Combustion*. 1994. Elsevier.

162. Sohn, C., J. Kim, S. Chung, and K. Maruta, *Nonlinear evolution of diffusion flame oscillations triggered by radiative heat loss.* Combustion and Flame, 2000. **123**(1): p. 95-106.

163. Buckmaster, J.D., *Edge Flames.* Journal of Engineering Mathematics, 1997. **31**: p. 269-284.

164. Buckmaster, J. and R. Weber. *Edge-flame-holding*. in *Symposium (International) on Combustion*. 1996. Elsevier.

165. Kaplan, C., E. Oran, K. Kailasanath, and H. Ross. *Gravitational effects on sooting diffusion flames*. in *Symposium (International) on Combustion*. 1996. Elsevier.

166. Katta, V., L. Goss, and W. Roquemore, *Numerical investigations of transitional H2/N2 jet diffusion flames.* AIAA journal, 1994. **32**(1): p. 84-94.

167. Edelman, R.B., O.F. Fortune, G. Weilerstein, T.H. Cochran, and J.B. Haggard. *An analytical and experimental investigation ofgravity effects upon laminar gas jet-diffusion flames*. in *Symposium (International) on Combustion*. 1973. Elsevier.

168. *www.nasa.gov.*